TECHNISCHE UNIVERSITÄT ILMENAU

Fakultät für Elektrotechnik und Informationstechnik

Extending TDL Based Non-WSSUS Vehicle-to-Everything Channel Model

Nina Aziz Hassan Hassan

Dissertation zur Erlangung des
akademischen Grades Doktor-Ingenieur (Dr.-Ing.)

Anfertigung im : Fachgebiet Elektronische Messtechnik und Signalverarbeitung
Institut für Informationstechnik
Fakultät für Elektrotechnik und Informationstechnik

Gutachter : Univ.-Prof. Dr.-Ing. habil. Reiner S. Thomä
Univ.-Prof. Dr.-Ing. Jörg Robert
Univ.-Prof. Dr.-Ing. Joao Paulo Javidi da Costa

Vorgelegt am: 05.04.2022
Verteidigt am: 12.05.2023

DOI: 10.22032/dbt.57974
URN: urn:nbn:de:gbv:ilm1-2023000214

Abstract

In the past decades, wireless communication systems have undergone rapid development, and many investigations have been done since Maxwell predicted the existence of electromagnetic waves. In recent years, vehicle to X (V2X) communication research has been growing steadily. V2X describes the ability to transmit data between a vehicle (V) and "everything". In the future, vehicles might be able to communicate with their environment to prevent traffic accidents and reduce congestion by allowing vehicles to transmit and receive data through a vehicular ad hoc network at their speed and position. In order to achieve the ultimate goal of enhancing transportation safety, it is crucial to establish reliable communication links. The main challenge of vehicular communications introduces new properties because the physical layer properties are rapidly changing due to inherent mobility within the channel, high vehicle speeds, varying antenna positions, and many handovers due to smaller cells. This brings up a number of challenges in terms of channel characterization because it is a strong time-variant channel and many transitions occur; therefore, it is a non-stationary channel.

In this thesis, non-stationary tapped delay line (TDL) models are used to describe the vehicle to infrastructure (V2I) channels. This thesis proposes a new strategy to extract TDL channel model parameters from measurement data. The proposed approach is based on an existing method to derive parameters for a TDL model. It will be shown that with a different method of choosing taps, the number of taps necessary to regenerate the root mean square delay spread (RMS-DS) of a channel can be significantly reduced. An approach is proposed to verify the correctness of the channel model parameters derivation. The feasibility of the method will be confirmed using channel-sounding measurements.

This dissertation devises a generator to produce channel impulse responses (CIRs) and describes the non-stationary behavior of the channels via employing an ON/OFF process. Different order Markov chains are modeled with the aim of better capturing the non-stationary behavior. The investigation shows that first-order two-state Markov chains are preferable to represent multipath's frequent ON/OFF behavior, and the second- and third-order Markov models do not make enormous effects.

A method for extending a single input single output (SISO)-TDL model to multiple input multiple output (MIMO) under non-wide sense stationary uncorrelated scattering (non-WSSUS) assumption is introduced to develop TDL channel models for the V2I MIMO systems. The analysis evaluates SISO-with MIMO-configuration in terms of channel capacity. Different MIMO configurations are explored, and it will be illustrated that the position of antennas plays an important role. Using only four antennas at the transmitter (Tx) and receiver (Rx) that radiate towards different directions will make a qualitative leap in the performance of the system.

Zusammenfassung

In den vergangenen Jahrzehnten haben drahtlose Kommunikationssysteme eine rasante Entwicklung durchgemacht und es wurden viele Untersuchungen durchgeführt, seit Maxwell die Existenz von elektromagnetischer Wellen vorausgesagt hat. In den letzten Jahren hat die Forschung im Bereich der vehicle to X (V2X)-Kommunikation stetig zugenommen. V2X beschreibt die Fähigkeit, Daten zwischen einem Fahrzeug oder vehicle (V) und "allem" zu übertragen. In Zukunft könnten Fahrzeuge mit ihrer Umgebung kommunizieren, um Verkehrsunfälle zu vermeiden und Staus zu verringern. Dazu werden sie ihr Geschwindigkeits- und Positionsdaten über Ad-hoc-Fahrzeugnetze senden und empfangen können. Um die Verkehrssicherheit zu erhöhen, ist eine zuverlässige Kommunikationsverbindung notwendig. Die größte Herausforderung bei der Fahrzeugkommunikation besteht darin, dass sich die Eigenschaften des Physical Layers aufgrund der inhärenten Mobilität innerhalb des Kanals, der hohen Fahrzeuggeschwindigkeiten, der unterschiedlichen Antennenpositionen und der vielen Handover aufgrund kleinerer Zellen schnell ändern. Dies bringt eine Reihe von Herausforderungen in Bezug auf die Kanalcharakterisierung mit sich. Es handelt sich um einen Kanal mit starker Zeitvarianz und es treten viele Übergänge auf. Somit handelt es sich um einen nicht-stationärer (non-stationary) Kanal.

Das Hauptziel dieser Untersuchung ist es, eine Methode zu finden, mit der der Kanal einer komplexen Umgebung in einer einfachen Form mit weniger strengen Beziehungen zur Geometrie dargestellt werden kann. Dabei werden die statistischen Eigenschaften ähnlich der Messdaten beibehalten. In dieser Arbeit werden nicht-stationäre tapped delay line (TDL)-Modelle verwendet, um vehicle to infrastructure (V2I)-Kanäle zu beschreiben. Es wird eine neue Strategie zur Extraktion von TDL-Kanalmodellparametern aus Messdaten vorgeschlagen. Dieser Ansatz basiert auf einer bestehenden Methode zur Ableitung von Parametern für ein TDL-Modell. Es wird gezeigt, dass mit einer anderen Methode zur Auswahl der Taps die Anzahl der Abgriffe, die zur Rekonstruktion der root mean square delay spread (RMS-DS) eines Kanals erforderlich sind, erheblich reduziert werden kann. Ein neuer Ansatz zur überprüfen der Korrektheit der Ableitung der Kanalmodellparameter wird aufgezeigt. Die Durchführbarkeit der Methode wird anhand von Channel Sounding Messungen bestätigt.

In dieser Dissertation wird ein Generator zur Erzeugung von Kanalimpulsantworten entwickelt und das nicht-stationäre Verhalten der Kanäle durch die Verwendung eines ON/OFF-Prozesses beschrieben. Es werden Markov-Ketten unterschiedlicher Ordnung modelliert, um das nicht-stationäre Verhalten besser zu erfassen. Die Untersuchung zeigt, dass Markov-Ketten erster Ordnung mit zwei Zuständen vorzuziehen sind, um das häufige ON/OFF-Verhalten von Mehrwegpfaden darzustellen, und dass die Markov-Modelle zweiter und dritter Ordnung keine großen Auswirkungen haben.

Eine Methode zur Erweiterung eines single input single output (SISO)-TDL-Modells auf multiple input multiple output (MIMO) unter der non-wide sense stationary uncorrelated scattering (non-WSSUS)-Annahme wird eingeführt, um TDL-Kanalmodelle für V2I MIMO-Systeme zu entwickeln. Die Analyse

bewertet die SISO- mit der MIMO-Konfiguration in Bezug auf die Kanalkapazität. Es werden verschiedene MIMO-Konfigurationen untersucht, und es wird gezeigt, dass die Position der Antennen eine wichtige Rolle spielt. Die Verwendung von nur vier Antennen am transmitter (Tx) und receiver (Rx), die in unterschiedliche Richtungen abstrahlen, führt zu einem qualitativen Sprung in der Leistungsfähigkeit des Systems.

Acknowledgements

First and foremost, I would like to thank my supervisor prof. Reiner Thomä and my co-supervisor prof. Giovanni Del Galdo for the opportunities provided through the years to pursue my doctorate studies, especially working with and learning from them. Without their support, guidance, and knowledge, this thesis would hardly have been possible. I would also like to thank Prof. Joao Paulo, and Prof. Jörg Robert for agreeing to review my investigation.

I also like to thank three colleagues, Martin Käske, Christian Schneider, and Daniel Czaniera, for their scientific discussions and for providing the analysis of the surrounding environment of our measurement data. They analyzed the surrounding environment for the project named under V2X Measurements, Analysis and Modelling. A special thank goes to our great colleagues and friends inside and outside the department, especially Daniel Stanko, Maija Ozola-Schade, Mikus Grasis, Mostafa Alazab, Niklas Bräunlich, Myint Saw James, and Jhohan chavez Vega. I am especially grateful to Prof. David Matolak from University of South Carolina for his kind support, which has been essential throughout my scientific growth.

I would like to thank Dr Jürgen Beyer, Robert Linz, Jürgen Müller, and Heinz Droste from the Deutsche Telekom AG for their support during the channel sounding campaign, which was funded by the Deutsche Telekom AG. I would like to express my appreciation to Dr. Jürgen Beyer, who did a lot in detecting different scenarios in measurement data by using a raytracer. Thank you!

I love to thank Mario Schau, who has been there for me during my ups and downs, and listened to me all the time. Thanks to all my friends, who made my journey enjoyable, especially Yessi, Nesrine, Majia, Natasha, Sepideh, Miguel, Boris and Gise. Lastly, I extend my sincerest appreciation to my family for their unwavering encouragement and support throughout the years. No matter how old I am, I will always need you, Mom. Thank you for always being there for me.

Ilmenau, 23.02.2022

Nina Hassan

to my dad in heaven

Contents

Chapter 1

Introduction

1.1 Motivation and Context of the Goal

The Propagation Channel for Wireless Communication Systems

In the past decades, wireless communication systems have undergone rapid development, and many investigations have been done since Maxwell predicted the existence of electromagnetic waves. A significant number of techniques have been applied in a variety of ways in the area of wireless communication. For instance, it is easy to identify the use of wireless communication techniques for the operation of global positioning system (GPS) or cell phones. The term "wireless communication" comes from the earlier "radio communication," which describes transmitting any information without the use of cables such as fiber cables. It provides transmitting information with cheaper and more convenient alternatives, but sometimes worse qualities in comparison to the wired case. In communication systems, the physical medium between the transmitter (Tx) and receiver (Rx) is termed the channel, which may be subject to unpredictable signal distortions and delays. In wireless communication systems, there are other critical issues such as limited bandwidth, user privacy, and information security; therefore, in the design and deployment of a system, there are always numerous trade-offs to be addressed [96, 155]. Here, it is worth discussing the definition of channel characterization. The channel can be defined as the "object under study" [155]. The complete set of parameters for the complete set of paths in the frequency band of interest determines the channel. The term "characterization" refers to a good description of the channel over a spatial region of interest [155].

In recent years, vehicle to X (V2X) has been a hot topic and many researchers have performed research in the field of vehicular communication systems. V2X describes the ability to transmit data between a vehicle (V) and "everything" e.g., X. In general, there are mainly four possible node types to be deployed in V2X communication systems that are vehicle to vehicle (V2V), vehicle to infrastructure (V2I), vehicle to pedestrian (V2P), and Vehicle to Network (V2N) [3, 81]. V2X communication system is an essential topic of current research as it makes transportation safer and more efficient. In the future, vehicles might be able to communicate with their environments, such as other vehicles, roadside units, and many more. The goal of the V2X communication system is to prevent traffic accidents, improve transportation safety, and reduce congestion. In the event of presumed accident risk, a driver can receive a warning, or a vehicle might be able to take preventive actions itself, e.g., emergency braking. Furthermore, vehicle crashes are due to different factors, such as bad weather, vehicle mechanical problems, or drivers' behaviors. Drivers

are considered to cause around 90% of overall accidents, especially chain collisions caused by drivers' inability to react in time in emergency situations [24]. The study [161] shows that if the vehicle operator was provided a warning at least one-half second prior to a collision, about 60% of roadway collisions could be avoided. Hence, in order to achieve the ultimate goal to enhance transportation safety, it is crucial to establish reliable communication links between those various partners. The channel characterization of such applications should contain a set of channel models in order to assist evaluations. These models are defined by sets of parameters that are defined mathematically and by their structure. A way how to interpret there models is that they can be used as blocks in a cascade of models in wireless communication systems, as illustrated in Fig. 1.1 [96].

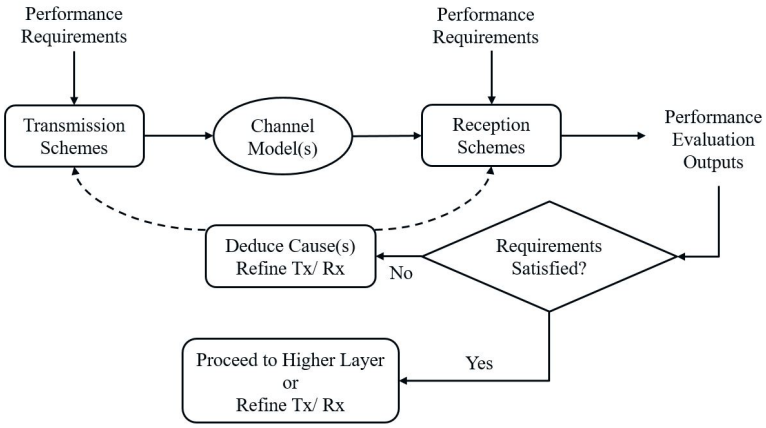

Fig. 1.1 Conceptual illustration of use of channel model, note adapted from [96]

In Fig. 1.1, the ellipse block and rectangular ends components lie within the physical layer (PHY) of the communications network stack, whereas the parameters and settings of the medium access control (MAC) layer and data link layer (DLL) can be incorporated. The value of parameters of the transmission scheme, such as the required bit rate, and the value of parameters of the reception scheme are specified performance requirements of the communication system, as indicated in Fig. 1.1. The performance evaluation output for a given transmission- and reception-scheme often depends strongly upon the channel model(s) used. If the performance evaluation outputs indicate that the system will not meet requirements, then appropriate remedies can be added at the transmission- or reception-scheme or both ends with knowledge of the channel, and the evaluation will be repeated. On the other hand, if the performance evaluation outputs will meet the system requirements, then system design can proceed on to higher layers. As a consequence, the design and performance prediction for higher layers in the communications protocol stack depends upon the physical layer performance characterization. Thus, it is an indispensable part of the system because it directly affects the medium access control and data link layers [1], and through those layers, it affects the performance of the higher layers [96, 134].

Channel Modeling

Universally, the use of channel models is accepted as an important element of system design, evaluation, and optimization [6, 96, 139, 155]. Proper developed models and simulations are much like a laboratory

[1] Examples of physical and data link layer design items such as forward error correction coding, companion interleaving schemes, modulation, signal bandwidth, and receiver processing algorithms. Example of channel parameters has a significant effect on the system design parameters, such as multipath delay spread affecting symbol rate, and channel attenuation affects transmit power, modulation, detection type, and link ranges [6, 16, 23, 27, 59, 90, 117, 133, 137, 139, 155].

implementation of a system; thus, a valuable tool for gaining insight into system behavior is simulation [146]. Since parameter values can be changed at will, such as signal to noise ratio (SNR) and filter bandwidth (B), the effects of these changes can quickly be observed on system performance [146]. The evaluation of a system using a channel model developed from measured data provides realistic estimates [6, 16, 90, 96, 133, 139, 155]. This brings us to the conclusion that an accurate propagation channel model is required to achieve the optimum performance of any wireless system. Before the system is actually deployed, an appropriate modulation scheme, error correction coding techniques, and equalization technique can be selected by using the precise knowledge of the channel [12, 23, 27, 59, 117, 137]. These are key steps before actual system deployment to avoid expensive remedial approaches after deployment.

The channel models developed in this investigation are based upon both theory and measurements; therefore, these models are in this dual sense more "realistic" than models based upon analysis only. These models can be used by any engineers or researchers, who evaluate the performance of V2I communication systems [2]. The goal of channel modeling is in general to find a method of describing or generating the channel impulse response (CIR) of the radio channel. There are different methods known in the literature, where either the CIR is determined directly or indirectly by means of a geometrical model of the propagation environment. In the literature, channel models can be categorized into two classes, which are stochastic models and geometry based deterministic models (GBDMs). The stochastic models can be classified as the non-geometrical stochastic models (NGSMs) and geometry based stochastic models (GBSMs) [85, 152]. GBDM is a deterministic approach and characterizes channel parameters in a deterministic manner as considered in [101]. The drawback of such models cannot easily be generalized. In the GBSMs, predefined stochastic distribution of effective scatters around the Tx, and the Rx is used to simulate the channel. The GBSMs can be further classified into the irregular-shaped geometry based stochastic model (GBSM) and the regular-shaped GBSM, more detail can be found in [14, 80]. The GBSMs can be generalized to more scenarios due to the static nature of the geometry. Static discrete scatters, mobile discrete scatters, and diffuse scatters are randomly generated, but as claimed in [85], the non-wide sense stationary uncorrelated scattering (non-WSSUS) properties of the V2X channels cannot be fully represented by this model. The non-geometrical stochastic model (NGSM) characterizes typical channel parameters in a completely statistical manner [7, 85, 152], and it can be extended via Markov chains models to represent the non-WSSUS properties of the V2X channels as in [93, 96, 129]. The main goal of this investigation is to find a method that captures the statistical properties of the channel in a similar way to real measurement data. By keeping the statistical measures similar to the measured data, researchers can evaluate the performance of communication systems, such as signal processing algorithms or wireless protocols under realistic channel conditions. Radio channel models for 20 MHz channel bandwidth in a form of tapped delay line (TDL) model will be developed to cover a different number of scenarios and capture the primary behavior of V2I channels. TDL models are based on the concept that the wireless channel can be represented as a superposition of delayed versions of the transmitted signal, each with a specific delay and amplitude. These taps correspond to the multipath components of the channel, including the direct path, scattering and reflections from various obstacles. A detailed literature review is provided to clearly confirm that our investigation in the environment of interest and the band of interest has not been previously studied.

Since the licensed frequency range for intelligent transport systems (ITS) applications is in a range of 5.85 GHz to 5.925 GHz [2], many channel measurements have been conducted in that range or close to

[2] V2I technologies allow vehicles to exchange information with road systems (such as traffic lights, lamps, cameras, lane markers) to collect data about a particular situation.

it as in [4, 12, 78, 111]; therefore, most likely communications of V2X applications are to be in the 5 GHz range. Other measurements have been made in slightly lower center frequencies, such as 5.2 GHz [77,112]. Besides the IEEE802.11p standard, another well-known standard for dealing with V2X communications is long term evolution-vehicle (LTE-V) [30,104]. Since the foundation is built by long term evolution (LTE), a variety of frequencies becomes available. This means, at those different frequencies, further measurements must be conducted in order to understand the respective characteristics of the V2X channel. Our measurement campaign was executed in the frequency region of about 2.5 GHz to fill that gap. It has been planned to collect data from different environments where V2I communication might be developed. Our aim was to measure a range of potential V2I conditions by varying Rx locations and collecting data under different traffic conditions, at different times of the day, and measuring on different streets. One of the crucial roles in the development of radio channel models is driving parameters. The underlying data model plays the most important part in any estimation framework.

A TDL Based Non-WSSUS V2X Channel Model

Many researchers have described the dispersive channel model in the form of TDL model for V2X channels as in [61,63–67,85,93,94,96,129,153] due to its low complexity and simple notation, and its straightforward implementation in channel emulators. The TDL modeling approach has been approved by standardization bodies not only as a reference model for universal mobile telecommunications system (UMTS) [72, 163], and global system for mobiles (GSM) [35], but also adopted by the IEEE802.11p standard for the vehicular radio channel [22, 79]. TDL models are widely used for cellular system evaluation and system level simulation for mobile communication scenarios [35, 103], but in particular, TDL models are based on the wide sense stationary uncorrelated scattering (WSSUS) assumption [21]. The same model assumption (TDL model based on WSSUS assumption) has been developed by Ingram and coworkers for the V2V channel [9, 11, 12], but as reported by Ingram in [9], the classical model is not useful for the V2X channel as it does not feature non-stationarity.

The main challenge of vehicular communications introduces new properties because the physical layer properties are rapidly changing. When a vehicle becomes a link partner, the communication system needs to be robust against inherent mobility within the channel, high vehicle speeds, varying antenna positions, and many handovers due to smaller cells. These properties bring up several challenges in terms of channel characterization. While low mobility is assumed in macro-cell communication scenarios in order to have reasonably high stationarity. In V2X communication system, this does not apply; therefore, it results in the invalidity of WSSUS assumption [22, 36, 92–94, 129, 164, 165]. Many measurement campaigns have shown non-stationarities of the channel statistics; for an overview see [36, 36, 102, 105, 123].

The non-wide sense stationary (non-WSS) property in the context of V2X communication channels refers to the fact that channel characteristics change over time due to the dynamically changing environment. The high speed of vehicles and the low antenna height of vehicles cause channel conditions to change. This means that the statistical properties of the channel may not remain constant over time. Correlated fading property (non-uncorrelated scattering (non-US)) refers to a common phenomenon where the transmitted signal reaches the receiver via reflections, scattering, and diffractions. Meaning multipaths with different delays are not uncorrelated. Instead, due to interactions between the different multipaths and objects in the environment, they are correlated. The combination of non-WSS and non-US properties of the channel gives rise to a new assumption called non-WSSUS [64,67,85,155]. The TDL channel model can be extended via Markov models to represent the non-WSSUS properties. Many sources are focusing

on developing accurate TDL models for V2X channels. The approach used in this investigation is based on [129], where a tap is a sample of the bandlimited CIR. The goal of defining TDL models is then to select only the relevant samples (or set of clusters) of the CIR, derive their parameters and then model their amplitudes and Doppler shifts properly. In [129], the authors proposed to sub-select the samples based on power to reproduce 99% of the total power. The proposed approach of [129] is applied, but the problem of using that approach is the under-estimated root mean square delay spread (RMS-DS) because it neglects the low power taps with large delays. On the other hand, it generates a large number of taps. Reducing the number of taps is a very important feature because the implementation of such a model in channel emulators is limited up to 12 taps [3]. Hence, in this investigation, a new approach is proposed based on an existing method [129]. The extension was done by a base delay compensation and a modified selection of taps. We concentrate on the channel taps, whose amplitudes and delays are necessary to compute the RMS-DS of the channel because the RMS-DS is the major factor in the performance of most digital communication systems, including the orthogonal frequency division multiplexing (OFDM) system proposed for V2X communication. When the RMS-DS is greater than a guard interval, this will lead to inter symbol interference (ISI) and degrade performance, in other words, individual symbols overlap with the following ones; as a result, transmission errors occur [37]. Hence, designers most often rely on RMS-DS, as that is directly relatable to communication system performance. As a result, the proposed approach has demonstrated that the model is fairly accurate when representing the statistics of the measured channel.

1.2 Thesis Outline and Contributions

This thesis is organized into seven chapters. Chapter 2 contains the main topics of theoretical basics of the time-variant wireless channels followed by a discussion on the non-stationary behavior of V2X channels and how to extend the conventional representation of CIR to feature non-stationary. It is followed by Chapter 3 "channel measurement campaign," which provides an overview of measurement equipment and then it presents underlying scenarios e.g. an insight into the surrounding buildings to provide a better understanding of the findings. Chapter 4 introduces a new algorithm for selecting taps for TDL channel models from measurement data with the aim of describing the CIR of any complex radio channel using a simple method. All essential parameters are derived from measured data, and to verify the correctness of parameters derivation, this chapter proposes an approach to verify those parameters. This is followed by Chapter 5, which discusses the implementation of TDL channel models for V2I channels and devises a generator to produce CIRs based on derived model parameters (in Chapter 4). Chapter 6 characterizes slow- and fast-fading variations of each tap by separating the received signal in respective scales of spatial variations. This is followed by Chapter 7, which introduces a method to develop multiple input multiple output (MIMO)-TDL model under the non-WSSUS assumption to devise a model, which is useful for testing V2I MIMO systems. The analysis evaluates single input single output (SISO)- with MIMO-configuration in terms of capacity. Finally, Chapter 8 summarizes the main thesis findings and highlights related research topics that are open for further investigation.

The summary and major contributions of each chapter are listed below.

1. **Chapter 2: Radio channel and multipath propagation.** It describes the theoretical basics of the time-variant wireless channels, including the viewpoint of mobile radio channels used throughout

[3] 6-tap and 12-tap are employed by IEEE802.11p [10, 12].

this investigation. A literature review on modeling non-stationary V2X channels is described. The non-WSSUS assumption is expressed by employing an additional term in the expression of the CIR that is so-called "persistence process".

2. **Chapter 3: Channel measurement campaign.** It provides an overview of radio channel-sounding measurement devices and underlying scenarios, such as an insight into the surrounding buildings to provide a better understanding of the found results. A raytracer tool is used to detect different scenarios, such as line of sight (LOS) and non line of sight (NLOS). After detecting all measurement points, three different scenarios (LOS, NLOS1, and NLOS2) exist in our measured data. A contribution of the thesis is each measurement file will be examined separately and then based on different scenarios, tracks will be merged into different data sets. Another contribution of this chapter is that statistical measures are used to examine the differentiation between those scenarios. Initial parameters such as RMS-DS and delay window (DW) are derived based upon information on the physical environment to differentiate between those scenarios.

   The results of this chapter are partially presented in [61, 64, 66].

3. **Chapter 4: SISO-TDL model parameter estimation**. The first contribution of this chapter is proposing a new strategy of extracting parameters for TDL channel models for V2X channels from measurements. The proposed approach is based on an existing method to derive parameters for a non-stationary TDL model using first-order Markov chains. It will be shown that by using different methods of choosing taps, the number of taps necessary to regenerate the RMS-DS of a channel can be significantly reduced. The proposed approach uses less taps while retaining the delay spread performances. Furthermore, this chapter addresses the amplitude fading of taps and investigates the correlation coefficient between the taps' amplitude and taps' persistence. The second major contribution of this chapter is proposing an approach as a solution to verify the correctness of the channel model parameters derivation.

   The material of this chapter is partially presented in [61, 64, 66].

4. **Chapter 5: SISO-TDL channel modeling and simulation**. The first contribution of this chapter is the development of a generator to produce CIRs based on derived model parameters from measurement data (the outcome of Chapter 4). Log-normal, Weibull, and Rayleigh generators are devised. Outcomes of those generators lead to the second major contribution of this chapter, which is modeling different order Markov Chains. The first-, second-, and third-order two-state Markov models are developed with the aim of better capturing the non-stationary behavior. The outcomes of those generators are evaluated by comparing statistical measures of the simulated sequences to the measured data sequences.

   A part of the research contributions covered in this chapter is published in [67].

5. **Chapter 6: Characterization of slow- and fast-fading of the active taps**. The main contribution of this chapter is the amplitude fading of taps, which is divided into two classes to characterize slow- and fast-fading variations of each tap. Received signal is separated into two scales of spatial variations, which are slow- and fast-variations. In total, nine various setups are studied, which are omnidirectional antenna, two antennas faced directly towards each other, and two antennas faced away from each other. In each scenario, LOS and two different NLOS categories are studied.

Some of the materials of this chapter are published in [62].

6. **Chapter 7: MIMO-TDL model**. The first contribution of Chapter 7 is extending a classical SISO-TDL model to MIMO under the non-WSSUS assumption to develop TDL channel models for V2I MIMO systems. The same algorithm as in Chapter 4 is used for selecting taps. Correlation among taps in each channel, as well as among the channels, is studied. The analysis evaluates SISO- with MIMO-configuration in terms of capacity and then results in terms of a different number of antennas and different values of SNR are investigated. These lead to the second contribution, which is studying the capacity as a function of distance and investigating the position of antennas with its role in achieving capacity.

   Some of the findings in Chapter 7 are presented in [63, 65].

Chapter 2

Radio Channel and Multipath Propagation

A communication system (wired/wireless) is designed to send data packets from a transmitter (Tx) to a receiver (Rx) via a physical medium, which is called a channel. In wireless communication systems, a transmitted wave propagates over an air-interface, whose called a propagation channel. The number of factors influence the propagation channel, such as the bandwidth (narrow-/wide-band), carrier frequency, number of Tx and Rx antennas (single input single output (SISO)/multiple input multiple output (MIMO) system), and the propagation environment [6]. The goal of channel modeling is in general to find a method of describing or generating the channel impulse response (CIR) of the radio channel. There are different methods known in the literature, where the CIR is either determined directly or indirectly by means of a geometrical model of the propagation environment. The derivation of a mathematical framework to describe an observation of the radio channel is focused in this chapter. It is important to note that the radio channel measurements contain finite information; therefore, it is sufficient to choose a channel model that can be derived from the measurement data. Since we want to estimate a specific channel class such as a tapped delay line (TDL) to capture the multipath propagation effect; thus, it is desirable to describe the data model as precisely as possible.

What is focused in this thesis is to get a statistical description of the propagation path to provide another step toward an engineering understanding and approximating characteristics of a radio channel for the vehicle to infrastructure (V2I) communication system, including shadowing and multipath effects. Understanding the properties of the propagation channel becomes extremely important for a system design because they ultimately define the performance of wireless communication systems such as the model can be used for preliminary testing and evaluating system before investing in prototype hardware [6, 61, 64].

In this chapter, the theoretical background on channel modeling is introduced and represented mathematically and then the model is extended to feature the non-stationary channel model to be suitable for vehicle to X (V2X) communication system.

2.1 Mobile Channel Terminology

In the scientific and technical literature, the term "mobile channel" takes on several meanings. The concept of different types of communications channels is defined in Fig. 2.1. Since each half of the link in radio communications can be viewed as a mirror image, only half of the link is demonstrated. For the typical speech user, the immediate environment (including room reverberation and any effects of acoustic noise) forms part of the communications channel. As depicted in Fig. 2.1, for (other) analogue information sensors and also speech, there is an information channel. Note that it includes the effects of the environment, multiple sensors, and any intentional signal conditioning [150].

The sensors convert the analogue information into electrical form, which is called raw data. This means a raw data channel is defined once the analogue information is converted into electrical form. A time-varying binary symmetric channel describes the digital channel once the electrical form is digitized by a (de)coder and then the signal undergoes data processing in preparation for transmission and reception [18, 150].

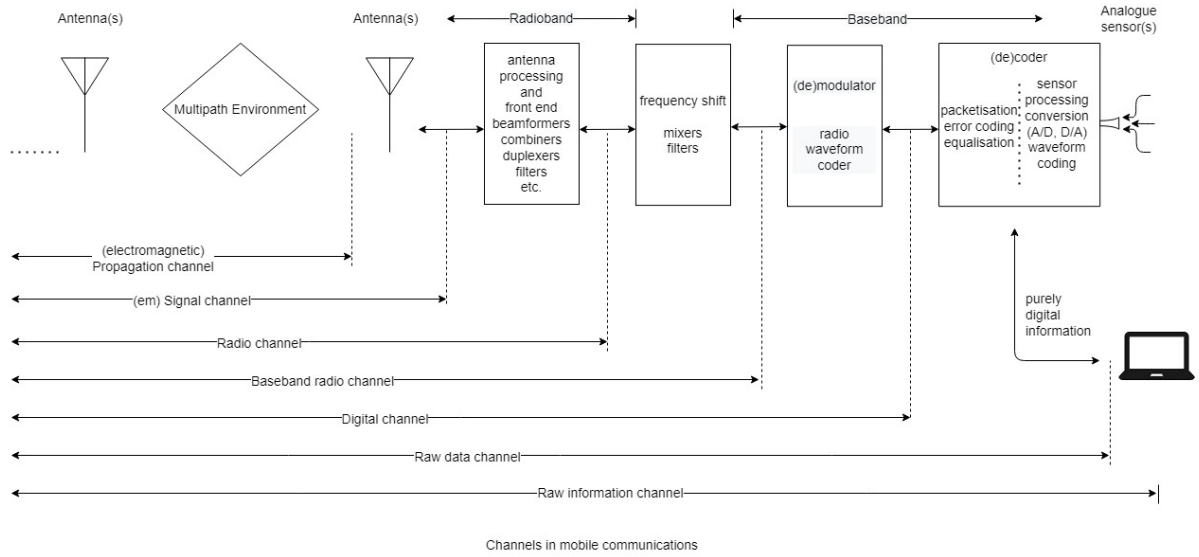

Fig. 2.1 A definition of different types of channels in radio communications, note adapted from [150]

The channel can be referred to as the radio channel when the data are modulated. The effects of antenna processing, front ends, antennas, and electromagnetic propagation are included in the radio channel. The antennas are often multiple ports in mobile communications, and each of them gathers different signals, which arrive via multiple paths. In particular, a clarification is required to define the channels here. Resulting of the fields via a multipath environment is considered as a channel transfer function (it is known as the (electromagnetic) propagation channel) at a receiving antenna.

In Fig. 2.1, the electromagnetic signal channel is referred to the received signal by a loaded antenna element. In the communications signal processing literature, this channel is often referred as the propagation channel. The effects of the fields, the interaction of the antenna, and the antenna itself are comprised by a transfer function of that channel. Therefore, the antennas contribute as a filter in the propagation signal channel, and it is difficult to separate them from measurement data [150]. In brief, the "mobile channel" will rise confusion unless a form of the channel, which is under discussion is understood. In this investigation, the term "mobile channel" is referred to the propagation channel. Several possible types

of communications channels have been described, to summarize them, the interpretation definition for each of them is illustrated below [150]

- **(Electromagnetic) Propagation channel**: It refers to the link between fields at the Tx and fields at the Rx.
- **(Electromagnetic) Signal channel**: It is the link between voltage source at the Tx and voltage across the load in the Rx.
- **(Base-band) Radio channel**: It is the link between (base-band) voltage from the modulator of Tx and (baseband) voltage into the demodulator of Rx.
- **Digital channel**: It is the link between digital data into the modulator and digital data from the demodulator.
- **Raw data channel**: It refers to the link between the electronic signal from receiving electronic sensor and the electronic signal at the actuator.
- **Raw information channel**: It is the link between information source signals to sensors such as sound waves and (reproduced) information signals from the actuator.

2.2 Definition of a Radio Wave

A radio wave is the smallest entity that is used to describe the radio channel. The transmitted wave may spread out in different directions and interact with objects in the environment. In a continuum of reflecting, diffracting, and scattering objects, wave propagation phenomena can be approximately modeled by a superposition of discrete waves with the assumption of ideal omnidirectional antennas [15]. The single wave model can be considered, as illustrated in Fig. 2.2. It has the following parameters, φ_T, θ_T, φ_R, and θ_R. The angle pair φ_T and θ_T are the transmit-azimuth and -elevation, which determine the part of the wave moving in the direction. The azimuth and elevation of the approaching wave reaching the Rx along this wave are determined by the angle pair φ_R, and θ_R. Due to propagation speeds within mediums along the wave, as well as the geometrical length of the wave, the transmitted wave needs a certain time (it is called the time-delay of arrival (TDoA)) to arrive at the receiving antenna. Therefore, the transmitted wave reaches the Rx after a certain time-delay (τ) and with some amplitude (γ) [135].

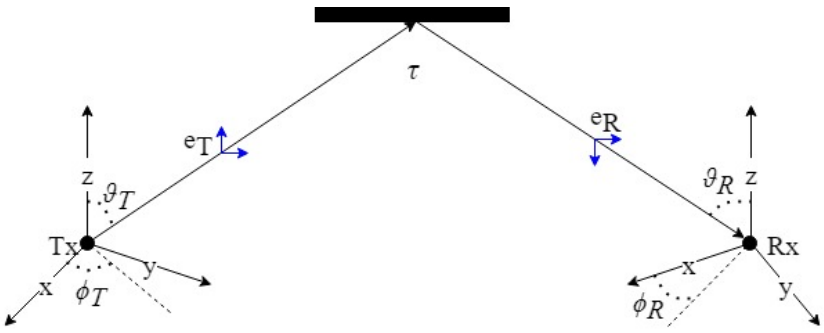

Fig. 2.2 Definition of a radio wave, note adapted from [125]

In the local coordinate systems, the angles at a Tx and Rx are defined. The angles information is gathered by the local antenna arrays at the Tx and Rx; thus, the angles of the waves can be related to

the local coordinate system. This means if the absolute positions of Tx and Rx are known, the wave parameters can always be projected into the global coordinate system; more detail can be found in [106]. The Poynting-vectors at the Tx- and Rx-position (k_T and k_R) are defined by using the transmit- and receive-angle pairs. The two linear polarized components e_{φ_T}, e_{θ_T} (of the wave leaving the Tx) and e_{φ_R}, e_{θ_R} (of the wave reaching the Rx) are defined by using the definitions of the azimuth and elevation angles, as well as the Poynting-vectors, more detail can be found in [47].

2.3 Definition of a Propagation Path

The ray model has been derived in Section 2.2, and it is useful to interpret wave propagation mechanisms and to generate a realization of the stochastic process radio channel (in simulations). Due to the limited resolution of any radio channel measurement system, only finite information about the underlying physical phenomena can be gathered, and the transmitted wave arrives at the Rx via multiple waves; therefore, it is desirable to introduce the propagation path. It is a superposition of multiple waves that are close together, such as a cluster [125], as anticipated in Fig. 2.3. A propagation path has unique characteristics, which are created by characteristics of those multiple rays (commonly termed multipath components (MPCs)) combined in the propagation path; thus, the parameters of a propagation path are the mean values of the parameters of multiple rays. To represent the propagation path mathematically, let us assume we transmit $x(t)$, which is a baseband representation of a narrow-band signal over a single propagation path. Then, a baseband representation of the received signal $y(t)$ can be expressed as

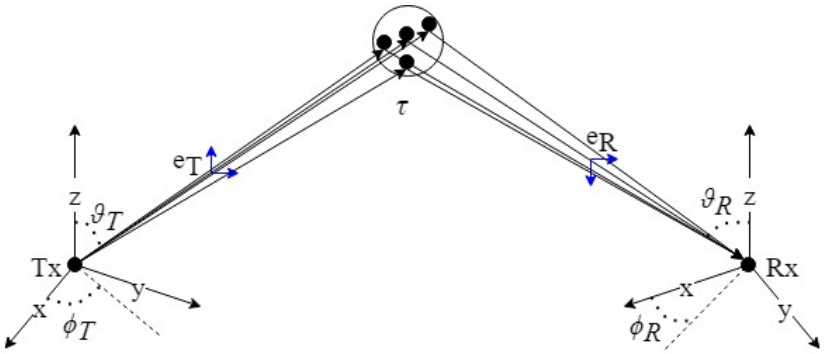

Fig. 2.3 Definition of a propagation path, note adapted from [125]

$$y(t) \;=\; \gamma_p^{'}\, g_{\mathrm{R}}\,(t) \;*\; g_{\mathrm{T}}(t) \;*\; x\left(t - \frac{l_p}{c}\right)\; e^{-j2\pi f_c \frac{l_p}{c}}\,, \tag{2.1}$$

where $g_{\mathrm{T}}(t)$ and $g_{\mathrm{R}}(t)$ are the impulse responses of a Tx and Rx, respectively. c is the wave velocity, f_c is a carrier frequency, l_p is the length, and $*$ denotes the convolution operator. The time a signal needs for the transmission over the p^{th} propagation path is denoted by $\tau_P = \frac{l_p}{c}$. All effects can be treated as frequency independent, such as free-space loss, complex antenna gains, loss on scattering or reflection points are described by $\gamma_p^{'}$. The frequency domain of the received signal $y(t)$ is expressed as follows

$$Y(f) = \; X(f) \cdot \; \gamma_p^{'} \cdot \; G_{\mathrm{R}}(f) \; \cdot G_{\mathrm{T}}(f) \cdot \; e^{-j2\pi f \tau_P} \; \cdot \; e^{-j2\pi f_c \frac{l_p}{c}}\,, \tag{2.2}$$

From the above, a frequency domain representation of a time-invariant SISO system is obtained as

$$H(f) = \gamma_p^{'} \cdot \; G_{\mathrm{R}}(f) \; \cdot G_{\mathrm{T}}(f) \cdot \; e^{-j2\pi f \tau_P} \; \cdot \; e^{-j2\pi f_c \frac{l_p}{c}}\,. \tag{2.3}$$

If the Tx, Rx, or any scatterer related to this propagation path is moving, (2.3) becomes time-variant system. Let us assume that within a short observation interval, the effective speed v_p of the moving object is constant; therefore, the time-variant frequency response $H(t, f)$ can be represented as (2.4) for a small change in l_p, which is the electrical length.

$$H(f,t) = \gamma_p^{'} \cdot \ G_{\mathrm{R}}(f) \ \cdot G_{\mathrm{T}}(f) \cdot \ e^{-j2\pi f \tau_P} \cdot \ e^{-j2\pi \frac{l_p + v_p t}{\lambda}} \,, \tag{2.4}$$

where $\lambda = \frac{c}{f_c}$ is the wavelength. This model (2.4) assumes a constant complex amplitude $\gamma_p^{'}$ and neglects any change in the parameter τ_P. This approximation (2.4) only valid as long as $\frac{c}{B} >> v_p \cdot t$, where B is the bandwidth of the measurement system [125]. If we introduce the Doppler-shift $\alpha_p = -\frac{f_c}{c} \cdot v_p$ in (2.4) and then merge the phase shift into the complex amplitude, then we obtain the following expression

$$\begin{aligned} H(f,t) =& \gamma_p^{'} \cdot \ G_{\mathrm{R}}(f) \ \cdot G_{\mathrm{T}}(f) \cdot \ e^{-j2\pi f \tau_P} \cdot \ e^{-j2\pi \frac{(l_p + v_p t) f_c}{c}} \\ =& \gamma_p^{'} \cdot \ G_{\mathrm{R}}(f) \ \cdot G_{\mathrm{T}}(f) \cdot \ e^{-j2\pi f \tau_P} \cdot \ e^{-j2\pi \frac{l_p f_c}{c}} \ e^{-j2\pi \frac{v_p f_c t}{c}} \\ =& \gamma_p^{'} \cdot \ G_{\mathrm{R}}(f) \ \cdot G_{\mathrm{T}}(f) \cdot \ e^{-j2\pi f \tau_P} \cdot \ e^{-j2\pi \frac{l_p f_c}{c}} \ e^{j2\pi \alpha_p t} \\ =& \gamma_p \cdot \ G_{\mathrm{R}}(f) \ \cdot G_{\mathrm{T}}(f) \cdot \ e^{-j2\pi f \tau_P} \cdot \ e^{j2\pi \alpha_p t} \,, \end{aligned} \tag{2.5}$$

where

$$\begin{aligned} \gamma_p =& \gamma_p^{'} \cdot e^{-j2\pi \frac{l_p f_c}{c}} \\ =& \gamma_p^{'} \cdot e^{-j2\pi \phi_p} \,, \end{aligned} \tag{2.6}$$

where ϕ_p denotes the starting (random) phase of the p^{th} path. To sum up, this section defines and derives a radio channel model for p^{th} propagation path (a SISO system with omnidirectional antennas at both the Tx and the Rx site).

2.4 Polarisation of Multipath Fields

In general, the Tx emits a field with most likely a defined polarization. The polarization of the field may be changed randomly after several reflections from rough surfaces or scatterers. At the Rx, the incident field (E_R) has three complex components as [150]

$$E_{\mathrm{R}}(\omega, r) = E_x(\omega, r)\hat{x} + E_y(\omega, r)\hat{y} + E_z(\omega, r)\hat{z} \,, \tag{2.7}$$

where each component (e.g., E_y) is a function of frequency (ω) and position (r), and it is a complex scalar. E_{R} is also dependent on both frequency (ω) and position (r). Figure 2.4 assists visualization of multiple random incident waves, each has an elliptical polarization with the plane of ellipse having a random direction. This means the polarization is elliptical at each point in space, and there will also be three magnetic field components at the same point in the space (2.8) [150]. Each magnetic field with its own plane of polarization. This means in multipath fields; there are six complex components in total.

$$H_{\mathrm{R}}(\omega, r) = H_x(\omega, r)\hat{x} + H_y(\omega, r)\hat{y} + H_z(\omega, r)\hat{z} \,. \tag{2.8}$$

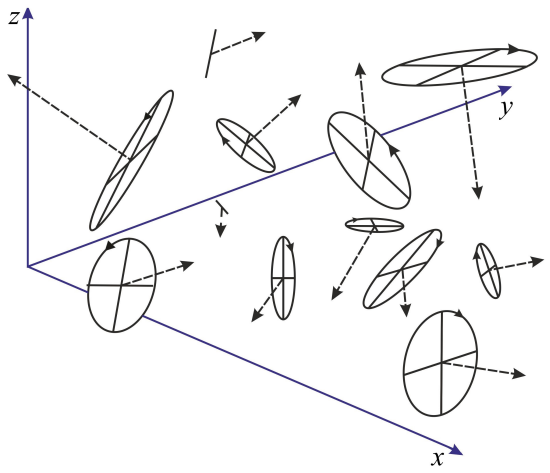

Fig. 2.4 Visualization of multiple random incident waves, each has elliptical polarization, note adapted from [150]

2.5 Frequency Flat Channel and Frequency Selective Channel

The transmitted signal undergoes either a flat- or frequency selective-fading due to time dispersion, which is caused by the multipath propagation [150]. The flat fading has been referred the channel when all the frequency components in the band fade together because the bandwidth is sufficiently small. In such a case, the bandwidth of the transmitted radio signal is less than the coherence bandwidth (Bc). Bc is a statistical measurement to approximate the range of bandwidth, where the channel can be assumed "flat". The opposite will hold for undergoing frequency selective-fading conditions. These types of fading can be interpreted in the following way, assuming that for a given bandwidth with two frequencies belonging to a transmitted signal, the different propagation paths will have approximately the same electrical lengths ($2\pi d/\lambda_1$ and $2\pi d/\lambda_2$), if these two frequencies are close. In other words, their corresponding received signals (such as amplitudes and phases) will vary in time in approximately the same way. This phenomenon is known as flat fading conditions, which is illustrated in Fig. 2.5(a). On the other hand, the fading behavior at one of the frequencies tends to be uncorrelated with respect to the other as the frequency separation increases because the electric lengths ($2\pi d/\lambda_1$ and $2\pi d/\lambda_2$) will be significantly different. In addition to that, the correlation between them depends on the time spreading caused by the environment; therefore, signals occupying larger bandwidth will be distorted. In this case, we would have frequency selective fading, as illustrated in Fig. 2.5(b). In the context of mobile channels, a wideband channel has frequency-selective fading, and a narrowband channel has flat fading [8, 121, 150]. The narrowband- and wideband-channel will be explained in the next section.

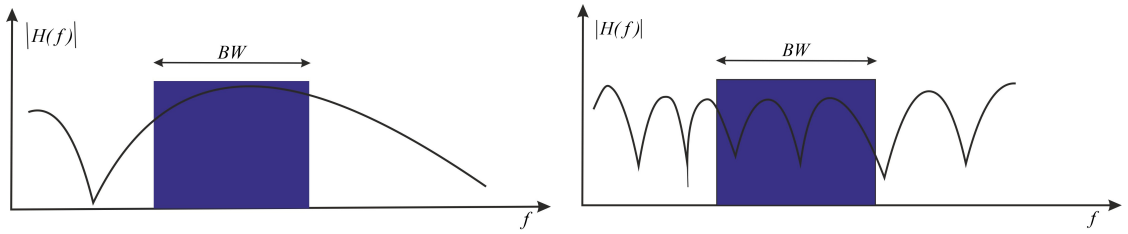

(a) (b)

Fig. 2.5 Channel frequency transfer function vs. transmitted signal bandwidth, note adapted from [48] (a) frequency flat channel, (b) frequency selective channel

2.6 Impulse Response of Narrowband and Wideband Channels

A narrowband channel is described as one where the fading is almost constant or the same across the band [8, 121, 150]. For an ideal static mobile channel, the impulse response and transfer function are expressed as

$$\gamma\ \delta\left(\tau-\tau_0\right)=h_{\mathrm{ph}}(\tau)\ \Longleftrightarrow\ H(\omega)=\gamma\ e^{-j\omega\tau_0}\,. \tag{2.9}$$

In the propagation and multipath processing study, it is important to understand and distinguish between the clock-time/time and delay-time/delay. τ denotes the delay, which is a signal propagation parameter, and t denotes time. From (2.9), τ_0 is the time-of-flight delay, ω is the radio-channel angular frequency. γ is a complex coefficient, which is defined as $\gamma=\gamma' e^{j2\pi\phi}\ \in\ \mathbb{C}$, with $\gamma'\ \in\ \mathbb{R}$ is the amplitude and ϕ is the (random) phase [1]. Mathematically, δ indicates the delta function notation for an infinite bandwidth. The impulse response at a given (clock) time is replaced by a sinc-shaped function (the Fourier transform of the frequency window), for a finite bandwidth imposed on the flat fading [150]. As the mobile starts changing position, the value of the delay τ_0, as well as the channel gain, start changing. The modeling equation is expressed by writing the parameters with time dependency, denoted as in (2.10) [2].

$$h_{\mathrm{ph}}(t,\tau)=\gamma(t)\delta(\tau-\tau_0(t))\,. \tag{2.10}$$

The alternative way to view the frequency-selective fading in a wideband channel is to consider the spreading of the CIR (over a delay range). Mathematically, the impulse response of a wideband channel is frequently expressed as a sum of delta functions (2.11), which represent collections of propagation paths or individual paths, with each function having its own complex amplitude and delay.

$$\sum_{p=1}^{P}\gamma_p\delta(\tau-\tau_p)=h_{\mathrm{ph}}(\tau)\ \Longleftrightarrow\ H(\omega)=\sum_{p=1}^{P}\gamma_p e^{-j\omega\tau_p}\,. \tag{2.11}$$

As the position of the mobile change, the dispersive impulse response (2.11) changes with time, as expressed in (2.12).

$$h_{\mathrm{ph}}(t,\tau)=\sum_{p=1}^{P}\gamma_p(t)\delta\left(\tau-\tau_p(t)\right)\,. \tag{2.12}$$

[1] $\Longleftrightarrow$ indicates the Fourier transform

[2] The same expression can be illustrated in terms of position dependency denoted by z', as in $\gamma(z')$ and $\tau_0(z')$

Here, the finite bandwidth complicates the situation. The channel bandwidth has an impact on the dispersion of the CIR, and it is defined by the communications system filters. On the other hand, the impact of the finite bandwidth signals at different delays being forced to mix together. Therefore, the propagation channel and the communications system govern the channel dispersion [150]. The impact of finite bandwidth on the CIR will be explained in Section 2.8.

2.7 Channel Impulse Response Form

The term "channel characterization" is a terminology used to define the characteristics of a propagation channel in a specific environment to understand the channel behavior. In general, waves propagate according to four mechanisms: free-space propagation due to a line of sight (LOS) path, reflection, diffraction, and scattering. The CIR contains information about all of these components, and it is given by the superposition of all these components at a certain instant. In other words, in the multipath case, the CIR is a summation of contributions from scatterers and reflectors in different directions and with different lengths (delays).

The propagation channel can be classified as a linear time-invariant (LTI) filter, whose CIR does not change over time (the channel is static), or a linear time-variant (LTV) filter, whose CIR varies with time. First, the behavior of a time-invariant channel is modeled in a deterministic way and then it will be extended to account for the dynamic nature of the V2X environment. In the case of constant point scatterers, the signal transfer function over a region, which typically comprises many multipath is modeled as a summation over many constant point scatterers (2.13) [150].

$$H(\omega, z') = \sum_{p}^{P} \gamma_p \cdot e^{-jkl_p}\,, \tag{2.13}$$

where γ_p is the complex amplitude of the p^{th} scatterer (it has been defined in Section 2.3), and z' is the position. The scalar electrical distance is represented by kl_p, where l_p is the physical distance and k is the scalar wave number [3]. When the Rx (or Tx) is moving, as depicted in Fig. 2.6, the electrical distance to the p^{th} point scatterer can be expressed as follows

$$\begin{aligned} kl_p(z') &= \frac{2\pi}{\lambda}\, l_p(z') \\ &= \omega\, \frac{l_p(z')}{c} \\ &= \omega\, \tau_p(z')\,, \end{aligned} \tag{2.14}$$

where z' is the position along the direction of motion, and τ_p is the time delay from p^{th} scatterer.

[3] Wave number is a direct acknowledge to frequency for waves in space as it to waves in time

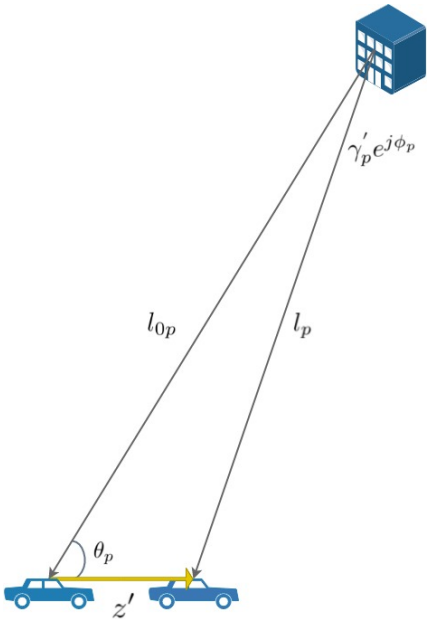

Fig. 2.6 Visualization for the changing phase, the distance moved by the Rx is much shorter than the distance to the scatterers, note adapted from 150

The assumption of this model is that the magnitude of the waves from the sources is no distance dependence, in other words, slowly varying magnitudes are neglected, and only delay variation with distance is kept as defined in (2.14). This phase mixing of the wave contributions is the reason for the fast-fading of the signal envelope [150] (it will be explained in detail in Section 6). Assuming that the distance moved by the Rx is much shorter than the distance to the scatterers (as shown in Fig. 2.6), the angle (θ_p) between the direction of movement and the direction to the scatterer can be defined by rearranging the electrical distance (2.14) in these following steps [4] 150.

$$\begin{aligned} kl_p &\approx k\, l_{0p} - k\, z' \cos(\theta_p) \\ &= \omega\, \tau_p - \frac{\omega}{c} \cos(\theta_p)\, z' \\ &= \omega\, \tau_p - u_p\, z' \,, \end{aligned} \tag{2.15}$$

$$\begin{aligned} u_p &= \frac{\omega}{c}\, \cos(\theta_p) \\ &= k\, \cos(\theta_p) \,, \end{aligned} \tag{2.16}$$

where u_p is the spatial Doppler shift in $\mathrm{rad\,m^{-1}}$. The phase shift is proportional to distance and by defining $z' = vt$, where v is the speed of the Rx, then the Doppler shift is

$$\begin{aligned} \omega_{Dp} &= u_p\, v \\ \omega_{Dp} &= k\, v \cos(\theta_p) \\ 2\pi\alpha_p &= \frac{2\pi}{\lambda}\, v \cos(\theta_p) \\ \alpha_p &= \frac{f_c}{c}\, v \cos(\theta_p) \,, \end{aligned} \tag{2.17}$$

where ω_{Dp} and α_p are obtained in $\mathrm{rad\,s^{-1}}$ and Hz, respectively. It is essential to distinguish between the

[4] By linearising the equation as in [150]

base-band frequency (ω_{BB}), which is shifted by the carrier frequency (ω_c), and the actual radio frequency (ω), namely

$$\omega = \omega_{BB} + \omega_c \,, \tag{2.18}$$

similarly, for the wave-number (2.19),

$$k = k_{BB} + k_c \,. \tag{2.19}$$

Therefore, the electrical distance to the scatterer from (2.15) may be written as follows

$$\begin{aligned} kl_p &= \omega\tau_p - \frac{\omega}{c}\cos(\theta_p)z' \\ &= \omega_c\tau_p + \omega_{BB}\tau_p - \frac{\omega_c}{c}\cos(\theta_p)z' - \frac{\omega_{BB}}{c}\cos(\theta_p)z' \\ &= \omega_c\tau_p + \omega_{BB}\tau_p - k_c\cos(\theta_p)z' - k_{BB}\cos(\theta_p)z' \\ &= \omega_c\tau_p + \omega_{BB}\tau_p - u_p z' - u_{BB}z' \,. \end{aligned} \tag{2.20}$$

The fourth term on the right-hand side of the equation can be neglected because it is small compared to the third term. This brings us to approximately model the transfer function of the channel (2.13) as follows

$$\begin{aligned} H(\omega, z') &= \sum_p^P \gamma_p \cdot e^{-jkl_p} \\ &= \sum_p^P \gamma_p \; e^{-j(\omega\tau_p - z'u_p)} \\ &= \sum_p^P \gamma_p \; e^{-j\omega\tau_p} \; e^{jz'u_p} \\ &= \sum_p^P \gamma_p \; e^{-j\omega\tau_p} \; e^{jk\cos(\theta_p)z'} \,. \end{aligned} \tag{2.21}$$

The change position of the Rx results in a movement of the CIR contribution along the time axis; hence, the time-varying frequency response is

$$\begin{aligned} H(f, t) &= \sum_p^P \gamma_p \; e^{-j2\pi f\tau_p} \; e^{j\frac{2\pi}{\lambda}\cos(\theta_p)vt} \\ &= \sum_p^P \gamma_p \; e^{-j2\pi f\tau_p} \; e^{j\frac{2\pi f_c}{c}v\cos(\theta_p)t} \\ &= \sum_p^P \gamma_p \; e^{-j2\pi f\tau_p} \; e^{j2\pi\alpha_p t} \,. \end{aligned} \tag{2.22}$$

The time-domain of the transfer function (2.22) is the impulse response (it can be obtained by taking the Fourier transform of (2.22))

$$h_{\text{ph}}(\tau, t) = \sum_p^P \gamma_p \delta(\tau - \tau_p) e^{j2\pi\alpha_p t} \,, \tag{2.23}$$

where δ indicates the delta function notation for an infinite bandwidth. It is defined by

$$\delta(t) = \begin{cases} +\infty & \text{if } t = 0 \\ 0 & \text{if } t \neq 0 \end{cases} \tag{2.24}$$

The impulse response at a given time is replaced by a sinc-shaped function, and this will be detailed in Section 2.8. Delays and angles could be used to resolve scatterers by using a sufficiently wide bandwidth (e.g. having infinite bandwidth), whereas the band limitation is usually imposed on the signal by the radio electronics and antennas [150]. From the propagation channel point of view, the effective scatterers[5] can be considered resolvable, but due to the bandwidth restriction of the radio channel, they are quantized in the delay domain, meaning the resolution is also correspondingly restricted. It is important to note that the resolvability of effective scatterers does not imply the resolvability of physical scatterers. There might be a case where numerous physical scatterers can make up a single resolvable scatterer [150]. From (2.17), it may be possible to keep track of the received Doppler spectrum to assess the angles of arrival because there is a direct relationship between the angle of arrival and the Doppler shift. The expression of Doppler shift is a function of echos angle of arrival. Depending on the Rx is moving away or toward the Tx, the Doppler shift can be +/− [48,63]. Fig. 2.7 shows a simple model containing three scatterers (A, B, and C) with the transmitter (T) and the receiver (R) positions. It is possible to distinguish between TCR [6] and TAR by their Doppler shifts despite having the same delay because by measuring the Doppler shift, the angles of arrival may be obtained [48,116]. Furthermore, paths TBR and TAR may be resolved by their delays while they have the same Doppler shift.

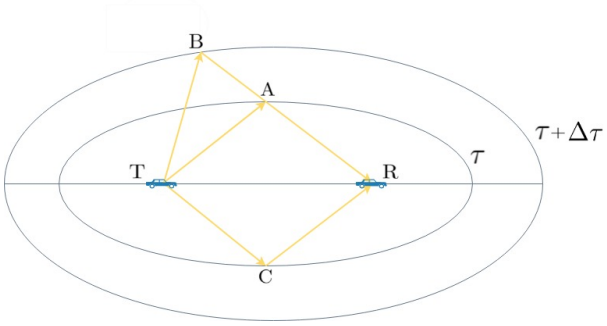

Fig. 2.7 Defining scattering points using ellipses, note adapted from [117]

To sum up, the CIR can be regarded as deterministic if the receive filter has infinite bandwidth. Therefore, each time delay and Doppler shift in the CIR is due to an individual physical scatterer. In other words, all the multipath components are resolvable. Mathematically, the channel model is expressed in (2.23) and a change in position of the Rx is imposing a new phase at each delay and it is proportional to u_p (the Doppler shift). In real-world scenarios, systems are bandlimited. This means multiple effective scatterers will be lumped together into delay bins.

2.7.1 WSSUS Assumption

In mobile communications, mathematical models for insightful system performance analysis and a statistical description of the transmission behavior are provided by wide sense stationary uncorrelated scatter-

[5]The term effective is used because the receiving pattern weights the signals from the physical sources
[6]T and R are the transmitter and receiver. C is a scatterer.

ing (WSSUS) assumption [35, 43, 84, 93, 148]. WSSUS assumption is often made because it allows Fourier theory for the channel description [150]. The assumption of randomly time-variant radio channels is wide sense stationary (WSS) combined with the uncorrelated scattering (US) assumption. In 1963, the characterization of randomly time-variant linear channels, as well as a set of system functions, were first introduced by Bello [21]. This assumption is used in traditional wireless channel modeling such as cellular communication system evaluation [35, 84, 93]. Different definitions of a stationarity behavior are used in literature, but most of them include at least the following three conditions for a time series to be stationary.

- The mean (μ) of the time series is constant.
- The standard deviation (σ) is constant overall time.
- Correlation between lags is zero; in other words, there is no correlation between the time series and the lag version of the time series.

It is interesting to note that if a time series is white noise, it is stationary because white noise conditions are similar except the mean needs to be zero, which is a constant. However, if a time series is stationary does not mean it is white noise because the mean may not be zero.

The second-order statistic of the channel is stationary in the time domain, this is understood as WSS, and the US means there is no correlation between these paths with respect to delay [5, 97, 129, 148]. A channel can be assumed to follow the WSSUS if both assumptions are satisfied. Through this assumption, four complex functions carry the same information for describing the characterization of the channel. Section 2.3 has illustrated how the input and output signals can be linked. Once any channel function is found, the other system functions can be derived by Fourier transformations, as sketched in Fig. 2.8. This is called the first set of Bello functions. The properties of the channel in time (t), delay (τ), frequency (f), and Doppler (f_D) domain are described. The channel time-variant transfer function $H(t, f)$ is recorded in our channel sounding measurement campaigns.

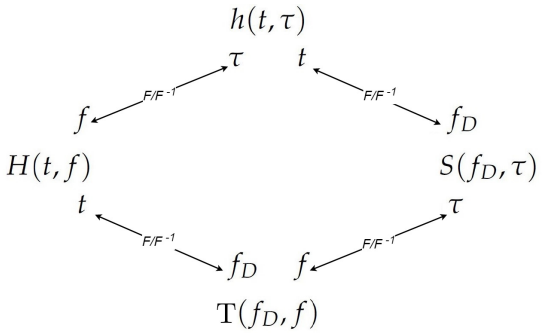

Fig. 2.8 Relations between the time-varying channel functions in time, frequency, Doppler and delay domain, note adapted from [48]

As stated previously, the second-order statistics of the channel are stationary in the time domain, and paths are uncorrelated with respect to delay [5, 97, 129, 148]. The so-called second set of Bello functions presents an approach to describe the channel statistically. Since a realistic mobile wireless channel is not fully deterministic but also includes a random process, the above-illustrated functions become stochastic. A stochastic description of the wireless channel is provided in detail in [48]. However, when the focus is shifted to vehicular communications, which is highly dynamic in time, frequency, and

space due to inherent mobility, it turned out that WSSUS assumptions are not fulfilled in V2X real-world channels [36, 64, 85, 110]. In V2X channels, this assumption has to be extended to non-WSSUS, and it will be provided in Section 2.9.

2.8 Finite Bandwidth Effects on the CIR

As illustrated in the previous section, the CIR of the physical wireless channel can be represented as follows

$$h_{\mathrm{ph}}(\tau, t) = \sum_{p}^{P} \gamma_p \delta(\tau - \tau_p) e^{j2\pi\alpha_p t}\,, \tag{2.25}$$

where $h_{ph}(\tau, t)$ is not bandlimited. The formulas that have been derived in the previous sections are not bandlimited. Thus, we cannot apply those formulas directly when we deal with measured channels because they are sampled and bandlimited. In other words, we employ bandlimiting filters at Tx and Rx sides. The CIR is obtained as following [8, 69]

$$h(t, \tau) = h_T(\tau) * h_{\mathrm{ph}}(t, \tau) * h_R(\tau)\,, \tag{2.26}$$

where $h_T(\tau)$ and $h_R(\tau)$ are the impulse responses of the filter at Tx and Rx sides, respectively. $*$ denotes the convolution operator. For instant, a root raised cosine filter[7] can be considered for both filters at the Tx and Rx sides (2.27) in [8, 69].

$$h_T(\tau) = h_R(\tau) = \sqrt{h_{\mathrm{RC}}(\tau)}\,, \tag{2.27}$$

where

$$h_{\mathrm{RC}}(\tau) = \frac{\sin(\pi\tau/T_c)}{\pi\tau/T_c} \frac{cos(\beta\pi\tau/T_c)}{1 - (2\beta\tau/T_c)^2}\,, \tag{2.28}$$

where β the roll-off factor, which can be any value within $[0, 1]$ and T_c represents the sampling in delay [8, 69]. This leads to a reduction of the deterministic model into a model with a limited number of taps with equally-spaced delay. This means the discrete signal delays of the propagation channel model are combined and quantized into P^{th} delay bins. Each bandlimited component at τ_P is composed of a superposition of individual MPCs, as visualized in Fig. 2.9. The magnitude of the CIR of the propagation channel is depicted in Fig. 2.9 with effectively infinite bandwidth versus bandlimited representation of the CIR. In band limited case, the delta functions, which describe different paths replaced by *sinc* functions that are quantized in the delay domain. Briefly, the radio-channel bandwidth is bandlimited by elements of the communications system itself, such as receiving antenna, filters, and the transmission system, which are related to the communications application. As a result, the final CIR is obtained by

$$h(t, \tau) = \sum_{p=1}^{P} \gamma_p\, h_{\mathrm{RC}}(\tau - \tau_p)\, \exp(j2\pi\alpha_p t)\,. \tag{2.29}$$

Our measured CIR is sampled in the delay domain with $T_c = 1/B$ (in (2.28)), where B is the communication bandwidth. In the time domain, the collected number of snapshots is represented by m, meaning by sampling (2.29), we obtain the discrete-time CIR as follows

[7] A root raised cosine filter in a cascade, result in a raised cosine filter with impulse response (2.28).

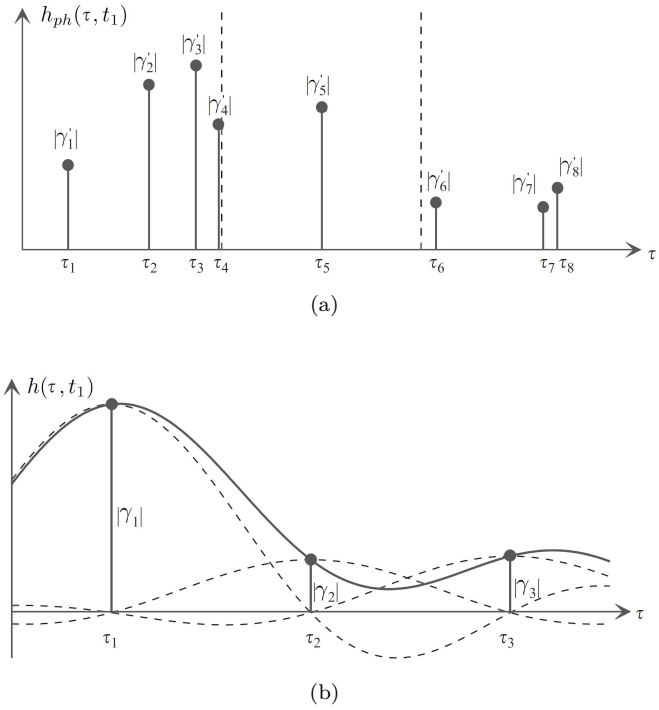

Fig. 2.9 Bandlimited representation of propagation channel, note adapted from [8], (a) infinite bandwidth, (b) bandlimited

$$h[m,n] = \sum_{p=1}^{P} \gamma_p \, h_{\mathrm{RC}}(nT_c - \tau_p) \exp(j2\pi\alpha_p m)\,, \tag{2.30}$$

where $n \in \{0, ..., N-1\}$ denoting the delay index, and $m \in \{0, ..., M-1\}$ denoting the snapshot index of measured CIR.

2.9 V2X CIR Form

The classical model (2.23) is not useful for the V2X channel as it does not feature non-stationarity. The main challenge of vehicular communications is that the environment has frequent and rapid changes due to the high mobility and low antenna heights of the mobiles [22, 92–94, 129, 164, 165]. Many measurement campaigns have shown non-stationarities of the channel statistics as in [36, 102, 105, 123]. In such an environment, strengths and the number of multipath components frequently change [58, 92, 93, 129]; thus, it is a strong time-variant channel [22], and these transitions are essential and need to be investigated. This means the individual radio paths and their associated delays vary over time [58]. In order to make this clear, Fig. 2.10 and 2.11 illustrate different scenarios. At time t_1 (Fig. 2.10), the Rx received three paths, and each path has an amplitude, a phase, and a delay. At time t_2, the Rx received only two paths with different amplitudes, different phases, and different delays; thus, the channel changes over time [58].

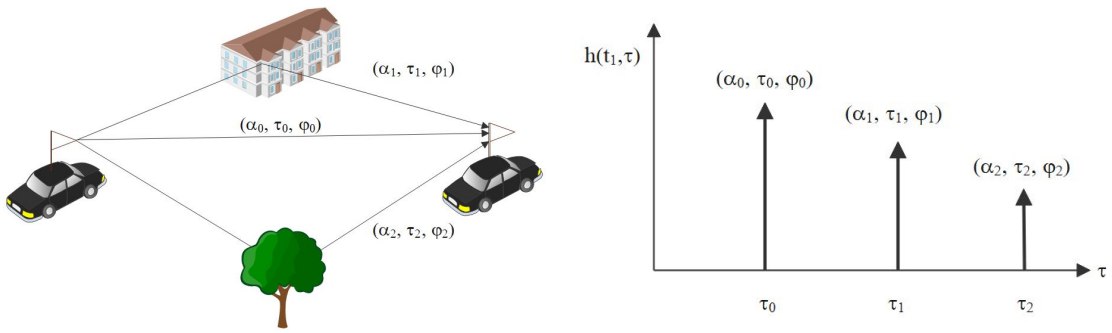

(a) (b)

Fig. 2.10 CIR at time t_1, the Rx received three paths, each path has an amplitude, a phase and a delay, note adapted from [58]

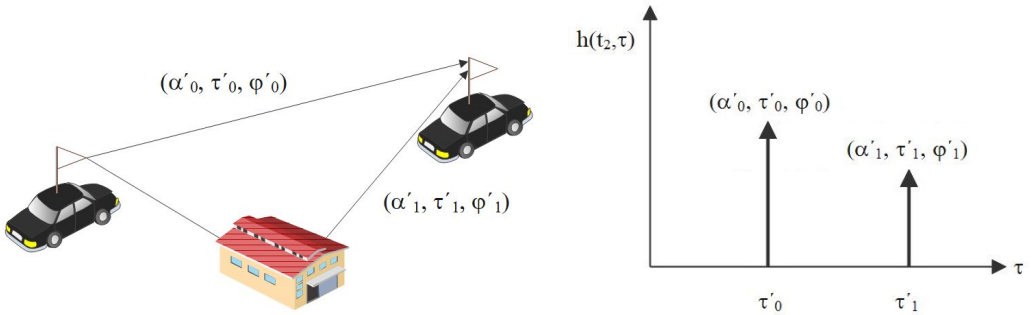

(a) (b)

Fig. 2.11 CIR at time t_2, the Rx received only two paths with different amplitudes, phases, and delays compared to Fig. 2.10, note adapted from [58]

In order to extend the model in (2.23) to feature non-stationary, an additional term ($z_p(t)$) is employed, which is an ON/OFF process or "persistence process (PP)" (2.31). It is to account for the finite "lifetime" of p^{th} multipath. This has been proposed by [129]. In order to make the model non-stationary, each tap could be selectively turned ON or OFF depending on a so-called PP.

$$h_{\text{ph}}(t,\tau) = \sum_{p=1}^{P} z_p(t)\ \gamma_p(t)\ \delta(\tau - \tau_p(t))\ \exp(j2\pi\alpha_p t)\,, \tag{2.31}$$

where z_p is a binary vector that determines whether tap p is currently switched ON or OFF. A first-order two-state Markov chains (MC) can be used to generate the ON/OFF process (in a generator); this will be explained in the following subsection. As explained in Section 2.8, the measured CIR is sampled; hence, the final discrete-time CIR is obtained by

$$h[m,n] = \sum_{p=1}^{P} z_p(m)\ \gamma_p(m)\ h_{\text{RC}}(nT_c - \tau_p(m))\ \exp(j2\pi\alpha_p m)\,. \tag{2.32}$$

2.9.1 Markov Chains Modeling of Persistence Process

As stated in Section 2.9, in order to account for the dynamic nature of the non-stationary V2X environment, a new term ($z_p(t)$) is employed in the conventional representation of CIR (2.31) to account for the finite "lifetime" of each tap. This PP will be estimated from measured data (it will be illustrated in Section 4.2.1). A first-order two-state Markov chain is the frequently used method to model the ON/OFF process (in a generator) [67,93,94,96,129,155]. Markov chain is a stochastic process that can be parameterized by estimating transition- and steady-state probabilities between discrete states [13]. In Fig. 2.12, transition graphs with nodes are used for visualizing Markov chains. The nodes and edges represent the states and transitions. The transition probabilities are represented by labels on the arrow on the graph.

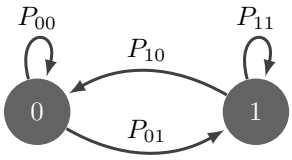

Fig. 2.12 The block diagram of first-order two-state Markov chains

The first order two-state Markov chains are stochastic processes for which future states depend only on the immediately preceding states, not any further previous states. This Markovian property can be expressed mathematically as in (2.33) [13]. The second or higher order Markov chain is the one in which the next state depends on two or more preceding ones [13].

$$P(X_{n+1} = j|X_n = i_n, X_{n-1} = i_{n-1}, ..., X_0 = i_0) = P(X_{n+1} = j|X_n = i_n)\,,^{8} \tag{2.33}$$

where P is the probability and j, i_n, i_{n-1},..., and i_0 are states of X_{n+1}, X_n, X_{n-1},..., and X_0, respectively. Symbol | indicates "the given condition". Namely, only the condition at time $n-1$ does affect the condition at time n. This means the conditions at time $n-2, n-3, ..., n_0$ do not affect the condition at time n [51]. At each time instant n, the Markov chain may remain in the same state or move from one state to another, according to the transition probabilities, which is $P(X_{n+1} = j|X_n = i_n)$ [155]. Mathematically, a transition-state matrix (TS) and a steady-state matrix (SS) represent a Markov chain parameters, which are given in (2.34) and (2.35), respectively.

$$TS = \begin{bmatrix} P_{00} & P_{01} \\ P_{10} & P_{11} \end{bmatrix}, \tag{2.34}$$

$$SS = \begin{bmatrix} SS_0 \\ SS_1 \end{bmatrix}, \tag{2.35}$$

where P_{01} defines as the probability of going from state-OFF to -ON, and P_{11} is defined as the probability of going from state-ON to -ON [9]. In the SS matrix, SS_1 gives the "steady-state probability" associated with the ON state, in other words, SS_1 represents the probability of being ON [10]. Those elements

[8] Equation (2.33) reads as "the probability of X_{n+1} being equal to j given that X_n,..., and X_0 are equal to i_n,..., and i_0 is equal to the probability of X_{n+1} being equal to j only if X_n is equal to i_n" [51]. It is important to note that in our case we only have two states, which are 0 and 1

[9] P_{10} is defined as the probability of going from state-ON to -OFF, and P_{00} is defined as the probability of going from state-OFF to -OFF.

[10] SS_0 gives the probability of being OFF.

are probabilities; thus, the sum of elements on each row yields one. $P_{00} + P_{01} = 1$, $P_{10} + P_{11} = 1$, and $SS_0 + SS_1 = 1$ [91]. The ON/OFF process is estimated from measured data to capture the non-stationary nature of the V2I environment, then Markov chains parameters TS and SS matrices are computed. Furthermore, q-order Markov chains are defined as processes having the property that can be expressed as follows

$$P(X_{n+1} = j|X_n = i_n, X_{n-1} = i_{n-1}, ..., X_0 = i_0) = P(X_{n+1} = j|X_n = i_n, X_{n-1} = i_{n-1}, ..., X_{n-q+1} = i_{n-q+1}), \quad (2.36)$$

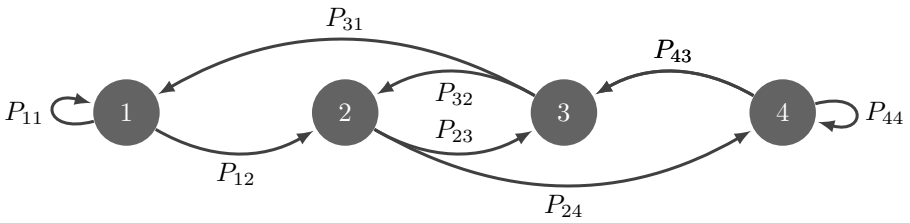

(a)

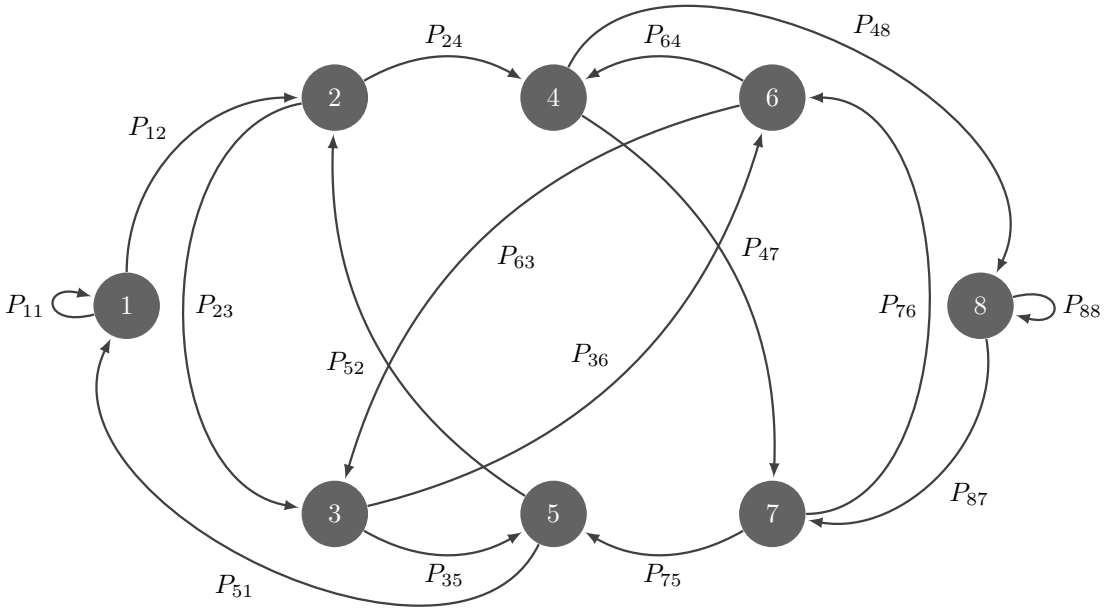

(b)

Fig. 2.13 The block diagram of different order Markov chains, (a) Second-order two-state Markov chains, (b) Third order two-state Markov chains

This defines the future state is influenced by the past q states. Fig. 2.13 shows second-order and third order two-state Markov chains. The transition matrix associated with the second/third-order can be represented by a $4 \times 4/8 \times 8$ matrix similar to a transition matrix of a 1st-order 4-state Markov chains

model. This will be illustrated in detail in Section 5.5.

2.10 MIMO CIR Form

A radio channel model for a SISO system at both Tx and Rx sides is derived in the previous sections. Here, we extend this to MIMO antennas on both sides. Accordingly, the channel has to be characterized for all transmit and receive antenna pairs. For example, consider a MIMO system with N_{R} receive- and N_{T} transmit-antennas; hence, it is an $N_{\mathrm{T}} \times N_{\mathrm{R}}$ MIMO system. From system-level viewpoint, the $N_T \times N_R$ channel matrix represents a linear time-variant MIMO channel (2.37) [28, 46, 63, 65, 76, 87, 107].

$$H_{\mathrm{ph}}(t,\tau) = \begin{bmatrix} h_{\mathrm{ph}11}(t,\tau) & h_{\mathrm{ph}12}(t,\tau) & \cdots & h_{\mathrm{ph}1N_{\mathrm{R}}}(t,\tau) \\ h_{\mathrm{ph}21}(t,\tau) & h_{\mathrm{ph}22}(t,\tau) & \cdots & h_{\mathrm{ph}2N_{\mathrm{R}}}(t,\tau) \\ \vdots & \vdots & \ddots & \vdots \\ h_{\mathrm{ph}N_T1}(t,\tau) & h_{\mathrm{ph}N_{\mathrm{T}}2}(t,\tau) & \cdots & h_{\mathrm{ph}N_{\mathrm{T}}N_{\mathrm{R}}(t,\tau)} \end{bmatrix}. \tag{2.37}$$

2.11 Channel Models

Channel models can be structured into two different groups

2.11.1 Geometry Based Deterministic Channel Models

For a specific environment, the Maxwell equations can be used in principle to obtain the time-variant CIR [163]. An approximate solution can be obtained by ray tracing by applying the fundamental geometric principles. Accordingly, the properties of every physical object must be known in detail [17,41,52,89]. Ray tracing has been applied by the authors in [99] for the modeling of vehicular communication channels. It is well known that ray tracing is an important and valuable tool for characterizing a cite-specific environment, whereas for describing general scenarios, it cannot be used [29, 163].

2.11.2 Stochastic Channel Models

The stochastic models can be classified as two classes

2.11.2.1 Geometry Based Stochastic Channel Models

In geometry based stochastic channel models (GSCMs), according to a given distribution, point scatters are randomly placed on a map [79, 103]; thus, able to capture the non-stationary properties of the propagation channel [163]. The Third Generation Partnership Project (3GPP) specified GSCMs as reference models for long term evolution (LTE). An example such as Wireless World Initiative New Radio (WINNER), describes modeling arbitrary double directional channels by randomly placing scatters around the Tx and Rx according to statistical distributions, which are characterized by large scale parameters [103]. The aim was to define channel models that meet the requirements beyond 3G simulations.

2.11.2.2 Non-Geometrical Stochastic Channel Models

The generated CIR fulfills given statistical properties such as first- and second-order moments, but an underlying geometry is not assumed. Most often, it describes in a form of TDL model to capture basic

statistical properties e.g., power delay profile (PDP) [156, 163]. TDL models are widely used for cellular system evaluation and system-level simulation for mobile communication scenarios [7, 35, 103]. Many researchers have described the dispersive channel model in the form of TDL model for V2X channels [93, 94, 96, 129] due to its low complexity and simple notation and its straightforward implementation in channel emulators [11, 12]. The TDL modeling approach has been adopted by standardization bodies not only as a reference model for universal mobile telecommunications system (UMTS) [72, 163] and global system for mobiles (GSM) [35] but also adopted by the IEEE802.11p standard for the vehicular radio channel [22, 79]. TDL model based WSSUS assumption has been developed by Ingram and coworkers for the vehicle to vehicle (V2V) channel [9, 11, 12], but as reported by Ingram, this assumption does not represent the non-stationary channel responses [9]. A TDL model with two active taps (one LOS and one strong reflector) and equal power for stress testing IEEE 802.11p modems are implemented by the authors in [151]. The main drawback underlying the TDL model is that path delays can only be equally spaced and be set in integer multiples of the sampling rate, but this can be solved via the Markov chain model. This modeling approach can be extended to be able to capture non-stationary behavior via first order/high order-two state Markov chain [61, 63–65, 67, 91, 93–96, 129].

Chapter 3

Channel Measurement Campaign

In this investigation, the conducted evaluations rely upon measurement data; thus, this chapter describes the underlying measurement data to allow interpretation of the modeling results. A measurement campaign was planned and conducted in 2013. Channel characteristics were measured in Cologne, Germany. In this chapter, we begin with a short explanation of channel sounding and then a description of underlying scenarios, including surrounding background, is provided. Widely used channel parameters such as multipath delay spread and delay window are defined and calculated from measured data.

3.1 Channel Sounding

The set of test equipment used to measure the channel's characteristics is called the channel sounder. To achieve this, a transmitter (Tx) transmits a signal into the (unknown) channel, and a receiver (Rx) collects the signal. Those two units together are known as the sounder [96]. The channel impulse response (CIR) can be estimated in a particular scenario with a channel sounder. The following formula is used to achieve an estimate of the CIR $h(t, \tau)$ by leveraging the system equation given below (3.1) [98, 163].

$$y(t) = \int_0^\infty h(t, \tau) s(t - \tau) d\tau + n(t)\,, \tag{3.1}$$

where $n(t)$ denotes the noise. The dimension of the collecting data depends on the type of channel sounder e.g. a channel sounder might directly obtain a sampled time-variant frequency response $H[m, f']$, where the discrete-time index is represented by $m \in \{0, \ldots, M-1\}$, and the discrete frequency index is denoted by $f' \in \{0, \ldots, F'-1\}$. In any multiple input multiple output (MIMO) system, the channel response matrix between all N_T antenna ports and all N_R antenna ports is measured by MIMO channel sounder. N_T and N_R denote the number of transmit- and receive-antenna ports, respectively. This can be interpreted as collecting data $N_T \times N_R$ single input single output (SISO) channels [105]. However, a truly parallel system is not only inflexible and susceptible to phase drift errors but also it is extremely expensive. In addition to that, the N_T transmitted signals have to be separated at the Rx; therefore, parallel operation of the Tx channels would cause problems (such that orthogonal transmit signals must be used). A much more suitable sounder architecture is the so-called switched-array architecture, as sketched in Fig. 3.1 [105, 142, 143, 145, 147]. In a switched-array sounder, through an electronic switch, a single available radio frequency (RF) chain is used to connect sequentially to the elements of an antenna array at Tx and Rx, respectively. Such a sounder is cheap and easy to calibrate, but it requires a long

time period to record a complete MIMO snapshot [105].

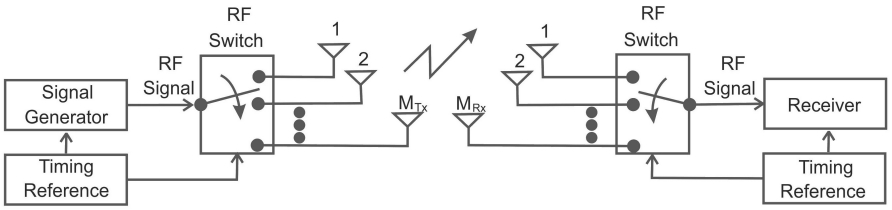

Fig. 3.1 Sketched drawing of switched-array architecture, note adapted from [105]

3.2 Underlying Scenario

The measurement data was measured in a vehicle to infrastructure (V2I)-MIMO channel sounding campaign using a MIMO-RUSK channel sounder [132]. The measurement campaign and signal setup are summarized in Table 3.2 and 3.1.

TABLE 3.1
Measurement Campaign description [132]

Measurement Campaign	
Scenario	Urban macro cell
Location	City center of Cologne, Germany
Measurement	Setup full 3D MIMO

TABLE 3.2
Measurement setup [132]

Measurement System	
Channel Sounder	RUSK (MEDAV GmbH)
Transmit power	46 dBm
Center frequency	2.53 GHz
Bandwidth	20 MHz
CIR length	12.8 µs
MIMO sub-channels	32x32 (#Tx x #Rx)
AGC switching	within MIMO sub-channels

The Tx was a base station mounted on a rooftop, and the Rx has been moving using a car. At the Tx and Rx sides, 2×8 antennas array stacked polarized uniform circular array (SPUCA) were installed (32 ports at Tx and Rx, respectively), as shown in Fig. 3.2 and Fig. 3.3. The Rx antenna height was 2.3 m, which is close to typical rooftop heights of passenger cars, and the antenna height of Tx was 33 m. More details of the antenna arrays are given in Table 3.3.

Fig. 3.2 The Tx (SPUCA 2x8) was a base station mounted on a roof top

Fig. 3.3 SPUCA 2x8 at the Rx has been moved using a car

TABLE 3.3
Measurement antenna setup [132]

Measurement Antenna Setup		
	Tx	Rx
Name(type)	SPUCA2x8	SPUCA2x8
Geometry	8 elements per ring two rings	8 elements per ring two rings
dual polarized	yes	yes
number of ports	32	32
Mounting Height	33 m	2,30 m

The measurement time under the RUSK channel sounder for a dual polarized 2×8 SPUCA configuration amounts to more than 27 ms per snapshot. Fig. 3.4 indicates a cylindrical arranged antenna array, which has been used during the channel sounding measurement campaign. In addition to that, the simulation model of the dual polarized circular arranged patch antenna array is illustrated in Fig. 3.5, and more detailed descriptions can be found in [109].

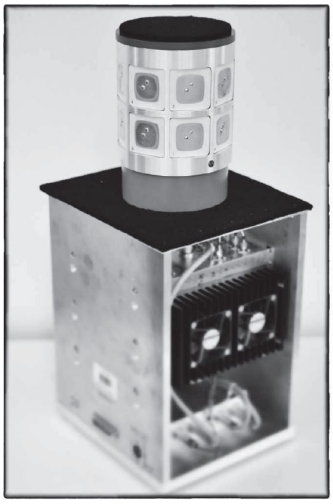

Fig. 3.4 Realized antenna array has been used during channel sounding measurement campaign, note copyright from [109]

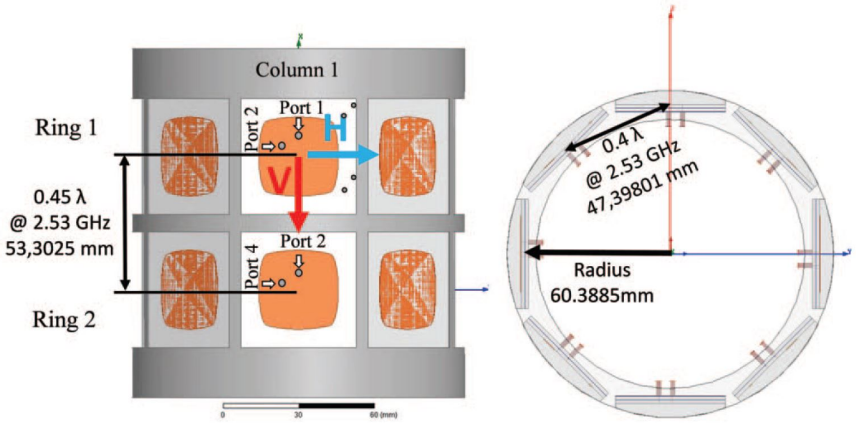

Fig. 3.5 Dimensions and simulation model of the SPUCA, which has been used during channel sounding measurement campaign, note copyright from [109]

During the measurements, the Rx car was driving approximately up to 9 $\mathrm{km\,h^{-1}}$, and the traveled distance between the Tx and Rx is known from recorded GPS data and given in Table 3.4. During the entire measurement campaign, positioning data was recorded using a global positioning system (GPS), which was mounted on the roof of both sides. Fig. 3.6 shows a top view of the realized measurement tracks, and the properties of all the collected files are summarized in Table 3.4. In this thesis, the entire measurement campaign will be investigated. A raytracer tool is used to detect different scenarios such as LOS and NLOS. After detecting all measurement points, three different scenarios (LOS, NLOS1, and NLOS2) exist in our measured data. This is illustrated in Fig. 3.7 and given in Table 3.4. Difference between NLOS1 and NLOS2 is a number of reflections/interactions. NLOS1 has one interaction, and NLOS2 assumes two or more interactions. The differentiation has been indicated by the raytracer. In this investigation, each measurement file will be examined separately and then based on different scenarios, tracks will be merged into different data sets. Three data sets will be used, which are LOS (1896 snapshots), NLOS1 (2714 snapshots) and NLOS2 (46402 snapshots).

TABLE 3.4
Basic track properties; a raytracer tool is used to detect different scenarios (LOS, NLOS1 and NLOS2); the mean delay spread is computed to examine the differentiation between those scenarios

Measurement site: Cologne										
					Scenarios			Mean RMS-DS per scenario [µs]		
Filename	**#Snap**	**Rx av. Speed**	**Distance Tx→ Rx**	**Rx track length**	**LOS**	**NLOS1**	**NLOS2**	**LOS**	**NLOS1**	**NLOS2**
Cologne_MT1-2	1831	5.0 km h^{-1}	230 m to 286 m	138 m		x	x		0.2054	0.2430
Cologne_MT2-3	2356	5.2 km h^{-1}	228 m to 258 m	185 m		x	x		0.1292	0.1905
Cologne_MT3-4	2681	3.9 km h^{-1}	258 m to 393 m	158 m			x			0.3837
Cologne_MT4-5	2958	3.5 km h^{-1}	393 m to 540 m	155 m			x			0.3684
Cologne_MT6-7	1013	5.9 km h^{-1}	562 m to 595 m	90 m			x			0.2183
Cologne_MT7-8	3231	6.1 km h^{-1}	359 m to 593 m	298 m			x			0.6102
Cologne_MT8-9	2381	4.5 km h^{-1}	343 m to 458 m	161 m			x			0.50
Cologne_MT9-10	1772	4.3 km h^{-1}	480 m to 538 m	113 m			x			0.3476
Cologne_MT10-11	883	2.9 km h^{-1}	538 m to 569 m	39 m			x			0.2189
Cologne_MT11-12	2103	3.0 km h^{-1}	533 m to 574 m	95 m			x			0.2898
Cologne_MT13-14	1607	4.6 km h^{-1}	363 m to 472 m	110 m		x			0.1040	
Cologne_MT14-15	1792	4.8 km h^{-1}	234 m to 363 m	130 m			x			0.2666
Cologne_MT15-16	2643	4.4 km h^{-1}	226 m to 326 m	176 m			x			0.2806
Cologne_MT16-17	1244	5.0 km h^{-1}	326 m to 402 m	92 m			x			0.4686
Cologne_MT17-18	2362	4.5 km h^{-1}	402 m to 546 m	160 m			x			0.4778
Cologne_MT19-20	907	5.6 km h^{-1}	491 m to 526 m	76 m			x			0.4479
Cologne_MT21-22	1814	5.0 km h^{-1}	392 m to 473 m	137 m			x			0.4057
Cologne_MT23-24	599	6.1 km h^{-1}	184 m to 237 m	55 m			x			0.3370
Cologne_MT24-25	1291	6.9 km h^{-1}	85 m to 184 m	134 m	x	x	x	0.0561	0.1781	0.3679
Cologne_MT25-26	1308	5.9 km h^{-1}	83 m to 185 m	117 m	x	x		0.067	0.1348	
Cologne_MT27-28	1625	8.2 km h^{-1}	82 m to 211 m	201 m	x	x		0.0901	0.1057	
Cologne_MT28-29	708	8.5 km h^{-1}	211 m to 293 m	90 m		x			0.1710	
Cologne_MT30-31	1545	7.2 km h^{-1}	282 m to 433 m	166 m			x			0.5983
Cologne_MT31-32	1587	9.1 km h^{-1}	433 m to 646 m	218 m			x			0.3755
Cologne_MT33-34	1762	5.0 km h^{-1}	643 m to 648 m	132 m			x			0.2233
Cologne_MT34-35	1497	5.3 km h^{-1}	531 m to 645 m	120 m			x			0.2267
Cologne_MT35-36	1167	6.3 km h^{-1}	424 m to 531 m	110 m			x			0.4113
Cologne_MT36-37	896	6.6 km h^{-1}	414 m to 425 m	88 m			x			0.4580
Cologne_MT37-38	1810	4.0 km h^{-1}	310 m to 417 m	109 m			x			0.6195
Cologne_MT38-39	2097	4.1 km h^{-1}	295 m to 311 m	128 m			x			0.4243

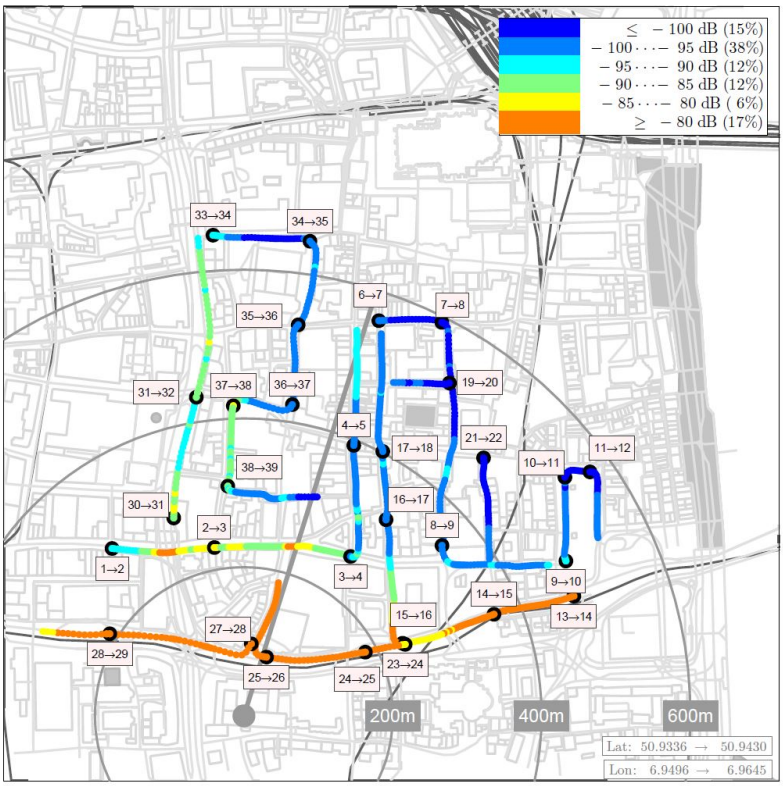

Fig. 3.6 A top view of the realized measurement tracks in Cologne

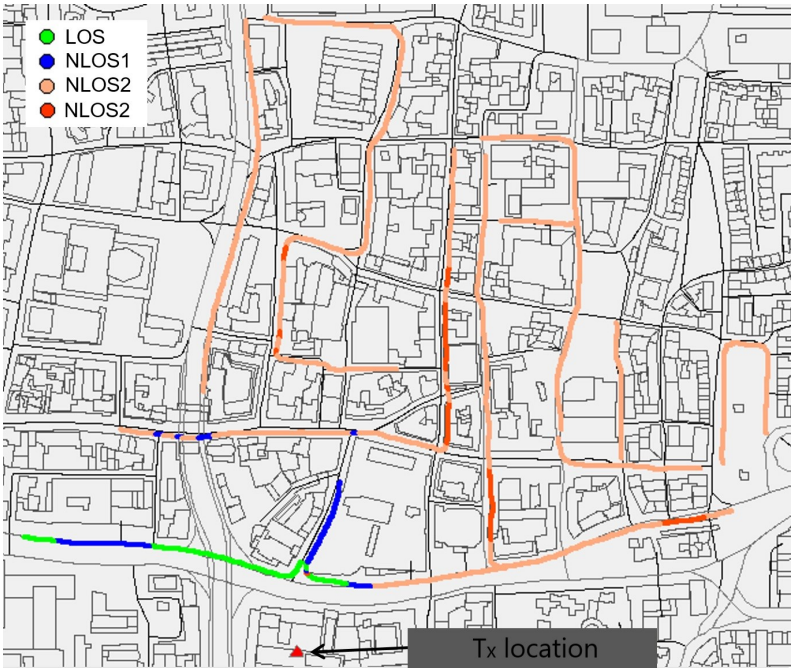

Fig. 3.7 A raytracer tool is used to detect different scenario in each measurement track; three different scenarios (LOS, NLOS1, and NLOS2) exist in our measured data

3.3 Surroundings

An insight into the surrounding buildings and other elements in the environment that may influence the propagation of the signal is given in this chapter. The following sub-sections may provide a better understanding of the found results. Latitude and longitude of the Rx are provided for each measurement file such that the reader can use Google street view to get an overview of the surrounding environment. [1]. Due to a large number of measurement track, the surrounding environment is presented only for few measurement tracks. Appendix A.1 contains the surrounding detail of other measurement tracks. The selected tracks in this chapter briefly provide the reader another step towards a deeper understanding of surrounding environment, which includes wide streets, pedestrian areas, narrow street, small and large trees and etc. The Rx has been driven beside, behind, and in front of other vehicles.

3.3.1 Measurement track 3-4

The car was driving into a narrow street and the measurement track has been stopped after the car reached a square. Table 3.5 provides description of surrounding environment and the reader can use Google street view to get an overview of the surrounding environment.

[1]The pictures from Google street view have not been illustrated because street view imagery cannot not be used for any print purposes.

TABLE 3.5
Description of surrounding environment for measurement track 3-4

Description of surrounding environment				
	Starting point		End of measurement track	
File name	Latitude Rx	Longitude Rx	Latitude Rx	Longitude Rx
Cologne_MT3-4	50.936343	6.956245	50.937686	6.956308

3.3.2 Measurement track $24 \rightarrow 25$

Measurement track 24-25 goes through different scenarios. There was a wide street and the car was driving from NLOS2, then was driving to NLOS1 and then drove to LOS. Table 3.6 gives the approximated starting point of the measurement track (it is in NLOS2 scenario), which was in the middle of a wide street. Later on, the vehicle was driving into the line of sight (LOS) region. The Tx was on a roof top on the left hand side of the driving direction of the car. The measurement track was ended after the car turned to a crossroad.

TABLE 3.6
Description of surrounding environment for measurement track 24-25

Description of surrounding environment				
	Starting point		End of measurement track	
File name	Latitude Rx	Longitude Rx	Latitude Rx	Longitude Rx
Cologne_MT24-25	50.935187	6.956527	50.935126	6.954635

3.3.3 Measurement track 25-26

This track started directly after the track 24-25 was leaving the crossroad. The car was driving from LOS scenario and then it drove to NLOS1 scenario. The description of starting point and end point of measurement track are given in Table 3.7. The traveled street is passed over by a small bridge and the car drove the road until a pedestrian area occurred.

TABLE 3.7
Description of surrounding environment for measurement track 25-26

Description of surrounding environment				
	Starting point		End of measurement track	
File name	Latitude Rx	Longitude Rx	Latitude Rx	Longitude Rx
Cologne_MT25-26	50.935126	6.954634	50.936026	6.954865

3.3.4 Measurement track 30-31

In this measurement track, the car was driving on a wide street and then it was driving towards a crossroad. The measurement track ended before entering this crossroad. The description is given in Table 3.8.

TABLE 3.8
Description of surrounding environment for measurement track 30-31

Description of surrounding environment				
	Starting point		End of measurement track	
File name	Latitude Rx	Longitude Rx	Latitude Rx	Longitude Rx
Cologne_MT30-31	50.936809	6.952854	50.93827	6.953287

3.4 Extracting Initial Parameters

As explained in Chapter 3.2, three different scenarios (LOS, NLOS1, NLOS2) have been indicated by the raytracer. The aim of this chapter is to examine the differentiation between those scenarios using statistical measures such as mean delay spread. In [96], the authors divide different regions by using root mean square delay spread (RMS-DS). The RMS-DS and delay window (DW) are key parameters used to quantify the spread of a signal in time domain. The length of a power delay profile (PDP) that contributes x% of the total energy [2] is defined as the DW [73]. The RMS-DS (σ_{τ_k}) is calculated using (3.3) [25, 73, 92].

$$\mu_{\tau k} = \frac{\sum_{p=1}^{P} \tau_p \gamma_p'^2}{\sum_{p=1}^{P} \gamma_p'^2}\,, \tag{3.2}$$

$$\sigma_{\tau k} = \sqrt{\frac{\sum_{p=1}^{P} \tau_p^2 \gamma_p'^2}{\sum_{p=1}^{P} \gamma_p'^2} - \mu_{\tau k}^2}\,, \tag{3.3}$$

where μ_{τ_k} is a power weighted average delay of the k^{th} snapshot, τ_p and γ_p' are the delay and amplitude of p^{th} tap. The more dispersive the channel causes the larger value of the DW and RMS-DS. The value of the RMS-DS and DW are computed for each snapshot from the measured CIR and compared in Fig. 3.8(a). A difference in the values of both metrics can be noticed, whereas a strong correlation exists between them. Fig. 3.8(b) shows the corresponding RMS-DS for each scenario. The RMS-DS value increases under NLOS2 and NLOS1 conditions, compared with LOS scenario the RMS-DS oscillates around 80 ns.

[2] After the noise threshold and the multipath threshold (25 dB below the main peak)

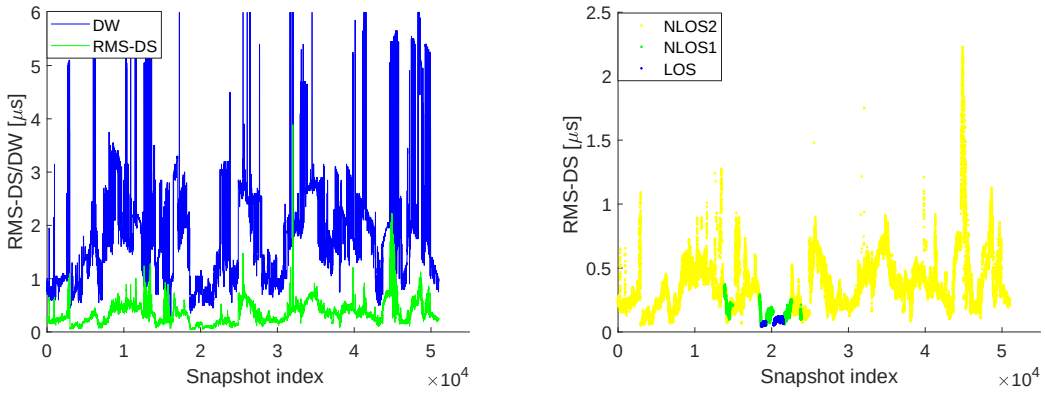

(a) (b)

Fig. 3.8 (a) Comparison between the RMS-DS and delay window versus snapshot index; a strong correlation between the RMS-DS and DW is existed, (b) The corresponding RMS-DS for each scenario; the RMS-DS value decreases under LOS condition and oscillates around 80 ns

As already stated previously, our aim is to differentiate between those three scenarios (LOS, NLOS1, NLOS2) using the statistical measures. The mean delay spread is computed to examine the differentiation between them. It is calculated for each measurement track in accordance with the scenario and given in Table 3.4. Based on the results, three different groups can be distinguished. The statistics result of NLOS1 (value of the mean delay spread) indicates that it lies between LOS and NLOS2 scenarios. For those specific regions (NLOS1), a transmitted wave is attenuated by only one interaction. Therefore, it has relatively large energy and smaller delay; thus, the value of the mean delay spread is smaller compared to NLOS2, which is assumed to undergo more than one interaction.

Chapter 4

SISO-TDL Model Parameter Estimation

4.1 Motivation and Related Work

Many researchers have described the dispersive channel model in a form of tapped delay line (TDL) model for vehicle to X (V2X) channels [93, 94, 96, 129] due to its low complexity and simple notation and its straightforward implementation in channel emulators [11, 12]. Mainly, the class of TDL model is single input single output (SISO) channel, and it is based on the assumption of wide sense stationary uncorrelated scattering (WSSUS), which is not realistic for V2X channels due to the frequent transitions [85, 129]. It can be extended to non-WSSUS using the first-order two-state Markov chains [61, 64, 67, 94, 96, 129], in contrast to the higher-order Markov Chain considered in [93], where it has been observed that the order of the Markov Chain does not need to be larger than second-order. As explained in Sections 2.7-2.9, from a mathematical point of view (2.31), the superposition of multiple rays constitutes the full CIR. Each individual ray could be identified as a tap and be used in a TDL model. However, deriving the parameters of each such tap from measurement data would require advanced signal processing methods such as high-resolution parameter estimation [82, 144], as the measured data is always done with limited bandwidth; thus, the individual Dirac-deltas are not directly visible. Therefore, different definitions of taps are used in literature, with less strict relations to the geometrical ray. Based on the definition in [95, 96, 129, 155], where a tap is a sample of the bandlimited channel impulse response (CIR). In general, a TDL model consists of at least one tap, each having a set of parameters. The TDL model is the discrete form representation of the CIR, and it is widely used to match the symbol period of a given system [96]. In literature, different strategies are available to select sufficient samples; in [129], the authors proposed to sub-select the samples based on power to reproduce 99% of the total power. In [157, 160], authors define dense- and sparse-taps, which are placed to cover the range with 80% and 20% power contribution, respectively. They have been developed by averaging samples along with the delay domain (after computing the mean power delay profile (PDP)) by dividing the delay axis of the mean PDP using an interval and then summing those samples in the delay domain that tend into the interval. Based on the definition in [108], a tap is a cluster of bins containing highly correlated amplitudes. In [56], the authors use a clustering technique to select the tap to reduce the number of taps. In other words, paths with similar properties, such as delay, are grouped together and represented as an active tap. The goal

of defining a TDL is to select only the relevant samples (or set of clusters) of the CIR and model their amplitudes and Doppler shifts properly.

The approach used in this investigation is based on the definition in [95,129], where a tap is a sample of the bandlimited CIR. Consequently, one tap can be a ray, multiple rays, or no ray at all. In this investigation, the proposed approach of [129] to extract TDL model parameters from measured data is extended. In addition to that, the proposed approach of [129] is applied to verify and compare to the extended model. We concentrate on the channel taps, whose amplitudes and delays are necessary to compute the root mean square delay spread (RMS-DS) of the channel because the RMS-DS is the major factor in the performance of most digital communication systems, including orthogonal frequency division multiplexing (OFDM) system proposed for V2X communication. When the RMS-DS is greater than a guard interval, this will lead to inter symbol interference (ISI) and degrade performance, in other words, individual symbols overlap with the following ones, as result transmission errors occur [1] [37,64]. Hence, designers most often rely on RMS-DS, which has been shown to be directly relatable to communication system performance.

To summarize, the classical TDL model is extended to a non-WSSUS model, which is suited for V2X communication systems. The proposed extension is based on a discussed model [92, 129] using a persistence process (PP). The remainder of this chapter is organized as follows. We first describe selecting the relevant samples of the CIR and estimating their parameters from measured data and then we address their amplitude fading. Next, an approach is proposed to verify the correctness of the channel model parameters derivation. The analysis investigates the correlation coefficient among taps amplitude as well as taps persistence. All those parameters are essential for implementing the channel models and building a generator, which will be devised in Chapter 5.

The material of this chapter is partially presented in [61, 64, 66].

4.2 Time-Delay of the Active Taps

As defined earlier, a tap is a sample of the bandlimited CIR. However, using all possible taps in a TDL model would not be feasible and also not necessary. For instance, in our case, where the total CIR length is $12.8\mu s$ and a bandwidth is 20 MHz; therefore, 256 taps need to be considered. In general, using only a subset is sufficient to characterize the channel (on average). The PDP is of high practical significance in terms of determining taps for the TDL model [61,63,64,66,95,129,157,160]. In this chapter two methods will be presented that can be used to determine the relevant or "active taps " [2]. The first approach is based on cumulative tap energy and was proposed by [129], the second one is a variant of the first, but it is based on finding "peak taps". Entire measurement campaign will be used in this investigation. As indicated in Chapter 3, three different scenarios (LOS, NLOS1, and NLOS2) exist in our measured data. In this chapter, each measurement file will be examined separately and then based on different scenarios, tracks will be merged into different data sets, which are LOS (1896 snapshots), NLOS1 (2714 snapshots) and NLOS2 (46402 snapshots). Then these data sets will be investigated. It is important to note that in this chapter illustration for parameter extraction will be presented exemplary for track number ($24 \rightarrow 25$) because it goes through all three different scenarios as described in Chapter 3.3.2.

[1] Although channels with the same RMS-DS, but different CIRs can yield different ISI effects, it is impossible to account for the infinite number of such "equal-RMS-DS" CIRs.

[2] Active taps are those samples, which is selected from measured data to fully describe the CIR

4.2.1 Determination of Active Taps Based on the Cumulative Energy

As already stated, this approach is proposed by [129]. The outcome of this method is called model-1 ($M1$). The algorithm to extract the model parameters is illustrated below:

1. **Hann Window:** The Hann window is applied to the data to reduce and confine the leakage [19].

2. **Noise Cutting:** The noise level is estimated using the algorithm in [44]. Subsequently, all samples in the measured impulse response below the noise threshold (6 dB above the noise level) are set to zero. In order to obtain a PDP for a single snapshot, the PDP is averaged over the channels of the transmitter (Tx) and receiver (Rx) antenna array. The PDP is calculated

$$P_k(t,\tau) = \frac{1}{N_{\mathrm{T}} N_{\mathrm{R}}} \sum_{u=1}^{N_{\mathrm{T}}} \sum_{v=1}^{N_{\mathrm{R}}} |h_k(t,\tau,u,v)|^2 \,, \tag{4.1}$$

   where $P_k(t,\tau)$ is the PDP of the k^{th} snapshot, N_{T} and N_{R} are the numbers of Tx- and Rx-antennas, respectively. An example of PDP with its noise threshold is shown in Fig. 4.1(a) and those multipaths that are below the noise threshold are set to zero.

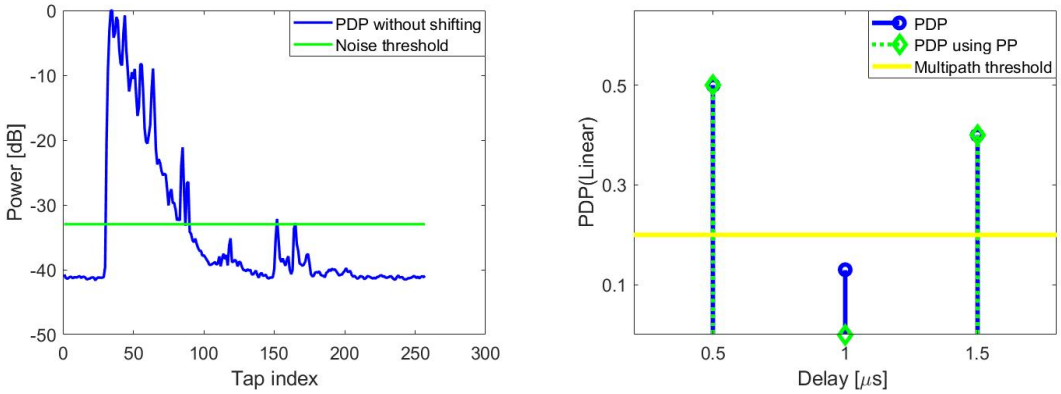

(a) (b)

Fig. 4.1 (a) Example of recorded PDP with its noise threshold; those multipaths that are below the noise threshold are set to zero, (b) PDP versus PDP with PP; each component whose power is below the multipath threshold is considered to be "OFF," which is indicated using green stems

3. **Persistence Process (PP):** The "ON"/"OFF"-state of each multipath is determined ($z_p(t)$ in 2.31). In order to make this clear, consider an example if we could measure the CIR with an ideally infinite delay resolution, and we get the PDP, which is depicted in Fig. 4.1(b). Blue stems show a PDP that contains three components. Each of those whose power is below a multipath threshold (MT) is considered to be "OFF," which is indicated using green stems. As a result, an ON/OFF sequence for each multipath will be obtained, which is relevant to compute a Markov chain parameters (these parameters is essential for a generator). Fig. 4.3(a) provides an example of measured PDP versus applying MT to obtain the persistence process (PP). In this investigation, the MT is set to be 25 dB below the main peak in each snapshot. Fig. 4.2(a) shows a dynamic range of the normalized PDP corresponding to the CIR in each snapshot. Additionally, the normalized PDP under NLOS2 condition is plotted in Fig. 4.2(b), where a dynamic range of 37 dB is achieved.

Fig. 4.3(b) illustrates PP versus tap index, the yellow color indicates when a tap is "ON," and the blue color indicates the "OFF" state. The lifetime of tap is determined by the number of snapshots, where a tap is in the "ON" state. Additionally, an exemplary life time of a tap is shown in Fig. 4.4(a).

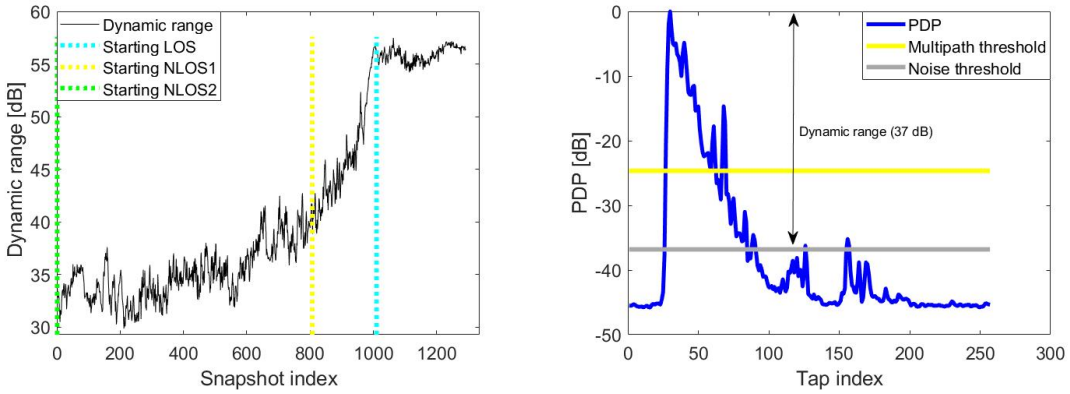

(a) (b)

Fig. 4.2 (a) Dynamic range of the normalized PDP versus snapshot index (track number 24 →25), (b) Normalized PDP corresponding to one of the CIRs under NLOS2 condition, where a dynamic range of 37 dB is achieved

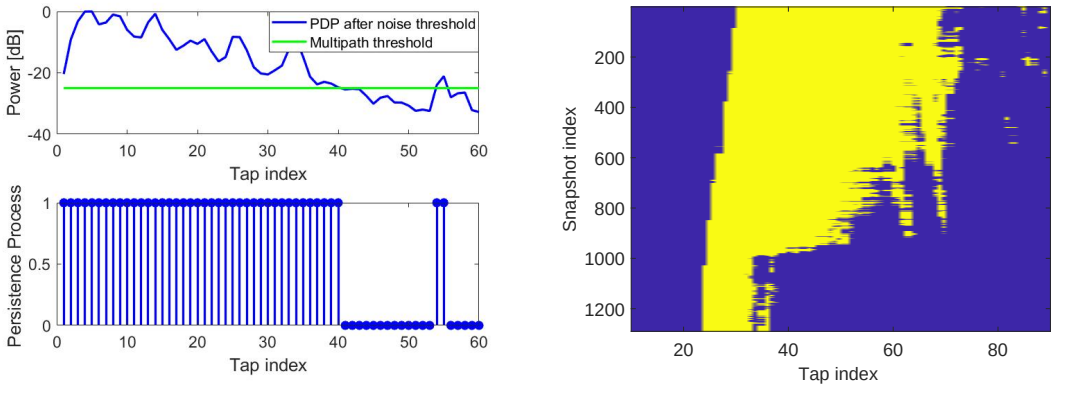

(a) (b)

Fig. 4.3 (a) An example of measured PDP versus applying MT to obtain the PP; the MT is set to be 25 dB below the main peak, (b) PP versus tap index, the yellow color indicates when a tap is "ON" and the blue color indicates the "OFF" state

4. **MC Parameters:** From the "ON"/"OFF"-sequence from step 3, we can find the probabilities of the TS matrix (4.2) of each multipath using (4.3) [155].

$$TS = \begin{bmatrix} P_{00} & P_{01} \\ P_{10} & P_{11} \end{bmatrix}, \tag{4.2}$$

where

$$P_{00} = \frac{n_{00}}{n} \; ; \; P_{01} = \frac{n_{01}}{n} \; ; \; P_{10} = \frac{n_{10}}{n} \; ; \; P_{11} = \frac{n_{11}}{n}, \tag{4.3}$$

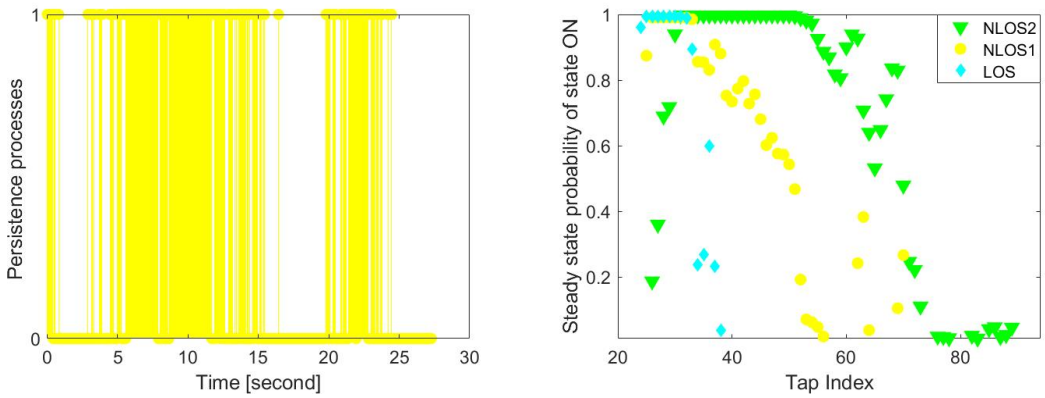

(a) (b)

Fig. 4.4 (a) An exemplary life time of a tap in $M1$ (track number 24 →25 start from NLOS2 scenario and it goes under NLOS1 condition), (b) A steady-state probability of taps being ON in $M1$; the SS_1 decreases as the tap index increases (track number 24 →25)

where n_{01} is the number of occurrences of a transition from state OFF to ON and n is the total number of possible transitions [3]. As a result, the TS matrix is obtained for each multipath. From the parameters of the TS matrix, then we can calculate the probabilities of the SS matrix using (4.5) and (4.6) [155].

$$SS = \begin{bmatrix} SS_0 \\ SS_1 \end{bmatrix}, \tag{4.4}$$

where

$$SS_0 = \frac{P_{10}}{P_{10} + P_{01}}, \tag{4.5}$$

$$SS_1 = 1 - SS_0 = \frac{P_{01}}{P_{01} + P_{10}}. \tag{4.6}$$

Fig. 4.4(b) provides the steady-state probability of state ON (SS_1) versus tap index. The SS_1 decreases as the tap index increases.

5. **Average "ON"-Energy:** Find the average "ON" energy (4.7) for each tap by averaging the energy of a tap when it is in the "ON" state over snapshots.

$$E_p^{\text{ON}} = \frac{\sum_{k=1}^{K} E_p^k}{\sum_{k=1}^{K} z_p^k}, \tag{4.7}$$

where

$$E_p^k = P_p^k \cdot z_p^k, \tag{4.8}$$

where E_p^k is valid energy of p^{th} tap in the k^{th} snapshot, P_p^k is the power of the p^{th} tap in the k^{th} snapshot. z_p^k is the PP of the p^{th} tap in the k^{th} snapshot. E_p^{ON} is the average ON energy for the

[3] n_{00} is the number of occurrences of a transition from state OFF to OFF, n_{11} is the number of occurrences of a transition from state ON to ON, and n_{10} is the number of occurrences of a transition from state ON to OFF.

p^{th} tap. Fig. 4.5(a) depicts the average ON energy associated with each tap for the three scenarios. It is evident that the average ON energy decreases as the tap index increases. Additionally, it is observed that the rate at which the tap energy decreases with tap index is much slower under LOS conditions compared to the other two scenarios.

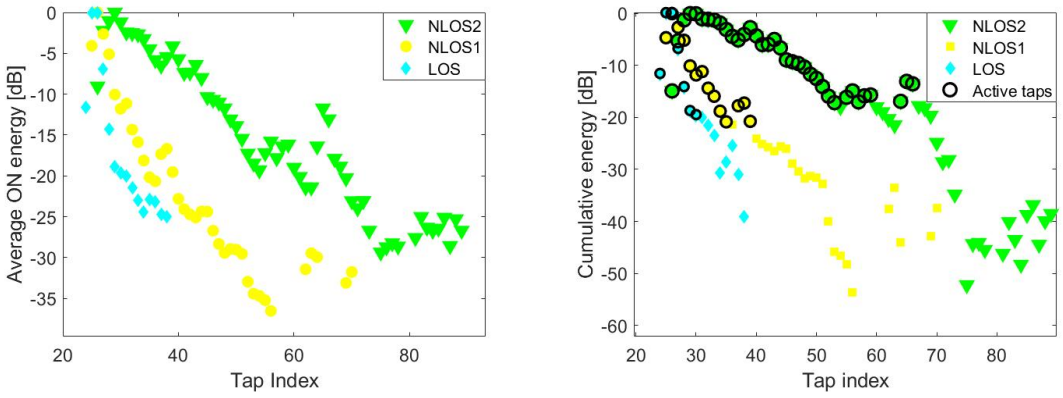

(a) (b)

Fig. 4.5 (a) Average ON Energy in $M1$; the rate at which the tap energy decreases with tap index is much slower under LOS condition compared to the other two scenarios (track number 24 →25), (b) The active taps and cumulative energy of the ON taps in $M1$ (track number 24 →25)

6. **Cumulative Energy:** Find the cumulative energy by multiplying the average "ON"-energy with SS_1 for each tap (4.9). The result is shown in Fig. 4.5(b).

$$C_{\mathrm{E}p} = E_p^{\mathrm{ON}} \cdot SS_{1p}\,. \tag{4.9}$$

7. **Active Taps:** Sort the result from step 6 by magnitude in descending order and select the taps that accumulate 99% of the total energy.

The outcome of this method ($M1$) is illustrated in Fig. 4.5(b). The plot depicts the cumulative energy (outcome of step 6) of every ON tap's for the three different scenarios. Black circles are used to indicate the active taps, being sub-selected from the ON-taps[4]. Except for the NLOS2 scenario, this method tends to select taps as active taps that are close to the main peak of the cumulative energy. We observe that the negligence of taps with low energy but large delays can have unfavorable effects on the capability of the TDL model to regenerate the RMS-DS. This will be illustrated in detail in Chapter 4.2.3.

4.2.2 Determination of the Active Taps Based on the Peak Energy

This section proposes a new approach to obtain the TDL model parameters that also select low-magnitude taps that have larger delays. We call this approach model-2 ($M2$), and it is based on the previous algorithm with some extensions. The extension introduces an additional step after the first step, which is a base delay compensation, and in the last step, the selection of active taps from the cumulative tap energy is modified.

In a V2X scenario, at least one of the Tx and Rx is mobile, and the CIR is subject to potential strong shifts in its base delay (delay of the first tap with significant energy). Therefore, we suggest first aligning

[4]ON-taps are the taps that at least once in ON-state.

the channel impulse responses (CIRs) to compensate for this. Consider an example where the Rx is first moving towards the Tx and after some time moving away. The PP in such a case could look like the example given in Fig. 4.6 (upper panel). Without any compensation of the base delay, this could lead to a large number of taps with a low lifetime. After alignment, the number of ON taps is lower, and their lifetime is increased; this is shown in Fig. 4.6 (lower panel). We also propose to perform the shifting of CIR based on the change in distance between the Tx and Rx (known from recorded GPS data). It is also possible to perform the shifting such that the first ON tap is always moved to the beginning of the CIR at 0 s. However, we decided this would not be the best way due to the possible mixing of taps. For example, if the first tap is OFF for the given snapshot; thus, the second tap would be shifted to 0 s. If the first tap is in the ON state in the next snapshot, it would be moved to 0 s. Doing so would result in the first tap (after shifting) being always ON. The impact of shifting can be clearly seen in our measurement data; Fig. 4.7 shows the impact of shifting on the valid energy of the CIR. As explained previously, all steps are identical to the previous method, except two steps are modified (called $1B$ and $7B$). These two steps are clarified below:

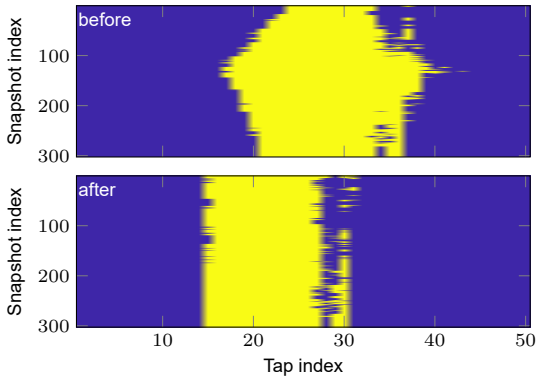

Fig. 4.6 PP of the taps before and after shifting CIR; the approach of upper panel leads to a large number of taps with low lifetime; after alignment the number of ON taps is smaller and their lifetime is increased (lower panel)

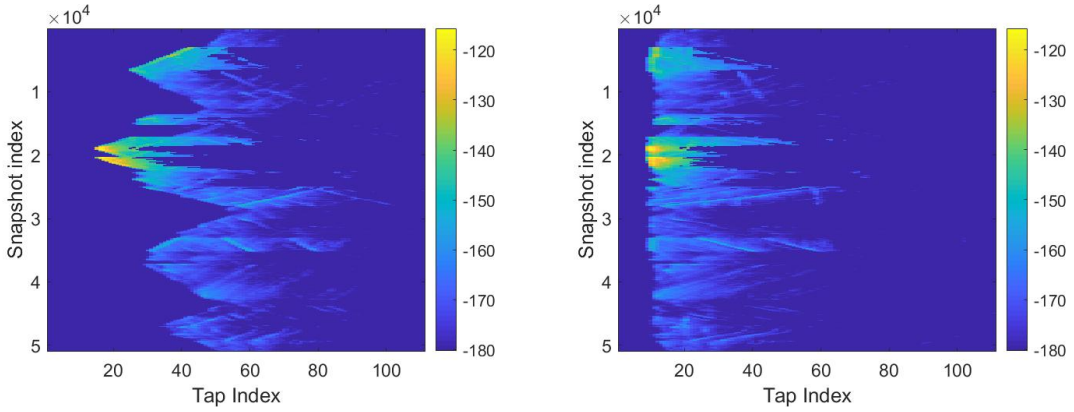

Fig. 4.7 Valid energy after merging the data, (a) Before shifting in $M1$, (b) After shifting in $M2$

$1B$. **Base Delay Compensation:** Determine the delay ($\Delta\tau$) caused by change in distance between

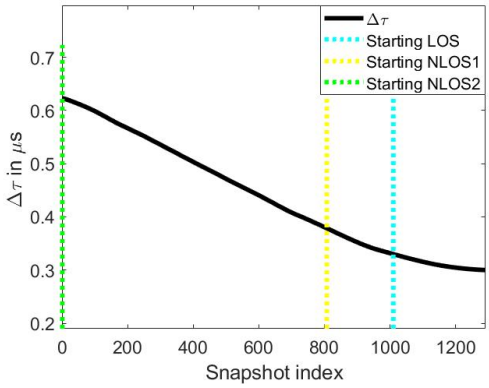

Fig. 4.8 $\Delta\tau$ versus snapshot index (track number 24 →25)

the Tx and Rx. The algorithm to compute the $\Delta\tau$ is illustrated below

$1B1$. Haversine distance: Distance between the Tx and Rx is calculated by using Haversine Formula (4.10) [154].

$$\Delta d_{\mathrm{H}} = 2r \sin^{-1}\left(\sqrt{\Delta M + \Delta W}\right), \tag{4.10}$$

where

$$\Delta M = \sin^2\left(\frac{\phi_2 - \phi_1}{2}\right), \tag{4.11}$$

$$\Delta W = \cos(\phi_1)\cos(\phi_2)\sin^2\left(\frac{\lambda_2 - \lambda_1}{2}\right), \tag{4.12}$$

where r is earth radius and set to 6367 km, ϕ_1 and ϕ_2 are the Tx and Rx latitude in radians. λ_1 and λ_2 are the Tx and Rx longitude in radians [154]. We have the latitude and longitude of Tx and Rx from the GPS positioning.

$1B2$. Find a distance between the Tx and Rx antennas (ΔD) using the Pythagoras theorem.

$$\Delta D = \sqrt{\Delta d_{\mathrm{H}}^2 + \Delta H^2}, \tag{4.13}$$

where Δd_H is the Haversine distance (the outcome of step $1B1$) and ΔH is a difference between the Tx and Rx antenna height.

$1B3$. Find LOS delay $\Delta\tau$ using (4.14)

$$\Delta\tau = \frac{\Delta D}{c}, \tag{4.14}$$

where c is the speed of light. The value of $\Delta\tau$ versus snapshot index is depicted in Fig. 4.8. As can be seen in the map (Fig. 3.6 and 3.7), over the different snapshot indices, the car was coming closer to the Tx; thus, the value of $\Delta\tau$ decreases gradually because the distance decreases.

$1B4$. Find Δs using (4.15). Δs is the number of samples to be shifted.

$$\Delta s = \frac{\Delta\tau}{\frac{1}{B}}, \tag{4.15}$$

where B is the bandwidth. Apply a fast Fourier transform (FFT) of the CIR to obtain a time varying channel transfer function, then perform shifting.

To sum up, the value of $\Delta\tau$ is computed for each snapshot and then the number of samples to be shifted is calculated. Next, apply the FFT of CIR to obtain a time-varying channel transfer function, then perform shifting. Fig. 4.9(a) shows one of the measured PDPs. Blue color shows PDP without shifting. The LOS delay is 0.3129 μsec, which is corresponded to 6.2588 samples (Δs) to be shifted. When the shifting is performed, the PDP looks like a green color in Fig. 4.9(a). Fig. 4.9(b) illustrates the PP after shifting the CIR, and it can be noticed that the shifting has an impact (compare Fig. 4.3(b) with Fig. 4.9(b)).

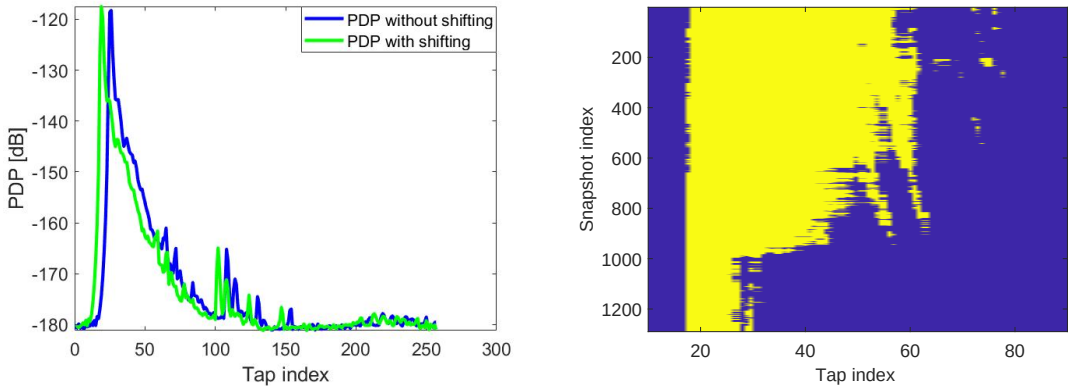

(a) (b)

Fig. 4.9 (a) An example of the measured PDP with and without Shifting; the blue color shows PDP without shifting and when the shifting is performed, the PDP looks like the green color, (b) PP of the taps after shifting the CIR in M2; the impact of shifting can be noticed by comparing Fig. 4.9(b) with Fig. 4.3(b) (track number 24 $\rightarrow$25)

7B. **Active Taps:** Active taps are chosen at the peaks of the cumulative energy. Any sample in the data set more prominent than their couple neighboring samples is assumed to be a peak tap.

Fig. 4.10 shows the outcome of the second method ($M2$). Because of the shifting of the CIR, the tap indices and cumulative energy changes in comparison to Fig. 4.5(b). It can be seen that when only the peak taps are considered, fewer taps are selected as the active taps. Additionally, those taps are also selected as active taps, which have lower energy with larger delays compared to the first approach.

TABLE 4.1
TAP NUMBER COMPARISON IN $M1$ AND $M2$ FOR EACH MEASUREMENT TRACK

Tap number comparison in $M1$ and $M2$ for each file						
	$M1$			$M2$		
File name	**LOS**	**NLOS1**	**NLOS2**	**LOS**	**NLOS1**	**NLOS2**
Cologne_MT1-2		17	19		7	9
Cologne_MT2-3		13	22		4	7
Cologne_MT3-4			37			14
Cologne_MT4-5			37			10
Cologne_MT6-7			27			5
Cologne_MT7-8			47			11
Cologne_MT8-9			39			17
Cologne_MT9-10			33			10
Cologne_MT10-11			19			6
Cologne_MT11-12			22			7
Cologne_MT13-14		14			4	
Cologne_MT14-15			25			10
Cologne_MT15-16			22			11
Cologne_MT16-17			40			11
Cologne_MT17-18			44			14
Cologne_MT19-20			32			14
Cologne_MT21-22			31			11
Cologne_MT23-24			31			14
Cologne_MT24-25	7	14	36	2	6	12
Cologne_MT25-26	9	14		2	3	
Cologne_MT27-28	13	12		2	4	
Cologne_MT28-29		18			4	
Cologne_MT30-31			53			18
Cologne_MT31-32			38			12
Cologne_MT33-34			20			4
Cologne_MT34-35			22			7
Cologne_MT35-36			38			20
Cologne_MT36-37			35			11
Cologne_MT37-38			49			14
Cologne_MT38-39			39			8

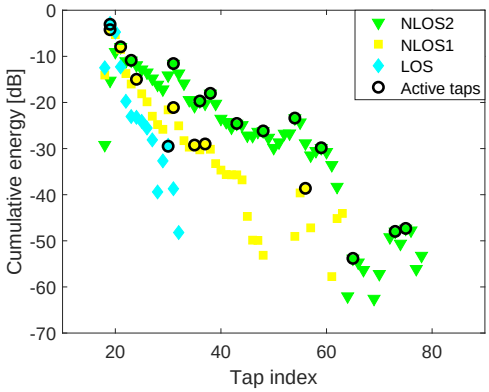

Fig. 4.10 The active taps and cumulative energy of the ON taps in $M2$; only the peak taps are considered, this leads to selecting fewer taps as the active taps (track number 24 →25)

4.2.3 Evaluation of the Outcome from $M1$ and $M2$

In Section 4.2.1 and 4.2.2, two algorithms have been clarified in order to derive the TDL model parameters from the measurement data. The model parameters are extracted for each measurement track, and the number of active taps for both models is compared in Table 4.1. The same characteristics of three different groups, which are indicated in Table 3.4 are also noticeable in Table 4.1. From the results, the outcome of model $M2$ is reducing the number of taps by more than 50%. The active taps for track number ($24 \rightarrow 25$) are plotted in Fig. 4.5(b) and 4.10 and indicated using a black circle. The outcome of model $M2$ is not only reducing the number of taps substantially compared to $M1$ but also includes those

taps that have low power with the large delay that are important for regenerating the delay spread. In the literature, the accuracy of the channel models is verified and evaluated based on how well they agree in terms of RMS-DS [38, 55, 129]. Here, an approach is proposed to verify the correctness of the channel model parameters derivation. First, the RMS-DS is computed (3.3) for the measurement data (after the noise threshold and the multipath threshold, 25 dB below the main peak) using all possible taps. After that, the RMS-DS is calculated only for the tap indices where the models $M1$ and $M2$ would place an active tap. The result is plotted in Fig. 4.11 for track number (24 $\rightarrow$ 25). The CDF of RMS-DS for the NLOS1 region [5] is shown in Fig. 4.11(a), and for probabilities lower than 0.2, $M1$ fits better with the measurement data. In order to explain this, a new term will be defined, which is active-ON tap. Those taps that are active and in ON-state are called active-ON taps. This is referred to the PP; active taps are not always active-ON taps due to incorporating ON/OFF behavior (PP). The PP of active taps indices under NLOS1 conditions is plotted in Fig. 4.12 [6]. From the figure, it is observed that $M1$ selects almost all the ON taps and tends to generate more than 91% of the active-ON taps because the active taps are close to the main peak (this is shown in Fig. 4.5(b)). Therefore, they carry lots of energy, as a result, they are active-ON taps most of the time. On the other hand, $M2$ generates 66% [7] of the active-ON taps, as a consequence, for those regions $M1$ fits better.

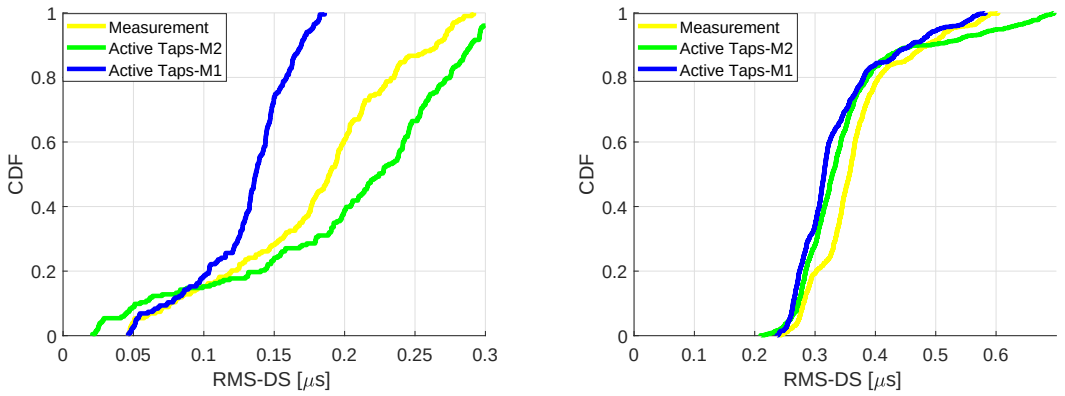

Fig. 4.11 CDF comparison of the RMS-DS between the measurement data and the active taps only (track number 24 $\rightarrow$ 25), (a) NLOS1, (b) NLOS2

[5] Underlying different scenarios have been defined in Section 3.2
[6] The PP under NLOS1 scenario for one of those snapshots that the CDF-DS probabilities lower than 0.2
[7] Number of active tap= 6, Number of active-ON taps=4; range = $\frac{4}{6} = 66\%$

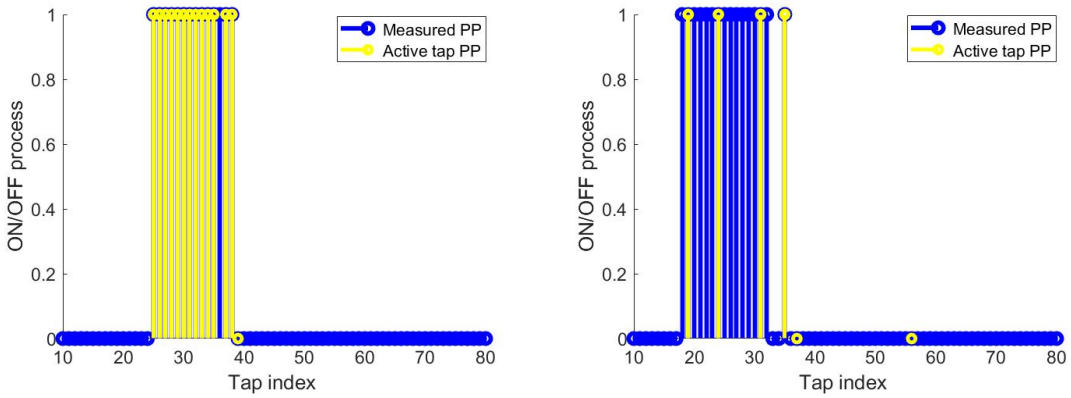

(a) (b)

Fig. 4.12 PP under NLOS1 scenario for one of those snapshots that the CDF-DS probabilities lower than 0.2 (track number 24 → 25), (a) $M1$, (b) $M2$

Table 4.2 provides a metric, which is the difference of mean RMS-DS to compare those CDFs in Fig. 4.11. The overall statistic of the outcome from $M1$, the delay spread is under-estimated because it neglects the low power taps with large delays. The outcome from $M2$ shows improvement of the delay spread while reducing the number of taps significantly[8], and it is closer to the measurement data. Therefore, we assume $M2$ works better because at 0.5 value of the CDF its closer to the measurement.

TABLE 4.2
DIFFERENCE OF THE MEAN RMS-DS [μsec] BETWEEN THE MEASURED DATA AND ACTIVE TAPS FOR TRACK NUMBER (24→25)

Scenario	$M1$	$M2$
NLOS1	0.04	0.02
NLOS2	0.03	0.01

Fig. 4.11(b) illustrates the CDF of RMS-DS under the NLOS2 conditions. It is not surprising that both models could generate almost the same delay spread because $M1$ filtered more than half of the ON taps. Nevertheless, $M2$ could generate almost the same results, or even it is better in some areas by filtering only 20% of the ON taps. For probabilities greater than 0.9, $M1$ fits better to the measurement data due to the high percentage of active-ON taps, which is illustrated in Fig. 4.13, and the reason is clarified for the NLOS1 scenario. Fig. 4.13 shows PP under the NLOS2 scenario for one of those snapshots that the CDF-DS probabilities greater than 0.9. However, in most of the areas, both models are equally good (it is illustrated in Fig. 4.11(b)), then we prefer the one that has fewer taps due to less complexity, easier for computation, and channel emulator is limited to a finite number of taps.

[8]Reducing number of taps is very important feature because implementation of such a model in channel emulators is limited up to 12 taps. In addition to that 6-tap and 12-tap are employed by IEEE 802.11p [10, 12]

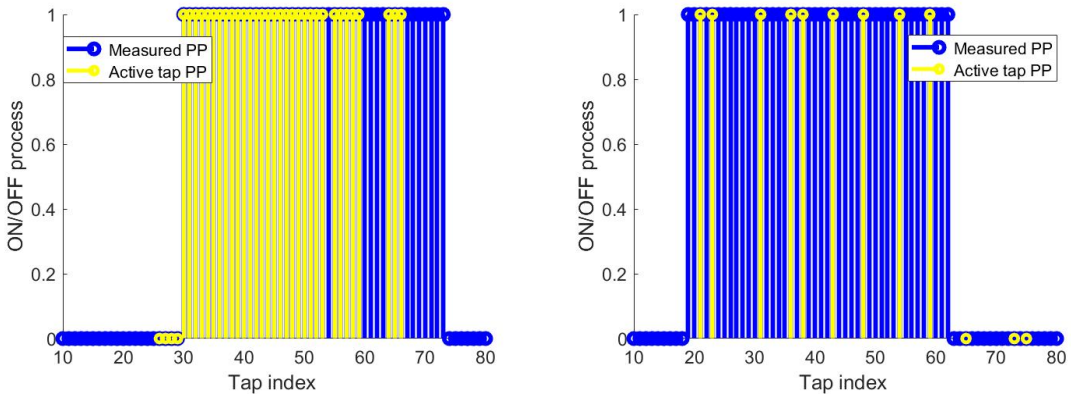

(a) (b)

Fig. 4.13 PP under NLOS2 condition for one of those snapshots that the CDF-DS probabilities higher than 0.9 (track number 24 → 25), (a) $M1$, (b) $M2$

As mentioned previously, measurement tracks are merged into different data sets depending on the scenario. As a consequence, we have three data sets, which are LOS (1896 snapshots), NLOS1 (2714 snapshots) and NLOS2 (46402 snapshots). Both algorithms are applied, and the number of active taps for both models is compared in Table 4.3, and the CDFs of RMS-DS are illustrated in Fig. 4.14. Moreover, a comparison of CDF-RMSDS statistics between $M1$ and $M2$ with respect to the measured data is provided in Table 4.4. As a result, $M2$ works better than $M1$ in retaining the RMS-DS. In brief, the advantages of the new approach ($M2$) are reducing the number of required taps while retaining the RMS-DS performance and the active taps are more spread over the cumulative energy; thus, low energy taps with large delay are selected as they are necessary to regenerate the RMS-DS. As a result, this method illustrates a better representation of the measured CIR. Therefore, all results pertain to the new approach $M2$ for the following chapters. However, after merging the data in the line of sight (LOS) scenario, we have only one active tap, which cannot regenerate RMS-DS. This will be illustrated in detail in the next subsection.

TABLE 4.3
Tap number comparison in $M1$ and $M2$ after merging the data

Scenario	LOS	NLOS1	NLOS2
Active taps in $M1$	12	17	33
Active taps in $M2$	1	4	6

TABLE 4.4
Difference of the mean RMS-DS [μsec] between the measured data and active taps after merging the data

Scenario	$M1$	$M2$
NLOS1	0.05	0.02
NLOS2	0.13	0.03

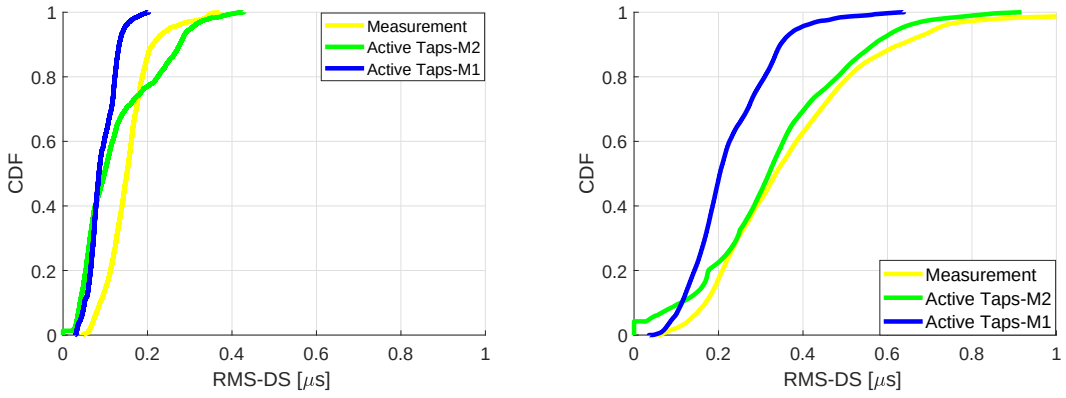

Fig. 4.14 CDF Comparison of the RMS-DS between the measurement data and the active taps only after merging the data (a) NLOS1 (b) NLOS2

4.2.3.1 Under LOS Condition

In the proposed approach ($M2$), the number of active taps depends on the number of peaks of the cumulative energy. After merging the data under LOS conditions, we only have one active tap. As explained previously, the aim of this approach is to regenerate the RMS-DS, which is close to the measurement data. Using only one tap cannot provide such a result, as shown in Fig. 4.15. As a consequence, we need to extend this approach.

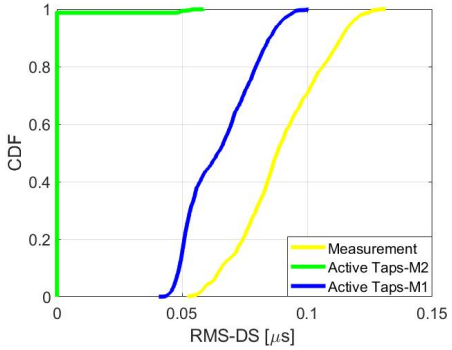

Fig. 4.15 CDF comparison of the RMS-DS between the measurement data and the active taps in LOS scenario

Here, the tap number is calculated based on the maximum RMS-DS (4.16) [129].

$$P = \lceil max(\sigma_\tau)/(1/B) \rceil + 1\,, \tag{4.16}$$

where σ_τ is the delay spread and B is the bandwidth. Based on (4.16), we need to select four taps, one of them is selected based on the peak, and the other three are based on a steady-state probability of being ON (SS_1), in other words, those taps have been selected as active taps, which are ON taps for a long period of time, and they are beyond the first peak tap. This extension is indicated in red color in the block diagram in Fig. 4.16. As a result, for this model, we have four taps; one of them is the peak tap, which is based on $M2$, and the other three are the stationary taps in terms of considering where is the highest value of SS_1.

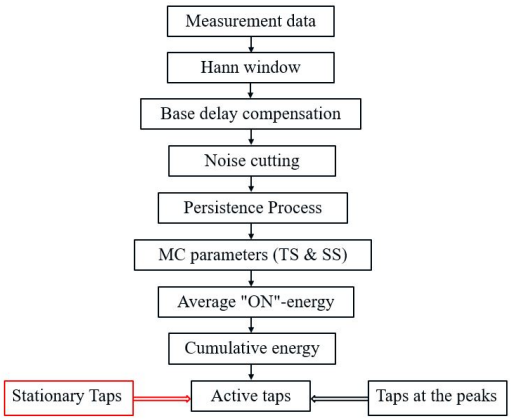

Fig. 4.16 Flow diagram of TDL model parameters extraction under LOS condition

cumulative distribution function (CDF) of the RMS-DS is compared ($M1$, $M2$ with measurement data) and plotted in Fig. 4.17. $M2$ could generate better results in some areas (especially at the 0.5 value of the CDF). The difference of the mean RMS-DS between measured data and active taps is less than $\frac{1}{B}$ (it is 0.026 µs), while reducing the number of taps by more than 60%. We declare if the error is in the range of $\frac{1}{B}$, this will be equal to zero error because we sub-select taps out of many and our system does not have higher resolution; thus, it always introduces these kinds of errors.

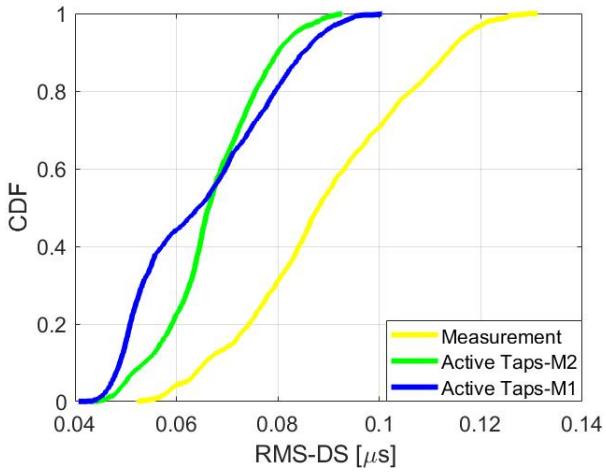

Fig. 4.17 CDF comparison of the RMS-DS between the measurement data and the active taps after extension under LOS condition

4.3 Doppler Shift of the Active Taps

The time selectivity of wireless channels is described by the Doppler shift. This is due to relative motion between the Tx and Rx. Consider an example where the Rx is moving towards the Tx; in a very short period, the Doppler frequency changes from a positive value to a negative value [167]. The aim of this section is to characterize the Doppler frequency for each tap. The COST-207 model has defined four types of Doppler spectra conditioned to taps associated with time delays [35, 48].

- Rice spectrum used for the first tap under LOS condition

- Classic spectrum (bathtub-shaped Jakes Doppler spectrum) has been used for a tap, whose delay is not greater than 0.5 µs
- Gaussian spectrum-1 associated with tap-delays in the range between 0.5 µs and 0.002 ms
- Gaussian spectrum-2 associated with delays in excess of 0.002 ms

The Doppler feature of the first tap can be specified as $-f_{\mathrm{Dmax}}$, and the rest can be described as a random variable that follows a uniform distribution, which is $f_v \sim U[-f_{\mathrm{Dmax}}, f_{\mathrm{Dmax}}]$ as proposed in [167]. In this investigation, the same approach is considered as in [63, 167]. The maximal Doppler frequency is computed (4.17)

$$f_D = \frac{v f_c}{c} \cos\theta = \frac{v}{\lambda} \cos\theta = f_{\mathrm{Dmax}} \cos\theta \,, \tag{4.17}$$

where f_{Dmax} is the maximum Doppler shift, f_c is a carrier frequency, c is the speed of light, v is the speed of Rx, and θ is the angle of Tx with respect to the Rx. Depending on the Rx is moving away or toward the Tx, the Doppler shift can be $+/-$. The result of the maximum Doppler shift is given in Table 4.5. The Doppler feature of the taps can be described as a random variable that follows a uniform distribution, $f_v \sim U[-f_{\mathrm{Dmax}}, f_{\mathrm{Dmax}}]$.

TABLE 4.5
Maximum Doppler shift in different scenario (after merging data)

Scenario	$v_{max}\,\mathrm{m\,s^{-1}}$	f_{Dmax} (Hz)
LOS	2.27	20
NLOS1	2.36	20
NLOS2	2.52	22

4.4 Amplitude Fading of the Active Taps

Fading is a signal deterioration by multiple propagation paths. As explained in Chapter 2, a radio signal propagates according to three mechanisms, which are reflection, diffraction, and scattering. These mechanisms give rise to two nearly independent phenomena, which are slow fading/large-scale fading caused by shadowing and path loss and fast fading/small-scale fading caused by multipath superposition. The received signal may be broken down into these two components, which are slow- and fast-fading, and we will study them individually and separately in Chapter 6. Nevertheless, in this section, the amplitude distribution of p^{th} tap is calculated from the superposition of delayed waves in the p^{th} delay bin. The large-scale fading will affect all taps the same over the large-scale fading duration. Typically, this duration is much longer than the coherence time of small-scale fading (which is why it is called large-scale fading or slow fading). Depending on vehicular velocities and how long a set of data samples is used to estimate small-scale effects, neglecting the large-scale variation may be fine. Consequently, large-scale fading and small-scale fading are not separated in this section. The aim of this assumption is to recreate CIRs that look similar to the measured data, and we would like to consider power fluctuations due to non-stationarity and regenerating the RMS-DS comparable with the measured one (a generator will be devised to produce the CIR based on the derived model parameters in Chapter 4). Fig. 4.18 summarizes the steps of discussed assumption.

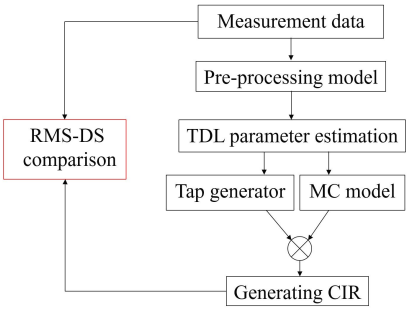

Fig. 4.18 Summary flow diagram of processing steps

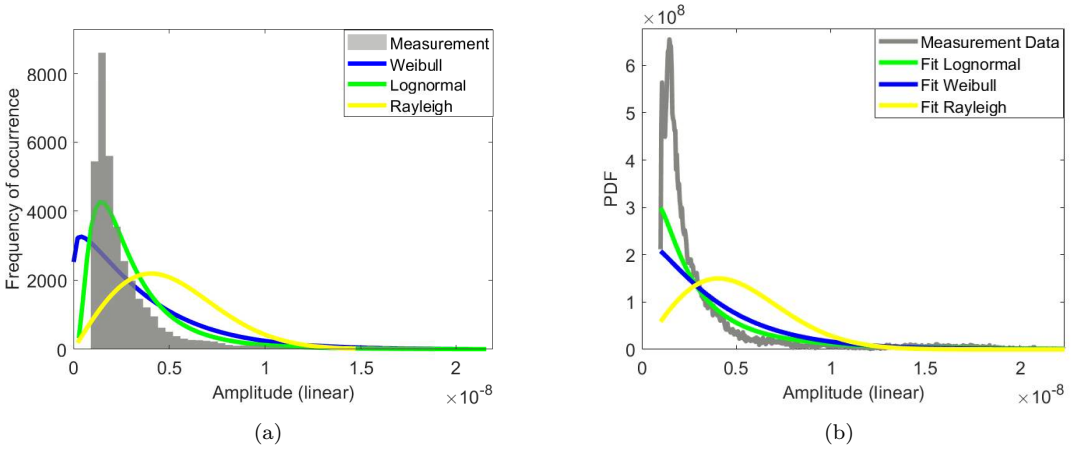

Fig. 4.19 Histograms and pdf fits for the third tap under NLOS2 condition; the log-normal distribution shows a better match between the probability density function (PDF) and the empirical histogram, (a) Histogram for the third tap under NLOS2 condition, (b) PDF Illustration for the third tap

The fading amplitude statistics of the p^{th} tap are computed from the square root of the power in the p^{th} delay bin. To address amplitude fading, we determine parameters for different distribution functions that fit best to the observed data meaning the histogram of the data, which is plotted in Fig. 4.19(a). In other words, the parameters of some known distributions are determined that fit best to the observed tap amplitudes. The log-normal distribution shows a better match between the PDF and the empirical histogram [9]. Additionally, a histogram intersection (HI) is computed between the empirical histogram of measurement data and the PDFs. In general, the HI calculates the intersected area between two histograms at the exact bin locations to measure the similarity between them; an example is illustrated in Fig. 4.20. HI = 1 when both histograms are identical. However, since we calculate the HI between the empirical histogram and the PDF, we need a different approach. This is specified in these steps:

1. Compute the empirical histogram for each tap amplitudes and then obtain the values of the histogram and the locations of the bins.

2. Derive the parameters of specified distribution from tap amplitudes, such as a scale parameter σ_R of Rayleigh distribution, a shape factor β and scale parameter a of Weibull and σ with μ of Log-normal distribution.

[9]The empirical histogram with the PDF curves for first and second taps amplitude under three different scenarios are illustrated in Fig. B.2 and B.3.

3. Compute the PDFs at locations of the center of the bins.

4. The HI is calculated (4.18) [88,120] after normalizing the empirical histogram and the PDF. This is illustrated in Fig. 4.19(b).

$$HI = \sum_{i}^{I} \min(M_i, F_i)\,, \tag{4.18}$$

where i is the number of bins in the PDF range. The sets of probability density values for both are indicated by M_i and F_i, in our case, M is the normalized empirical histogram, and F is the PDF.

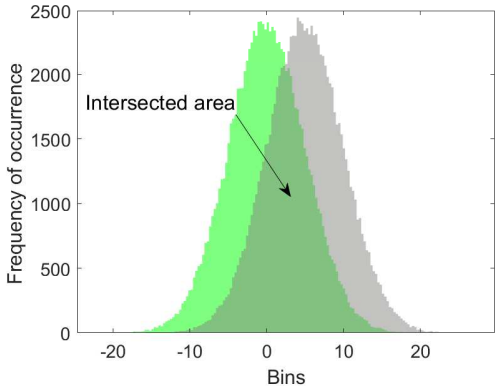

Fig. 4.20 Illustration of metric "Histogram Intersection," which calculates the intersected area between two histograms at the same bin locations to measure the similarity between them

A resemblance between the empirical histogram of tap amplitudes and the PDFs is computed using HI. The outcome is given in Table 4.6 and the log-normal distribution illustrates good agreement for a large number of taps in terms of considering where the highest value of HI is. 'It is likely that a large number of effects contribute to the attenuation of the signal, including diffraction, reflection, energy absorption, antenna losses, etc. Most of these effects are multiplicative or equivalently additive in the log domain. By the central limit theorem, a large number of random multiplicative effects will converge to a normal distribution in the log domain' [49]. In addition to that, in [127] the authors states in an urban environment, the randomness in building heights causes log-normality. The Weibull model has two parameters, which are a shape factor and scale parameter; thus, it offers substantial flexibility and provides a good fit to any data set that have been considered, but as stated in [129] it is based not on an underlying propagation theory. The Rayleigh approximation becomes poorer because not only the large-scale fading has not been removed, but also the range of delay resolution of our measurement system is narrow (50 ns) so that there are not many multipath components (MPCs) to justify the Rayleigh distribution. In [53], the authors also substantiate similar declarations.

4.5 Pairwise Tap Correlation Coefficient

The classical TDL model assumes uncorrelated scattering (US), whereas, in V2V/V2I scenarios, the taps are correlated because there might be a given scatterer that contributes to several multipaths associated with different delay bins; therefore, a collection of taps follow similar trend over time. A consequence

TABLE 4.6
OUTCOME OF HI BETWEEN MEASURED DATA AND FITTING CURVE; THE LOG-NORMAL DISTRIBUTION ILLUSTRATES GOOD AGREEMENT FOR A LARGE NUMBER OF TAPS IN TERM OF CONSIDERING WHERE IS THE HIGHEST VALUE OF HI

LOS			
Taps	Lognormal	Weibull	Rayleigh
1	0.7369	0.7131	0.6155
2	0.7098	0.6709	0.6665
3	0.6569	0.5996	0.6034
4	0.7207	0.6657	0.5976
NLOS1			
Taps	Lognormal	Weibull	Rayleigh
1	0.6768	0.7387	0.5424
2	0.7616	0.7308	0.6945
3	0.4643	0.4310	0.4050
4	0.3478	0.3079	0.3153
NLOS2			
Taps	Lognormal	Weibull	Rayleigh
1	0.7672	0.7168	0.2678
2	0.8125	0.7179	0.4224
3	0.7899	0.6864	0.4623
4	0.7422	0.6521	0.5053
5	0.7195	0.6394	0.4680
6	0.6985	0.6161	0.5186

of this is to study the correlation between them because in developed channel models, it is essential to account for this correlation during designing and evaluating advanced signal processing algorithms at the Rx. In general, the amount of correlation coefficient between the taps depends on the delay resolution, the capability of the sounder, the richness of the scattering environment, etc [64, 155]. Nevertheless, the PP associated with each tap; thus, the correlation coefficient between each pair of taps is estimated from the channel only when both taps are valid ON taps, in other words, both of them must exist for the same snapshot. This phenomenon is happening due to the PP; therefore, different number of snapshots are used [63, 64]. This is demonstrated in Fig. 4.21.

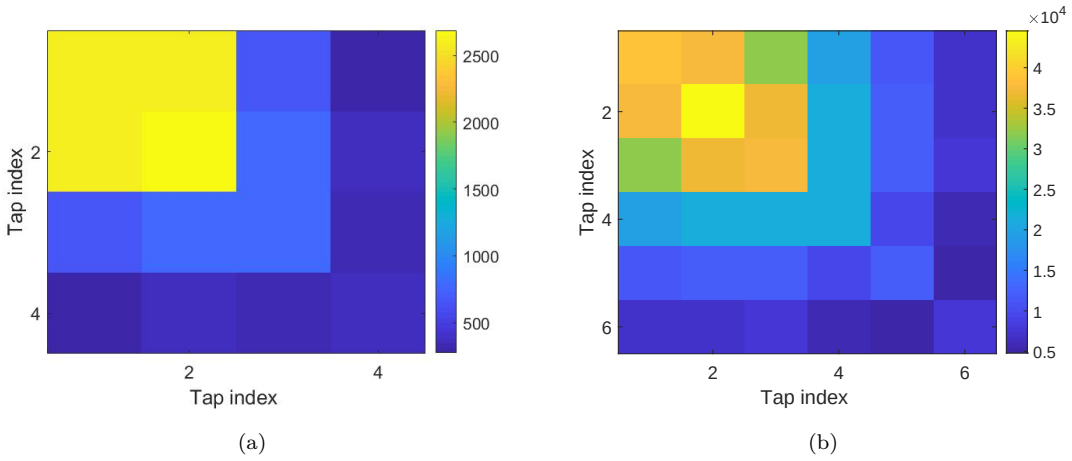

Fig. 4.21 Number of snapshots used to compute correlation matrix; the PP associated with each tap; therefore, the correlation coefficient between each pair of taps is estimated from the channel only when both taps are valid ON taps; thus, different number of snapshots are used, (a) NLOS1, (b) NLOS2

The correlation coefficient between two taps is estimated from the channel using(4.19) [61, 63, 64, 122,

129, 155].

$$\rho_{i,j} = \frac{cov(\gamma_i'\gamma_j')}{\sqrt{var(\gamma_i')var(\gamma_j')}}, \tag{4.19}$$

where γ_i' and γ_j' are magnitudes of tap i and j. cov and var denote the covariance and variance functions, which are derived in the following expressions

$$\begin{aligned} cov(\gamma_i'\gamma_j') =& E(\gamma_i'\gamma_j') - E(\gamma_i')E(\gamma_j') \\ =& \frac{\sum_1^M \gamma_i'\gamma_j'}{M} - \bar{\gamma_i'}\bar{\gamma_j'}, \end{aligned} \tag{4.20}$$

$$\begin{aligned} var(\gamma_i') &= \frac{\sum_{i=1}^M \gamma'^2_i}{M} - \bar{\gamma'}^2_i \\ var(\gamma_j') &= \frac{\sum_{j=1}^M \gamma'^2_j}{M} - \bar{\gamma'}^2_j, \end{aligned} \tag{4.21}$$

where

$$\bar{\gamma_i'} = E(\gamma_i') = \frac{\sum_{i=1}^M \gamma_i'}{M}, \bar{\gamma_j'} = E(\gamma_j') = \frac{\sum_{j=1}^M \gamma_j'}{M}, \tag{4.22}$$

where M is the total number of snapshots that tap i and j are valid ON taps. The pairwise tap correlation coefficient matrix is defined as 4.23.

$$C_\gamma = \begin{bmatrix} c_{11} & c_{12} & \cdots & c_{1P} \\ \vdots & \vdots & \ddots & \vdots \\ c_{P1} & c_{P2} & \cdots & c_{PP} \end{bmatrix}, \tag{4.23}$$

where P is the selected active taps. The correlation coefficient matrix is computed, and the result is given below ($C_{\gamma-\mathrm{LOS}}$ and $C_{\gamma-\mathrm{NLOS}}$), which will be entries of the generator in Chapter 5. The correlation coefficient matrices are symmetric; therefore, the upper and lower triangular parts are used for different consequences in $C_{\gamma-\mathrm{NLOS}}$. The lower triangular indicates the NLOS2 scenario, and the upper part depicts under NLOS1 condition. There is a strong correlation among the active taps, whereas the correlation coefficient decreases as the tap index increases.

$$C_{\gamma-\mathrm{NLOS}} = \begin{bmatrix} 1 & 0.8415 & 0.9196 & 0.315 & – & – \\ 0.7683 & 1 & 0.7996 & 0.5813 & – & – \\ 0.7273 & 0.7715 & 1 & 0.3475 & – & – \\ 0.6017 & 0.616 & 0.649 & 1 & – & – \\ 0.6682 & 0.715 & 0.633 & 0.560 & 1 & – \\ 0.5934 & 0.627 & 0.549 & 0.451 & 0.295 & 1 \end{bmatrix}$$

$$C_{\gamma-\mathrm{LOS}} = \begin{bmatrix} 1 & 0.5216 & 0.2016 & 0.2845 \\ 0.5216 & 1 & 0.0184 & 0.5147 \\ 0.2016 & 0.0184 & 1 & 0.3213 \\ 0.2845 & 0.5147 & 0.3213 & 1 \end{bmatrix}$$

4.6 Correlation between Taps Persistence Processes

The author in [155] has observed the correlated PP. Consider an example when a large truck causes multiple adjacent paths to be present or absent at the same time; thus, a collection of taps PP might

be highly correlated [155]. The correlation coefficient among taps persistence can be obtained using (4.24) [67, 155].

$$c_{i,j} = \frac{cov(z_i z_j)}{\sqrt{var(z_i)var(z_j)}}, \tag{4.24}$$

where $c_{i,j}$ is the correlation coefficient between persistence processes among tap i and j. cov and var denote the covariance and variance functions, which have been derived in Section 4.5. z_j and z_i are the PP of tap j and tap i, respectively. In brief, it is the same as the pairwise tap correlation coefficient, but instead of using γ', the entries are the finite "lifetime " of the γ', which is a binary vector and estimated from measured data. The correlation coefficient matrix between taps persistence processes is given below ($C_{z-\mathrm{NLOS}}$), and the upper triangular part depicts under NLOS1 condition, and the lower triangular indicates the NLOS2 scenario. The average correlation of PP between taps is around 0.0841 and 0.0825 under NLOS1 and NLOS2 conditions, respectively. As a consequence, the PP between different tap indices is uncorrelated.

$$C_{z-\mathrm{NLOS}} = \begin{bmatrix} 1 & 0.0197 & 0.2772 & 0.4507 & - & - \\ 0.1567 & 1 & 0.0617 & 0.039 & - & - \\ 0.1027 & 0.1382 & 1 & 0.4972 & - & - \\ 0.1591 & 0.1747 & 0.3981 & 1 & - & - \\ 0.1753 & 0.0293 & 0.2403 & 0.4027 & 1 & - \\ 0.1272 & 0.0144 & 0.1901 & 0.2865 & 0.3729 & 1 \end{bmatrix}$$

4.7 Parameter Extraction

In Section 4.2.1 and 4.2.2, two algorithms have been clarified to derive the TDL model parameters from the measured data. Fig. 4.22 summarizes all the steps to select active taps for both models. Depending on the model ($M1/M2$) scheme, the delay of active taps are derived from the cumulative energy of the CIR. For example, Fig. 4.10 shows cumulative energy versus tap index; thus, we know the location of the taps in the CIR; therefore, all essential parameters can be estimated. To compromise between number of pages and precision (due to a large number of measurement tracks), the TDL tables parameters are only given for the NLOS1 scenario (track number 24 → 25). It is given in Table 4.7 to compare both models' outcomes.

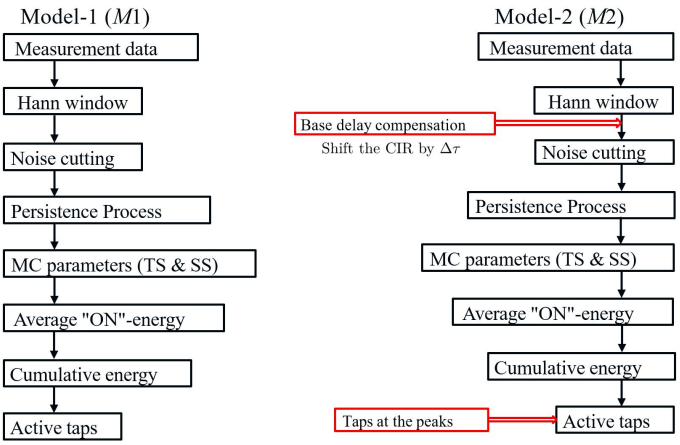

Fig. 4.22 Tap selection block diagram in $M1$ and $M2$

TABLE 4.7
TDL TABLE PARAMETERS FOR NLOS1 SCENARIO FOR TRACK NUMBER (24 → 25)

			$M1$				
Taps	Delay (μ sec)	Energy(lin)	SS_1	SS_0	P_{11}	P_{00}	f_D
1	1.25	0.381	0.9903	0.0097	0.9951	0.5	f_v
2	1.3	0.2076	0.9903	0.0097	0.9951	0.5	f_v
3	1.2	0.1489	0.8743	0.1257	0.9938	0.9565	f_v
4	1.35	0.1174	0.9903	0.0097	0.9951	0.5	f_v
5	1.4	0.0377	0.9903	0.0097	0.9951	0.5	f_v
6	1.5	0.0293	0.9903	0.0097	0.9951	0.5	f_v
7	1.45	0.0253	0.9903	0.0097	0.9951	0.5	f_v
8	1.55	0.014	0.9903	0.0097	0.9951	0.5	f_v
9	1.6	0.0099	0.9854	0.0146	0.9901	0.3333	f_v
10	1.85	0.0082	0.8807	0.1193	0.9786	0.8421	f_v
11	1.8	0.007	0.9082	0.0918	0.9845	0.8462	f_v
12	1.65	0.0059	0.8559	0.1441	0.9895	0.9375	f_v
13	1.9	0.0043	0.7532	0.2468	0.9887	0.9655	f_v
14	1.7	0.0037	0.8545	0.1455	0.9838	0.9048	f_v
			$M2$				
Taps	Delay (μ sec)	Energy(lin)	SS_1	SS_0	P_{11}	P_{00}	f_D
1	0.9	0.8962	0.9903	0.0097	0.9951	0.5	f_v
2	1.15	0.0753	0.9903	0.0097	0.9951	0.5	f_v
3	1.5	0.0204	0.8899	0.1101	0.9897	0.9167	f_v
4	1.7	0.0034	0.8148	0.1852	0.9773	0.9	f_v
5	1.8	0.0037	0.7907	0.2093	0.9706	0.8889	f_v
6	2.75	0.0009	0.3447	0.6553	0.9155	0.9556	f_v

In Section 4.2.3, an approach has been proposed to verify the correctness of the active taps. The overall statistic of the outcome from $M1$, the delay spread is under-estimated because it neglects the low power taps with large delays. The outcome from $M2$ shows improvement of the delay spread while reducing the number of taps significantly[10], and it is closer to the measurement data; thus, we assume $M2$ works better (comparison is provided in Table 4.4). As explained in Section 3.2, measurement tracks are merged into different data sets (depending on the scenario) and then the TDL tables parameters are derived and given in Table 4.8. From Table 4.8, the energy of the taps is the average "ON" energy. SS_0 and SS_1 are steady-state probability of the tap being OFF and ON, P_{00}/P_{11} is the probability of going from state OFF to OFF or ON to ON. $\sigma_{Lognormal}$ and $\mu_{Lognormal}$ are the standard deviation and mean of the log-normal distribution. $\beta_{Weibull}$ and $a_{Weibull}$ are shape and scale factors of Weibull distribution, and $\sigma_{Rayleigh}$ is a scale parameter of Rayleigh distribution. It is important to note that the delay of the first tap is not equal to 0 s because the CIR is shifted in accordance with the distance change between the Rx and Tx instead of shifting the first tap to the beginning of the CIR.

4.8 Concluding Remarks

One of the limitations of channel emulators is limited emulating the number of propagation paths simultaneously; thus, it is essential to find a proper approach to reduce the number of taps. This chapter introduced an algorithm for selecting taps of a tapped delay line (TDL) model from measurement data. The new approach is a modification of an existing method and improves the model ($M2$) with respect

[10]One of the limitation of channel emulators is limited emulating the number of propagation paths simultaneously. For instance, the channel emulator described by authors in [12, 56] allow for a maximum number of ten- and twelve-delay tap, respectively. Therefore, it is important to find a proper approach to reduce the number of taps.

TABLE 4.8
TDL TABLE PARAMETERS FOR $M2$ AFTER MERGING THE DATA

LOS						
Taps	Delay (μ sec)	Energy(lin)	SS_1	SS_0	P_{11}	P_{00}
1	0.95	0.79	0.999	0.001	0.99	0.5
2	1.05	0.13	0.999	0.001	0.99	0.5
3	1.15	0.04	0.999	0.001	0.99	0.5
4	1.25	0.017	0.999	0.001	0.99	0.5
Taps	$\sigma_{\text{Lognormal}}$	$\mu_{\text{Lognormal}}$	a_{Weibull}	β_{Weibull}	σ_{Rayleigh}	f_D
1	0.23	-13.38	$1.7 * 10^{-6}$	4.38	$1.15 * 10^{-6}$	f_v
2	0.52	-14.48	$6.6 * 10^{-7}$	1.9	$4.7 * 10^{-7}$	f_v
3	0.4	-14.89	$4.16 * 10^{-7}$	2.39	$2.8 * 10^{-7}$	f_v
4	0.24	-15.29	$2.58 * 10^{-7}$	3.79	$1.7 * 10^{-7}$	f_v
NLOS1						
Taps	Delay (μ sec)	Energy(lin)	SS_1	SS_0	P_{11}	P_{00}
1	0.95	0.9818	0.9670	0.033	0.9981	0.9439
2	1.35	0.0175	0.9897	0.0103	0.9974	0.75
3	2.1	0.0005	0.277	0.723	0.9558	0.9831
4	2.35	0.0001	0.133	0.867	0.9	0.9847
Taps	$\sigma_{\text{Lognormal}}$	$\mu_{\text{Lognormal}}$	a_{Weibull}	β_{Weibull}	σ_{Rayleigh}	f_D
1	0.9344	-15.7	$1.99 * 10^{-7}$	0.86	$2.3 * 10^{-7}$	f_v
2	0.697	-17.4	$3.9 * 10^{-8}$	1.46	$3.15 * 10^{-8}$	f_v
3	0.6744	-19.1216	$7.02 * 10^{-9}$	1.533	$5.5 * 10^{-9}$	f_v
4	0.4619	-19.61	$3.8 * 10^{-9}$	2.22	$2.6 * 10^{-9}$	f_v
NLOS2						
Taps	Delay (μ sec)	Energy(lin)	SS_1	SS_0	P_{11}	P_{00}
1	1	0.8864	0.8346	0.1654	0.9919	0.9591
2	1.5	0.0671	0.9596	0.0404	0.9965	0.9168
3	1.85	0.0197	0.8089	0.1911	0.9802	0.9161
4	2.35	0.0093	0.4635	0.5365	0.9643	0.9692
5	2.65	0.0109	0.2615	0.7385	0.9444	0.9803
6	2.95	0.0066	0.1642	0.8358	0.9438	0.989
Taps	$\sigma_{\text{Lognormal}}$	$\mu_{\text{Lognormal}}$	a_{Weibull}	β_{Weibull}	σ_{Rayleigh}	f_D
1	1.3016	-18.7	$1.16 * 10^{-8}$	0.6866	$1.7 * 10^{-8}$	f_v
2	1.0681	-19.505	$5.8 * 10^{-9}$	0.9684	$7.4 * 10^{-9}$	f_v
3	0.9874	-19.9532	$3.6 * 10^{-9}$	1.0892	$4 * 10^{-9}$	f_v
4	0.903	-20.167	$2.8 * 10^{-9}$	1.2304	$2.7 * 10^{-9}$	f_v
5	1.0255	-20.3244	$2.7 * 10^{-9}$	1.179	$3.01 * 10^{-9}$	f_v
6	0.7604	-20.1	$2.7 * 10^{-9}$	1.3674	$2.3 * 10^{-9}$	f_v

to the delay spread and the number of taps. Model $M2$ in all scenarios uses a smaller number of taps while retaining the delay spread performance. The taps are spread more widely over the cumulative energy; thus, low energy and large delay taps are selected, which are relevant to regenerating the delay spread. Furthermore, an approach was discussed to evaluate the model outcome. The feasibility was investigated using channel-sounding measurement data. From the results, it was additionally observed that more accurately shifting the channel impulse response (CIR) is necessary to reduce the number of required taps.

Due to different communication environments, it is important to assess the amplitude fading by using statistical measures. It has been illustrated that the amplitude fading of a large number of taps follows the Log-normal distribution. Statistical measures were considered to address the fading amplitudes per tap in contrast to the typical tap model that assumes independent Rayleigh fading. It was additionally observed that there are strong correlations among taps amplitudes, but the persistence process (PP) between different tap indices are uncorrelated; thus, the correlated Markov model is not necessary. Detection results in different regions from the raytracer, and statistical measures that we applied show a good match.

As mentioned previously, an essential tool in the performance analysis of communication systems is an accurate propagation channel model. The aim of the next chapter is to discuss the implementation of TDL channel model for vehicle to infrastructure (V2I) channels and devise a generator to produce a CIR based on already derived model parameters from measurement data (Table 4.8). The root mean square delay spread (RMS-DS) will be used for a model validation between simulated and collected data based on how well they agree.

A part of the research contributions covered in this chapter is published in [61, 64, 66]

Chapter 5

SISO-TDL Channel Modeling and Simulation

5.1 Motivation and Related Work

As explained in previous chapters, many researchers have described the dispersive channel model in the form of tapped delay line (TDL) structure due to its simplicity, low complexity, and straightforward implementation in channel emulators [7, 61, 129]. In [11, 12], the authors have considered TDL models for vehicle to vehicle (V2V) channels for six scenarios (for certain RF channel emulators e.g., SPIRENT 5500 [1]), but they assumed that the different taps are uncorrelated and independent of each other, so those models are based on wide sense stationary uncorrelated scattering (WSSUS). However, as mentioned before, the propagation characteristics of V2V/vehicle to infrastructure (V2I) channels are different from those of traditional cellular channels [61,64,85,129,155], and for an accurate description of V2V/V2I radio communication channel, the WSSUS assumption is not valid. In [129], the non-WSS property of channel is described by modeling multipath persistence via Markov chains, and the authors have observed often correlated scattering among neighboring taps; thus, they have developed a generator to produce correlated Weibull random variables [1]. The correlated Nakagami fading model was devised by [166]. In [155], the authors have investigated the correlation between taps persistence and modeled through correlated first-order two-state Markov model. In [85], the authors have developed a generator by considering not only the amplitude correlation but also the phase correlation between different taps. Then, the switching function with the first-order two-state Markov chains is used to represent the non-WSS properties. The phase of active taps is often modeled as uniformly distributed over the interval $U \sim [-\pi\ \pi]$ [40, 68, 155], but in [85] the Laplace distribution is used to describe the angle distribution of the active taps.

This chapter continues of Chapter 4, where a new approach was proposed for selecting taps and estimating their parameters from measured data. In this chapter, the implementation of TDL channel model will be examined, and generators will be developed based on already derived model parameters (Table 4.8). Log-normal, Weibull, and Rayleigh generators are devised, and uncorrelated persistence process (PP) via the first-order two-state Markov model is modeled in those generators. Then, the first-order two-state Markov model will be extended to the higher orders Markov model to better capture the non-stationary behavior. To devise such generators, three components are essential to be addressed for

[1] It has been found that the Weibull distribution is a better fit over all measured data that have been considered [129]

each tap. The first one is the amplitude fading and then generating correlated random variables with a certain distribution, and the last one is modeling a PP for each tap.

A part of the research contributions covered in this chapter is published in [67].

5.2 Modeling the Active Tap Amplitude

As noted before, γ_p in (2.31) is the complex active tap amplitudes. The sum of relevant scattered components of the received signals can be modeled by addressing the magnitude fading of the active taps, and their phase can be assumed uniformly distributed. As illustrated in Section 4.4, the (histogram intersection (HI)) is applied to assess the amplitude fading of the active taps. Tap amplitudes are generated using multivariate Log-normal, Weibull, and Rayleigh random variables with defined average fading amplitudes, fading parameters, and correlation coefficients. In this section, two methods are addressed to generate correlated random variables.

5.2.1 Correlated Multi-variate Log-normal Random Variable

As stated previously, the best fit for a large number of active taps is the Log-normal distribution; thus, to compromise between the number of pages and precision, only the Log-normal generator is illustrated. The following algorithm is used to obtain correlated multi-variate Log-normal random variables [20].

1. **Correlated normal random variable:** Generate random samples that follow standard Normal distribution. The correlation matrix is considered as a covariance matrix since variance is one.

2. **Mean and standard deviation:** Compute the mean (m) and standard deviation (s) for active taps only for those snapshots that are valid ON taps due to the PP.

3. σ **and** μ**:** Find Log-normal parameters using (5.1) and (5.2) [60].

$$\sigma = \sqrt{\log\left(\frac{s^2}{m^2} + 1\right)}, \tag{5.1}$$

$$\mu = \log\left(\frac{m}{e^{\frac{\sigma^2}{2}}}\right), \tag{5.2}$$

   where m and s are computed from step 2.

4. **Computation of the parameters** Use (5.3) to generate multivariate Log-normal random variables with a specified correlation matrix [20].

$$X = e^{\mu + \sigma Z}, \tag{5.3}$$

   where Z is the result from step 1, σ and μ are results from step 3. Fig. 5.1 summarizes discussed steps.

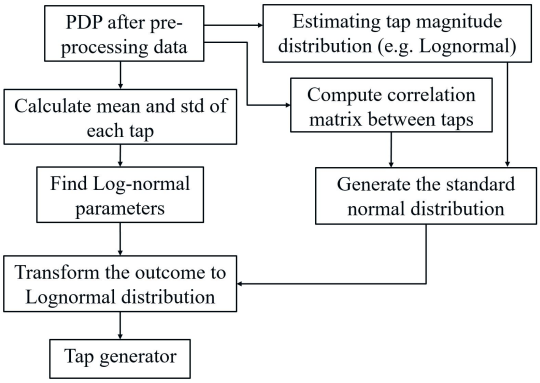

Fig. 5.1 Tap generator block diagram to generate correlated multi-variate Log-normal random variable

5.2.2 Inverse Transform Sampling

In a data science concept, a certain distribution can be taken (e.g., uniform distribution) and transformed to turn it into a different distribution. This method is called inverse sampling transform [48]. It can be used to generate correlated random variables following a specific distribution by using its inverse cumulative distribution. Fig. 5.2 illustrates the inverse cumulative distribution function (CDF) method to generate random samples following the wanted distribution. Uniform random samples on the probability axis (ordinates) are drawn and then we were able to generate a Lognormal-distributed series by reading the corresponding abscissa [58].

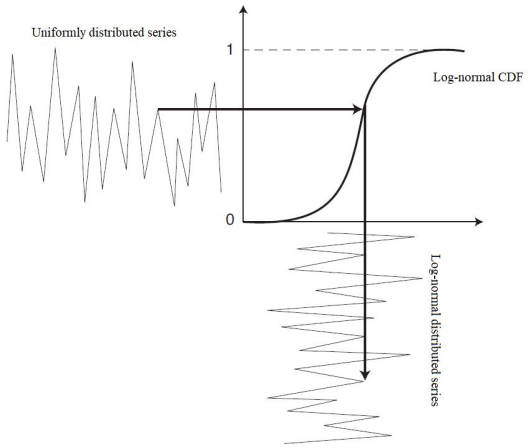

Fig. 5.2 Inverse CDF method to generate random samples following the wanted distribution, note adapted from [48]

In order to illustrate the discussed method, uniform distribution is transformed to generate an exponential distribution [2] [42, 45]. The transformation operation of the uniform distribution is represented in (5.4).

$$T(U) = X\,, \tag{5.4}$$

where T is a transformation function. U is a random variable uniformly distributed over an interval $\sim U[0,1]$. X is an exponential random variable. Using the definition of CDF, which is given in (5.5) and substituting (5.4) into (5.5), equation (5.6) will be achieved.

[2]The exponential distribution is selected due to simplicity

$$F_X(x) = Pr(X \leq x)\,, \tag{5.5}$$

$$F_X(x) = Pr\left(T(U) \leq x\right)\,, \tag{5.6}$$

then take the inverse transformation function (T^{-1}) in (5.6)

$$\begin{aligned} F_X(x) &= Pr(T^{-1}T(U) \leq T^{-1}(x)) \\ &= Pr(U \leq T^{-1}(x)) \\ &= T^{-1}(x)\,, \end{aligned} \tag{5.7}$$

then take inverse of both sides

$$F_X^{-1}(x) = T(x)\,, \tag{5.8}$$

From (5.8), we observe that if we are able to calculate the inverse cumulative distribution of any certain distribution, then we are able to generate the specified distribution. To illustrate this, the exponential distribution is generated in the following steps

1. Generates uniformly distributed random variables $\sim U[0,1]$.

2. The exponential distribution has the following probability density function (PDF) (5.9), and the corresponding CDF is given by (5.10)

$$f(x) = \begin{cases} e^{-\lambda x} & , x \geq 0 \\ 0 & , x < 0 \end{cases} \tag{5.9}$$

$$F_X(x) = \begin{cases} 1 - e^{-\lambda x} & , x \geq 0 \\ 0 & , x < 0\,, \end{cases} \tag{5.10}$$

   where λ is the exponential parameter (often called the rate parameter).

3. Here, compute the transformation function of the exponential distribution. Assume y is equal to exponential CDF.

$$y = 1 - e^{-\lambda x}\,, \tag{5.11}$$

   then take the natural log of both sides as in (5.12) and then divide both sides by λ

$$\begin{aligned} 1 - y &= e^{-\lambda x} \\ \ln(1-y) &= -\lambda x \\ x &= \frac{-\ln(1-y)}{\lambda}\,, \end{aligned} \tag{5.12}$$

   from (5.12), we can observe that we are able to generate the exponential distribution by entering a uniform distribution, meaning instead of y, our input is U, as shown in (5.13).

$$\begin{aligned} x &= \frac{-\ln(1-y)}{\lambda} \\ x &= \frac{-\ln(1-U)}{\lambda} \\ x &= \frac{-\ln(U)}{\lambda}\,. \end{aligned} \tag{5.13}$$

5.2.3 Tap Phase

The uniform distribution is used to represent the angle distribution of the active taps as considered in [40, 68, 155]. It is uniformly distributed over the interval $U \sim [-\pi\ \pi]$. From the polar coordinates (γ', θ), where γ' is generated random samples following the wanted distribution. Then convert polar coordinates to Cartesian coordinates (x, y) as follow

$$\begin{aligned} x =& \gamma' cos(\theta) \\ y =& \gamma' sin(\theta)\,, \end{aligned} \tag{5.14}$$

Therefore, the complex amplitude of the active taps is

$$\gamma = x + iy\,. \tag{5.15}$$

5.3 Modeling Persistence Processes

As previously indicated, the non-WSS property of channel is described by modeling multipath persistence via Markov chains as considered in [67, 85, 129, 155]. In order to account for the dynamic nature of the non-stationary vehicle to X (V2X) environment, a binary vector (PP) is added to the conventional representation of channel impulse response (CIR) in (2.32). In this section, the first-order two-state Markov chains are used to model the persistence of each active tap. From Table 4.8, the probabilities of going from state ON to ON and OFF to OFF are given; therefore, P_{01} and P_{10} can be calculated by $P_{01} = 1 - P_{00}$ and $P_{10} = 1 - P_{11}$ [3]. The algorithm to generate PP is illustrated as a block diagram in Fig. 5.3, where r is uniformly distributed pseudo-random numbers [118]. The algorithm can be interpreted as follows: assume that the current state is 1 ("ON"-state) and the value of r is less than or equal to P_{10}; thus, the next state will be 0 ("OFF"-state); therefore, this process produce binary sequences of 0's and 1's for each tap [4].

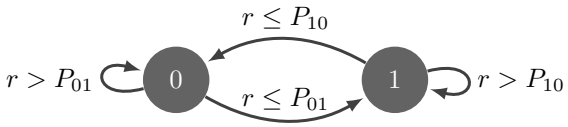

Fig. 5.3 The block diagram to generate the PP using first-order two-state Markov chain, where r is uniformly distributed pseudo random numbers

The non-stationary CIR is obtained by multiplying the outcome from Section 5.2 (γ) by 5.3 (PP). It has been shown in Fig. 4.18.

[3] P_{00} and P_{11} are computed from predetermined ON/OFF sequence of each tap and here we use them to model PP

[4] The Markov chains parameters are obtained from the generated binary sequences and then they are compared with those from the measured data and the results show good agreement.

5.4 Performance Evaluation of the Simulated Channel Model

In the literature, the accuracy of the model with respect to collected data is compared based on how well they agree in terms of the root mean square delay spread (RMS-DS) [55, 129]. The RMS-DS ($\sigma_{\tau k}$) is computed using (3.3). In addition to that, the TDL model parameters are obtained from the simulated channel models and then they are compared with those for the measured data. The results show good agreement.

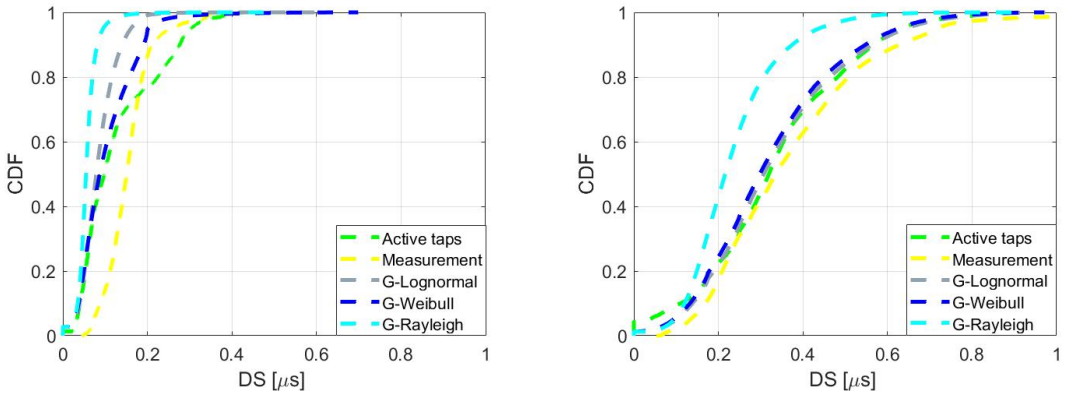

Fig. 5.4 CDF comparison of the RMS-DS, the Log-normal and Weibull distribution are a better fit over all collected data in contrast to the Rayleigh distribution, which underestimates the RMS-DS, (a) NLOS1, (b) NLOS2

Fig. 5.4 [5] compares CDF of the RMS-DS for the measured data with simulated channel models [6] [7] [8]. For each simulated model, 100000 PDPs are generated using the proposed algorithm. The outcome of the histogram intersection criterion (given in Table 4.6) indicates a good agreement between the measured data and Log-normal fits. However, we generate not only correlated multivariate Log-normal random variables but also correlated multivariate Weibull and Rayleigh random variables in order to examine their effects in terms of RMS-DS. From Fig. 5.4, we observe that the Log-normal and Weibull distribution are a better fit overall collected data in contrast to the Rayleigh distribution, which underestimates the RMS-DS [9]. Therefore, the amplitude distribution of taps has an impact on regenerating the RMS-DS; thus, it is important to use statistical measures to assess the fading amplitudes per tap.

It is important to note that, so far, our PP model is assumed to be uncorrelated Markov random process, whereas the PP from measured data is different from the generated one. This is illustrated in Fig. 5.5, where the ON- and OFF-state are indicated using yellow and blue colors, respectively. As it has been observed that there are no correlations among taps persistence (in Section 4.6); hence, they are uncorrelated, but as can be noticed in Fig. 5.5, the change between states is less frequent in the "Measured PP" than "Generated PP". This might indicate that we need to extend first-order two-state Markov chains to higher orders Markov model, which considers previous states to generate the current

[5] Underlying different scenarios have been defined in Section 3.2
[6] Using the term "Active taps" in the figure, we mean the RMS-DS is computed only for active tap indices from measured data as explained in Section 4.2.3
[7] Using the term "G-x" in Fig. 5.4 means that we calculate RMS-DS for the tap amplitudes generated from x-generator.
[8] NLOS1 and NLOS2 scenarios have been defined in Section 3.2
[9] It is a sort of important to study different types of distribution and its effect on generators and investigate the reasoning for that, but it is not a part of this thesis.

state; thus, it is more difficult to change the state. Higher orders Markov model will be developed in Section 5.5.

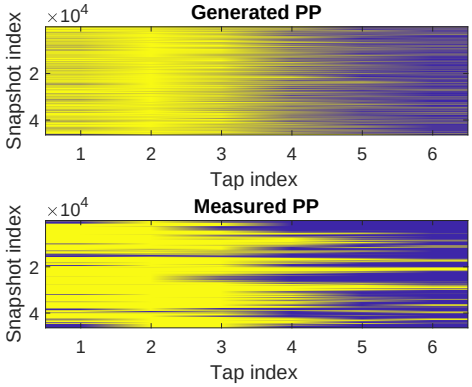

Fig. 5.5 PP comparison under NLOS2 condition, the OFF-state is indicated using blue color, and the ON-state is indicated using yellow color; the change between states is less frequent in the "Measured PP" than "Generated PP", this might indicate that we need to extend first-order two-state Markov chains to higher orders Markov model

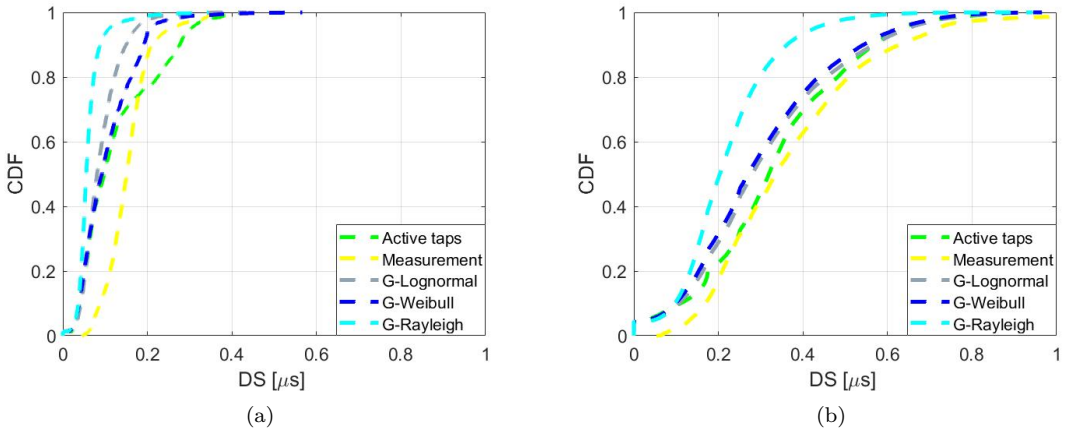

Fig. 5.6 CDF comparison of the RMS-DS (using estimated PP from measured data), (a) In NLOS1 scenario, there is no difference in the results (compare Fig. 5.4(a) with Fig. 5.6(a)), (b) In NLOS2 scenario, the measured PP is underestimating the RMS-DS

Furthermore, in order to investigate the influence of measured PP, the "ON" /"OFF"-state of each tap from measured data is used in our simulated channel models (46402 and 2714 PDPs are generated; hence, the measurement contains 46402 and 2714 snapshots under NLOS2 and NLOS1 conditions, respectively). Here, we assume modeling higher order Markov chains is considered, despite the fact it is only the "ON"/"OFF" sequence of each tap that has been predetermined from our collected data. Fig. 5.6 illustrates the CDF of RMS-DS. Our results show that under the NLOS1 scenario, there is no difference in the results (compare Fig. 5.4(a) with Fig. 5.6(a)). The difference of the mean RMS-DS is 0.002, 0.005, and 0.0007 for G-Lognormal, G-Weibull, and G-Rayleigh, respectively. This has happened because the steady-state probability associated with the "ON"-state (SS_1 from Table 4.8) of some of the taps are very high, and the rest is very low. Nevertheless, in the NLOS2 scenario, the measured PP is underestimating the RMS-DS. In order to investigate this, we examine the influence of generated PP on our collected data and then the influence of measured PP on our simulated data (the results pertain to the Log-normal

generator). The CDF of RMS-DS for the NLOS2 region is shown in Fig. 5.7. It is important to note that from Fig. 5.7, "Active Taps + PP Generator" means that we calculate RMS-DS for the tap indices from measured data while our simulated PP is used to turn ON or OFF each tap [10] [11] [12]. By comparing the statistics between green, blue and cyan curves, on the other hand, we know the measured PP is accurate. As a consequence, we need to extend our PP model to the higher orders Markov model, which will be studied in Section 5.5. It is obvious that the generator is artificially increasing the RMS-DS, although the PP is not "accurate" (compare the gray curve in Fig. 5.4 with Fig. 5.7 under NLOS2 condition); this is caused by the stochastic nature of the generator. To sum up, our simulated PP between different tap indices is uncorrelated and independent. From the results, it is observed that the correlated Markov model is not necessary, but the taps persistence Markov model needs to be extended to higher orders Markov model.

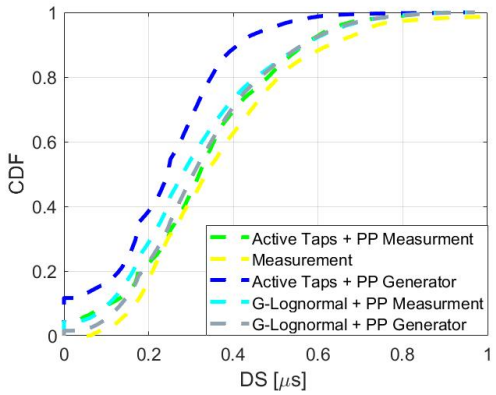

Fig. 5.7 The influence of PP under NLOS2 condition

5.5 Higher Orders Markov Modeling Of Persistence Process

This section is a continuity of our previous section, and the higher order Markov chain models are anticipated to describe the non-WSS properties more accurately. In Section 5.3, a first-order two-state Markov Chain process is used to model PP, as considered in [67,85,96,129], but it has been observed that our first-order two-state Markov model needs to be extended to higher orders Markov model. In [86,155], the authors have considered higher-order Markov Chains to model PP, and in [93], the author has stated that the order of the Markov Chain does not need to be larger than the second order. Higher-order Markov model considers previous states to generate the current state; hence, it is expected to show more accurate results at the expense of increased complexity. Here, we first extend our first-order two-state Markov model to the second-order two-state Markov model and then to the third-order two-state Markov model, which yields greater implementation complexity and required memory space such as they imply exponentially increasing size of the state space. For example, third-order Markov chains require 8 states space ($2^3 = 8$). The algorithms of second-order and third-order two-state Markov chains are illustrated

[10] "Active Taps + PP Measurement" means that we calculate RMS-DS for the tap indices from measured data with the estimated PP from measured data.
[11] "G-Lognormal + PP Measurement" means that we calculate RMS-DS for the tap amplitudes generated from Log-normal generator with the estimated PP from measured data.
[12] "G-Lognormal + PP Generator" means that we calculate RMS-DS for the tap amplitudes generated from Log-normal generator with PP from the generator.

in Fig. 5.8 and 5.9, where r is uniformly distributed pseudo-random numbers [118] and state sequence are interpreted in the following example.

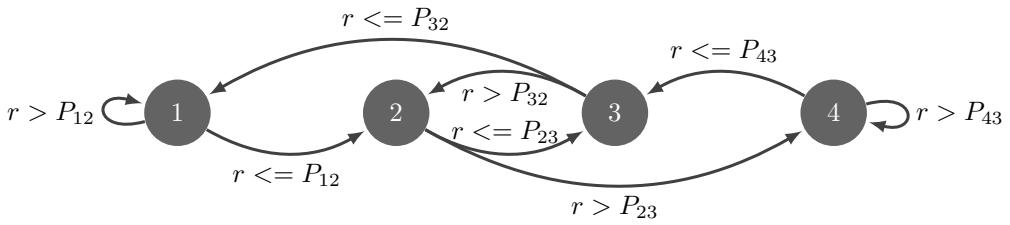

Fig. 5.8 The block diagram to model the PP using second-order two-state Markov chain

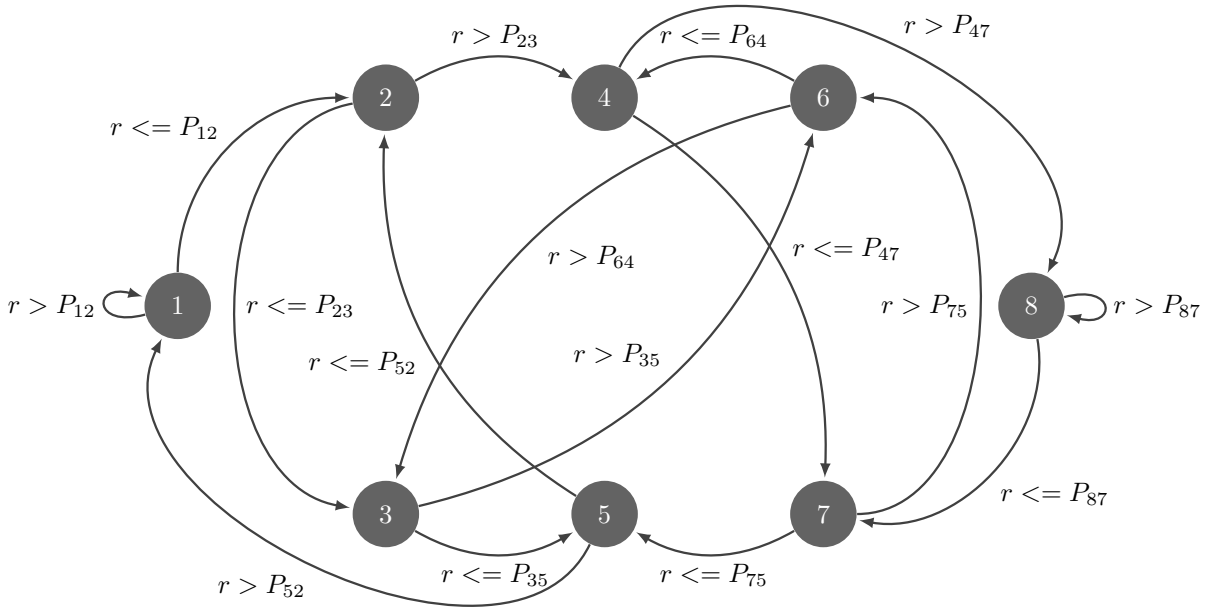

Fig. 5.9 The block diagram to model the PP using third-order two-state Markov chain

Example :
Obtain state sequence of this following PP, $z_p(t) = 1001101011$

- **First-order two-state Markov model:** Two states ($2^1 = 2$ states). state sequence → 1,0,0,1,1,0,1,0,1,1
- **Second-order two-state Markov model:** Four states ($2^2 = 4$ states).

$$\left.\begin{array}{l} 10 \rightarrow state\ 3 \\ 00 \rightarrow state\ 1 \\ 01 \rightarrow state\ 2 \\ 11 \rightarrow state\ 4 \\ 10 \rightarrow state\ 3 \\ 01 \rightarrow state\ 2 \\ 10 \rightarrow state\ 3 \\ 01 \rightarrow state\ 2 \\ 11 \rightarrow state\ 4 \end{array}\right\} \text{state sequence} \rightarrow 3,1,2,4,3,2,3,2,4$$

- **Third-order two-state Markov model:** Eight states ($2^3 = 8$ states).

$$\left.\begin{array}{l} 100 \rightarrow state\ 5 \\ 001 \rightarrow state\ 2 \\ 011 \rightarrow state\ 4 \\ 110 \rightarrow state\ 7 \\ 101 \rightarrow state\ 6 \\ 010 \rightarrow state\ 3 \\ 101 \rightarrow state\ 6 \\ 011 \rightarrow state\ 4 \end{array}\right\} \text{state sequence} \rightarrow 5,2,4,7,6,3,6,4$$

Fig. 5.10 compares generated PP from higher-order Markov chain with pre-estimated PP from measurement. The PP of third-order Markov chains tends to show that the change between states is less frequent compared to the other models due to considering two previous states to generate the current state. Therefore, it is more difficult to change the ON-/OFF-state; hence, it increases complexity and memory space.

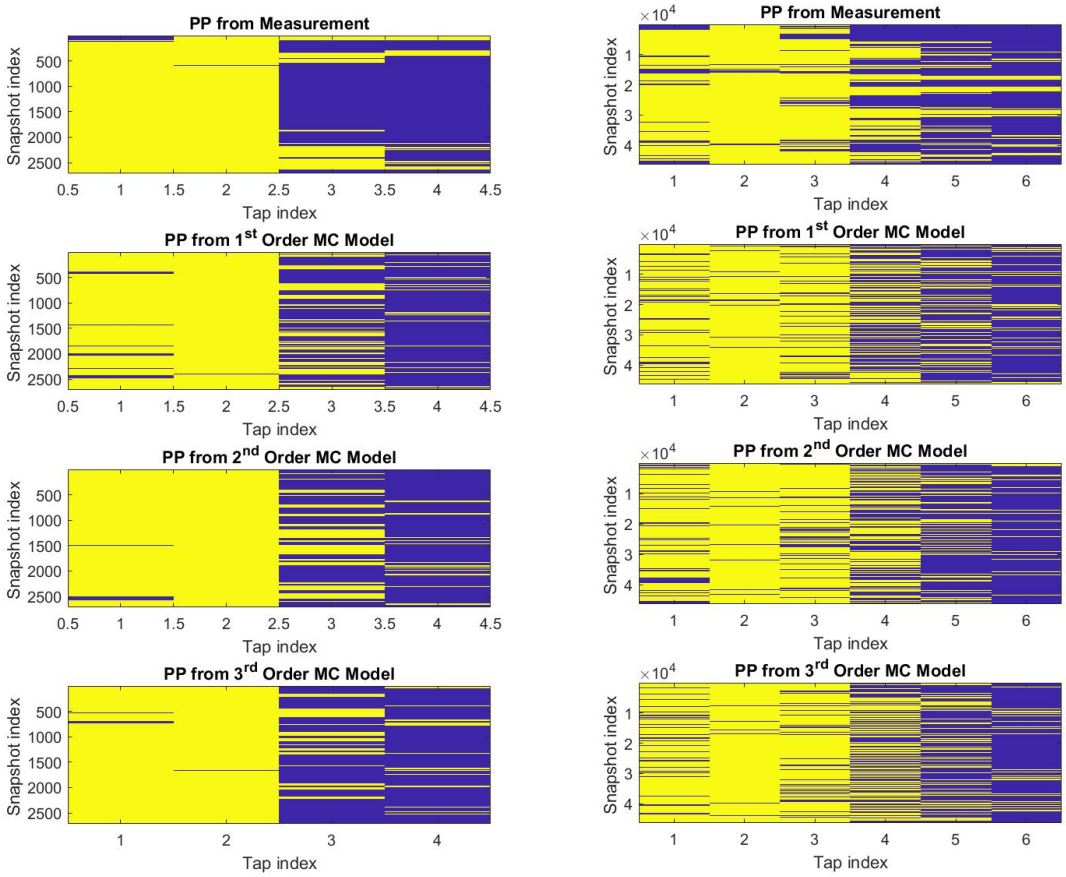

(a) (b)

Fig. 5.10 PP comparison, the "OFF"-state is indicated using blue color, and "ON"-state is indicated using yellow color; the PP of third-order Markov chain tends to show the change between states is less frequent compared to the other models, (a) NLOS1, (b) NLOS2

5.6 Comparing Models to Measured Data

Different order Markov chains models are evaluated by comparing statistics of the simulated sequences with the data sequences. Fig. 5.11 and 5.12 depict RMS-DS comparison with respect to high order Markov model under NLOS1 and NLOS2 scenarios, respectively. Our goal here is to develop a higher-order Markov model with the aim of better capturing the non-stationary behavior. It is observed that different order does not make an enormous affect, as shown in Fig. 5.11 and 5.12 because there might be very high-order Markov chains needed (such as 100^{th}-order or more) to generate PP closer to estimated PP. In order to show this, three different order Markov models for Log-normal generator is depicted in Fig 5.13, the RMS-DS of third order Markov model, which is denoted by a gray curve, is closer to the RMS-DS of estimated PP, which is depicted by a green/yellow curve, but it does not make an enormous

effect [13] [14]. Therefore, to compromise between fidelity and complexity, the first-order two-state Markov model will be used to describe the non-stationary processes of the channel.

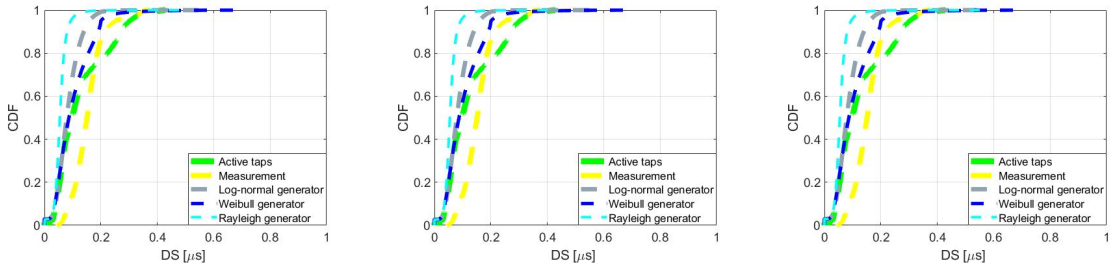

(a) (b) (c)

Fig. 5.11 RMS-DS comparison with respect to high order Markov model under NLOS1 scenario, different order does not make an enormous affect, (a) first order, (b) second order, (c) third order

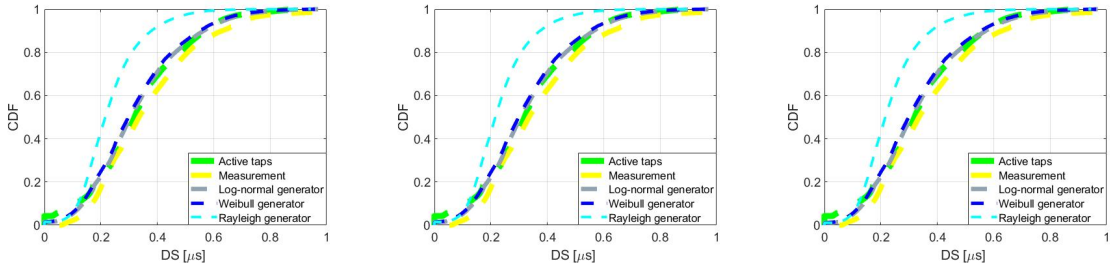

(a) (b) (c)

Fig. 5.12 RMS-DS comparison with respect to high order Markov model under NLOS2 scenario, different order does not make an enormous affect, (a) first order, (b) second order, (c) third order

[13] The results of the Weibull-, Rayleigh-generator are illustrated in Fig C.1.

[14] Different order Markov chains models can also be evaluated using other methods such as calculating variance and compared to the measured one, but this is not a part of this thesis.

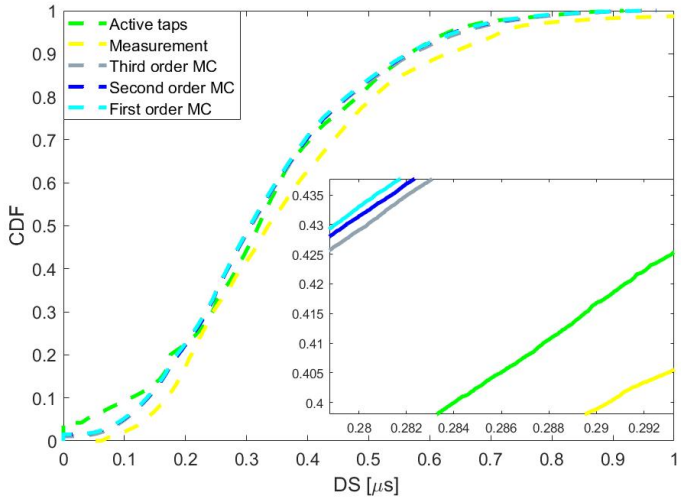

Fig. 5.13 RMS-DS comparison with respect to high order Markov model under NLOS2 scenario for Log-normal generator, the RMS-DS of third order Markov model, who is denoted by a gray curve is closer to the RMS-DS of estimated PP, which is depicted by a green/yellow curve

5.7 Concluding Remarks

In this chapter, the implementation of channel impulse response (CIR)s generators (under non-WSSUS) have been studied. The Log-normal, Weibull, and Rayleigh generators have been devised. The simulated CIRs were compared to the collected data in terms of the root mean square delay spread (RMS-DS) statistics. We observe that both models (Log-normal and Weibull) tend to retain the delay spread performance, but the Rayleigh generator underestimates the delay spread in all scenarios. Therefore, the amplitude distribution of taps has a high impact on recreating the delay spread; thus, it is important to use statistical measures to assess the fading amplitudes. The analysis investigated the correlation coefficient among taps, and there are strong correlations among taps amplitudes. However, the persistence process between different tap indices is uncorrelated; thus, a correlated Markov model is not necessary. From the results, it was additionally observed that the first-order two-state Markov model needs to be extended to higher orders Markov model, which has been modeled with the aim of better capturing the non-stationary behavior. Different order Markov chains were studied and evaluated by comparing statistical measures of the simulated sequences to the data sequences. However, it has been observed that different order does not have an enormous effect; thus, to compromise between fidelity and complexity in the following sections, the first-order two-state Markov model will be used to describe the non-stationary processes.

Some of the findings in this chapter are published in [67].

Chapter 6

Characterization of Slow- and Fast-Fading of the Active Taps

6.1 Motivation and Related Work

In this chapter, the variation in received signal due to the large- and small-scale fading will be characterized in the vehicle to infrastructure (V2I) channels. Nine various setups are investigated, such as quasi-omnidirectional antenna (by this, we mean that a power delay profile (PDP) for a single snapshot is obtained by averaging over the channels of the transmitter (Tx) and receiver (Rx) antenna array; therefore, we assumed it is quasi-omnidirectional PDP), two antennas faced directly to each other, and two antennas faced away from each other. In each scenario, LOS and two different NLOS categories are studied.

The usual starting point for developing basic performance results in the analysis of communication systems is the additive white Gaussian noise (AWGN) channel. Thermal noise is generated in the Rx, and it is the primary source of performance degradation. Practical systems are bandlimited, and defining bandlimited filters is essential in modeling practical systems. Equalization techniques and special signal design may be required to mitigate the inter symbol interference (ISI) because of the band-limiting and phase-distortion properties of filters [131]. One infers that the signal attenuation versus distance behaves as propagation takes place over ideal free space if a radio channel's propagating characteristics are not specified. This means the region between the Tx and Rx is treated as being free of all objects that might absorb or reflect the transmitted wave. This is called the free space model, which expresses the attenuation of transmit signal as a function of distance as expressed below [96, 131]

$$P_{\mathrm{L}}(d) = \left(\frac{4\pi d}{\lambda}\right)^2, \tag{6.1}$$

where λ is the wavelength of the propagating signal and d is the distance between the Tx and Rx. From 6.1, the received signal power can be predicted easily, but it is inadequate to describe the channel behavior and predict system performance because in practical channels, signal propagation takes place near the ground and in the atmosphere. A signal travels from a Tx to Rx over multiple reflective paths, as presented Fig. 6.1(a), in other words, the received signal is the combination of many replicas of the transmitted signal that can constructively or destructively interfere with each other; this refers as multipath propagation. This phenomenon can cause fluctuations in the received signal, giving rise

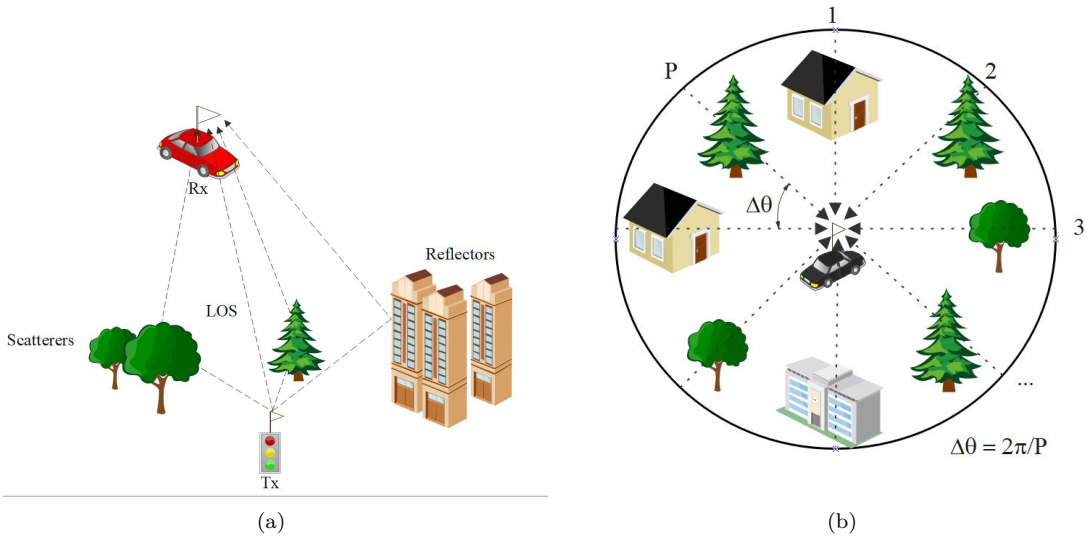

Fig. 6.1 (a) The wireless propagation environment, (b) Dense scattering environment

to the terminology multipath fading [1] [83, 119, 126, 131, 150]. The knowledge of underlying multipath fading and modeling the terminology multipath fading are an essential part of the propagation channel model. In the system design and end-to-end modeling, techniques are incorporated in order to mitigate the effects of fading [131]. Fading depends on various factors such as the channel between Tx and Rx (can be fixed or time-varying channel), position of the Tx and Rx, atmospheric conditions e.g., rainfall, etc. Fading can be grouped into two types, which are slow-fading (or large-scale fading) occurs due to path loss and shadowing effects, and fast-fading (or small-scale fading) occurs mainly due to multipath superposition. Path loss is the dissipation of the transmitted power as it propagates, and when obstacles between the Tx and Rx absorb power cause deviation of the received power from the average value; this is called shadowing [130, 131]. Since these variations occur over large distances (path loss and shadowing occur over 100-1000 m and 10-100 m, respectively) such that they are referred to large-scale fading effects. On the other hand, small-scale fading occurs over very short distances on the order of half-wavelength [58, 71]. Fast fading is more relevant to the design of reliable and efficient communication systems, such as designing Rx, coding, and bit error rate (BER), on the other hand, slow fading is more relevant to coverage issues such as cell-site planning[2]. The aim of this chapter is to describe the fundamental fading manifestations and types of degradation and, in so doing, to characterize the fading amplitude for each active tap.

As expressed in Chapter 2, a path is composed of a number of sub-paths, which are not observable. Each path has its characteristics, which are created by the characteristics of these sub-paths [34]. In narrowband systems, the Rx cannot resolve different paths e.g., early FM radios (25-30 kHz); therefore, in such a system, all multipath are indistinguishable and may interfere constructively or destructively at the Rx and are seen as a single composite signal [121]. This means that due to the bandwidth limitations, it is assumed that all paths arrive at the same time [34]. By assuming a rich scattering environment, as presented in Fig. 6.1(b), an amplitude of a signal varies according to the Rayleigh distribution by the central limit theorem [74, 121]. Therefore, in traditional wireless channel models, Rayleigh fading is used

[1] Fading is the deviation of the signal attenuation (the gradual loss in intensity) [83]
[2] Coverage is the largest distance between the Tx and Rx at which communication can reliably take place (with a limit on the transmit power) [149].

as a statistical model to illustrate the effect of multipath propagation. In cellular channels, narrowband fading statistics are commonly described to be Rice (for line of sight (LOS) scenario) and Rayleigh (for non line of sight (NLOS) scenario) [105]. However, the authors in [141] have shown Rayleigh conditions hold in many cases, but not always. It was found that a good agreement between the measured data and Nakagami with Rice distributions for the narrowband small-scale fading statistics in [100]. Nonetheless, the vehicle to X (V2X) channel corresponds to a wideband channel because it exchanges mass data at a short moment and demands on the communication link ranging from low latency and ultra-reliable. The effect of wideband on the Rx is that the Rx able to resolve multipath. Each is made up of many distinct sub-path, which are received from a variety of directions. Thus, each multipath has unique characteristics by employing averaging over sub-path tends to be received in the range of $\frac{1}{B}$ (B is the bandwidth). The statistical characteristics of fading change as the number of resolvable paths increases [34]. In [31], the authors argue that large- and small-scale fading cannot easily be distinguished, and they suggest to fit the Nakagami distribution for the compound fading statistics same as what we have considered in Section 4.4. In the wideband system, the Rayleigh approximation becomes poorer because the range of delay resolution of the Rx is narrow (because the bandwidth is wide) such that there are not many multipath components to justify the Rayleigh distribution [50].

Some of the materials in this chapter are published in [62].

6.2 Frequency Selective Fading

Analytically, we might be able to count the number of fades across the bandwidth. Consider an example of two-path model, as shown in Fig. 6.2. They have different path lengths, d_1, and d_2, but let us assume they have equal power. A phase of each path is measured at the Rx using (6.2) and (6.3) [34]. The phase difference between them is $\Delta\phi = \phi_2 - \phi_1$. The interaction of constructive (i.e. $\Delta\phi = 0$) and destructive (i.e. $\Delta\phi = \pi$) produces frequency selective fading, as presented in Fig. 6.3 [3]. The idea of how fading might arise in practice is illustrated in Fig. 6.4. A Tx and Rx are surrounded by objects, and the transmitted wave may interact with the objects, which reflect and scatter the transmitted signal; therefore, the transmitted wave arrives at the Rx via different routes. The received signal is the combination of many replicas of the transmitted signal that can constructively or destructively interfere with each other depending on the relative phase shift, as shown in Fig. 6.3. The phase difference between signals plays a key role, and it depends on the frequency of transmission, speed of motion, and relative path lengths. It can be associated with the phase relationship as in (6.4).

$$\phi_1 = \frac{2\pi d_1}{\lambda}\,, \tag{6.2}$$

$$\phi_2 = \frac{2\pi d_2}{\lambda}\,, \tag{6.3}$$

$$\Delta\phi \;= \phi_2 - \phi_1 = \;\frac{2\pi\,(d_2 - d_1)}{\lambda}\;=\;\pi(2n-1)\,, \tag{6.4}$$

where n is an integer number. When phase differences are odd multiples of π, the frequency selective fades are occurred [34]. Analytically, the number of fades across the bandwidth (e.g., $f_2 - f_1 = \Delta f$) might be counted ambiguity as follows

[3]When the phases between two paths nearly align, the signals are adding constructively and vice versa.

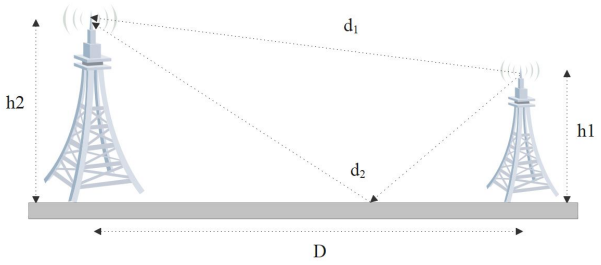

Fig. 6.2 The two path channel model

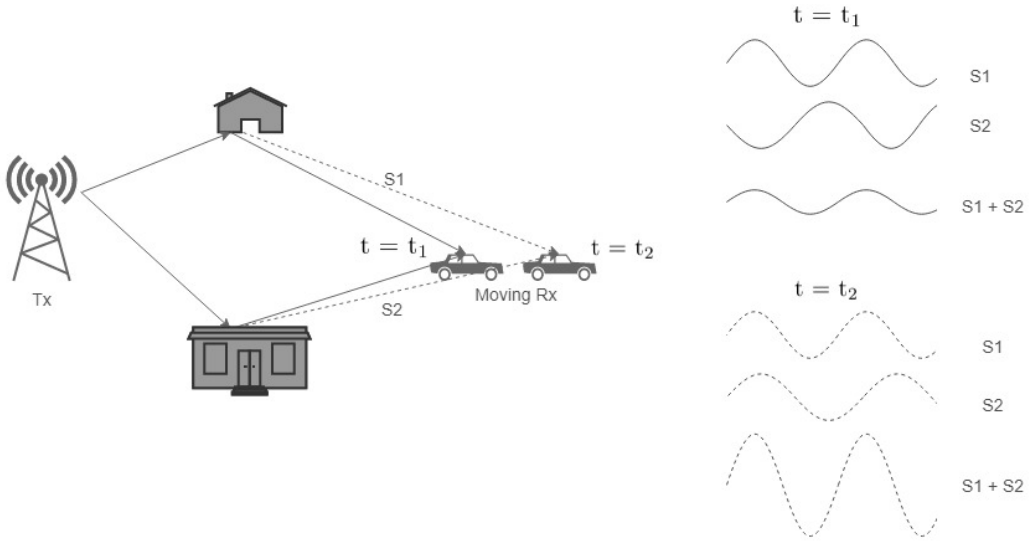

Fig. 6.3 Representation of constructive and destructive interference between two signals

$$\lambda = \frac{2(d_2 - d_1)}{2n-1} = \frac{2\Delta d}{2n-1} \longrightarrow f = \frac{(2n-1)c}{2\Delta d}, \tag{6.5}$$

$$f_1 = \frac{(2n_1 - 1)c}{2\Delta d}, \tag{6.6}$$

$$f_2 = \frac{(2n_2 - 1)c}{2\Delta d}, \tag{6.7}$$

from (6.7), assume $n_2 = n_1 + m$, where m is the number of fades across the band, and it is an integer number. Hence, we can derive the following formula to predict the number of fades across the bandwidth.

$$\Delta f = f_2 - f_1 = \frac{c\,(2n_1 + 2m - 1 - 2n_1 + 1)}{2\Delta d} = \frac{c\,m}{\Delta d} \longrightarrow m = \frac{\Delta f \Delta d}{c}. \tag{6.8}$$

For example, if $\Delta d = 60$ m and $\Delta f = 20$ MHz, the number of fades across the band is 4. In brief, the signals are added constructively when the phases between two paths nearly align, but when the two paths are out of phase; thus, they are canceling each other.

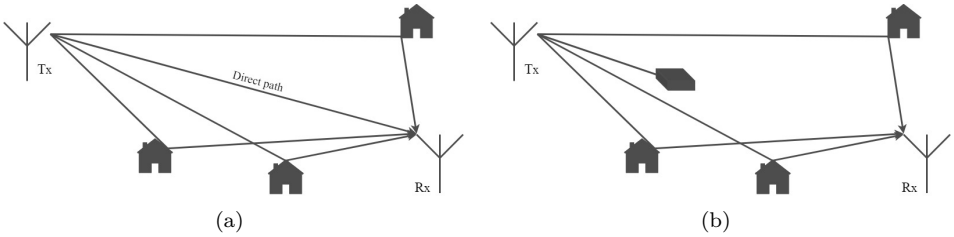

Fig. 6.4 Multipath propagation, (a) LOS scenario, (b) NLOS scenario

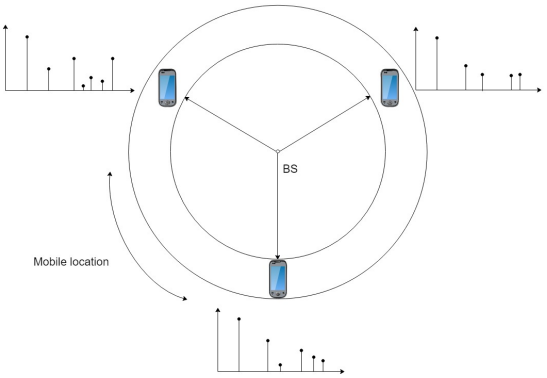

Fig. 6.5 Variation of path profiles encountered at a fixed range from a base station, note adapted from [126]

6.3 The Fading Amplitude Analysis and Processing of the Measurement Data

In general, a radio signal propagates according to three basic mechanisms, which are reflection, diffraction and scattering.

- Reflection occurs when a transmitted wave impinges on an object, which has a smooth surface with dimensions that are very large when compared to a wavelength.
- Diffraction occurs when the propagation path between the Tx and Rx is obstructed by an object with large dimensions compared to the transmitted signal wavelength, causing secondary waves to propagate behind the obstructing body.
- Scattering occurs when a transmitted wave impinges on an object, either a surface whose dimensions are on the order of wavelength or less or any large rough surface, causing the transmitted signal to be reflected in all directions or spread out (scattered). Street lights, signs, and foliage are typical objects that cause scattering [4].

These mechanisms give rise to two nearly independent phenomena, which are slaw- and fast-fading. Fig. 6.5 illustrates the impact of the slow fading on an object, which is moving around a base station (BS) at a constant range, some paths will be less obstructed and have increased signal strength, whereas others will suffer increased loss [119, 126]. The aim of this section is to model the slow and fast fading for each relevant multipath, which we called the active tap, and it is a continuity of our preliminary Section 4. In

[4]Keeping this in mind, any obstruction in the propagation path that causes a signal to be reflected or scattered can be named a scatterer.

general, the received signal is composed of slow- and fast-fading. It is feasible to study them individually and separately. Presuming, $r_t(t)$ is the received field strength in the time domain. $r_t(t)$ may be broken down into two components, which are the slow- or long-term variations $r_s(t)$ and the fast- or short-term variations $r_f(t)$. Therefore, the product of these two terms describes the received signal in linear units (6.9) [48, 62, 83]. The product becomes addition in dB scale (6.10).

$$r_t(t) = r_s(t).r_f(t)\,. \tag{6.9}$$

$$R_t(t) = R_s(t) + R_f(t)\,. \tag{6.10}$$

In the literature, deriving the large scale parameters from measurement data by eliminating the small scale variations is a commonly used assumption. Depending on the size of the stationary interval, PDPs have to be averaged over a number of snapshots. Typically, the length of 10λ to 40λ is used to define the stationary interval [48, 83, 128]. The total power per stationarity interval is necessary, which leads to a sum along the delay domain [128]. In certain cases, averaging channel impulse response (CIR) over snapshots is used in "removing " or mitigating the effects of fast fading, and this leads to sum along the delay domain to smooth out fast fading components. However, this approach is inconsistent for tapped delay line (TDL) model because a tap is a sample of the bandlimited CIR (summing along the delay domain is not an appropriate option for this case) and we are interested in characterizing the slow- and fast-fading for each tap individually. Another approach would be the slow fading effect might be removed by PDP normalization as considered in [155]. However, we decided to model and separate fading for each tap from overall received variations. As explained previously, three data sets will be studied. In the first data set, the PDP is obtained over a channel of Tx and Rx antenna array, which was faced directly to each other and then between two antennas faced away from each other. In the third data set, the PDP is obtained by averaging over the channels of the Tx and Rx antenna array; therefore, we assumed quasi-omnidirectional PDP. In each data set, LOS and two different NLOS categories are studied; hence, in total nine various setups are investigated. The data is pre-processed by estimating a noise threshold and multipath threshold (25 dB below the main peak in each snapshot) and not considering any values below them as presented in Chapter 4. Depending on how long a set of data samples is used to estimate large-scale fading, neglecting the path-loss may be fine; thus, a determination of quasi-stationarity interval is important [62].

6.3.1 Processing Interval

An appropriate measure is needed to determine and assess quasi-stationarity regions. The same assumption as in [71] is applied. Depending on the scenario (LOS, NLOS1 or NLOS2), those measurement sites are taken into account to find the maximal velocity of Rx that has been occurred and then maximum Doppler frequency is computed from (2.17), where α_p can be $+/-$ depending on the Rx is moving away or toward the Tx. In order to estimate quasi-stationarity interval, a minimal stationarity time is obtained using (6.11), where a minimal stationarity length (d_{smin}) is assumed to be $d_{smin} \approx 20\lambda = 2.38m$ as has been assumed in [158, 159]. The window length or the length of stationary interval (w) depends on the values of T_{snap} ($T_{snap} = 27.033ms$ in our case) and T_{smin} as expressed in (6.12). This results in slightly different numbers of snapshots for each scenario, as presented in Table 6.1 [5].

[5]Keeping this in mind, obtaining these values are not fully satisfactory because they rely on parameters that are somewhat arbitrary. For example, it is questionable and remains unclear how to choose v_{max}, whether v_{max} is set to the maximal speeds of the Rx as it has been done in [71], or the maximal speeds of the mobile scatterers.

$$T_{\text{smin}} \equiv \frac{1}{\Delta f_{\text{Dmax}}} = d_{\text{smin}}/v_{\max}\,, \tag{6.11}$$

$$w = \frac{T_{\text{smin}}}{T_{\text{snap}}}\,. \tag{6.12}$$

TABLE 6.1
Parameters to measure quasi-stationarity region (omnidirectional antenna)

Scenario	v_{max} (mps)	f_{Dmax} (Hz)	T_{smin} (s)	w
LOS	2.27	20	1.04	39
NLOS1	2.36	20	1	38
NLOS2	2.52	22	0.93	36

6.3.2 Separating Slow- and Fast-Fading

As illustrated in Chapter 2, the CIR is defined as a function of time and delay. The amplitude fading statistics of p^{th} tap are computed from the square root of power in the p^{th} delay bin. Among the stationary interval, slow variations are extracted from overall variations by using a moving average filter, which is a specific type of FIR filter. This method is proposed in [48,83]. Figure 6.6 illustrates five taps moving average filter that takes the previous four samples and the current sample of the input signal and computes the average namely, this operation is a convolution (6.13) [162].

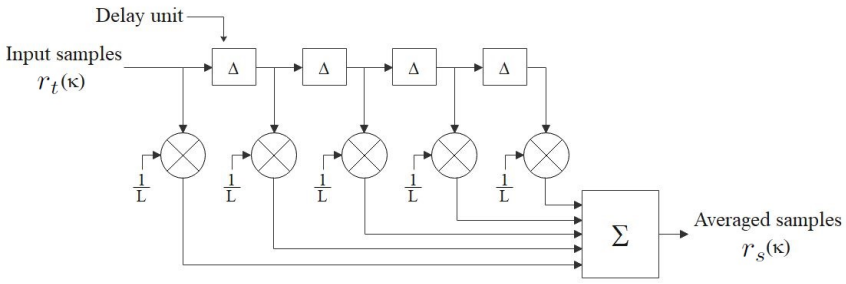

Fig. 6.6 Five taps moving average FIR filter

$$r_s(k) = \sum_{j=0}^{L-1} u(j) r_t(k-j)\,, \tag{6.13}$$

where $u(j)$ is the coefficient of the filter, which is $\frac{1}{L}$ and L is the length of the filter that depends on the value of w. The output of filter (r_s) is slow variation, k is the point at which the output is considered, r_t is the input samples (overall variations). Fig. 6.7 shows a particular example of the measured signal containing fast- and slow-components. The received signal is seen to vary by approximately 15 dB over distances as small as $\frac{\lambda}{2}$. From the figure, we can analyze that the received signal can vary by 20 dB over a distance of few meters. This rapid fluctuation of the received signal over small areas is the fast fading, and a change in the average due to the variation in the nearby buildings is the slow fading [119,124]. We assumed that the fast variations are superposed on the slow variations; therefore, the fast fading can be obtained by subtracting the slow variations (r_s) from overall variations (r_t) in dB scale (6.10) [48]. The result of extracting slow variations from the overall variations for a particular number of snapshots is

indicated in Fig. 6.8(a). Figure 6.8(b) illustrates the fast variations after filtering out the slow variations in the NLOS1 scenario for the first tap [6].

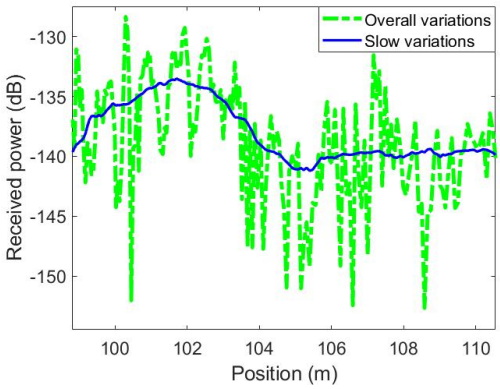

Fig. 6.7 Amplitude of the second tap under NLOS1 condition, an example of the measured signal contains both fast and slow components

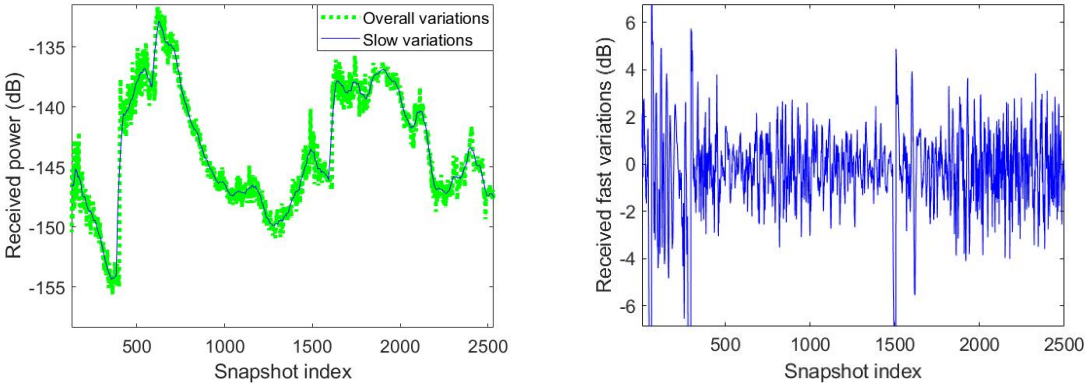

Fig. 6.8 Slow, fast and overall variations of the first tap under NLOS1 condition-omnidirectional antenna, the fast variations are derived after filtering out the slow variations, (a) Overall and slow variations, (b) Fast variations after removing the slow variations

6.3.3 Model Based Evaluation

The time-varying amplitudes with their corresponding distributions are generated to consider the slow- and fast-signal variations. This means we mixed two distributions, such as we combine Rayleigh/Weibull distribution with Log-normal distribution to model fast- and slow-fading variations, which are present in the received signal. In general, Rayleigh plus Log-normal distribution is known as Suzuki distribution [138], but we also combine Weibull- plus Log-normal-distribution to investigate the robustness of this approach, and the same proposed approach as in Section 6.3.2 is applied. The implementation of the model is summarized as a block diagram with its results and illustrated in Fig. 6.9 for Rayleigh- plus

[6]Fig. D.1 and D.2 illustrate another two exemplary graphs of the slow and fast fading components under LOS and NLOS2 scenarios for the first tap.

Log-normal-distribution [7]. From the results, it is obvious that we are able to separate both types of fading.

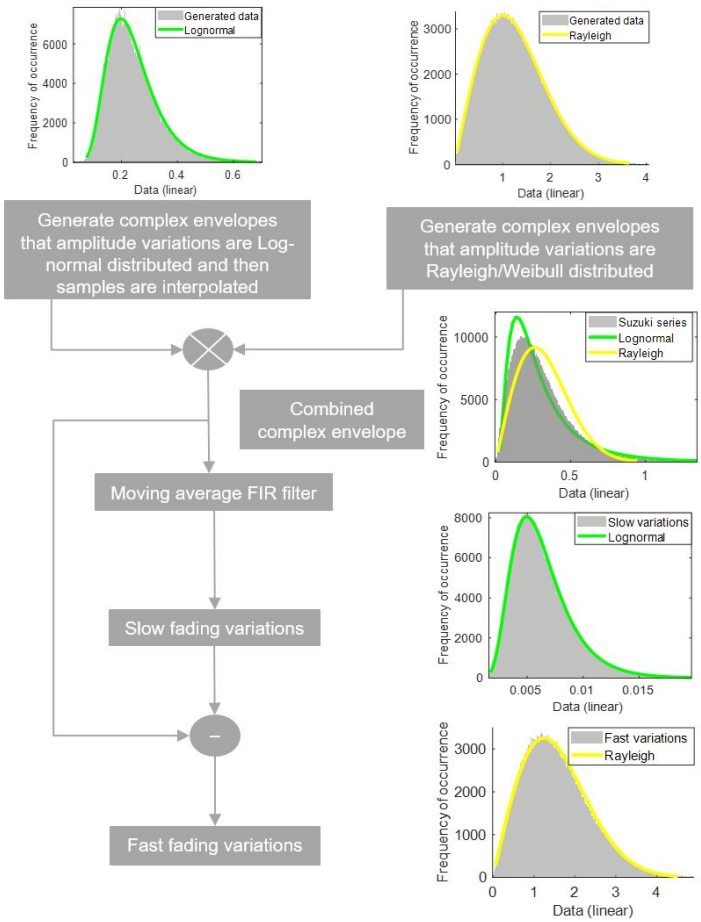

Fig. 6.9 Block diagram of separating slow and fast fading variation

6.4 Results and Evaluation

In the previous sections, an approach has been illustrated to extract the slow variations from overall variations by computing a running mean. The results pertain to the NLOS1 scenario in the case of omnidirectional antenna unless mentioned. The exemplary graphs of extracting slow variations from the overall variations and the fast variations after filtering out the slow variations are indicated in Fig. 6.8. To assess amplitude fading, the empirical histogram is calculated and then known distributions such as Rayleigh-, Log-normal-, Weibull-, and Rice-distribution are fitted. The exemplary graph of the selected PDFs fitted to the empirical distribution of the slow- and fast-fading magnitudes in linear scale is shown in Fig. 6.10. As one can see, the shape of the Log-normal and Rice-distribution are the closest to the empirical histogram of slow- and fast-variations, respectively. Additionally, some more examples of tap amplitude fading with its fitting curves are presented in Section D.3. The histogram intersection is used to compute the intersected area between the empirical histogram, and probability density function (PDF)

[7]The implementation of the approach for Weibull- plus Log-normal-distribution with its results are presented in Fig. D.3.

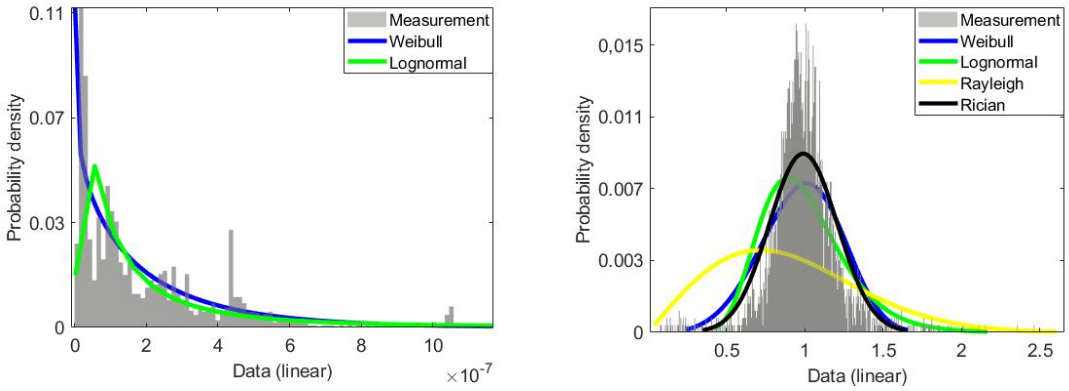

Fig. 6.10 Histograms and pdf fits for the first tap under NLOS1 condition-omnidirectional antenna, the Log-normal and Rice-distribution are the closest to the empirical histogram of slow- and fast-variations, respectively, (a) Slow variations, (b) Fast variations

fits using the algorithm proposed in Section 4.4 in order to select the best-fitted distribution among those. The outcome of histogram intersection is given in Table 6.2.

In the case of two antennas faced directly to each other and an omnidirectional antenna, the empirical evidence of small scale fading supports the Rice distribution for the largest number of taps. We can propose a physical explanation regarding the case of two antennas faced directly to each other. When a strong dominant component/wave with many random weaker components are present, the tap amplitudes follow Rician fading. Rician behavior was observed in our measurements data because there might always be a strong reflection from Cologne Cathedral ($\approx$144 $\times$ 86 $\times$ 157 m) with some numbers of reflected and scattered waves. On the other hand, in the case of omnidirectional antenna, since directive antennas have been used; thus, we are doing the summation in the power domain and not in the signal level (complex domain). As a result, the path from the different directions do not interact anymore in the same time slot; therefore, the fading also is more tending to Rice. The Weibull model has two parameters, which are a shape factor and scale parameter; thus, it offers substantial flexibility and provides a good fit to any data set that have been considered, but it is not based on an underlying theory of propagation effects [96]. From our results, the Rayleigh approximation becomes poorer because the range of delay resolution of the Rx is narrow so that there might not be enough multipath to justify the Rayleigh distribution. To model propagation paths, not only estimating the type of distribution is important, but also parameters of the specified probability distribution are essential. Table 6.3 gives the parameters for selected PDFs.

Regarding the large scale fading (in the case of two antennas faced directly to each other and an omnidirectional antenna) as is extensively reported in the literature [100, 116], a large scale fading is characterized by Log-normal distribution because most practical situations in terms of the local-mean received power fluctuations caused by obstacles are fitted by Log-normal. Our results (Table 6.2) show that Lognormal distribution fits well with the measured data for all taps in all scenarios. We have derived this in terms of considering where is the highest value of histogram intersection (HI). Table 6.4 gives the PDF fits parameters of the large scale fading. According to our measurements, the shadowing standard deviation is found to be between 2 and 11 dB. The variation factor decreases with decreasing Tx - Rx distance, a similar finding has been observed by [113]. In the case of two antennas faced away from each other, fitting any set of data, e.g., LOS, NLOS1, and NLOS2, the histogram intersection is approximately

TABLE 6.2
DISTANCE BETWEEN MEASURED DATA AND PDF FITS USING HI (SLOW AND FAST VARIATIONS) IN THE CASE OF OMNIDIRECTIONAL ANTENNA

	Outcome of HI-Slow variations			**Outcome of HI-Fast variations**			
			LOS				
Taps	Lognormal	Weibull	Rayleigh	Lognormal	Rician	Weibull	Rayleigh
1	0.6300	0.6480	0.5740	0.7549	0.7691	0.5937	0.3705
2	0.5974	0.5315	0.4850	0.7717	0.7866	0.7114	0.5055
3	0.5744	0.5571	0.5573	0.7852	0.7867	0.6997	0.4775
4	0.5903	0.5720	0.5682	0.7801	0.7807	0.6596	0.4412
			NLOS1				
Taps	Lognormal	Weibull	Rayleigh	Lognormal	Rician	Weibull	Rayleigh
1	0.6003	0.6486	0.5105	0.7087	0.7816	0.7221	0.4915
2	0.6926	0.6544	0.6419	0.7752	0.7552	0.6306	0.4261
3	0.4127	0.3872	0.3691	0.5704	0.5729	0.5093	0.3221
4	0.3021	0.2729	0.2804	0.4858	0.4664	0.3953	0.2465
			NLOS2				
Taps	Lognormal	Weibull	Rayleigh	Lognormal	Rician	Weibull	Rayleigh
1	0.7279	0.6768	0.2705	0.8683	0.9078	0.8048	0.3943
2	0.7695	0.6882	0.4235	0.8710	0.8826	0.6883	0.3189
3	0.7282	0.6459	0.4584	0.8579	0.8778	0.7352	0.3111
4	0.6249	0.5789	0.4861	0.8416	0.8426	0.6496	0.3256
5	0.6013	0.5824	0.4552	0.8419	0.8466	0.7104	0.3341
6	0.6008	0.5507	0.4885	0.8105	0.8131	0.6709	0.3572

similar for all kinds of distributions. In other words, a fitting error of slow- and fast-variations of the received signal is almost the same for known distributions. Thus, we are not able to define the distribution type; an example is shown in Fig. 6.11.

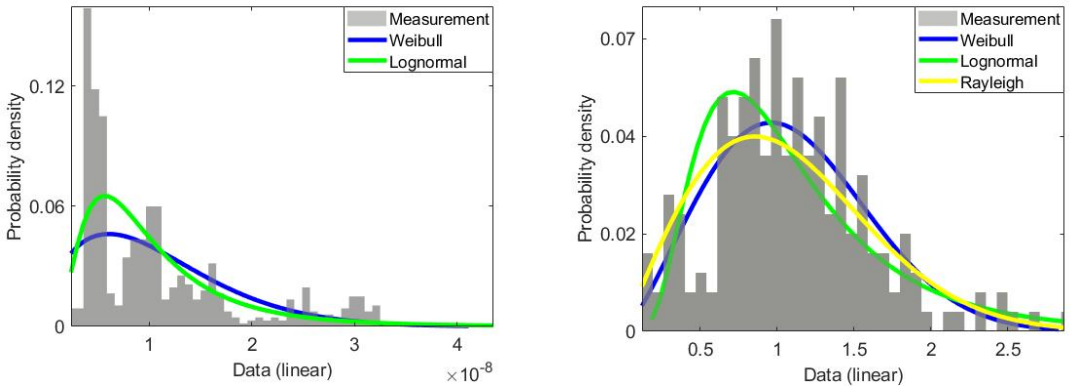

(a) (b)

Fig. 6.11 Histograms and pdf fits under NLOS1 condition-two antennas faced away from each other, a fitting error of slow- and fast-variations of the received signal is almost same for known distributions, (a) Slow variations, (b) Fast variations

TABLE 6.3
PDF FITS PARAMETERS OF SMALL SCALE FADING IN THE CASE OF OMNIDIRECTIONAL ANTENNA

LOS							
Taps	$\mu_{\text{Lognormal}}$	$\sigma_{\text{Lognormal}}$	a_{Weibull}	β_{Weibull}	σ_{Rayleigh}	s_{Rice}	σ_{Rice}
1	0	0.093	1.056	6.468	0.716	1.002	0.103
2	0	0.130	1.068	6.083	0.718	0.996	0.138
3	0	0.123	1.064	6.15	0.717	0.997	0.131
4	0	0.127	1.067	5.59	0.718	0.997	0.138
NLOS1							
Taps	$\mu_{\text{Lognormal}}$	$\sigma_{\text{Lognormal}}$	a_{Weibull}	β_{Weibull}	σ_{Rayleigh}	s_{Rice}	σ_{Rice}
1	0	0.270	1.07	4.34	0.717	0.96	0.21
2	0	0.11	1.05	6.139	0.71	0.99	0.12
3	0	0.15	1.07	6.01	0.72	0.99	0.15
4	0	0.17	1.11	4.73	0.74	1.01	0.19
NLOS2							
Taps	$\mu_{\text{Lognormal}}$	$\sigma_{\text{Lognormal}}$	a_{Weibull}	β_{Weibull}	σ_{Rayleigh}	s_{Rice}	σ_{Rice}
1	0	0.14	1.05	6.9	0.71	0.98	0.13
2	0	0.10	1.03	7.1	0.70	0.99	0.09
3	0	0.098	1.03	8.7	0.70	0.99	0.09
4	0	0.093	1.03	7.3	0.70	0.99	0.09
5	0	0.097	1.04	8.3	0.70	0.99	0.09
6	0	0.10	1.04	7.7	0.70	0.99	0.1

6.5 Concluding Remarks

In this chapter, the amplitude fading of active taps has been divided into two classes by separating the received signal into two scales of spatial variations, which are slow- and fast-fading. In total, nine various setups were studied. Estimating stationary interval is necessary to separate the slow- and fast-fading. The fast variations in received signal strength between two antennas faced directly to each other follow Rice distribution. Rician behavior is observed in our measurements data because when a strong dominant component with many random weaker components is present, the tap amplitudes follow Rician fading. In the case of omnidirectional antennas, the fading also is more tending to Rice because we have used directive antennas; thus, we are doing the summation in the power domain and not in the signal level (complex domain). As a result, the path from the different directions does not interact anymore in the same time slot. From our results, the Rayleigh approximation becomes poorer because the range of delay resolution of the receiver (Rx) is narrow, so there might not be enough multipath to justify the Rayleigh distribution. Few models for slow fading have been considered, and in the case of two antennas faced directly to each other and an omnidirectional antenna, the empirical evidence supports the Log-normal distribution. From the results, it was additionally observed that when two antennas faced away from each other, a fitting error and histogram intersection between the empirical histogram and probability density function (PDF) fits of known distributions are approximately the same for all kinds of distributions; thus, we were not able to select specific distribution for those scenarios. It has been found that the shadowing standard deviation is between 2 and 11 dB, and the variation factor increases with increasing transmitter (Tx) - Rx distance. Moreover, environments with a large number of scatterers, such as in NLOS2 regions, lead to smaller quasi-stationarity intervals than regions under line of sight (LOS) conditions.

TABLE 6.4
PDF FITS PARAMETERS OF LARGE SCALE FADING IN THE CASE OF OMNIDIRECTIONAL ANTENNA

LOS				
Taps	$\mu_{\text{Lognormal}}$	$\sigma_{\text{Lognormal}}$	a_{Weibull}	β_{Weibull}
1	-13.83	0.2469	$0.11 * 10^{-5}$	5.2
2	-14.49	0.2480	$0.05 * 10^{-5}$	3.3
3	-14.97	0.4732	$0.04 * 10^{-5}$	2.05
4	-15.187	0.5411	$0.03 * 10^{-5}$	1.84
NLOS1				
Taps	$\mu_{\text{Lognormal}}$	$\sigma_{\text{Lognormal}}$	a_{Weibull}	β_{Weibull}
1	-16.03	1.29	$2 * 10^{-7}$	0.89
2	-17.38	0.62	$3.9 * 10^{-8}$	1.4
3	-19.07	0.54	$6.9 * 10^{-9}$	1.59
4	-19.06	0.47	$3.7 * 10^{-9}$	2.3
NLOS2				
Taps	$\mu_{\text{Lognormal}}$	$\sigma_{\text{Lognormal}}$	a_{Weibull}	β_{Weibull}
1	-18.9	1.25	$1.17 * 10^{-8}$	0.69
2	-19.4	0.86	$5.89 * 10^{-9}$	0.97
3	-19.8	0.71	$3.6 * 10^{-9}$	1.09
4	-20	0.6	$2.85 * 10^{-9}$	1.24
5	-20	0.57	$2.71 * 10^{-9}$	1.19
6	-20	0.59	$2.76 * 10^{-9}$	1.39

A part of the research contributions covered in this chapter is published in [62].

Chapter 7

MIMO-TDL Model

7.1 Motivation and Related Work

Many researchers have described the dispersive channel model in the form of tapped delay line (TDL) model for vehicle to X (V2X) channels, and there have been several papers on that topic [61, 63–66, 93, 96, 129, 155]. Mainly, the class of TDL model is a single input single output (SISO) channel, and all the discussions so far have dealt with the SISO channel. In this chapter, we propose a modeling method to extend the SISO-TDL model to multiple input multiple output (MIMO) under the non-WSSUS assumption; this has not been studied yet. Techniques such as multiple antennas are attracting the attention of industry; thus, MIMO systems are one of the most active research topics in the field of wireless communication systems. Channel capacity of a MIMO system is increased as compared to a SISO system, without any additional transmit power [87, 114]. In conventional SISO systems, data rates can be increased by using high gain directional antennas or increasing transmit power. However, those techniques have certain limitations, such as reducing battery life and increasing interference [114]. MIMO systems can be used to either increase the data transmission rate by sending independent bit streams from transmit antennas (spatial multiplexing) or to obtain reliable communication by sending the same bit streams (spatial diversity) [87, 107]. Before implementing any MIMO system, a proper and accurate MIMO channel model is required for optimizing, testing, and evaluating the performance of wireless communication systems such that various scenarios can be taken into account to ensure the system can work efficiently in any scenario [87, 114, 167]. Briefly, multiple antenna technology gives advantages that can be drawn as improving fading environments, extending the range, and providing higher data throughput over conventional single antenna systems [39, 107].

As mentioned previously, we propose a method for MIMO-TDL modeling under the non-WSSUS assumption via employing an ON/OFF process. The aim is to develop a MIMO-TDL model based upon MIMO vehicle to infrastructure (V2I) measurements. The analysis investigates the correlation coefficient among taps persistence process, as well as among taps amplitude. In addition to that, amplitude fading will be addressed. The analysis evaluates the extended approach in terms of channel capacity. The channel capacity gain for various antenna configurations, as well as different values of signal to noise ratio (SNR), will be studied. Additionally, we propose another modeling method to develop a time-varying MIMO-TDL model, whose parameters (such as power, delay, fading parameters, etc.) vary over time. Section E.2 provides the description of the proposed approach.

Some of the findings in this chapter are presented in [63, 65].

7.2 MIMO System Concepts

In this section, some MIMO-related concepts are introduced to clarify how multiple antennas can achieve high data rates. The Shannon theorem provides a quantification of the capacity over a Gaussian communication link, and it is expressed as follows [26, 58]

$$C = \log_2(1 + \zeta) \quad \text{b/s/Hz} \tag{7.1}$$

where ζ is a signal-to-noise ratio. This is a theoretical maximum, in other words, the maximum bits per second per Hertz rate achievable for error-free transmission over a Gaussian communication link, whereas this is unachievable in practice. We can get closer to that by using turbo codes as considered in [58]. If we multiply B by C, where B is the bandwidth, the capacity is achieved in b/s [26,58]. For an n-antenna array system, the capacity array is as (7.2). It means the received signal will be n times larger [58].

$$C_{\text{array}} = \log_2(1 + n^2\, \zeta) \quad \text{b/s/Hz} \tag{7.2}$$

The combined capacity (C_n) would be (7.3) if we had n equal independent channels [58]

$$C_n = n \log_2(1 + \zeta) \quad \text{b/s/Hz} \tag{7.3}$$

When we compare the above expressions, we can observe that we might achieve a much larger capacity with n independent channels than with an array of n antennas. Here, we introduce the concept of the MIMO transmission matrix in order to look into how this can be achieved. As presented in Chapter 2, in the SISO system, the relationship between the input and output can be expressed as

$$y(f) = h(f) \cdot x(f)\,, \tag{7.4}$$

where $h(f)$ is the channel transfer function, and $y(f)$ and $x(f)$ are the received and transmitted signals. We drop the f variable in the following expressions for simplicity. The notation may seem misleading, whereas we are referring h to a tap at a given frequency.

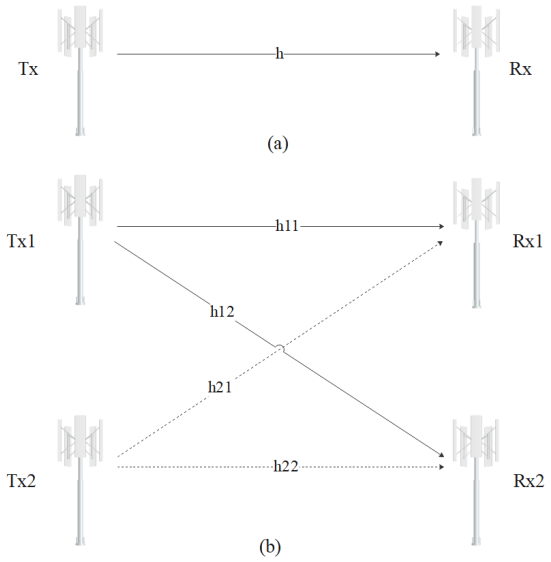

Fig. 7.1 Propagation between antenna pairs, (a) Single antenna system, (b) Multiple antenna system

As illustrated in Fig. 7.1, the propagation conditions are different between each transmitter (Tx) and receiver (Rx) antenna; hence, a single-channel function is not sufficient to characterize the MIMO system. A set of as many channel functions as possible (Tx-Rx antenna pairs) is required, e.g., for the scenario in Fig. 7.1(b), we need 2×2 channel matrix [58].

$$\begin{aligned} y_1 &= h_{11}x_1 + h_{12}x_2 \\ y_2 &= h_{21}x_1 + h_{22}x_2\,, \end{aligned} \tag{7.5}$$

where h_{mn} is the complex transfer function between transmit antenna m and receive antenna n. y_n and x_m are the output and input complex voltages at receive antenna n and transmit antenna m, respectively. We can put the above equation in a matrix form as follows

$$\begin{bmatrix} y_1 \\ y_2 \end{bmatrix} = \begin{bmatrix} h_{11} & h_{12} \\ h_{21} & h_{22} \end{bmatrix} \begin{bmatrix} x_1 \\ x_2 \end{bmatrix}, \tag{7.6}$$

or

$$\mathbf{y} = \mathbf{H} \cdot \mathbf{x}\,, \tag{7.7}$$

where $\mathbf{H}$ is the transmission matrix, and $\mathbf{x}$ and $\mathbf{y}$ are the input and output complex voltage vectors. When the channels are independent, the capacity will be maximum, in other words, when the transmission matrix is diagonal (7.8). This means each Rx antenna receives only from a single Tx antenna as in (7.9) [58].

$$\mathbf{H} = \mathbf{D} = \begin{bmatrix} h_{11} & 0 \\ 0 & h_{22} \end{bmatrix} = \begin{bmatrix} d_1 & 0 \\ 0 & d_2 \end{bmatrix}, \tag{7.8}$$

$$\begin{bmatrix} y_1 \\ y_2 \end{bmatrix} = \begin{bmatrix} d_1 & 0 \\ 0 & d_2 \end{bmatrix} \begin{bmatrix} x_1 \\ x_2 \end{bmatrix} + \begin{bmatrix} n_1 \\ n_2 \end{bmatrix}, \tag{7.9}$$

or

$$\mathbf{y} = \mathbf{D} \cdot \mathbf{x} + \mathbf{n}\,, \tag{7.10}$$

where $\mathbf{n}$ is a noise vector and introduced for the sake of completeness but hardly occurs in reality. What we can do is 'diagonalizing' matrix $\mathbf{H}$ by performing some sort of signal processing at both ends. It converts the signal processing ensemble and channel into a diagonal matrix. It can be achieved by introducing two matrices, e.g., $\mathbf{P_t}$ and $\mathbf{P_r}$ at the Tx and Rx sides as follows [58]

$$\mathbf{P_r^H} \cdot \mathbf{H} \cdot \mathbf{P_t} = \mathbf{D}\,, \tag{7.11}$$

where $^{\mathbf{H}}$ means conjugate transposed (transposed hermitic matrix). The overall signal processing and transmission chain is expressed by

$$\mathbf{y} = \mathbf{P_r^H} \cdot \mathbf{H} \cdot \mathbf{P_t} \cdot \mathbf{x} = \mathbf{D} \cdot \mathbf{x}\,. \tag{7.12}$$

As a result, we obtain independent propagation paths. Performing singular value decomposition (SVD) of the transmission matrix leads to achieving the 'diagonalization' process. For example, we have a $m \times m$ transmission matrix and we put it in the form as [58, 75]

$$\mathbf{H} = \mathbf{U} \cdot \mathbf{D} \cdot \mathbf{V^H}\,, \tag{7.13}$$

where $\mathbf{U}$ and $\mathbf{V}$ are unitary orthonormal matrices (7.14), and $\mathbf{D}$ is a diagonal matrix

$$\begin{aligned} \mathbf{V} \cdot \mathbf{V^H} &= \mathbf{I} \\ \mathbf{U} \cdot \mathbf{U^H} &= \mathbf{I}\,, \end{aligned} \tag{7.14}$$

where $\mathbf{I}$ is the identity matrix ($m \times m$). By performing the operation (7.15), we will arrive at the signal processing, which is required to perform 'diagonalization' of the transmission matrix [58, 75].

$$\mathbf{D} = \mathbf{U^H} \cdot \mathbf{H} \cdot \mathbf{V} \tag{7.15}$$

The square roots of the eigenvalues of $\mathbf{H^H} \cdot \mathbf{H}$ and $\mathbf{H} \cdot \mathbf{H^H}$ are the diagonal elements of matrix $\mathbf{D}$. We will look into this in the given example below.

Example: Assuming a transmission matrix as

$$\mathbf{H} = \begin{bmatrix} 0.48 & 0.31 \\ -j0.57 & j0.41 \end{bmatrix}$$

Its hermitic transposed is

$$\mathbf{H^H} = \begin{bmatrix} 0.48 & j0.57 \\ 0.31 & -j0.41 \end{bmatrix}$$

The product $\mathbf{H^H} \cdot \mathbf{H}$ is

$$\mathbf{H^H} \cdot \mathbf{H} = \begin{bmatrix} 0.5553 & -0.0849 \\ -0.0849 & 0.2642 \end{bmatrix}$$

The eigenvalues of $\mathbf{H^H} \cdot \mathbf{H}$ can be calculated using MATLAB function *eig*. The elements of the diagonal matrix $\mathbf{D}$ can also be calculated using square roots of the eigenvalues or MATLAB function *svd*.

$$\mathbf{U} = \begin{bmatrix} -0.5030 & -0.8643 \\ j0.8643 & -j0.5030 \end{bmatrix}$$

$$\mathbf{D} = \begin{bmatrix} 0.7604 & 0 \\ 0 & 0.4912 \end{bmatrix}$$

$$\mathbf{V} = \begin{bmatrix} -0.9653 & -0.2610 \\ 0.2610 & -0.9653 \end{bmatrix}$$

As a result, matrices $\mathbf{P_t}$ and $\mathbf{P_r}$ have been computed. This means obtaining as many independent output signals as pairs of antennas is possible, such as

$$y_i = d_i \cdot x_i\,, \tag{7.16}$$

where $i = 1, 2, 3, ..., n$. $|d_i|^2$ gives the amount of power transferred between x_i and y_i. Channel i is known as propagation mode i. The achievable capacity through mode i is directly influenced by the coefficient d_i. The larger d_i is, the greater its SNR ratio becomes [58].

We look at different examples represented by their transmission matrices to illustrate the influence of the values of d_i^2 on the mode capacity and their importance [58]. The first example corresponds to

line of sight (LOS) propagation conditions. The corresponding diagonal and transmission matrices are exemplary as follows

$$\mathbf{H} = \begin{bmatrix} 1 & 1 \\ 1 & 1 \end{bmatrix},$$

$$\mathbf{D} = \begin{bmatrix} 2 & 0 \\ 0 & 0 \end{bmatrix},$$

Thus, $|d_1|^2 = 4$, and $|d_2|^2 = 0$. In the second example, we will assume the differences between antennas are very small such that

$$\mathbf{H} = \begin{bmatrix} 1 & 0.98 \\ 0.98 & 1 \end{bmatrix}$$

$$\mathbf{D} = \begin{bmatrix} 1.985 & 0 \\ 0 & 0.015 \end{bmatrix},$$

Thus, $|d_1|^2$ and $|d_2|^2$ are 3.9403 and 0.0002, respectively. Finally, significant differences are shown in the third example, such as

$$\mathbf{H} = \begin{bmatrix} 0.48 & 0.31 \\ -j0.57 & j0.41 \end{bmatrix}$$

$$\mathbf{D} = \begin{bmatrix} 0.7604 & 0 \\ 0 & 0.4912 \end{bmatrix}$$

This one would correspond to a multipath-rich propagation scenario, and $|d_1|^2$ and $|d_2|^2$ are 0.5782 and 0.2413, respectively. In the LOS example, only one antenna pair (d_1) contributes all the power; in other words, all the power is transmitted through d_1. In the second and third examples, the relevance of the power at the output of the first antenna decrease; there starts to be power in the second antenna as propagation differences appear. As a conclusion, when only one mode is excited, in other words, when the direct LOS signal dominates, a MIMO system does not provide any practical advantage. MIMO systems provide advantages when the propagation conditions between the various antenna pairs are different. From those examples, it is observed that a rich multipath environment can lead to increased channel capacity if multiple antennas are used [58, 70].

7.3 MIMO Channel Capacity

As stated before, MIMO systems can offer substantial improvements over conventional SISO antenna systems in either transfer rate or quality of service (QoS) [48,54]. A fundamental understanding, limitation of MIMO channels, and an overview of the extensive results on the Shannon capacity were provided by the authors in [57]. The MIMO channel capacity highly depends on its propagation characteristics, antenna element correlations, and statistical properties of the channel [32, 46, 57]. The capacity of SISO systems is given by [33, 48, 54]

$$C_{\text{SISO}} = \log_2(1 + \zeta|h|^2) \qquad \text{b/s/Hz} \tag{7.17}$$

where ζ and h are a signal-to-noise ratio and the normalized complex gain of a particular realization of the channel, respectively. Another option of interest is a single input multiple output (SIMO) system with N-Rx antennas. For a $1 \times N$ SIMO system, the capacity is given by [48, 54].

$$C_{\text{SIMO}} = \log_2 \left(1 + \zeta \sum_{i=1}^{N} |h_i|^2 \right) , \tag{7.18}$$

where h_i is the channel gain for i^{th} Rx antenna. Another configuration is a multiple input single output (MISO) system with M-Tx antenna, and the capacity is expressed as follow [48, 54].

$$C_{\text{MISO}} = \log_2 \left(1 + \frac{\zeta}{M} \sum_{i=1}^{M} |h_i|^2 \right) , \tag{7.19}$$

where h_i is the channel gain from i^{th} Tx antenna and the transmit power is equally split between the M transmit antennas [48, 54]. Finally, the capacity of MIMO configuration with M-Tx and N-Rx antennas is given by [48, 54, 136]

$$C_{\text{MIMO}} = \log_2 \left[\det \left(\mathbf{I_N} + \frac{\zeta}{M} \mathbf{H} \mathbf{H}^* \right) \right] , \tag{7.20}$$

where $(.)^*$ is transpose-conjugate and $\mathbf{H}$ is the $N \times M$ channel transmission matrix. Equation (7.20) can be simplified to (7.21) by using the eigen decomposition (d_i^2) of matrix HH^H [48, 140]. From (7.21), the capacity of the MIMO channel is expressed as a sum of the capacities of M-SISO channels [48, 140].

$$C_{\text{MIMO}} = \sum_{i=1}^{n} \log_2 \left(1 + \frac{\zeta}{M} d_i^2 \right) , \tag{7.21}$$

where the term d_i^2 and $n = min(M, N)$ were already defined in Section 7.2. N and M denote the number of Rx and Tx antennas, respectively. As we can see from (7.21), the summation operator is now outside the logarithm operator; hence, we can see the significant capacity enhancement brought about by the MIMO configuration. However, our model corresponds to a wideband channel because we observe more than one tap. Thus, the same approach (7.22) as in [32, 46, 75, 76] is performed to compute the channel capacity of our model.

$$C_{\text{MIMO}_{\text{WB}}}(t) = \frac{1}{F} \sum_{f=1}^{F} \sum_{i=1}^{n} \log_2 \left[\left(1 + \frac{\zeta}{M} d_{i,f}^2 \right) \right] , \tag{7.22}$$

where F is the total number of frequencies (the total number of taps). We can obtain two kinds of statistics: in the narrow-band case with $F = 1$ or number of tap $= 1$, and in the wideband case, (7.22) is used, and it is equivalent to averaging the narrow-band capacity over frequency [75].

7.4 Processing of the Measurement Data

A representation of the channel in a multiple antenna system has been defined (2.37) in Chapter 2. Assume that $h(s, \tau, M, N)$ expresses the measured channel impulse response (CIR), where s is the number of collected CIR, τ is the number of samples in the delay domain. M and N are the numbers of Tx- and Rx-antennas, respectively. 4×4 elements (v-polarized) are being sub-selected from 32×32 elements[1].

[1]The measurement antenna setup was presented in Table 3.3.

The simulation model of our antenna array has been shown in Fig. 3.4 and 3.5. Antennas on the left and right sides and in front and rear are chosen at the Tx and Rx, respectively. This follows 90° rotated antenna arrangement. The selected antennas position is indicated using a red circle in Fig. 7.2, where number 1 and 3 correspond to antenna position in the front and rear sides, and number 2 and 4 indicate antenna position on the left and right sides. In total, 16-link channels will be used in this investigation. Keep in mind, this section is an extension of our previous sections, and a performance comparison will be illustrated in terms of channel capacity. The algorithm for devising this channel model is given below.

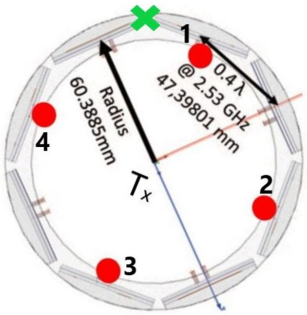

Fig. 7.2 Simulation model of the selected antennas' position

7.4.1 Quasi-stationary Interval

The same algorithm as in Section 6.3.1 is applied to estimate the stationary interval. In brief, a minimal stationarity time is obtained using (6.11) and then the quasi-stationary interval (w) is estimated (6.12). The resulting parameters are presented in Table 7.1.

TABLE 7.1
PARAMETERS TO MEASURE QUASI-STATIONARITY INTERVAL

Scenario	$v_{\max}$ ($\mathrm{m\,s^{-1}}$)	T_{smin} (s)	w	f_{Dmax} (Hz)
LOS	1.22	1.94	72	10.3
NLOS1	1.27	1.85	68	10.7
NLOS2	1.23	1.91	70	10.4

7.4.2 Determination of the Acive Taps

Our algorithm to select taps and derive their parameters has been detailed in Chapter 4. Fig. 7.3 presents a summary of our algorithm in a form of a block diagram. Briefly, the measurement data is affected by noise such that a noise threshold is estimated, and samples under the threshold are discarded. The finite "lifetime" of the propagation paths is obtained by applying 25 dB below the main peak in each snapshot; therefore, the persistence process (PP) for each multipath is obtained. The PP is associated with the measured power delay profile (PDP) to obtain cumulative energy as expressed in (4.9). Finally, active taps are sub-selected at the peaks of the cumulative energy. Selecting taps based on peak samples are essential to avoid the negligence of taps with low energy but large delays because they can have unfavorable effects on the capability of regenerating the root mean square delay spread (RMS-DS) that has been experimentally proven in Section 4.2.3. The number of active taps for the three different scenarios

is presented in Fig. 7.4. Fig. 7.5 illustrates the tap energy matrices. We normalize the computed tap energy with respect to its maximum.

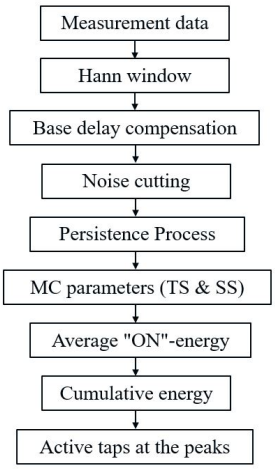

Fig. 7.3 Tap selection block diagram

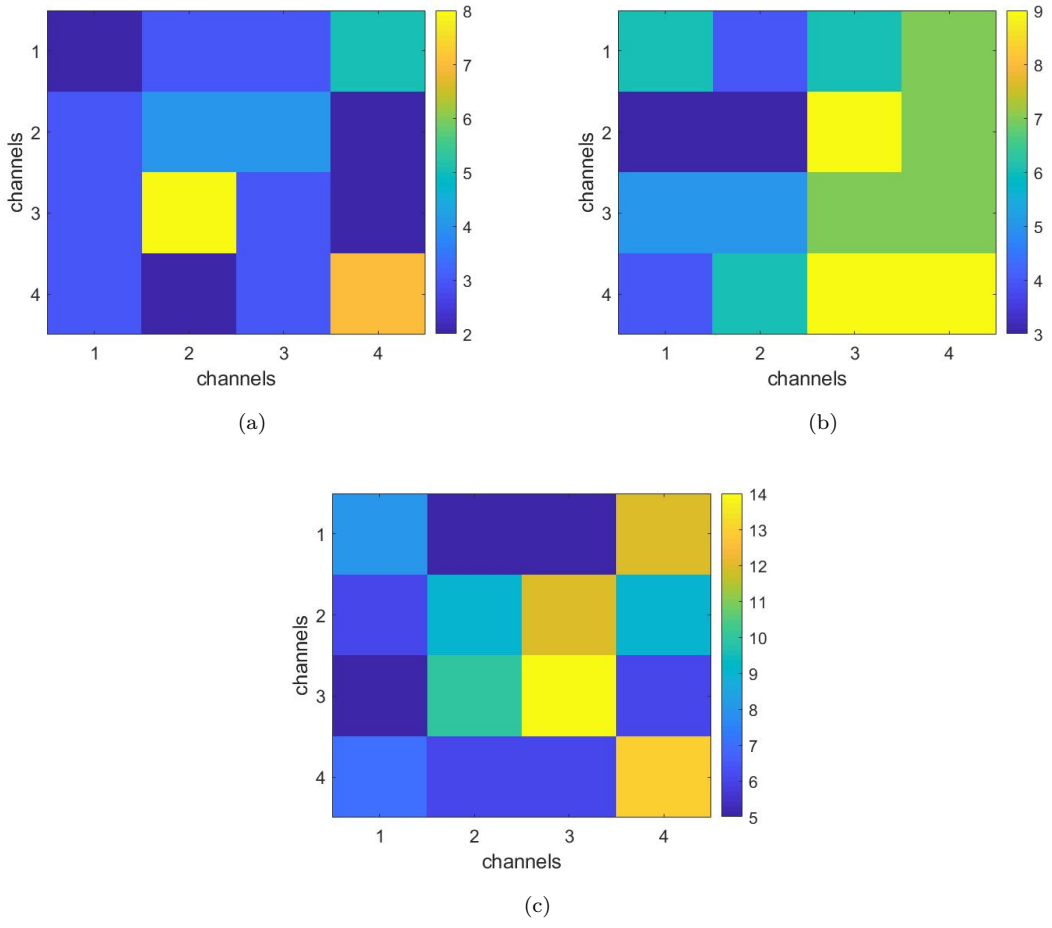

Fig. 7.4 Number of active taps, (a) LOS, (b) NOS1, (c) NLOS2

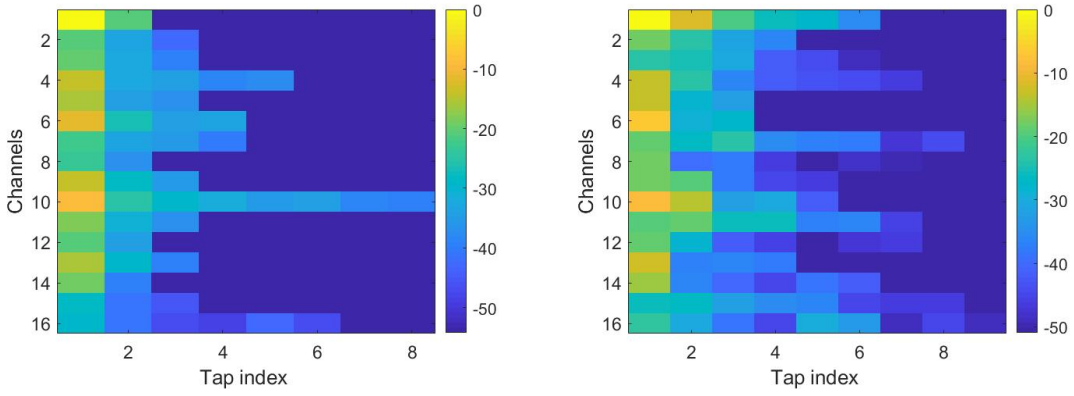

(a)

(b)

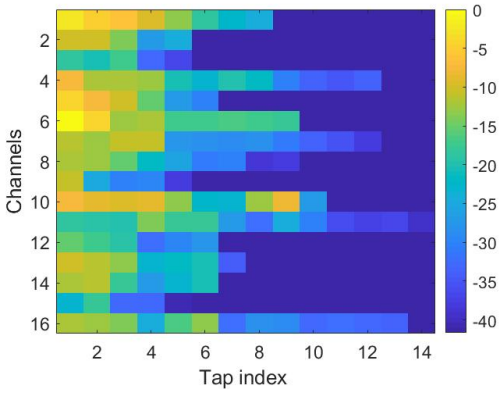

(c)

Fig. 7.5 Tap energy matrices, the computed tap energy is normalized with respect to its maximum, (a) LOS, (b) NOS1, (c) NLOS2

7.4.3 Fading Statistics of the Active Taps

The amplitude distribution of p^{th} tap can be obtained along the whole route in each scenario as in [159,160] after separating and breaking down the measured received amplitude into slow- and fast-fading variations. The same approach is applied as in Section 6.3.2. A moving average FIR filter is used to extract slow variations from overall variations by computing a running mean (6.13), then fast variations are obtained by subtracting the slow fading variations from overall fading variations using (6.10). A particular example of the measured signal that contains both fast and slow components is depicted in Fig. 7.6. The result of extracting slow variations from the overall variations for a particular number of snapshots with its empirical histogram is indicated in Fig. 7.6(a) and 7.6(c). In Fig. 7.6(a), the received signal is seen to be varied by more than 15 dB over small distances. This rapid fluctuation of the received signal over small areas is a fast fading, which is extracted from overall fading and presented in Fig. 7.6(b) and 7.6(d).

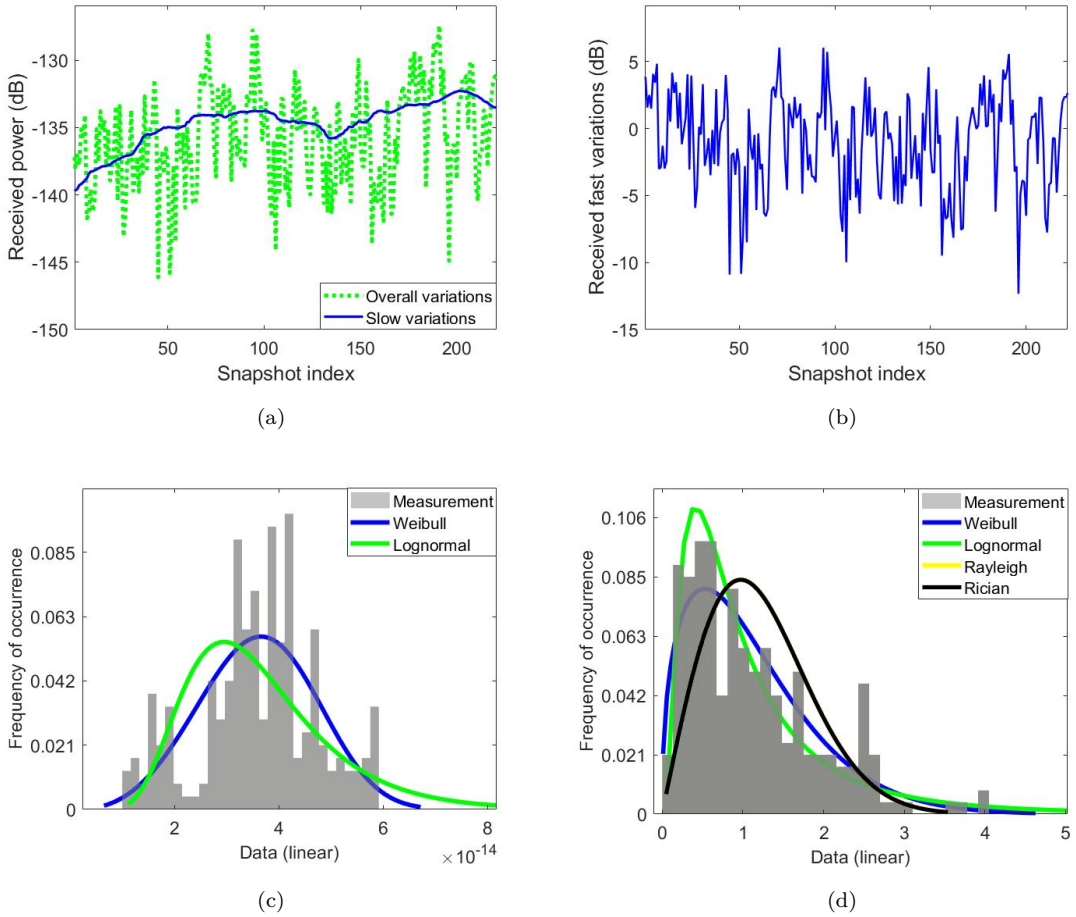

Fig. 7.6 Amplitude of the second tap under LOS condition between Tx-2 and Rx-2, extracting slow variations from the overall variations for a particular number of snapshots with its empirical histogram, (a) Slow variations vs overall variations, (b) Fast fading variations, (c) Slow fading distribution, (d) Fast fading distribution

The empirical histogram of fast variations is calculated and then the selected PDFs such as Weibull, Lognormal, Rician, and Rayleigh distributions are fitted to the empirical distribution; exemplary graphs under LOS, NLOS1, and NLOS2 conditions are presented in Fig. 7.7. In order to measure similarity between the empirical histogram and probability density function (PDF) fits, the histogram intersection (HI) is computed using the algorithm proposed in Section 4.4. The outcome depicts that the Weibull distribution illustrates a better match for a large number of taps and the first tap under LOS conditions follows Rician distribution, as shown in Fig. 7.7(a). The Weibull distribution provides a good fit to any data set that have been considered due to substantial flexibility (a shape factor and scale parameter). In the exemplary graphs Fig. 7.7(b) and 7.7(c), the Rician K factor is zero; thus, Rayleigh fading is recovered. The conclusion can be drawn as a large number of taps follows the Weibull distribution. Additionally, some more graphs of the selected PDFs fitted to the empirical distribution of the fast fading are presented in Section E.1.1.

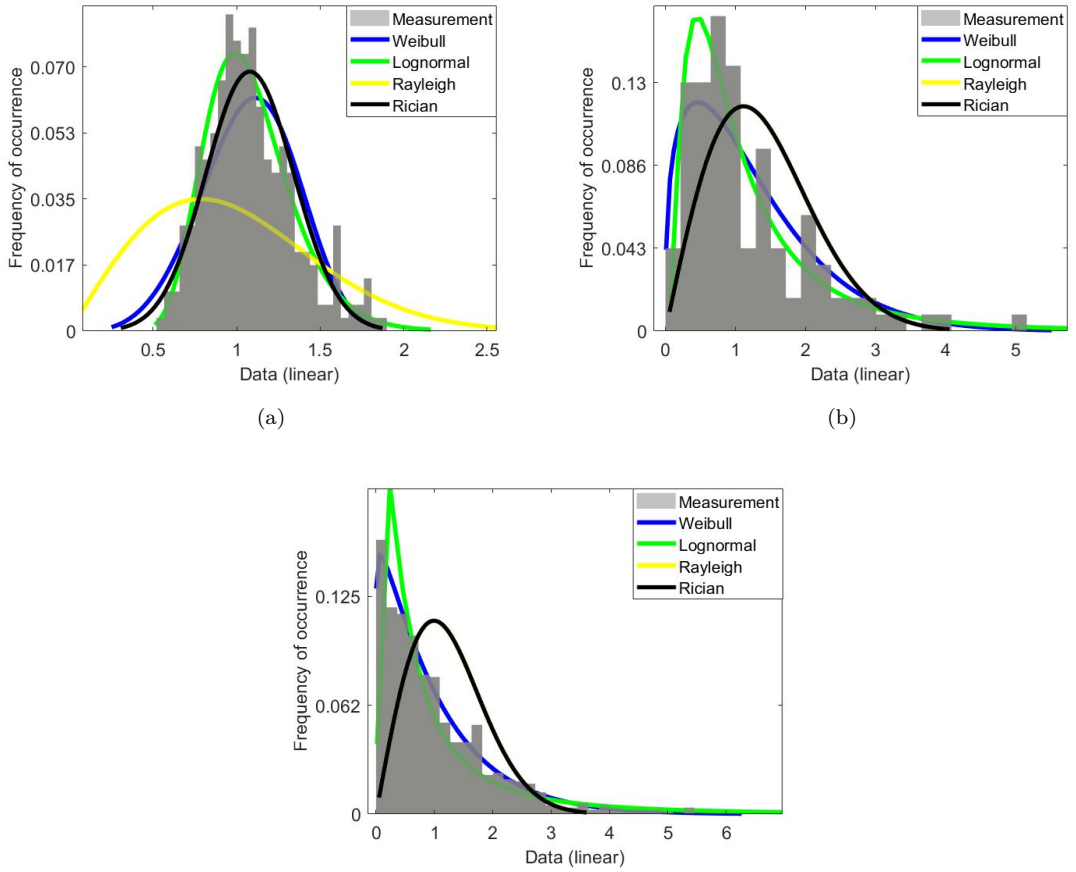

Fig. 7.7 Tap amplitude distribution, the outcome depicts that the Weibull distribution illustrates a better match under NLOS1 and NLOS2 and the first tap under LOS condition follows Rician distribution, (a) First tap under LOS condition between Tx-1 and Rx-1, (b) Second tap under NLOS1 condition between Tx-2 and Rx-2, (c) Second tap under NLOS2 condition between Tx-4 and Rx-4

7.4.4 Doppler Shift of the Active Taps

The time selectivity of wireless channels due to relative motion between the Tx and Rx is described by the Doppler shift. In order to characterize the Doppler frequency for each active tap, the same approach as in Section 4.3 is considered. The maximum Doppler frequency is computed and then the Doppler feature of the active taps is described as a random variable that follows a uniform distribution, which is $f_v \sim U[-f_{\mathrm{Dmax}}, f_{\mathrm{Dmax}}]$.

7.4.5 Pairwise Tap Correlation Coefficient and Correlation between Taps Persistence Processes

As described in Section 4.5, tap i and j do not always for the same snapshot because PP is associated with each tap; thus, correlation coefficient among the taps should be calculated using those snapshots when both taps exist. Fig. 7.8 demonstrates different numbers of snapshots are used to calculate the correlation matrix under LOS, NLOS1, and NLOS2 conditions. In order to make this clear, one of the matrices is indicated using a red square in Fig. 7.8(b), and this portion of the figure is zoomed in and

indicated in Fig. 7.9. As can be seen in Fig. 7.9, $\rho_{1,2}$ is computed using more than 170 snapshots, and $\rho_{2,3}$ may have been computed using about 120 snapshots. The number of snapshots decreases as the distance (delay) between taps increases. Note that for higher-indexed taps, it is possible that there might not be any snapshots where both the taps exist.

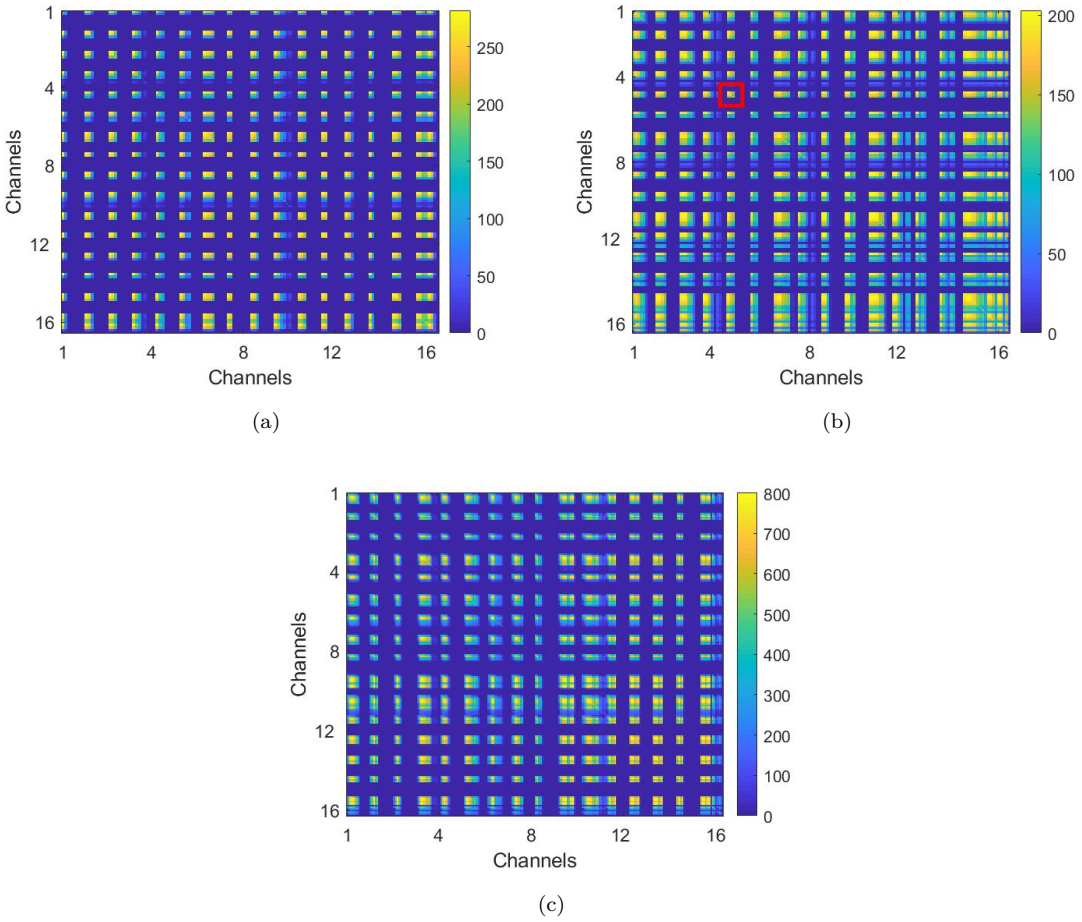

Fig. 7.8 Number of snapshots used to calculate correlation matrix, (a) LOS, (b) NLOS1, (c) NLOS2

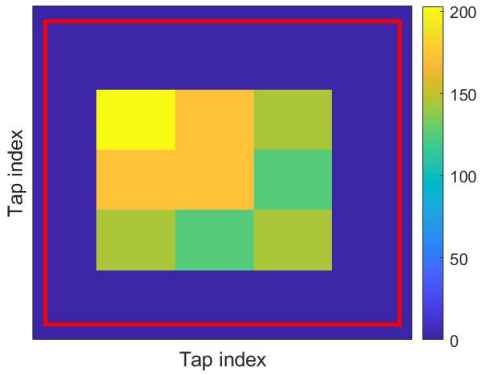

Fig. 7.9 Number of snapshots to calculate tap correlation coefficient under NLOS1 condition after zooming a red square in Fig. 7.8(b), $\rho_{1,2}$ is computed using more than 170 snapshots and $\rho_{2,3}$ may have been computed using 120 snapshots

The pairwise tap correlation coefficient is obtained using (4.19). In MIMO systems, the pairwise taps correlation coefficients are described by a matrix of coefficients, which has three dimensions $C_\gamma(P', M \times N, M \times N)$, where P' is the number of active taps, M and N are the numbers of Tx- and Rx-antennas, respectively. On the other hand, the correlation coefficient among taps persistence is estimated using (4.24). The result (C_z) is a correlation matrix expressed as $C_z(P', M \times N, M \times N)$. Pairwise tap correlation coefficient matrix with correlation matrix between taps persistence is demonstrated in Fig. 7.10 and 7.11, respectively. From the results, the following conclusions can be drawn:

- **Under LOS condition:**
  - There is no correlation among taps amplitudes, as well as among taps persistence process, and the mean values are 0.17 and 0.12, respectively.
- **Under NLOS1 condition:**
  - As can be seen in Fig. 7.10(b), some of the taps amplitude are highly correlated in each channel, as well as, among the channels, and the mean value of C_γ is 0.44.
  - There is no correlations among the taps persistence process and the mean value of C_z is 0.1.
- **Under NLOS2 condition:**
  - Some of the taps amplitude are correlated, and the mean value of C_γ is 0.35
  - The correlation coefficient among taps persistence process is low, and the mean value is around 0.25

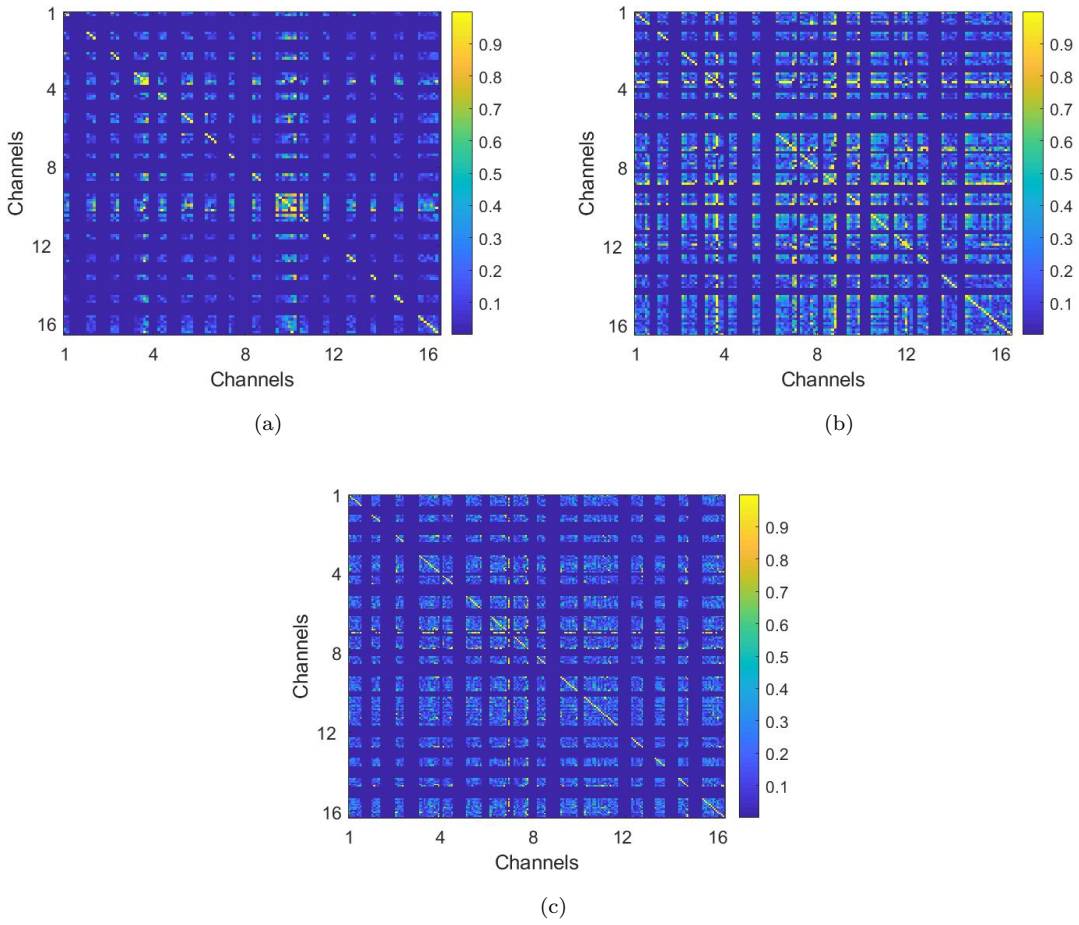

Fig. 7.10 Pairwise tap correlation coefficients matrix, (a) In LOS scenario, there is no correlation among taps amplitudes, (b) In NLOS1 scenario, some of the taps amplitude are highly correlated in each channel, as well as among the channels, (c) In NLOS2 scenario, some of the taps amplitude are correlated

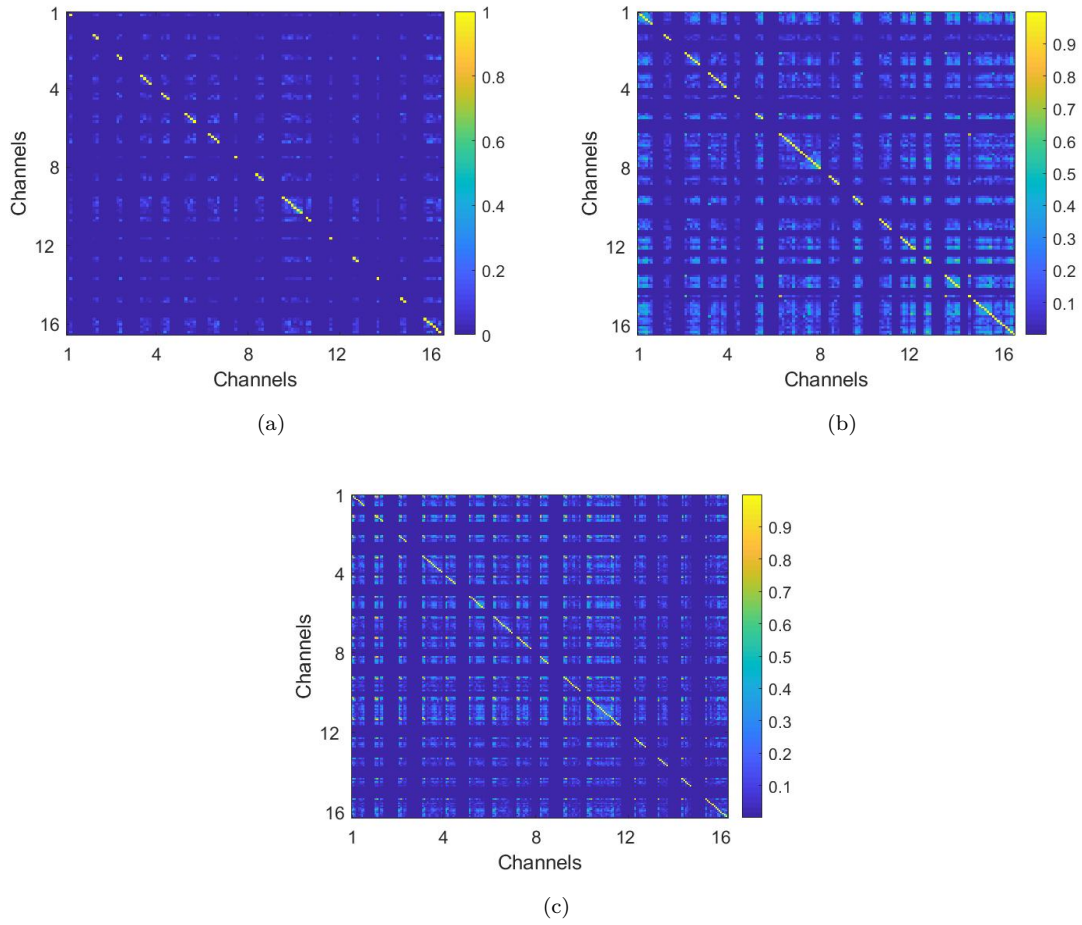

Fig. 7.11 Correlation matrix among ON/OFF process, there is no correlation among taps persistence process, (a) LOS, (b) NLOS1, (c) NLOS2

7.5 Analysis of MIMO Channel Capacity

In this section, gains offered by MIMO in terms of capacity bounds are explored. Fundamental results such as a comparison between SISO- and MIMO- channel capacity in terms of different values of SNR and a different number of antennas will be presented. Additionally, we want to investigate how well the capacity of our channel model matches with the simulated channel. By simulated channel model, we mean that our algorithm in Chapter 5 is used to create generators to produce channel impulse responses based on the derived model parameters from measurement data. In total, three generators are devised that are Log-normal, Weibull, and Rayleigh generators.

For each scenario (LOS, NLOS1, and NLOS2) four different configurations will be investigated, which are SISO and three different MIMO setups. As explained previously, our 4×4 MIMO scenario follows the basic 90° rotated antenna arrangement. This means antennas on the left and right sides, as well as in the front and rear, are chosen at the Tx and Rx, as presented in Fig. 7.12. Note that the position of antennas is indicated using red circles, and the front of the uniform circular array is depicted using a green cross, which is equivalent to the green cross in Fig. 7.13. As explained previously, two different scenarios of 2×2 MIMO configurations are studied to investigate the role of the position of antennas, and

they will be called scenarios A and B. In scenario A, antennas in front and rear are chosen at the Tx and Rx [2]. Scenario B selects antennas on the left and right at both sides [3]. It is important to note that those figures are only presenting the positions of selected antennas. Regarding the propagation environment, the reader should refer/imagine this installation in Fig. 3.6, where the Tx was acting as a base station mounted on a rooftop, and the Rx has been moving using a car.

Fig. 7.12 Simulation model of antenna installation MIMO case 4×4 antennas, antennas on the left and right sides, as well as in front and rear, are chosen at the Tx and Rx; note that the position of antennas is indicated using red circles and the front of the uniform circular array is depicted using a green cross, which is equivalent to the green cross in Fig. 7.13

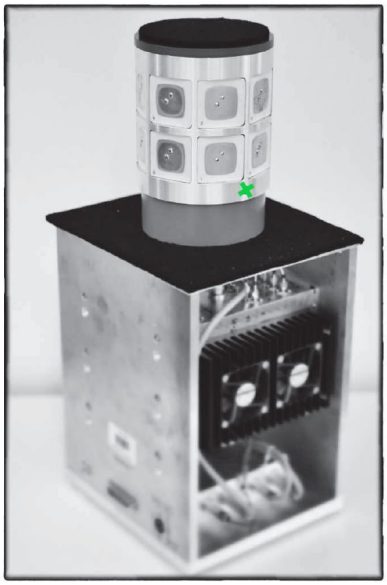

Fig. 7.13 Realized antenna array has been used during channel sounding measurement campaign, note copyright from [109]

In Section 7.3, a method for calculating the channel capacity is presented. Fig. 7.14 shows the cumulative distribution function (CDF) graphs of channel capacity for three different scenarios, which are LOS and two different NLOS categories. In each scenario, SISO channel capacity is first determined,

[2] This corresponds to antenna number 1 and 3 in Fig. 7.12
[3] This means antenna number 4 and 2 in Fig. 7.12

followed by three different MIMO setups. In each setup, the channel capacity is first determined for measured data and compared to the simulated CIRs. These results are given for the SNR fixed at 20 dB and they reveal that by increasing the number of receive and transmit antennas, MIMO models bring about a drastic increase in capacity. The capacity of 4×4 MIMO channel is greater than the capacity of 2×2 MIMO channel and SISO channel. Gain of approximately 18 b/s/Hz with 4×4 MIMO channel over SISO channel is obtained. Additionally, we look at the capacity as a function of distance between Tx and Rx, minor changes in the capacity with increasing distance between the Tx and Rx are found, as shown in Fig. 7.14, where the distance from the Tx to Rx is between 85-100 m in Fig. 7.14(a) and is between 110-185 m in Fig. 7.14(c). Moreover, comparisons between blue, yellow curves indicate that the position of antennas plays an important role. The received power level can drop significantly if the antenna has a poor gain in the direction of the Tx, as shown in scenario B, which is the blue curves. Therefore, using multiple antennas that radiate towards different directions, as in the case of 4×4 MIMO, which is indicated using the green curves retains high capacity performance.

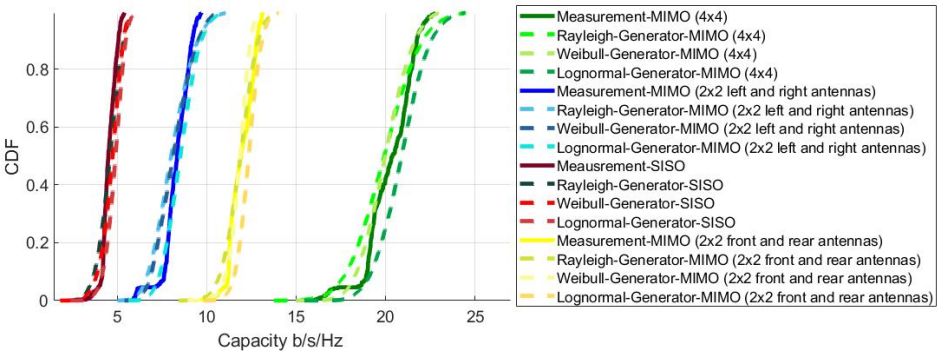

(a)

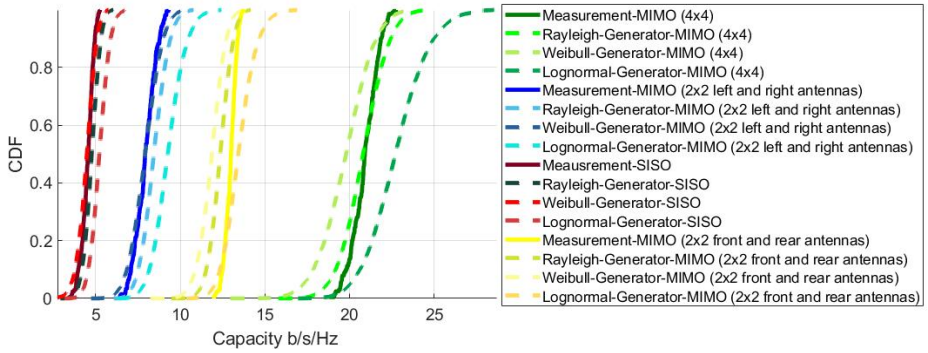

(b)

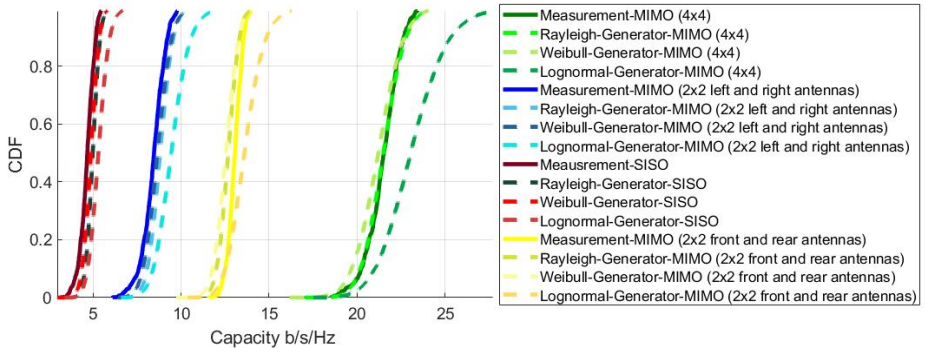

(c)

Fig. 7.14 CDF comparison of the channel capacity between the measurement data and generators in term of different number of antenna, the SNR fixed at 20 dB; MIMO models bring about a drastic increase in capacity by increasing the number of receive and transmit antennas; minor changes in the capacity observed with increasing distance between the Tx and Rx (the distance is between 85-185 m), (a) LOS, (b) NLOS1, (c) NLOS2

As presented in Section 7.2 and 7.3, the SNR plays a key role in determining the channel capacity. To explore the importance of the SNR and study the channel capacity in terms of different SNR values, simulations are carried out to estimate the channel capacity at SNR of -20, -10, 0, 5, 10, 15, 20, 25, 30, 40 dB and results for 10 dB and 25 dB are illustrated in Fig. 7.15.

The complementary cumulative distribution function (CCDF) of the channel capacity is given in Fig. 7.16 [4]. Due to a large number of results, here we present the results only for the Weibull generator

[4]CCDF is defined as the probability that X will take a value more than x, $\overline{\mathrm{F}}_X(x) = P(X > x) = 1 - F_x(x)$ [115].

under the NLOS1 scenario. From the figure, it can be seen that with increasing SNR, we can achieve more capacity gain. At SNR = 25 dB, there is 90% certainty that there is at least 24 b/s/Hz of capacity available from the MIMO channel, and at SNR = 10 dB, there is 90% certainty that there is more than 8 b/s/Hz of capacity available. The capacity of MIMO configuration is approximately four times the capacity of SISO. Additionally, Section E.2.1 provides the CDF of channel capacity for different SNR values, such as -20, -10, 0, 5, 8, 15, 20, 30, 40 dB. As can be seen, the capacity variation decreases significantly with increasing SNR.

Consequently, the following conclusions can be outlined, the channel capacity increases with the increase of the number of Tx-Rx antenna pairs. When SNR increases, the variation of channel capacity reduces. The capacity of MIMO system is approximately four times the capacity of the SISO system. Additionally, it is observed that the position of antennas plays an essential role in achieving high channel capacity performance.

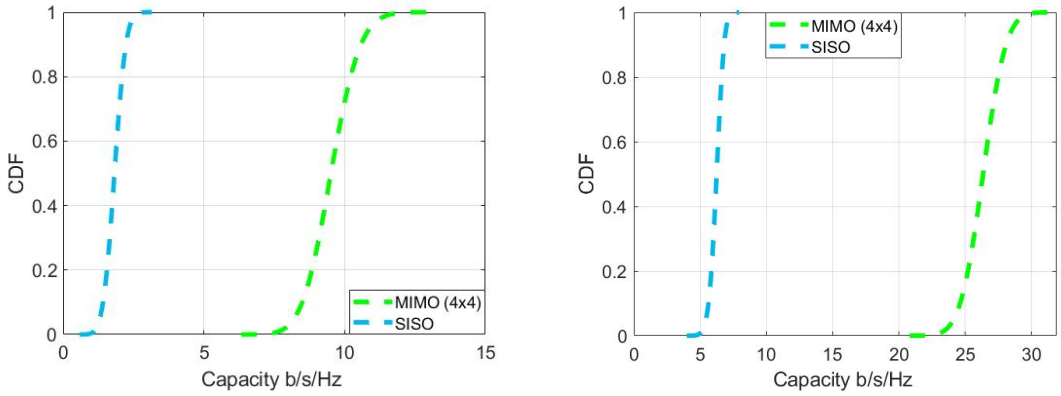

Fig. 7.15 CDF comparison of the channel capacity between SISO and MIMO cases, with increasing SNR capacity gain increases, (a) SNR = 10, (b) SNR = 25

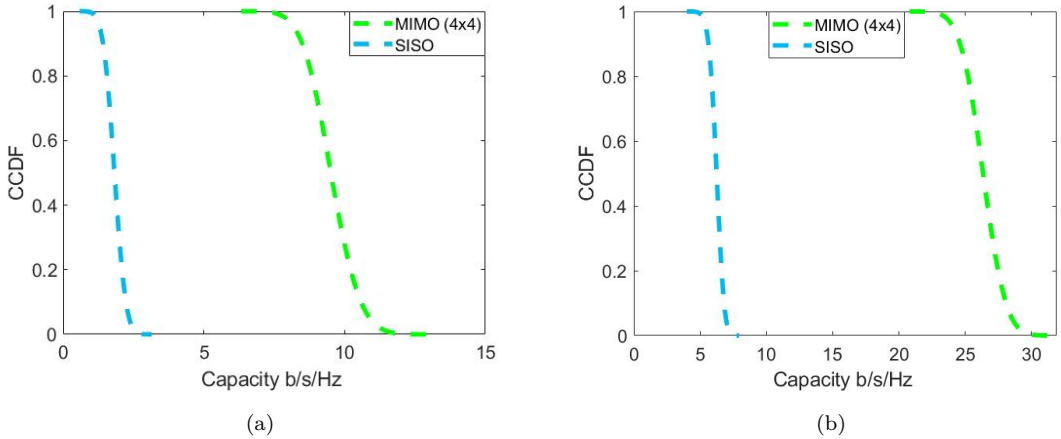

Fig. 7.16 CCDF comparison of the channel capacity between SISO and MIMO cases, (a) SNR = 10, (b) SNR = 25

7.6 Concluding Remarks

In this chapter, a method for extending a classical single input single output (SISO)-TDL model to multiple input multiple output (MIMO) under the non-WSSUS assumption was introduced to develop tapped delay line (TDL) channel models for vehicle to infrastructure (V2I) MIMO systems. An algorithm for selecting taps was presented, and the taps were selected at the peaks of the cumulative energy. The fading distribution of taps has been addressed. The results have been shown that a large number of taps follow the Weibull distribution. It was additionally observed that there is no correlation among the taps persistence process, on the other hand, there is a correlation between some of the taps amplitude in each channel, as well as among the channels under NLOS1 and NLOS2 scenarios. Regarding the LOS scenario, there is no correlation among the taps amplitudes.

The analysis evaluates SISO- with MIMO- configuration in terms of capacity and then results in terms of different numbers of antennas, and different values of signal to noise ratio (SNR) were investigated. The analysis shows that a drastic increase in capacity can be achieved by increasing the number of receive and transmit antennas. The capacity of the MIMO system is approximately four times the capacity of the SISO system. The channel capacity is directly proportional to SNR. Not only the channel capacity of MIMO systems increase linearly with the increase of SNR, but also the variation of channel capacity decreases. Moreover, we looked at the capacity as a function of distance, and from the results, minor changes in the capacity with increasing distance between the transmitter (Tx) and receiver (Rx) were found. Additionally, throughout this chapter, it has been observed that the position of antennas plays an important role, as the received power level can drop significantly if the antenna has a poor gain in the direction of the Tx. We conclude that using multiple antennas that radiate towards different directions, as in the case of 4×4 MIMO is important for V2I application. As a conclusion, in V2I communication systems, it is possible to make a qualitative leap by placing arrays of antennas on both sides of the system, and when a large SNR value is applied, we will achieve a higher capacity, consequently remarkable stability in the performance of the system.

The material of this chapter is partially presented in [63, 65].

Chapter 8

Conclusions and Outlook

8.1 Conclusions and Outlook

The promising potential of vehicle to X (V2X) communication systems to optimize traffic flow and drastically reduce car accidents has led to a rich body of research in this field. One of the fundamentals in the design of a communication system is the characterization of a channel. Throughout this investigation, it has been noted that communication systems design and deployment cannot be performed without an accurate knowledge of the underlying physical channel. The main goal of this thesis was to develop vehicle to infrastructure (V2I) channel models in a form of tapped delay line (TDL) model that could describe most of the propagation conditions in an urban area. The TDL model is one of the well-accepted models e.g., in the Third Generation Partnership Project (3GPP) and long term evolution (LTE) standards. The TDL model can be extended via Markov chains models to represent the non-wide sense stationary uncorrelated scattering (non-WSSUS) properties of the V2X channels. Markov chains are a proper choice for vehicular channel modeling because they offer the combination of statistical channels based on stochastic processes. This type of model is based on the probability of an event given another past event. The channel is then characterized through a certain number of states. In this thesis, non-stationary TDL models have been used to describe the V2I channels.

An algorithm for selecting taps for TDL models from measurement data was introduced. The proposed approach accurately captures the channels' statistics (e.g., statistical measures of root mean square delay spread (RMS-DS)); hence, our model is useful for communication systems design and deployment. The RMS-DS is the major factor in the performance of most digital communication systems, including the orthogonal frequency division multiplexing (OFDM) systems proposed for V2X communication systems. When the RMS-DS is greater than a guard interval, this leads to inter symbol interference (ISI) and degrades performance. In this case, individual symbols overlap with the following ones; as a result, transmission errors occur. Therefore, designers most often rely on RMS-DS, as it has been shown to be directly relatable to communication system performance. The proposed approach did not previously exist, which further motivated this work for wideband stochastic channel models for V2I communication systems.

TDL channel models at 20 MHz bandwidth are provided for all propagation regions encountered in the city of Cologne to describe the physical propagation conditions accurately. These models are developed to evaluate the performance of V2I communication systems that would be deployed in urban areas, and they can be used by researchers who investigate vehicular communication system design. One of the key

features presented for these models is modeling non-stationary behavior via an ON/OFF process using first-order two-state Markov chains. Numerical results and examples have been illustrated to clarify all algorithms that have been used.

8.1.1 Summary of Contributions and Further Details

This thesis provides several contributions. A summary of contributions is provided, and each is followed by further details.

- Statistical measures, e.g., mean RMS-DS were used to examine the differentiation between different scenarios such as line of sight (LOS) and non line of sight (NLOS).

  A raytracer tool has been used to detect different scenarios such as LOS and NLOS. After detecting all of the measurement points, three different scenarios (LOS, NLOS1, and NLOS2 [1]) existed in our measured data. Statistical measures such as mean RMS-DS and delay window (DW) were computed to examine the differentiation between those scenarios. For example, the mean RMS-DS was calculated for each measurement track in accordance with the scenario. Based on these results, it is concluded that three different groups can be distinguished. The statistical results of NLOS1 scenario indicated that they laid between LOS and NLOS2 scenarios. For those specific regions (NLOS1), a transmitted wave was attenuated by only one interaction; therefore, it had relatively large energy and smaller delay. Thus, the value of the mean RMS-DS was smaller than NLOS2, which was assumed to undergo more than one interaction. The RMS-DS value increased under NLOS2 and NLOS1 conditions, compared with LOS scenario, where the RMS-DS oscillated around 80 ns. Consequently, the RMS-DS and DW clearly showed a decrease as the receiver (Rx) entered the LOS region. Detection results in different regions from the raytracer and applied statistical measures showed a good match.

- A new strategy for extracting parameters for a TDL model was proposed.

  The new approach is a modification of an existing method, which has been proposed in [129]. The proposed approach [129] was applied to verify and compare to the extended model. The extended approach has improved the model with respect to the RMS-DS and number of taps. One of the limitations of channel emulators is that it is limited to emulating the number of propagation paths simultaneously; thus, it is important to find a proper approach to reduce the number of taps. A complete set of V2I TDL models for 20 MHz channel bandwidth has been extracted from measurement data. A complete description of the tap energies, tap amplitude statistics, tap correlation coefficient matrices have been derived. There are strong correlations among taps amplitudes, but the persistence process (PP) between different tap indices is uncorrelated. Additionally, each tap's transition probabilities and steady-state probabilities have been provided, which can be directly used in the channel simulation. In the LOS region, taps persist longer, and multipath delay dispersion is smaller than in NLOS1 and NLOS2 regions.

- An approach was proposed as a solution to verify the correctness of the channel model parameters derivation.

  An approach was discussed to evaluate the model outcome. First, the RMS-DS was determined for the measurement data (after the noise threshold and the multipath threshold (MT), 25 dB below

[1] Underlying different scenarios have been defined in Section 3.2

the main peak) using all possible taps. After that, the RMS-DS was calculated only for the tap indices where the models $M1$ and $M2$ would place an active tap. It has been determined that our proposed model $M2$ represents the channel with enhanced accuracy compared to model $M1$. Model $M2$ uses a smaller number of taps in all scenarios while retaining the delay spread performance. The taps are spread more widely over the cumulative energy; thus, low energy and large delay taps are selected, which are relevant to regenerating the RMS-DS. From the results, it was additionally observed that shifting the channel impulse response (CIR) based on the change in transmitter (Tx)- and Rx-distance is necessary to reduce the number of required taps. It has been demonstrated that model $M2$ is fairly accurate when representing the statistics of the measured channel, even when it does not accurately represent the actual channel taps when they are not resolvable.

- Devising a generator to produce channel impulse responses (CIRs) based on derived model parameters.

  Algorithms have been developed to generate multivariate Lognormal, Weibull, Rayleigh, and Rician random variables with derived fading parameters and correlations from measured data. Hence, the amplitudes of taps have been modeled as correlated Lognormal, Weibull, Rayleigh, and Rician variables. In order to capture the frequent ON/OFF behavior of multipath, the PP has been modeled via first-order two-state Markov chains. The results showed that the used Markov model needs to be extended to the higher order Markov model.

- The higher orders two-state Markov chains have been modeled with the aim of better capturing the non-stationary behavior.

  Second- and third-order two-state Markov models have been modeled but introduce simulation complexity. Different Markov models (first-, second-, and third-order two-state Markov model) were compared and evaluated in terms of their ability to represent various statistics. The results showed that the second- and third-order Markov models do not make significant effects or improvements. Therefore, to compromise between fidelity and implementation complexity, the first-order two-state Markov model is preferable to describe the non-stationary processes of the channel, and it matched well with the data. From the analysis, it was found that the persistence process between different tap indices was uncorrelated; accordingly, a correlated Markov model is not necessary.

- The amplitudes fading of active taps have been divided into two classes by separating the received signal in two scales of spatial variations, which are slow- and fast-variations to characterize slow- and fast-fading variations of each active tap.

  In Chapter 6, the amplitudes fading of active taps has been divided into two classes by separating the received signal in two scales of spatial variations, which are slow- and fast-variations. In total, nine various setups were studied. The variations in received signal strength between two antennas faced directly to each other and omnidirectional antennas follow Rice and Log-normal distributions for fast- and slow-fading, respectively. From the results, it was observed that when two antennas faced away from each other, a fitting error and histogram intersection between the empirical histogram and probability density function (PDF) fits of known distributions were approximately the same for all kinds of distributions; thus, a specific distribution was not selected for those scenarios. Moreover, environments with a large number of scatterers, such as in NLOS2 regions, lead to smaller quasi-stationarity intervals than regions under LOS conditions. It was discovered that when a LOS path

exists between Tx and Rx, individual multipath does not fade significantly; on the other hand, for higher indexed taps, deeper fading was observed as in the NLOS2 scenario.

- A method for extending a single input single output (SISO)-TDL model to multiple input multiple output (MIMO) under non-WSSUS assumption was introduced to develop TDL channel models for the V2I MIMO systems.

  In all of the above, SISO-TDL models were considered. A method for extending a classical SISO-TDL model to MIMO under the non-WSSUS assumption was introduced. Taps have been selected using the proposed approach $M2$. The fading distribution of taps has been addressed. It was observed that there is no correlation among the taps persistence process in all scenarios. On the other hand, low correlations exist between some of the taps amplitude in each channel and among channels under NLOS1 and NLOS2 conditions. Regarding the LOS scenario, there is no correlation among taps amplitudes. Observing such a low correlation between taps may be due to the antenna positions on the Tx and Rx [2].

- The analysis evaluated SISO- with MIMO-configuration in terms of channel capacity and then results of a different numbers of antennas and different values of signal to noise ratio (SNR) were investigated. Different MIMO configurations have been explored to investigate the role of antenna placement and then the capacity as a function of distance between Tx and Rx has been studied.

  The analysis investigates SISO- with MIMO-configuration in terms of channel capacity. Different MIMO configurations have been explored to investigate the role of antenna placement. Throughout the results, it has been observed that the position of antennas plays an important role; the received power level can drop significantly if the antenna has a poor gain in the direction of the Tx. The use of four antennas that radiate towards different directions can bring substantial performance gains, and the capacity was approximately four times the capacity of the SISO system. It is obvious that the channel capacity is directly proportional to SNR, not only the channel capacity increases linearly with the increase of SNR but also the variation of channel capacity decreases. Moreover, we have looked at the capacity as a function of distance between Tx and Rx. Minor changes in the capacity with increasing distance between the Tx and Rx were found.

To sum up, channel statistics have been analyzed in an urban city, and channel models were developed for a 20 MHz channel bandwidth. In this study, each measurement file has been examined separately and then based on different scenarios, the tracks have been merged into different data sets. The model specifies tap amplitude fading with its persistence process for modeling the appearance and disappearance of multipath. Both severe fading and multipath persistence arise in all measurement tracks; thus, the modeling techniques, which were presented here, may be applicable in other environments. The first-order two-state Markov model with the higher-order Markov model has been modeled to capture the non-stationary behavior of multipath. It was concluded that to compromise between fidelity and implementation complexity, the fast time-varying channel of V2I communications should be modeled via first-order two-state Markov chains. The received signal strength is stronger in the LOS regions, taps persist is longer, and multipath delay dispersion is smaller than in the NLOS1 and NLOS2 regions. Moreover, different MIMO configurations have been explored, and it was concluded that using multiple antennas that radiate towards different directions, as in the shown case of 4×4 MIMO, is important to make a qualitative leap in V2I applications. When a large SNR value is applied, it will achieve a higher

[2]The position of antennas has been illustrated in Section 7.5.

capacity and consequently remarkable stability in the performance of the system. Numerical results and examples have been illustrated to clarify all algorithms that have been used. The results presented in this thesis have implications for the purposes of performance evaluation and system design in V2I systems. Researchers or engineers who evaluate the performance of waveforms or systems can use the developed channel models, which are based upon both theory and measurements; thus, they are dual in sense.

8.1.2 Further Research Areas

In this section, based on the results, the various avenues for future research will be described. One of the research areas is the "drift" of multipath, which has been reported from several V2X measurements, as well as in measurement data [3], in which the delay of the tap changes over time and the tap moves from one delay bin to another. Based on our knowledge, in the existing TDL models, this is not tracked. Future research comprehends the incorporation of this "drift" effect into the considered models by using a segmentation approach, which has been proposed in Section E.2. Consequently, the model parameters such as power, delay, etc., will vary over time. Another extended focus should be the modeling of multipath transition, more measurement data need to be investigated to find whether repeating transitions exist or not and what are their causes. Moreover, incorporating the quasi-stationary region into a non-stationary channel appears to be of advantage; thus, the ON/OFF process will not be completely random. The main purpose of developing a stochastic channel model is to evaluate the system performance in real environments. A further research topic would be to evaluate the performance of different modulation waveforms such as OFDM under these stochastic channel models. Such a thorough evaluation would be of potential interest to members of industry and academia.

Throughout Chapter 5, it was observed that different types of distributions lead to different effects on the generator in terms of RMS-DS; therefore, it is important to study them and investigate their causes. Another future work could be applying the proposed model to other sets of measurement data to generalize the verification of the new approach or applying to the propagation conditions for highly dynamic vehicle to vehicle (V2V) channels. Furthermore, the measurement data were carried out in the summer season, from which those channel models have been developed, and accounting for different seasonal effects such as snow/rain during winter has not been considered. A research area, which has been widely ignored up to now, is to develop channel models for various seasons, which would then account for different seasonal effects. Another research following this thesis could be to determine the agreement between results of the presented stochastic models and the ray-tracing approach and how well they agree in terms of statistical measures. In addition to that studying another way to find different methods of modeling the non-stationary process in a way other than by multiplying the tap amplitude process with the persistence process. One idea might be to model the fading more compactly as a single non-stationary process, instead of separating amplitude tap fading and multipath persistence as two multiplicative processes. To achieve this, one possible approach might be the use of a fading process, whose statistics vary over time. This approach has already been discussed in E.2.

The use of MIMO is not only essential in recent wireless communication systems, but also is planned in future V2X communications. It is interesting to see how the time-varying MIMO-TDL model [4] would perform in terms of key parameters, e.g., channel capacity, and compared to our model. Another investigation could be investigating the influence of antennas and their placement on the car. For example, the antenna has difficulties "seeing" if it is placed on a backward-slanted roof.

[3] It has been illustrated in Fig. 4.7

[4] The proposed approach in Section E.2.

Chapter 9

Appendix

Appendices

Appendix A

Measurement Surroundings

A.1 Surrounding

This section is continuity of Section 3.3.

A.1.1 Measurement track 2-3

In this measurement track, the car that was traveled through a pedestrian area. Then, the car left a square over the street and then it drove toward the narrow crossroad, which is the end point of the track. The Figures can be seen via Google StreetView using latitude and longitude of the receiver (Rx) from Table A.1.

TABLE A.1
Description of surrounding environment for measurement track 2-3

Description of surrounding environment				
	Starting point		End of measurement track	
File name	Latitude Rx	Longitude Rx	Latitude Rx	Longitude Rx
Cologne_MT2-3	50.936451	6.953634	50.936343	6.956245

A.1.2 Measurement track 4-5

The measurement track 4-5 started directly on the same square, as the end point of measurement track 3-4, then the car drove through a street. Table A.2 gives the description of surrounding environment for measurement track 4-5.

TABLE A.2
Description of surrounding environment for measurement track 4-5

Description of surrounding environment				
	Starting point		End of measurement track	
File name	Latitude Rx	Longitude Rx	Latitude Rx	Longitude Rx
Cologne_MT4-5	50.937687	6.956308	50.939078	6.956366

A.1.3 Measurement track 8-9

In the starting point of track 8-9, the car drove through the street and then it turned to the left. Before entering the crossroad, the measurement track was ended. Forward and rear views of surrounding environment are given in Table A.3.

TABLE A.3
DESCRIPTION OF SURROUNDING ENVIRONMENT FOR MEASUREMENT TRACK 8-9

Description of surrounding environment				
	Starting point		End of measurement track	
File name	Latitude Rx	Longitude Rx	Latitude Rx	Longitude Rx
Cologne_MT8-9	50.936475	6.957999	50.936239	6.960055

A.1.4 Measurement track 15-16

The description of surrounding environment is given in Table A.4. It was started on a square besides a wide road. The car crossed two crossroads. Before the car was reaching a third crossroad, the measurement track was ended.

TABLE A.4
DESCRIPTION OF SURROUNDING ENVIRONMENT FOR MEASUREMENT TRACK 15-16

Description of surrounding environment				
	Starting point		End of measurement track	
File name	Latitude Rx	Longitude Rx	Latitude Rx	Longitude Rx
Cologne_MT15-16	50.935294	6.957241	50.936788	6.956926

A.1.5 Measurement track 16-17

The following track 16-17 started directly after track 15-16. The vehicle was traveled along a narrow street and then it passed by a large intersection. The measurement track ended before entering the crossroad. The Figures can be seen via Google StreetView using latitude and longitude of the Rx from Table A.5.

TABLE A.5
DESCRIPTION OF SURROUNDING ENVIRONMENT FOR MEASUREMENT TRACK 16-17

Description of surrounding environment				
	Starting point		End of measurement track	
File name	Latitude Rx	Longitude Rx	Latitude Rx	Longitude Rx
Cologne_MT16-17	50.936789	6.956926	50.937614	6.956866

A.1.6 Measurement track 17-18

This measurement track follows the previous track 16-17 directly. The starting point of track 17-18 was at the crossroad and then driving through a street and after traveling through the street, an intersection on the right hand side occurred. The car continued to drive through a narrow street and this measurement track was ended in the middle of the narrow street. The Figures can be seen via Google StreetView using latitude and longitude of the Rx from Table A.6.

TABLE A.6
DESCRIPTION OF SURROUNDING ENVIRONMENT FOR MEASUREMENT TRACK 17-18

Description of surrounding environment				
	Starting point		End of measurement track	
File name	Latitude Rx	Longitude Rx	Latitude Rx	Longitude Rx
Cologne_MT17-18	50.937615	6.956866	50.939037	6.956834

A.1.7 Measurement track 31-32

A starting point of this track was on the crossroad and it kept following the wide street. The car traveled along the wide street. While the car drove along the street, it went over another crossroad. Then, the track followed the street and it has been ended before entering another crossroad. The Figures can be seen using the description of surrounding environment in Table A.7.

TABLE A.7
DESCRIPTION OF SURROUNDING ENVIRONMENT FOR MEASUREMENT TRACK 31-32

Description of surrounding environment				
	Starting point		End of measurement track	
File name	Latitude Rx	Longitude Rx	Latitude Rx	Longitude Rx
Cologne_MT31-32	50.938271	6.953287	50.9402	6.953323

A.1.8 Measurement track 33-34

The measurement track 33-34 was started after the car turning right the crossroad. The car drove along a street, then it traveled by an intersection. At the end of the road, this measurement track was stopped. Table A.8 gives the description of surrounding environment for measurement track 33-34.

TABLE A.8
DESCRIPTION OF SURROUNDING ENVIRONMENT FOR MEASUREMENT TRACK 33-34

Description of surrounding environment				
	Starting point		End of measurement track	
File name	Latitude Rx	Longitude Rx	Latitude Rx	Longitude Rx
Cologne_MT33-34	50.940229	6.95361	50.940157	6.955467

Appendix B

SISO-TDL Model Parameter Estimation Results

B.1 A Steady-State Probability of Active Taps Being ON

Fig. B.1 shows the steady state probability of state ON (SS_1) versus active tap index. In both models, the $SS1$ is higher under LOS condition compared to other scenarios. Nevertheless, only the outcome of $M2$ provides similar representation (the SS_1 decreases as the tap index increases) as we have seen in the measurement data that is shown in Fig. 4.4(b).

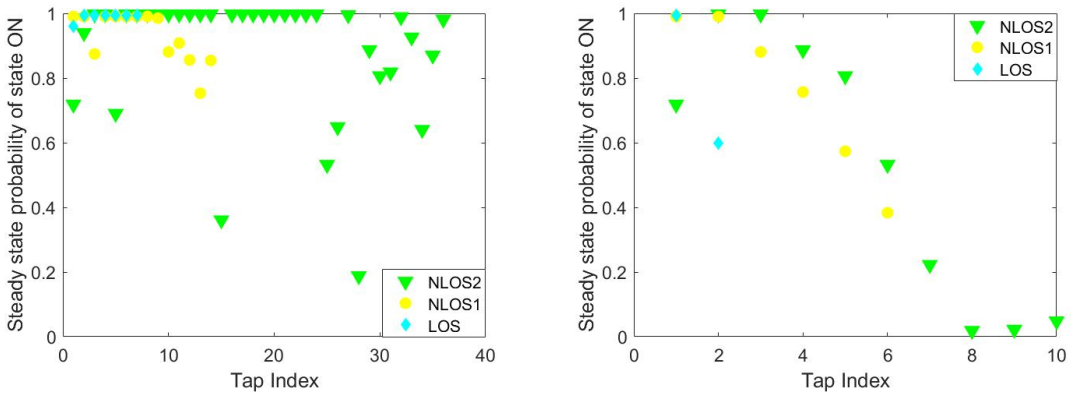

Fig. B.1 A steady-state probability of active taps being ON track number 24 →25 (a) in $M1$ (b) in $M2$

B.2 Amplitude Fading of the Active Taps

Fading tap amplitudes has been addressed in Section 4.4. Fig. B.2 and B.3 provide the empirical histogram and the probability density function (PDF) curves for the first and second taps amplitude under three different scenarios (under LOS condition, we only have one tap).

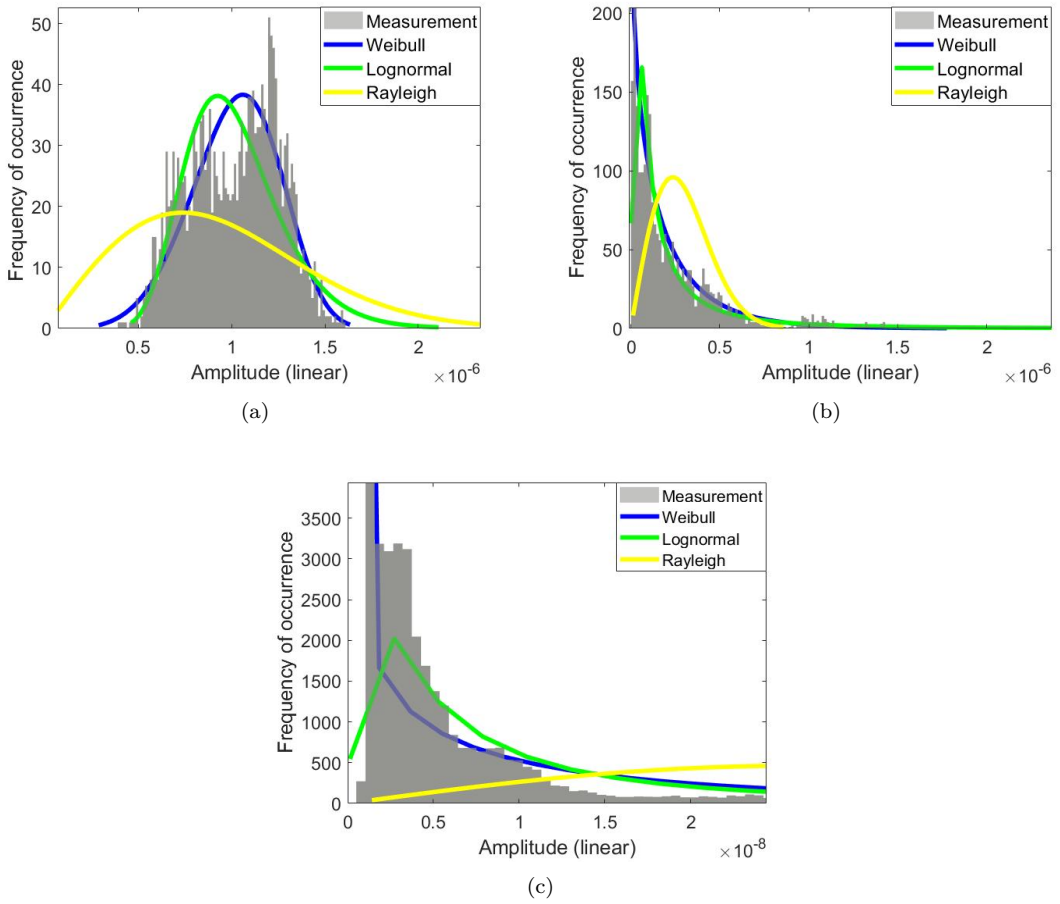

Fig. B.2 Histogram for the first tap, the log-normal distribution shows a better match between the PDF and the empirical histogram, (a) under LOS condition, (b) under NLOS1 condition, (c) under NLOS2 condition

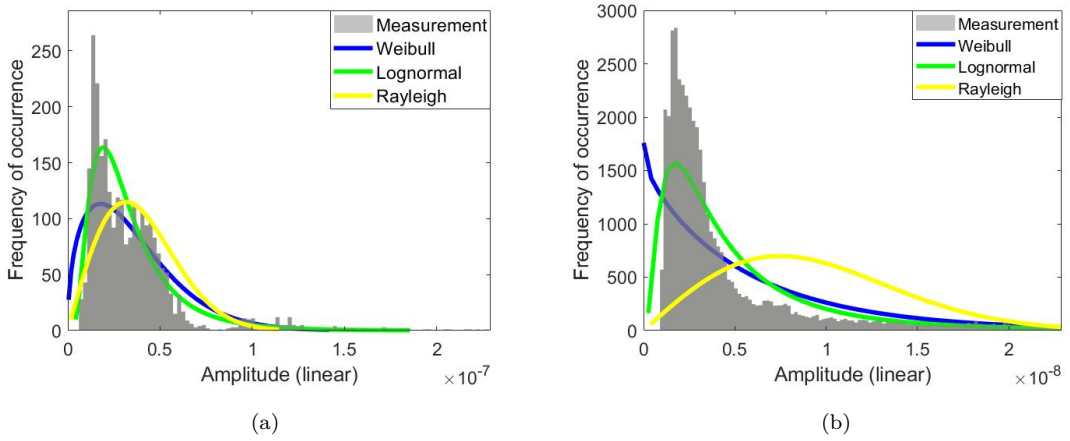

Fig. B.3 Histogram for the second tap, the log-normal distribution shows a better match between the PDF and the empirical histogram, (a) under NLOS1 condition, (b) under NLOS2 condition

Appendix C

Higher orders Markov modeling of Persistence Process

C.1 Results of Higher orders Markov modeling of Persistence Process

In this section, different order Markov chains models is illustrated for Weibull-, Rayleigh-generator. As it can been seen, the root mean square delay spread (RMS-DS) of third order Markov model, who is denoted by a gray curve is closer to the RMS-DS of estimated persistence process (PP) from measurement data.

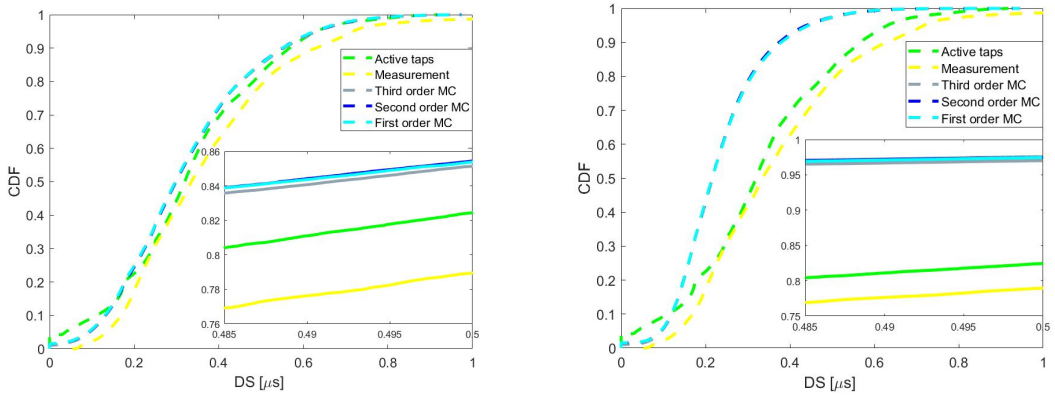

(a) (b)

Fig. C.1 Delay spread comparison with respect to high order Markov model under NLOS2 scenario, the RMS-DS of third order Markov model, who is denoted by a gray curve is closer to the RMS-DS of estimated PP, which is depicted by a green/yellow curve (a) Weibull generator, (b) Rayleigh generator

Appendix D

Characterization of Slow and Fast Fading of the Active Taps

D.1 Separating Slow- and Fast-Fading

D.1.1 Omnidirectional Antenna

D.1.1.1 LOS Scenario

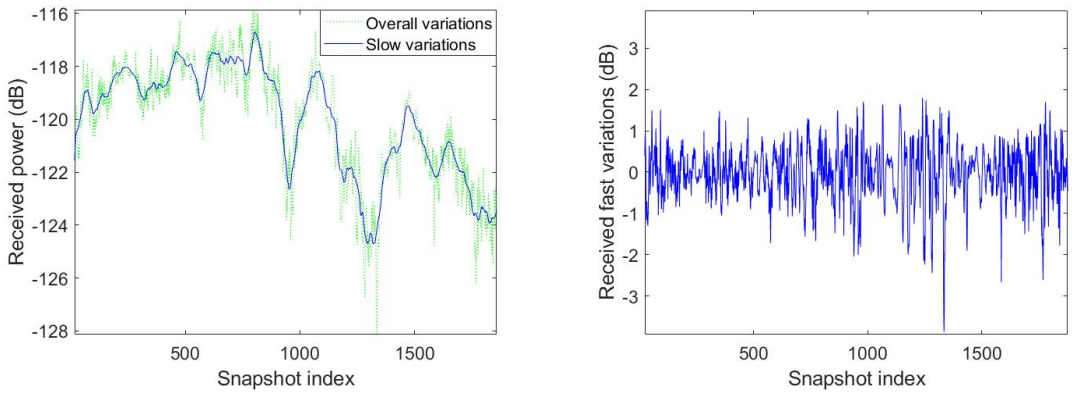

(a) (b)

Fig. D.1 Magnitude of the first tap under LOS condition-omnidirectional antenna, (a) Overall and slow variations, (b) Fast variations after removing the slow variations

D.1.1.2 NLOS2 Scenario

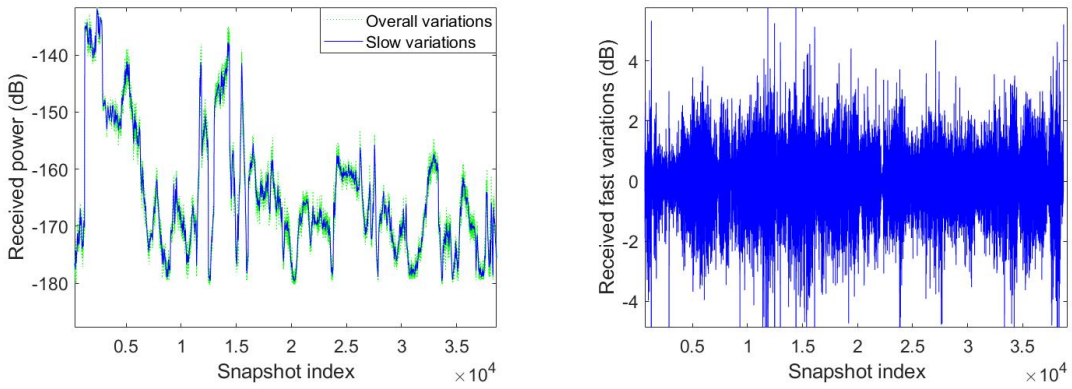

(a) (b)

Fig. D.2 Magnitude of the first tap under NLOS2 condition-omnidirectional antenna (a) Overall and slow variations (b) Fast variations after removing the slow variations

D.2 Model Based Evaluation

As explained in Section 6.3.3, to verify the robustness of the approach Weibull plus Log-normal are combined (which means the time-varying amplitudes with their corresponding distributions is generated to consider the slow and fast signal variations). The same proposed approach as in Section 6.3.2 is applied to separate the slow- and fast-variations. The implementation of the model with its results are illustrated in Fig. D.3.

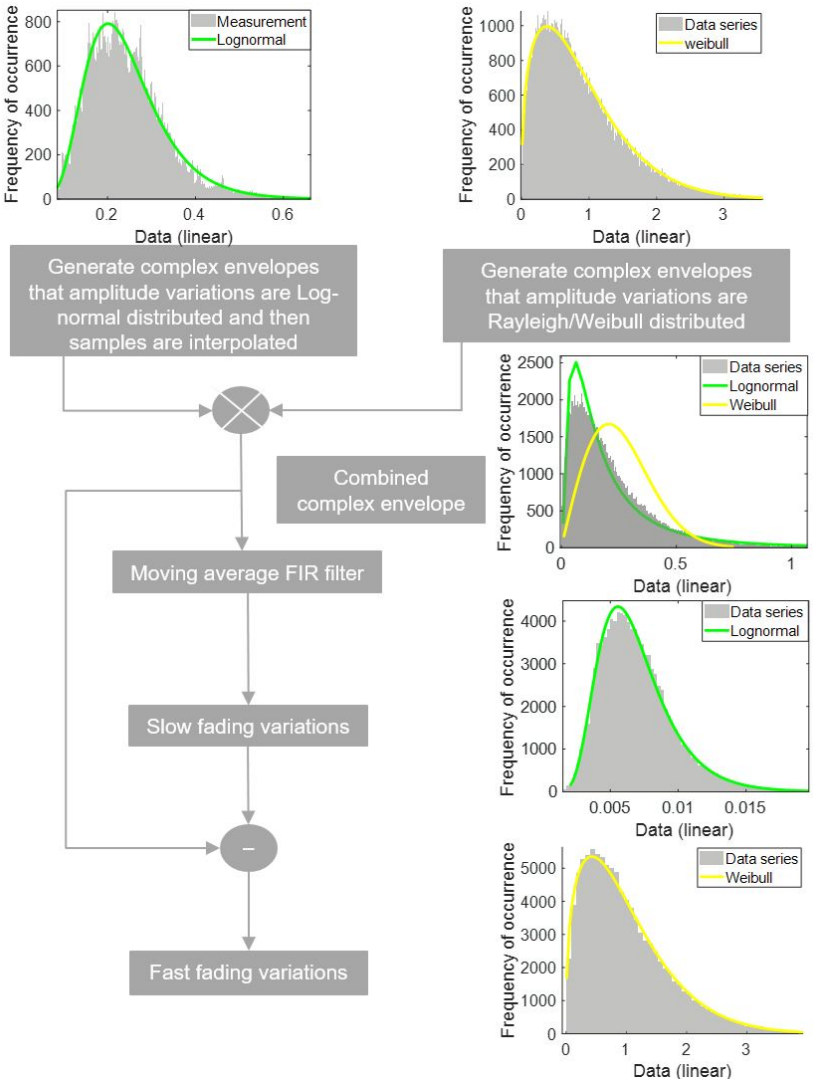

Fig. D.3 Block diagram of separating slow and fast fading variation

D.3 Amplitude Fading of the Active Taps

This section provides some examples of the empirical histogram of slow- and fast-fading with selected fitting curves.

D.3.1 Omnidirectional Antenna

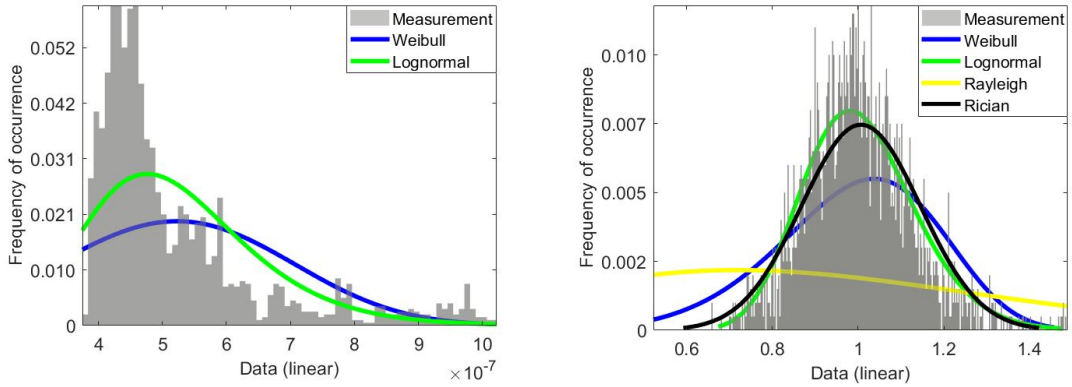

(a) (b)

Fig. D.4 Histograms and pdf fits for the Second tap under LOS condition-omnidirectional antenna, the Log-normal and Rice-distribution are the closest to the empirical histogram of slow- and fast-variations, respectively, (a) Slow variations, (b) Fast variations

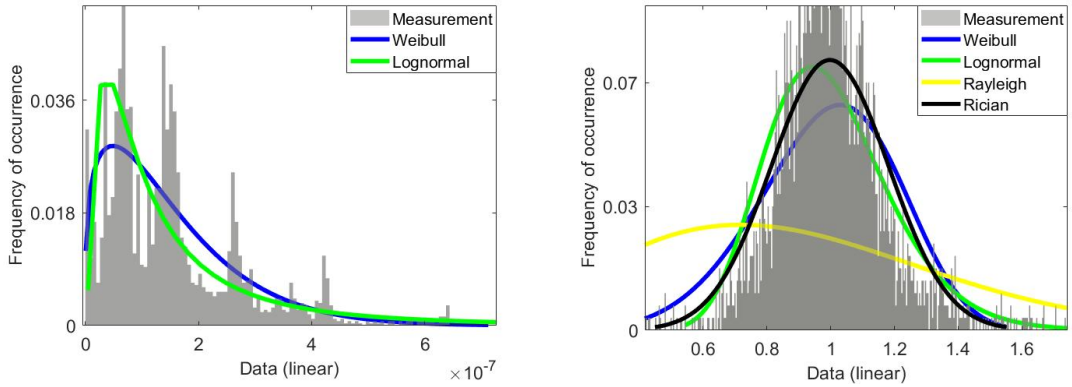

(a) (b)

Fig. D.5 Histograms and pdf fits for the Second tap under NLOS1 condition-omnidirectional antenna, the Log-normal and Rice-distribution are the closest to the empirical histogram of slow- and fast-variations, respectively, (a) Slow variations, (b) Fast variations

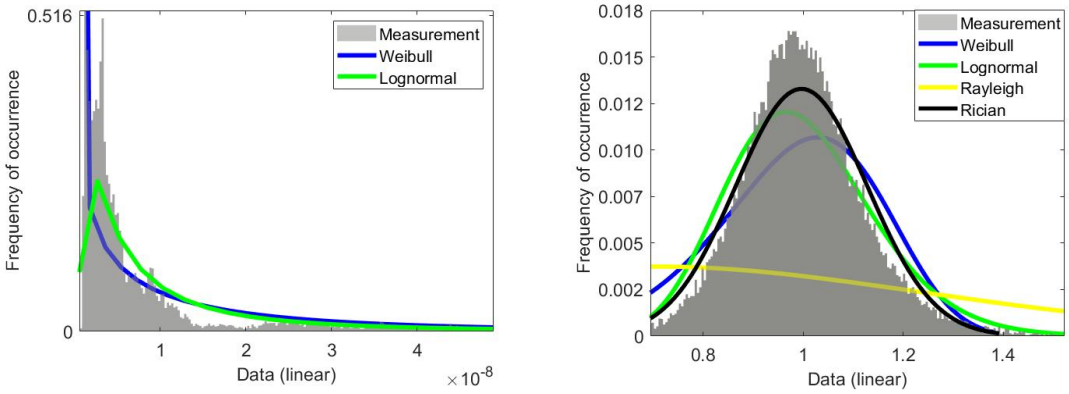

(a) (b)

Fig. D.6 Histograms and pdf fits for the first tap under NLOS2 condition-omnidirectional antenna, the Log-normal and Rice-distribution are the closest to the empirical histogram of slow- and fast-variations, respectively, (a) Slow variations, (b) Fast variations

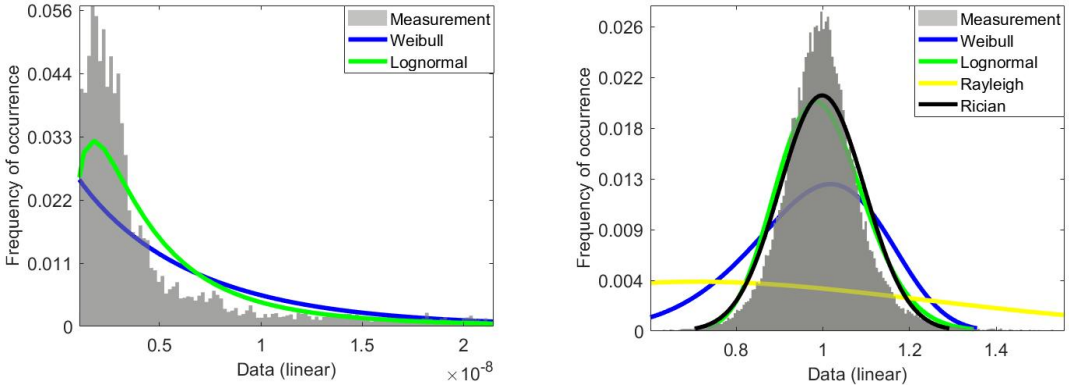

(a) (b)

Fig. D.7 Histograms and pdf fits for the Second tap under NLOS2 condition-omnidirectional antenna, the Log-normal and Rice-distribution are the closest to the empirical histogram of slow- and fast-variations, respectively, (a) Slow variations, (b) Fast variations

D.3.2 Two Antennas Faced Directly to Each Other

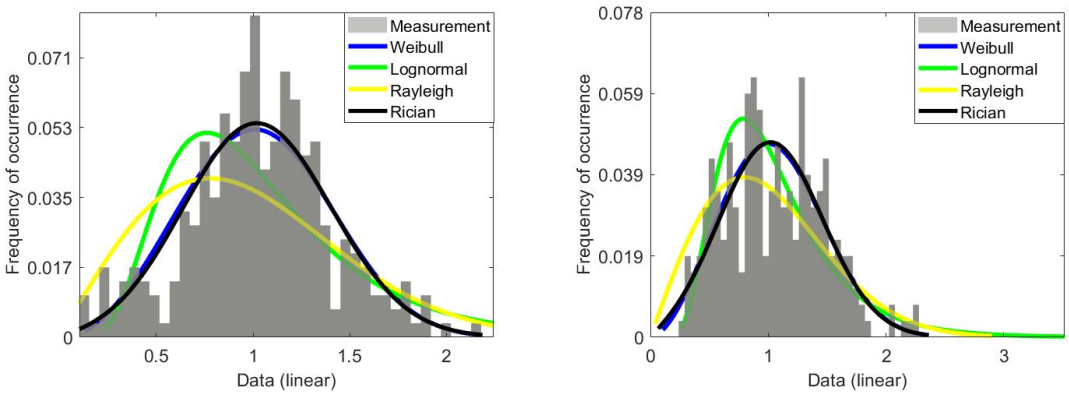

(a) (b)

Fig. D.8 Histograms and pdf fits of fast fading variations under LOS condition-two antenna faced each other, Rice-distribution are the closest to the empirical histogram, (a) First tap, (b) Second tap

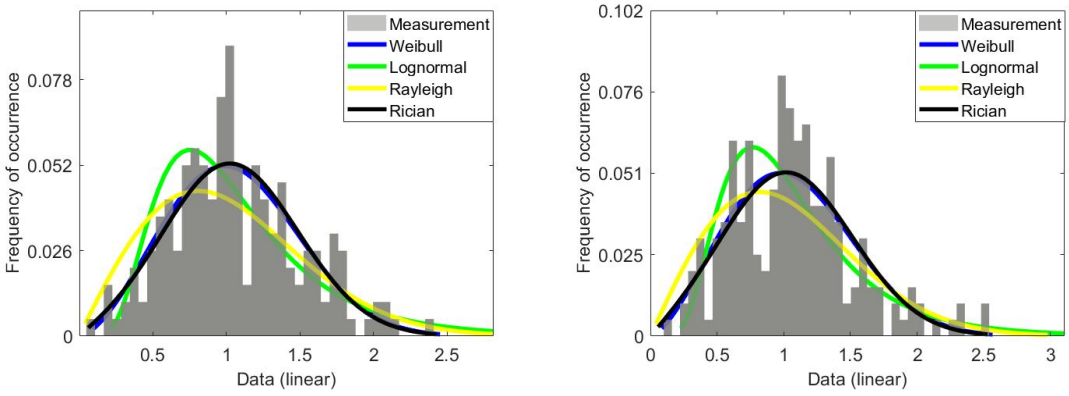

(a) (b)

Fig. D.9 Histograms and pdf fits of fast fading variations under NLOS1 condition-two antenna faced each other, Weibull-distribution are the closest to the empirical histogram, (a) First tap, (b) Second tap

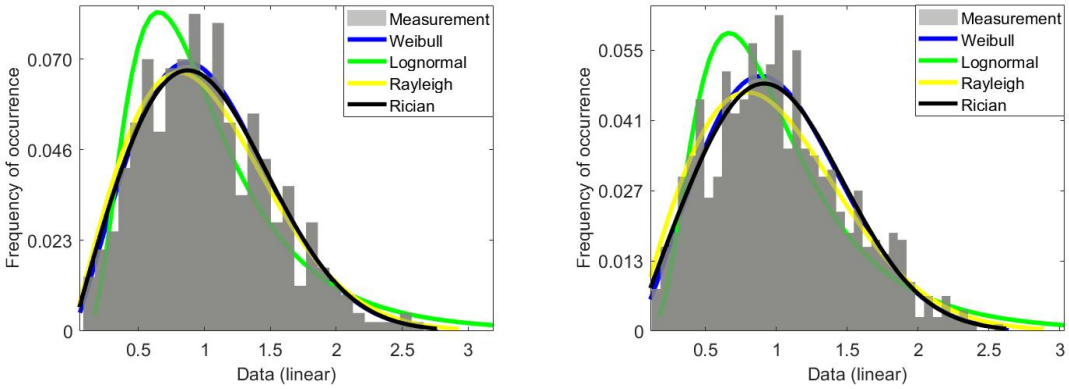

(a) (b)

Fig. D.10 Histograms and pdf fits of fast fading variations under NLOS2 condition-two antenna faced each other, Weibull-distribution are the closest to the empirical histogram, (a) First tap, (b) Second tap

D.3.3 Two Antennas Faced Away from Each Other

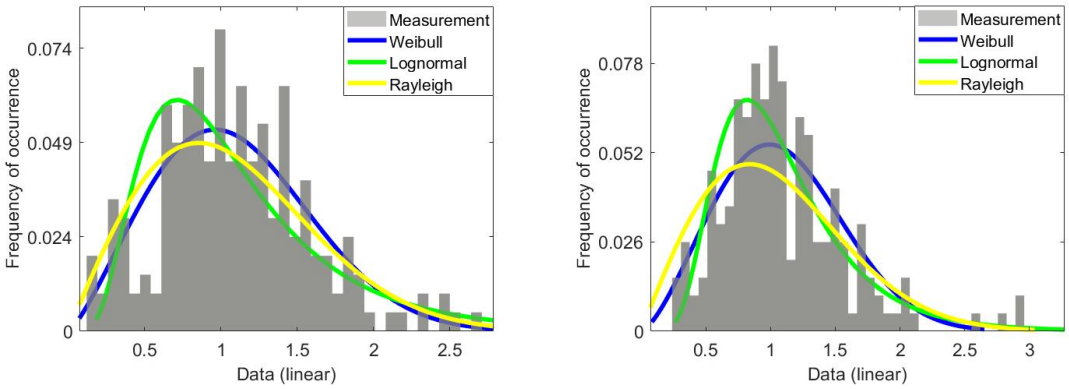

(a) (b)

Fig. D.11 Histograms and pdf fits of fast fading variations under NLOS1 condition-two antenna faced away from each other, a fitting error of fast-variations of the received signal is almost same for known distributions, (a) First tap, (b) Fourth tap

Appendix E

MIMO-TDL Model

E.1 Processing of the Measurement Data

E.1.1 Fading Statistics of the Active Taps

This section illustrates some more graphs of amplitude fading statistic.

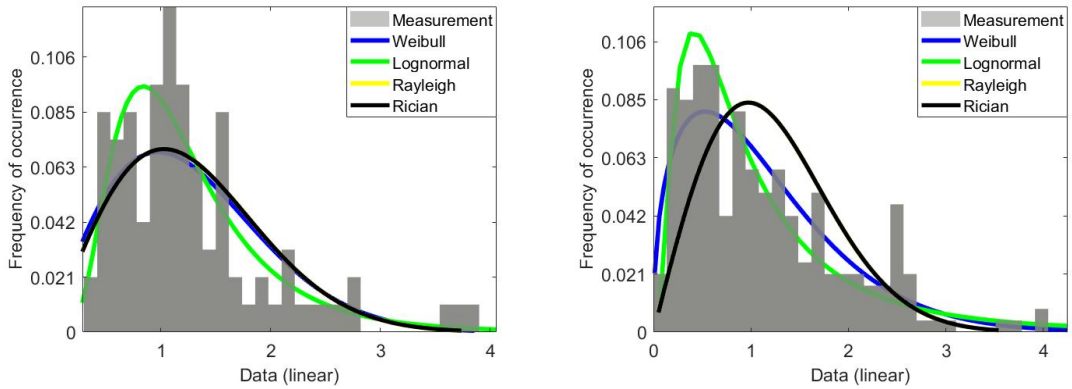

Fig. E.1 Amplitude fading statistic of second tap in LOS scenario, Rice-distribution are the closest to the empirical histogram, (a) Between Tx-1 and Rx-1, (b) Between Tx-2 and Rx-2

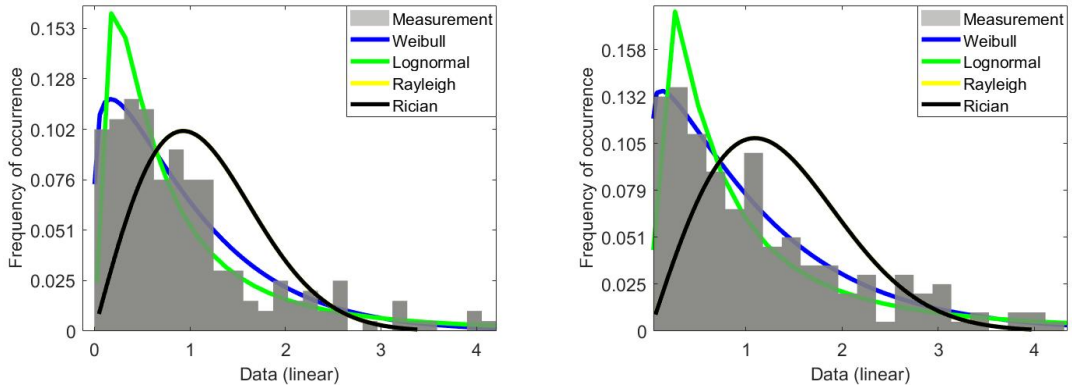

(a) (b)

Fig. E.2 Amplitude fading statistic in NLOS1 scenario, Weibull-distribution are the closest to the empirical histogram, (a) First tap between Tx-2 and Rx-2, (b) Second tap between Tx-1 and Rx-1

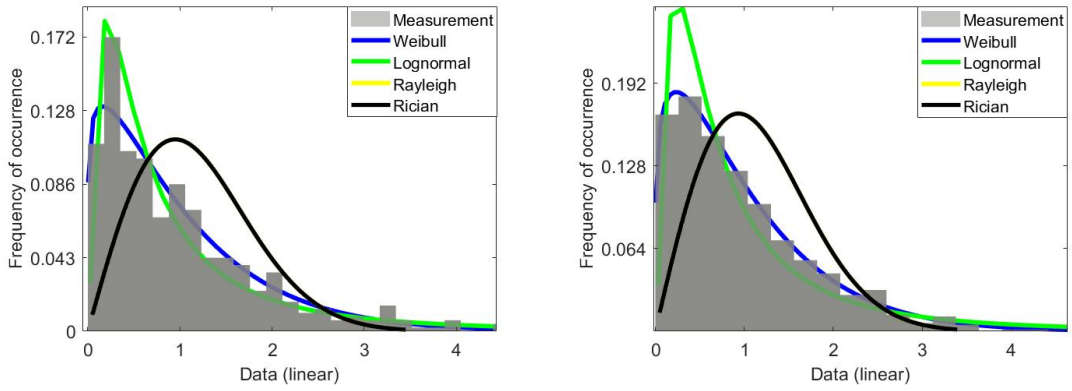

(a) (b)

Fig. E.3 Amplitude fading statistic in NLOS2 scenario, (a) Second tap between Tx-1 and Rx-1, Weibull-distribution are the closest to the empirical histogram, (b) Second tap between Tx-2 and Rx-2

E.2 Time-Varying MIMO-TDL Model

This Section provides another contribution, which is a modeling method to develop a time-varying multiple input multiple output (MIMO)-tapped delay line (TDL) model, whose parameters (such as power, delay, etc.) vary over time. To achieve this, a segmentation approach is taken. The whole set of measured channel impulse response (CIR) is segmented based on the quasi-stationarity intervals (outcome from Section 7.4.1), and for each segment, a unique TDL model is derived. From there, we able to track active taps. Hence, the resulted model is much more complex than our previous approach because the length of segments of each scenario (e.g., LOS, NLOS1, and NLOS2) are different, as well as each scenario also has different numbers of segments.

Briefly, the whole set of measured CIR is divided into N_i subsets. The length of each subset (N_i) is equal to w, which has been obtained in Section 7.4.1. As assumed previously, the measured CIR is expressed as $h(s, \tau, M, N)$. In this step, for each subset of N_i, we get a matrix as $h(N_i, \tau, M, N, N_a)$.

Where N_i is the length of the subsets and N_a is the number of subsets.

For each subset of N_i, we first select the taps using the same algorithm as considered in Section 7.4. Hence, the outcome of each subset will be a matrix as $h(N_i, P', \tau_{P'}, M, N, N_a)$, where P' is the selected taps, and $\tau_{P'}$ is the delays corresponding to the selected active taps. Consequently, the taps are sub-selected in each subset and then their parameters are derived from measured data. Consider an example and choose one of the subsets of N_i and then the delay of the taps is derived at the peaks of the cumulative energy; therefore, we know the location of the taps in the CIR; thus, all essential parameters can be derived. Then, the correlation coefficients between the taps and taps persistence processes can be obtained for each segment. The amplitude distribution of each tap can be addressed and studied among each subset using a similar method, as illustrated in Section 7.4.3. Consequently, the model parameters vary over time.

E.2.1 Analysis of MIMO Channel Capacity

This section presents the cumulative distribution function (CDF) comparison of the channel capacity between SISO and MIMO setup for different signal to noise ratio (SNR) values.

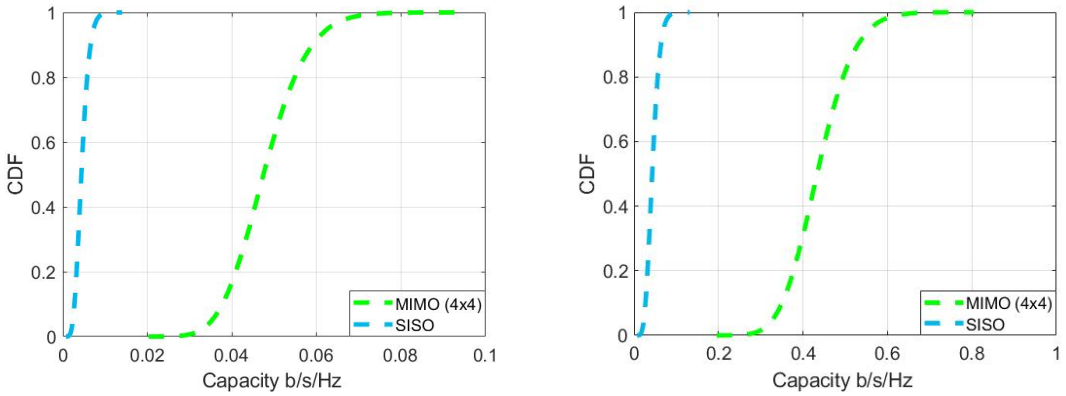

(a) (b)

Fig. E.4 CDF comparison of the channel capacity between SISO and MIMO cases, (a) SNR = -20 dB, (b) SNR = -10 dB

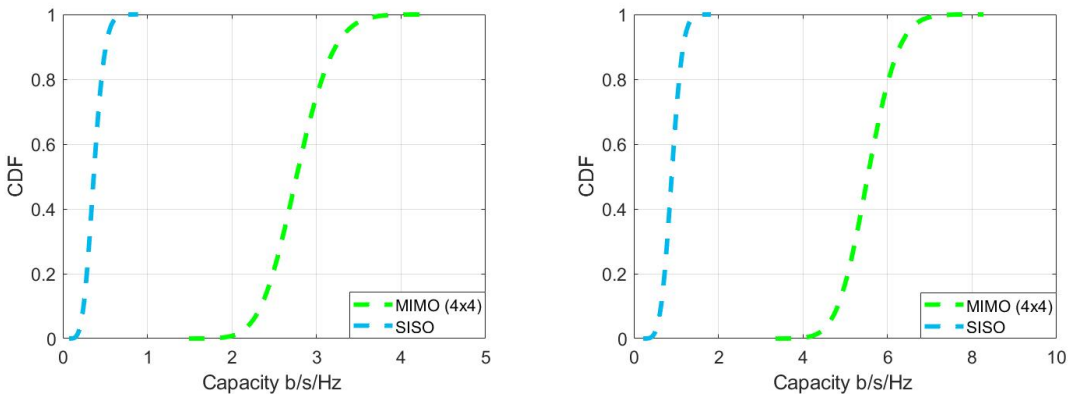

(a) (b)

Fig. E.5 CDF comparison of the channel capacity between SISO and MIMO cases, (a) SNR = 0 dB, (b) SNR = 5 dB

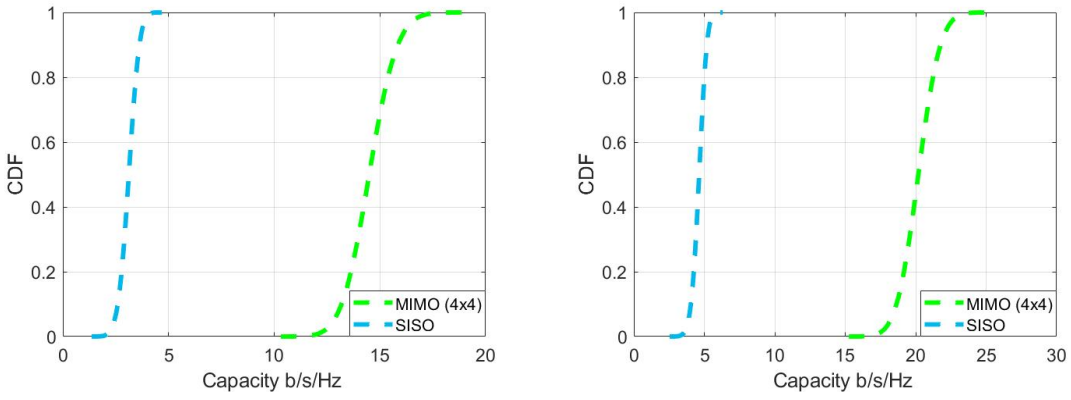

(a) (b)

Fig. E.6 CDF comparison of the channel capacity between SISO and MIMO cases, (a) SNR = 15 dB, (b) SNR = 20 dB

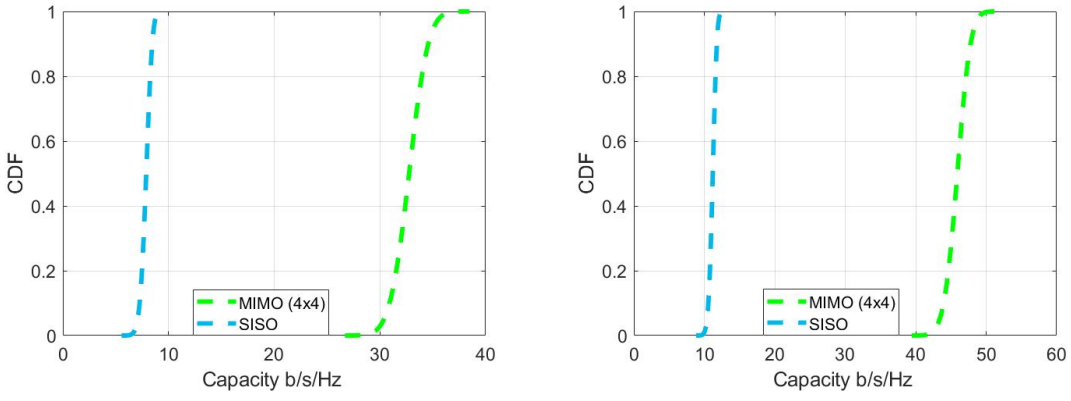

(a) (b)

Fig. E.7 CDF comparison of the channel capacity between SISO and MIMO cases, (a) SNR = 30 dB, (b) SNR = 40 dB

List of Figures

List of Tables

Acronyms

3GPP Third Generation Partnership Project. 25, 106

AWGN additive white Gaussian noise. 73

B bandwidth. 3

Bc coherence bandwidth. 13

BER bit error rate. 74

BS base station. 77

CCDF complementary cumulative distribution function. 103

CDF cumulative distribution function. 50, 62, 63, 65, 101, 104, 128

CIR channel impulse response. 3, 5, 6, 8, 14, 15, 17, 18, 20, 22, 23, 25, 27, 34, 36, 37, 38, 41, 42, 44, 48, 51, 56, 59, 64, 72, 78, 79, 91, 108, 127, 128, 130, 131

CIRs channel impulse responses. iii, 42, 108

DW delay window. 6, 34, 35, 107

FFT fast Fourier transform. 44

GBDMs geometry based deterministic models. 3

GBSM geometry based stochastic model. 3

GBSMs geometry based stochastic models. 3

GPS global positioning system. 1, 30

GSCMs geometry based stochastic channel models. 25

GSM global system for mobiles. 4, 26

HI histogram intersection. 52, 53, 54, 61, 82, 95, 134

ISI inter symbol interference. 5, 37, 73, 106

ITS intelligent transport systems. 3

LOS line of sight. 6, 15, 33, 48, 49, 75, 77, 78, 84, 90, 95, 96, 107, 108, 109, 132

LTE long term evolution. 4, 25, 106

LTE-V long term evolution-vehicle. 4

LTI linear time-invariant. 15

LTV linear time-variant. 15

MIMO multiple input multiple output. iii, v, vi, 5, 7, 8, 25, 27, 28, 86, 87, 88, 90, 91, 98, 100, 102, 103, 104, 105, 109, 110, 127

MISO multiple input single output. 91

MPCs multipath components. 11, 20, 53

MT multipath threshold. 38, 39, 107, 130

NGSM non-geometrical stochastic model. 3

NGSMs non-geometrical stochastic models. 3

NLOS non line of sight. 6, 75, 77, 78, 107, 132

non-US non-uncorrelated scattering. 4

non-WSS non-wide sense stationary. 4

non-WSSUS non-wide sense stationary uncorrelated scattering. iii, v, 3, 4, 5, 6, 7, 106, 109

OFDM orthogonal frequency division multiplexing. 5, 37, 106, 110

PDF probability density function. 52, 53, 63, 81, 82, 84, 95, 108, 116, 117, 132

PDP power delay profile. 26, 34, 36, 37, 38, 39, 44, 73, 78, 92, 130, 139

PP persistence process. 22, 23, 38, 39, 40, 42, 44, 46, 47, 48, 54, 55, 56, 59, 60, 61, 64, 65, 66, 67, 68, 69, 70, 72, 92, 96, 107, 108, 118, 130, 131, 139

QoS quality of service. 90

RF radio frequency. 27

RMS-DS root mean square delay spread. iii, v, 5, 6, 34, 35, 37, 41, 46, 47, 48, 49, 50, 51, 59, 65, 66, 67, 70, 71, 72, 92, 106, 107, 108, 110, 118, 130, 131, 139

Rx receiver. iii, vi, 1, 3, 4, 8, 10, 11, 12, 15, 16, 17, 18, 20, 21, 22, 25, 27, 28, 29, 30, 32, 38, 41, 42, 43, 50, 51, 54, 73, 74, 75, 77, 78, 82, 84, 88, 91, 92, 96, 98, 100, 101, 102, 103, 104, 105, 107, 108, 109, 113, 114, 130, 139, 140

SIMO single input multiple output. 91

SISO single input single output. iii, v, vi, 5, 7, 8, 11, 12, 25, 27, 36, 86, 87, 90, 91, 100, 101, 102, 104, 105, 109

SNR signal to noise ratio. 3, 7, 86, 89, 100, 102, 103, 104, 105, 109, 128, 129, 133

SPUCA stacked polarized uniform circular array. 28, 29

SVD singular value decomposition. 88

TDL tapped delay line. iii, v, 3, 4, 5, 6, 7, 8, 25, 26, 36, 37, 41, 53, 56, 57, 59, 60, 65, 78, 86, 105, 106, 107, 109, 110, 127

TDoA time-delay of arrival. 10

Tx transmitter. iii, vi, 1, 3, 8, 10, 11, 12, 15, 18, 20, 25, 27, 28, 29, 30, 33, 38, 41, 42, 43, 50, 51, 73, 74, 75, 77, 78, 82, 84, 88, 91, 92, 96, 98, 100, 101, 102, 103, 104, 105, 108, 109, 130, 139, 140

UMTS universal mobile telecommunications system. 4, 26

US uncorrelated scattering. 19, 53

V2I vehicle to infrastructure. iii, v, 1, 3, 4, 5, 7, 8, 24, 28, 59, 60, 73, 86, 105, 106, 107, 109, 110

V2N Vehicle to Network. 1

V2P vehicle to pedestrian. 1

V2V vehicle to vehicle. 1, 4, 26, 60, 110

V2X vehicle to X. iii, v, 1, 3, 4, 5, 6, 8, 15, 20, 21, 23, 26, 36, 37, 41, 64, 75, 86, 106, 110

WINNER Wireless World Initiative New Radio. 25

WSS wide sense stationary. 19

WSSUS wide sense stationary uncorrelated scattering. 4, 18, 19, 20, 26, 36, 37, 60

List of Symbols

List of Frequently Used Symbols will be provided in this section

Symbol	Description
φ_T	Azimuth of departure (Tx)
φ_R	Azimuth of arrival (Rx)
θ_T	Elevation of Departure (Tx)
θ_R	Elevation of Arrival (Rx)
γ	complex path weights
τ	time-delay of arrival
f_c	carrier frequency
c	speed of light
δ	dirac delta function
γ_p	complex amplitude of the p^{th} multipath
τ_p	p^{th} multipath delay
α_p	p^{th} multipath Doppler shift
z_p	binary vector that determines whether tap p is currently switched ON or OFF
P_{01}	probability of going from state-OFF to -ON
P_{00}	probability of going from state-OFF to -OFF
P_{10}	probability of going from state-ON to -OFF
P_{11}	probability of going from state-ON to -ON
TS	transition-state matrix
SS	steady-state matrix
SS_1	"steady-state probability" associated with the ON state
SS_0	"steady-state probability" associated with the OFF state
N_T	numbers of transmitting antennas
N_R	numbers of receiving antennas

Symbol	Description
μ_{τ_k}	power weighted average delay of the k^{th} snapshot
σ_{τ_k}	RMS-DS of the k^{th} snapshot
P_k	PDP of the k^{th} snapshot
n_{01}	number of occurrences of a transition from state OFF to ON
n_{00}	number of occurrences of a transition from state OFF to OFF
n_{10}	number of occurrences of a transition from state ON to OFF
E_p^{ON}	average "ON" energy of p^{th} tap
E_p^k	valid energy of p^{th} tap in the k^{th} snapshot
P_p^k	power of the p^{th} tap in the k^{th} snapshot
z_p^k	PP of the p^{th} tap in the k^{th} snapshot
$C_{\mathrm{E}p}$	cumulative energy of the p^{th} tap
SS_{1p}	"steady-state probability" associated with the ON state of the p^{th} tap
Δd_{H}	Haversine distance
ϕ_1	latitude of Tx
ϕ_2	latitude of Rx
λ_1	longitude of Tx
λ_2	longitude of Rx
ΔD	distance between the Tx and Rx antennas
ΔH	difference between the Tx and Rx antenna height
$\Delta\tau$	LOS delay
f_{Dmax}	maximum Doppler shift
v	speed of Rx
θ	angle of the Tx with respect to the Rx
$\sigma_{\mathrm{Rayleigh}}$ / σ_R	scale parameter of Rayleigh distribution
β_{Weibull} / β	shape factor of Weibull distribution
a_{Weibull} / a	scale parameter of Weibull distribution
$\mu_{\mathrm{Lognormal}}$ / μ	mean value of the log-normal distribution
$\sigma_{\mathrm{Lognormal}}$ / σ	standard deviation of the log-normal distribution
$\rho_{i,j}$	correlation coefficient between tap i and j
$c_{i,j}$	correlation coefficient between persistence processes among tap i and j

Symbol	Description
m	mean value
s	standard deviation
r	uniformly distributed pseudo-random number
λ	wavelength
d	distance between the Tx and Rx
r_t	overall variations of the received signal
r_s	slow- or long-term variations of the received signal
r_f	fast- or short-term variations of the received signal
R_t	overall variations of the received signal in dB scale
R_s	slow- or long-term variations of the received signal in dB scale
R_f	fast- or short-term variations of the received signal in dB scale
d_{smin}	minimal stationarity length
w	window length of stationary interval
v_{max}	maximal speeds of the Rx
T_{smin}	minimal stationarity time
ζ	signal-to-noise ratio

Bibliography

[1] Spirent communications SR5500 wireless channel emulator operations manual. www.spirent-com.com [Online].

[2] IEEE standard for information technology– local and metropolitan area networks– specific requirements– part 11: Wireless LAN medium access control (MAC) and physical layer (PHY) specifications amendment 6: Wireless access in vehicular environments. *IEEE Std 802.11p-2010 (Amendment to IEEE Std 802.11-2007 as amended by IEEE Std 802.11k-2008, IEEE Std 802.11r-2008, IEEE Std 802.11y-2008, IEEE Std 802.11n-2009, and IEEE Std 802.11w-2009)*, pages 1–51, 2010.

[3] 3GPP-TS 22.185. Service requirements for V2X services. pages 1–16, version 14.3.0 Release 14, 2017.

[4] T. Abbas, L. Bernado, A. Thiel, C. F. Mecklenbrauker, and F. Tufvesson. Measurements based channel characterization for vehicle-to-vehicle communications at merging lanes on highway. In *2013 IEEE 5th International Symposium on Wireless Vehicular Communications (WiVeC)*, pages 1–5, 2013.

[5] T. Abbas, J. Karedal, F. Tufvesson, A. Paier, L. Bernado, and A. F. Molisch. Directional analysis of vehicle-to-vehicle propagation channels. In *2011 IEEE 73rd Vehicular Technology Conference (VTC Spring)*, pages 1–5, May 2011.

[6] Taimoor Abbas. *Measurement Based Channel Characterization and Modeling for Vehicle-to-Vehicle Communications*. PhD thesis, Department of Electrical and Information Technology, 2014.

[7] Taimoor Abbas. *Measurement Based Channel Characterization and Modeling for Vehicle-to-Vehicle Communications*. PhD dissertation, Lund university, 2014.

[8] M. A. Abu-Rgheff. *Introduction to CDMA wireless communication*. 1st Edition, Academic Press is an imprint of Elsevier, 2007.

[9] G. Acosta and M. A. Ingram. Model development for the wideband expressway vehicle-to-vehicle 2.4 GHz channel. In *IEEE Wireless Communications and Networking Conference, 2006. WCNC 2006.*, volume 3, pages 1283–1288, 2006.

[10] G. Acosta and M.A. Ingram. Model development for the wideband expressway vehicle-to-vehicle 2.4 ghz channel. In *IEEE Wireless Communications and Networking Conference, 2006. WCNC 2006.*, volume 3, pages 1283–1288, 2006.

[11] G. Acosta-Marum and M. A. Ingram. Six time- and frequency- selective empirical channel models for vehicular wireless LANs. *IEEE Vehicular Technology Magazine*, 2(4):4–11, 2007.

[12] G. Acosta-Marum and M. A. Ingram. Six time- and frequency-selective empirical channel models for vehicular wireless LANs. In *2007 IEEE 66th Vehicular Technology Conference*, pages 2134–2138, 2007.

[13] Shamshad Ahmad, Bawadi MA, W Wanhussin, Taksiah Majid, S. Ahamad, and Mohd Sanusi. First and second order Markov chain models for synthetic generation of wind speed time series. *Energy*, 30:693–708, 04 2005.

[14] A.S. Akki and F. Haber. A statistical model of mobile-to-mobile land communication channel. *IEEE Transactions on Vehicular Technology*, 35(1):2–7, 1986.

[15] P. Almers, E. Bonek, A. Burr, N. Czink, M. Debbah, V. Degli-esposti, H. Hofstetter, P. Kyösti, D. Laurenson, G. Matz, A. F. Molisch, C. Oestges, and H. Özcelik. Survey of channel and radio propagation models for wireless MIMO systems. *EURASIP Journal on Wireless Communications and Networking*.

[16] P. Almers, E. Bonek, A. Burr, N. Czink, M. Debbah, V. Esposti, H. Hofstetter, P. Kyosti, D. Laurenson, G. Matz, A. Molisch, C. Oestges, , and H. Ozcelik. Survey of channel and radio propagation models for wireless MIMO systems. *EURASIP Journal on Wireless Communications and Networking*, (1), 2007.

[17] G. E. Athanasiadou, A. R. Nix, and J. P. McGeehan. A microcellular ray-tracing propagation model and evaluation of its narrow-band and wide-band predictions. *IEEE Journal on Selected Areas in Communications*, 18(3):322–335, 2000.

[18] T. Aulin. Characteristics of a digital mobile radio channel. *IEEE Transactions on Vehicular Technology*, 30(2):45–53, 1981.

[19] J. Barros and R. I. Diego. Effects of windowing on the measurement of harmonics and interharmonics in the IEC standard framework. In *2006 IEEE Instrumentation and Measurement Technology Conference Proceedings*, pages 2294–2299, April 2006.

[20] N. C. Beaulieu. An extended limit theorem for correlated Lognormal sums. *IEEE Transactions on Communications*, 60(1):23–26, January 2012.

[21] P. Bello. Characterization of randomly time-variant linear channels. *IEEE Transactions on Communications Systems*, 11(4):360–393, December 1963.

[22] L. Bernadó, N. Czink, T. Zemen, and P. Belanović. Physical layer simulation results for IEEE 802.11p using vehicular non-stationary channel model. In *2010 IEEE International Conference on Communications Workshops*, pages 1–5, 2010.

[23] J. A. C. Bingham. Multicarrier modulation for data transmission: an idea whose time has come. *IEEE Communications Magazine*, 28(5):5–14, 1990.

[24] S. Biswas, R. Tatchikou, and F. Dion. Vehicle-to-vehicle wireless communication protocols for enhancing highway traffic safety. *IEEE Communications Magazine*, 44(1):74–82, Jan 2006.

[25] A. Boettcher, C. Schneider, M. Narandzic, P. Vary, and R. S. Thomä. Power and delay domain parameters of channel measurements at 2.53 GHz in an urban macro cell scenario. In *Proceedings of the Fourth European Conference on Antennas and Propagation*, pages 1–5, April 2010.

[26] Santana Burintramart, Nuri Yilmazer, Tapan K. Sarkar, and Magdalena Salazar-Palma. Different perspective on channel capacity theorem. In *2007 IEEE Antennas and Propagation Society International Symposium*, pages 3241–3244, 2007.

[27] S. Catreux, V. Erceg, D. Gesbert, and R. W. Heath. Adaptive modulation and MIMO coding for broadband wireless data networks. *IEEE Communications Magazine*, 40(6):108–115, 2002.

[28] S. Chatzinotas, M. A. Imran, and R. Hoshyar. On the ergodic capacity of the wideband MIMO channel. In *VTC Spring 2009 - IEEE 69th Vehicular Technology Conference*, pages 1–5, 2009.

[29] Jalel Chebil, Hanene Zormati, and Jamel Belhadj Taher. Geometry-based channel modelling for vehicle-to-vehicle communication: A review. *International Journal of Antennas and Propagation*, 2021(Article ID 4293266):1–10, 2021.

[30] S. Chen, J. Hu, Y. Shi, and L. Zhao. LTE-V: A TD-LTE-based V2X solution for future vehicular network. *IEEE Internet of Things Journal*, 3(6):997–1005, 2016.

[31] L. Cheng, B. E. Henty, D. D. Stancil, F. Bai, and P. Mudalige. Mobile vehicle-to-vehicle narrowband channel measurement and characterization of the 5.9 GHz dedicated short range communication (DSRC) frequency band. *IEEE Journal on Selected Areas in Communications*, 25(8):1501–1516, 2007.

[32] M. Chiani, M. Z. Win, and A. Zanella. On the capacity of spatially correlated MIMO rayleigh-fading channels. *IEEE Transactions on Information Theory*, 49(10):2363–2371, 2003.

[33] Chun-Liang Liu, Chung-Hsin Huang, and Chien-Ching Chiu. Channel capacity for various materials of partitions in indoor ultra wideband communication system with multiple input multiple output. In *2007 3rd IEEE/IFIP International Conference in Central Asia on Internet*, pages 1–5, 2007.

[34] Spirent Communications. Fading basics narrowband, wideband, and spatial channels. pages 1–16, 08 2018.

[35] COST207. Digital land mobile radio communications. *Office for Official Publications in European Communities*, pages final report, Luxembourg, Tech. Rep., 1989.

[36] D. Czaniera, M. Käske, G. Sommerkorn, C. Schneider, R. S. Thomä, G. Del Galdo, M. Boban, and J. Luo. Investigation on stationarity of V2V channels in a highway scenario. In *2019 13th European Conference on Antennas and Propagation (EuCAP)*, pages 1–5, 2019.

[37] M. Dababneh. Mobile environment coverage issues and delay spread calculations in modern communications systems. *Journal of Applied Sciences*, (5):597–603, 2005.

[38] J. A. Dabin, Nan Ni, A. M. Haimovich, E. Niver, and H. Grebel. The effects of antenna directivity on path loss and multipath propagation in UWB indoor wireless channels. In *IEEE Conference on Ultra Wideband Systems and Technologies, 2003*, pages 305–309, Nov 2003.

[39] F. Darbari, R. W. Stewart, and I. A. Glover. *MIMO Channel Modelling*. InTech, 2010.

[40] Faisal Darbari, Robert W. Stewart, and Ian Glover. MIMO channel modelling. In Sebastian Miron, editor, *Signal Processing*. InTech, March 2010.

[41] V. Degli-Esposti, F. Fuschini, E. M. Vitucci, and G. Falciasecca. Measurement and modelling of scattering from buildings. *IEEE Transactions on Antennas and Propagation*, 55(1):143–153, 2007.

[42] Marc Peter Deisenroth, A. Aldo Faisal, and Cheng Soon Ong. *Mathematics for Machine Learning*. Cambridge University Press, 2019.

[43] Do-Sik Yoo and W. E. Stark. Characterization of WSSUS channels: normalized mean square covariance and diversity combining. *IEEE Transactions on Wireless Communications*, 4(4):1307–1310, July 2005.

[44] Diego Dupleich, Müller Robert, and Reiner Thomä. Practical aspects on the noise floor estimation and cut-off margin in channel sounding applications. In *15th EuCAP*, pages 1–5, 2021.

[45] P. Embrechts and M. Hofert. A note on generalized inverses. pages 1–11, february 2014.

[46] W. Fan, P. Kyösti, J. Ø. Nielsen, and G. F. Pedersen. Wideband MIMO channel capacity analysis in multiprobe Anechoic chamber setups. *IEEE Transactions on Vehicular Technology*, 65(5):2861–2871, 2016.

[47] B.H. Fleury. First- and second-order characterization of direction dispersion and space selectivity in the radio channel. *IEEE Transactions on Information Theory*, 46(6):2027–2044, 2000.

[48] F. Perez Fontan and P. Marino Espineira. *Modeling the Wireless Propagation Channel*. 1st Ed., John Wiley, New York, NY, 2008.

[49] A. Fort, C. Desset, P. De Doncker, P. Wambacq, and L. Van Biesen. An ultra-wideband body area propagation channel model-from statistics to implementation. *IEEE Transactions on Microwave Theory and Techniques*, 54(4):1820–1826, June 2006.

[50] A. Fort, C. Desset, P. De Doncker, P. Wambacq, and L. Van Biesen. An ultra-wideband body area propagation channel model-from statistics to implementation. *IEEE Transactions on Microwave Theory and Techniques*, 54(4):1820–1826, 2006.

[51] G FU and D Debraj. Methodology of homogeneous and non-homogeneous Markov chains for modeling bridge element deterioration, 2008.

[52] T. Fugen, S. Knorzer, M. Landmann, R. S. Thomä, and W. Wiesbeck. A 3-D ray tracing model for macrocell urban environments and its verification with measurements. In *The Second European Conference on Antennas and Propagation, EuCAP 2007*, pages 1–6, 2007.

[53] R. Ganesh and K. Pahlavan. Statistics of short time and spatial variations measured in wideband indoor radio channels. *IEE Proceedings H - Microwaves, Antennas and Propagation*, 140(4):297–302, Aug 1993.

[54] D. Gesbert, M. Shafi, Da-shan Shiu, P. J. Smith, and A. Naguib. From theory to practice: an overview of MIMO space-time coded wireless systems. *IEEE Journal on Selected Areas in Communications*, 21(3):281–302, 2003.

[55] S. S. Ghassemzadeh, L. J. Greenstein, T. Sveinsson, A. Kavcic, and V. Tarokh. UWB delay profile models for residential and commercial indoor environments. *IEEE Transactions on Vehicular Technology*, 54(4):1235–1244, July 2005.

[56] G. Ghiaasi, M. Ashury, D. Vlastaras, M. Hofer, Zhinan Xu, and T. Zemen. Real-time vehicular channel emulator for future conformance tests of wireless its modems. In *2016 10th European Conference on Antennas and Propagation (EuCAP)*, pages 1–5, 2016.

[57] A. Goldsmith, S. A. Jafar, N. Jindal, and S. Vishwanath. Capacity limits of MIMO channels. *IEEE Journal on Selected Areas in Communications*, 21(5):684–702, 2003.

[58] Andrea Goldsmith. *Wireless Communications*. Cambridge University Press40 W. 20 St. New York, NY United States, 2005.

[59] H. V. Poor and G. W. Wornell. *Wireless Communications: Signal Processing Perspectives*. Prentice Hall, Upper Saddle River, NJ, 1998.

[60] P. S. Harvey, Henri P. Gavin, and Jeffrey T. Scruggs. Probability distributions. pages 1–15, Spring 2016.

[61] N. Hassan, M. Käske, C. Schneider, G. Sommerkorn, and R. Thomä. Measurement based determination of parameters for in-stationary TDL models with reduced number of taps. In *2019 13th European Conference on Antennas and Propagation (EuCAP)*, pages 1–5, March 2019.

[62] N. Hassan, C. Schneider, R. Thomä, and G. Del Galdo. Characterization of slow and fast fading in V2I channels for smart cities. In *2021 15th European Conference on Antennas and Propagation (EuCAP)*, pages 1–5, March 2021.

[63] Nina Hassan, Diego A. Dupleich, Christian Schneider, Reiner Thomä, and Giovanni Del Galdo. MIMO-TDL model parameter estimation from V2I channel sounding. In *2021 15th European Conference on Antennas and Propagation (EuCAP)*, pages 1–5, 2021.

[64] Nina Hassan, Martin Käske, Christian Schneider, Gerd Sommerkorn, Reiner Thomä, and David Matolak. Measurement-based determination of parameters for non-stationary TDL models with reduced number of taps. *IET Microwaves, Antennas & Propagation*, 14(14):1719–1732, 2020.

[65] Nina Hassan, Christian Schneider, Giovanni Del Galdo, and Reiner Thomä. Analysis of V2I MIMO radio channels for Non-WSSUS TDL modeling. In *EUROPEAN COOPERATION IN SCIENCE AND TECHNOLOGY (EURO-COST)*, pages 1–9, 2020.

[66] Nina Hassan and Reiner Thomä. Extended TDL modeling for V2X channels. In *EUROPEAN COOPERATION IN SCIENCE AND TECHNOLOGY (EURO-COST)*, pages 1–8, 2018.

[67] Nina Hassan, Reiner Thomä, and David W. Matolak. In-stationary tapped delay line channel modeling and simulation. In *2020 14th European Conference on Antennas and Propagation (EuCAP)*, pages 1–5, 2020.

[68] Konrad Hofbauer and Gernot Kubin. Aeronautical voice radio channel modelling and simulation–a tutorial review. 01 2006.

[69] M. Hofer, Z. Xu, D. Vlastaras, B. Schrenk, D. Löschenbrand, F. Tufvesson, and T. Zemen. Real-time geometry-based wireless channel emulation. *IEEE Transactions on Vehicular Technology*, 68(2):1631–1645, 2019.

[70] Justin T. Holzer. Wideband channel characterization for MIMO scenario. In *Brigham Young University*, 2004.

[71] A. Ispas, G. Ascheid, C. Schneider, and R. Thomä. Analysis of local quasi-stationarity regions in an urban macrocell scenario. In *2010 IEEE 71st Vehicular Technology Conference*, pages 1–5, 2010.

[72] ITU. Guidlines for evalutation of radio transmission technologies for IMT-2000, 1997.

[73] ITU-R-P.1407-1. Multipath propagation and parameterization of its characteristics. pages 1–4, 1999.

[74] W.C. Jakes. *Microwave Mobile Communications*. New York: Wiley, 1974.

[75] Volker Jungnickel, Stephan Jaeckel, Lars Thiele, Lei Jiang, Udo Kruger, Armin Brylka, and Clemens von Helmolt. Capacity measurements in a cooperative MIMO network. *IEEE Transactions on Vehicular Technology*, 58(5):2392–2405, 2009.

[76] A. A. Kalachikov and N. S. Shelkunov. Measurement of wireless MIMO channel parameters at 2.3 GHz. In *2015 International Siberian Conference on Control and Communications (SIBCON)*, pages 1–4, 2015.

[77] J. Karedal, N. Czink, A. Paier, F. Tufvesson, and A. F. Molisch. Path loss modeling for vehicle-to-vehicle communications. *IEEE Transactions on Vehicular Technology*, 60(1):323–328, 2011.

[78] J. Karedal, F. Tufvesson, T. Abbas, O. Klemp, A. Paier, L. Bernadó, and A. F. Molisch. Radio channel measurements at street intersections for vehicle-to-vehicle safety applications. In *2010 IEEE 71st Vehicular Technology Conference*, pages 1–5, 2010.

[79] J. Karedal, F. Tufvesson, N. Czink, A. Paier, C. Dumard, T. Zemen, C. F. Mecklenbrauker, and A. F. Molisch. A geometry-based stochastic MIMO model for vehicle-to-vehicle communications. *IEEE Transactions on Wireless Communications*, 8(7):3646–3657, 2009.

[80] Johan Karedal, Fredrik Tufvesson, Nicolai Czink, Alexander Paier, Charlotte Dumard, Thomas Zemen, Christoph F. Mecklenbrauker, and Andreas F. Molisch. A geometry-based stochastic mimo model for vehicle-to-vehicle communications. *IEEE Transactions on Wireless Communications*, 8(7):3646–3657, 2009.

[81] M. Kawser, S. S. Sajjad, S. Fahad, S. Ahmed, and H. A. Rafi. Perspective of vehicle-to-everything (V2X) communication towards 5G. *IJCSNS International Journal of Computer Science and Network Security*, 19(4), 2019.

[82] Markus Landmann, Martin Käske, and Reiner S. Thomä. Impact of incomplete and inaccurate data models on high resolution parameter estimation in multidimensional channel sounding. *IEEE Transactions on Antennas and Propagation*, 60(2):557–573, 2012.

[83] V. Lavanya, G. Sasibhushana Rao, and Bharati Bidikar. Fast fading mobile channel modeling for wireless communication. *Procedia Computer Science*, 85:777 – 781, 2016. International Conference on Computational Modelling and Security (CMS 2016).

[84] Y. Li, B. Ai, D. G. Michelson, S. Lin, Q. Wang, and Z. Zhong. A method for generating correlated taps in stochastic vehicle-to-vehicle channel models. In *2015 IEEE 81st Vehicular Technology Conference (VTC Spring)*, pages 1–5, May 2015.

[85] Yan Li, Bo Ai, Xiang Cheng, Siyu Lin, and Zhangdui Zhong. A TDL based Non-WSSUS vehicle-to-vehicle channel model. *Hindawi*, 2013:8 pages, Jul 2013.

[86] Liu Liu, Cheng Tao, Rongchen Sun, Houjin Chen, and Zihuai Lin. Non-stationary channel characterization for high-speed railway under viaduct scenarios. *Chinese Science Bulletin*, 59(35):4988–4998, Dec 2014.

[87] Rachna Mahey and Jyoteesh Malhotra. On MIMO channel modeling for the mobile wireless systems. *International Journal of Future Generation Communication and Networking*, 8:23–38, 10 2015.

[88] S. Maji, A. C. Berg, and J. Malik. Efficient classification for additive kernel SVMs. *IEEE Transactions on Pattern Analysis and Machine Intelligence*, 35(1):66–77, Jan 2013.

[89] F. Mani and C. Oestges. Ray-tracing evaluation of diffuse scattering in an outdoor scenario. In *Proceedings of the 5th European Conference on Antennas and Propagation (EUCAP)*, pages 3439–3443, 2011.

[90] Z. Mansor, E. Mellios, G. Hilton, J. McGeehan, and A. Nix. MIMO exploitation of 3D multipath statistics in a heterogeneous lte-advanced network. *International Journal of Antennas and Propagation*, (1):15, 2013.

[91] D. W. Matolak. Channel modeling for vehicle-to-vehicle communications. *IEEE Communications Magazine*, 46(5):76–83, May 2008.

[92] D. W. Matolak and R. Sun. Air ground channel characterization for unmanned aircraft systems part I: Methods, measurements, and models for over-water settings. *IEEE Transactions on Vehicular Technology*, 66(1):26–44, Jan 2017.

[93] D. W. Matolak and Q. Wu. Vehicle-to-vehicle channels: Are we done yet? In *2009 IEEE Globecom Workshops*, pages 1–6, Nov 2009.

[94] D. W. Matolak and Q. Wu. Channel models for v2v communications: A comparison of different approaches. In *Proceedings of the 5th European Conference on Antennas and Propagation (EUCAP)*, pages 2891–2895, 2011.

[95] D. W. Matolak and Q. Wu. Channel models for V2V communications: A comparison of different approaches. In *Proceedings of the 5th European Conference on Antennas and Propagation (EUCAP)*, pages 2891–2895, 2011.

[96] David W. Matolak. Wireless channel characterization in the 5 GHz microwave landing system extension band for airport surface areas. *Final Project Report, NASA CR-2007-214456*, May 2007.

[97] G. Matz. On non-WSSUS wireless fading channels. *IEEE Transactions on Wireless Communications*, 4(5):2465–2478, Sep. 2005.

[98] G. Matz, A. F. Molisch, F. Hlawatsch, M. Steinbauer, and I. Gaspard. On the systematic measurement errors of correlative mobile radio channel sounders. *IEEE Transactions on Communications*, 50(5):808–821, 2002.

[99] J. Maurer, T. Fugen, T. Schafer, and W. Wiesbeck. A new inter-vehicle communications (IVC) channel model. In *IEEE 60th Vehicular Technology Conference, 2004. VTC2004-Fall. 2004*, volume 1, pages 9–13 Vol. 1, 2004.

[100] J. Maurer, T. Fugen, and W. Wiesbeck. Narrow-band measurement and analysis of the inter-vehicle transmission channel at 5.2 GHz. In *Vehicular Technology Conference. IEEE 55th Vehicular Technology Conference. VTC Spring 2002 (Cat. No.02CH37367)*, volume 3, pages 1274–1278 vol.3, 2002.

[101] Jurgen Maurer, Thomas Fügen, Thomas Schäfer, and Werner Wiesbeck. A new inter-vehicle communications (IVC) channel model. *in Proceedings of the IEEE 60th Vehicular Technology Conference (VTC 04)*, pages 9–13 pages, Sep 2004.

[102] C. F. Mecklenbrauker, A. F. Molisch, J. Karedal, F. Tufvesson, A. Paier, L. Bernado, T. Zemen, O. Klemp, and N. Czink. Vehicular channel characterization and its implications for wireless system design and performance. *Proceedings of the IEEE*, 99(7):1189–1212, 2011.

[103] WINNER II Channel Models. Wireless channel characterization in the 5 GHz microwave landing system extension band for airport surface areas. *IST-4-027756 WINNER II. D1.1.2 V1.1. IST.*, November 2007.

[104] R. Molina-Masegosa and J. Gozalvez. LTE-V for sidelink 5G V2X vehicular communications: A new 5G technology for short-range vehicle-to-everything communications. *IEEE Vehicular Technology Magazine*, 12(4):30–39, 2017.

[105] A. F. Molisch, F. Tufvesson, J. Karedal, and C. F. Mecklenbrauker. A survey on vehicle-to-vehicle propagation channels. *IEEE Wireless Communications*, 16(6):12–22, 2009.

[106] A.F. Molisch. A generic model for MIMO wireless propagation channels in macro- and microcells. *IEEE Transactions on Signal Processing*, 52(1):61–71, 2004.

[107] Andreas F. Molisch and Fredrik Tufvesson. MIMO channel capacity and measurements. *Hindawi*, pages 467–490, 2006.

[108] N. Moraitis and P. Constantinou. Measurements and characterization of wideband indoor radio channel at 60 GHz. *IEEE Transactions on Wireless Communications*, 5(4):880–889, 2006.

[109] R. Müller, M. Käske, P. Rauschenbach, G. Sommerkorn, C. Schneider, F. Wollenschläger, S. Häfner, and R. S. Thomä. Design of a circular antenna array for MIMO channel sounding application at 2.53 GHz. In *The 8th European Conference on Antennas and Propagation (EuCAP 2014)*, pages 239–243, 2014.

[110] M. Paetzold and C. A. Gutierrez. Definition and analysis of quasi-stationary intervals of mobile radio channels - invited paper. In *2018 IEEE 87th Vehicular Technology Conference (VTC Spring)*, pages 1–6, 2018.

[111] A. Paier, L. Bernadó, J. Karedal, O. Klemp, and A. Kwoczek. Overview of vehicle-to-vehicle radio channel measurements for collision avoidance applications. In *2010 IEEE 71st Vehicular Technology Conference*, pages 1–5, 2010.

[112] A. Paier, J. Karedal, N. Czink, H. Hofstetter, C. Dumard, T. Zemen, F. Tufvesson, C. F. Mecklenbrauker, and A. F. Molisch. First results from car-to-car and car-to-infrastructure radio channel measurements at 5.2 GHz. In *2007 IEEE 18th International Symposium on Personal, Indoor and Mobile Radio Communications*, pages 1–5, 2007.

[113] Alexander Paier, Thomas Zemen, Laura Bernado, Gerald Matz, Johan Karedal, Nicolai Czink, Charlotte Dumard, Fredrik Tufvesson, Andreas F. Molisch, and Christoph F. Mecklenbrauker. Non-WSSUS vehicular channel characterization in highway and urban scenarios at 5.2 GHz using the local scattering function. In *2008 International ITG Workshop on Smart Antennas*, pages 9–15, 2008.

[114] Diwaker Pant, Abhishek Gupta, Sarbjeet Singh, and S Sachan. MIMO channel modelling methods: An overview. 01 2013.

[115] Ravinder Singh Parneet Kaur. Complementary cumulative distribution function for performance analysis of OFDM signals. *IOSR Journal of Electronics and Communication Engineering (IOSR-JECE)*, 2(5):05–07, 2012.

[116] J. D. Parsons. *The Mobile Radio Propagation Channel*. 2nd Ed., JOHN WILEY, UK, 1992.

[117] J. D. Parsons. *The Mobile Radio Propagation Channel*. 2nd Ed., John Wiley, New York, NY, 2000.

[118] F. Perez-Fontan, M. A. Vazquez-Castro, S. Buonomo, J. P. Poiares-Baptista, and B. Arbesser-Rastburg. S-band LMS propagation channel behaviour for different environments, degrees of shadowing and elevation angles. *IEEE Transactions on Broadcasting*, 44(1):40–76, March 1998.

[119] S Popa, N Draghiciu, and R Reiz. Fading types in wireless communications systems. *Journal of Electrical and Electronics Engineering*, 1, 05 2008.

[120] Jiang Qiang-rong and Gao Yuan. Face recognition based on detail histogram intersection kernel. In *2009 IEEE International Conference on Intelligent Computing and Intelligent Systems*, volume 4, pages 71–74, Nov 2009.

[121] T. S. Rappaport. *Wireless Communications: Principles and Practice*. 2nd Ed., Prentice Hall, Upper Saddle River, NJ, 2002.

[122] O. Renaudin, V. Kolmonen, P. Vainikainen, and C. Oestges. Car-to-car channel models based on wideband MIMO measurements at 5.3 GHz. In *2009 3rd European Conference on Antennas and Propagation*, pages 635–639, March 2009.

[123] O. Renaudin, V. Kolmonen, P. Vainikainen, and C. Oestges. Non-stationary narrowband MIMO inter-vehicle channel characterization in the 5-GHz band. *IEEE Transactions on Vehicular Technology*, 59(4):2007–2015, 2010.

[124] A. Richter, R.S. Thomä, and T. Taga. Directional measurement and analysis of propagation path variations in a street micro-cell scenario. In *The 57th IEEE Semiannual Vehicular Technology Conference, 2003. VTC 2003-Spring.*, volume 1, pages 246–250 vol.1, 2003.

[125] Andreas Richter. *Estimation of Radio Channel Parameters: Models and Algorithms*. PhD thesis, Technische Universität Ilmenau, 2005.

[126] S. Saunders. *Antennas and Propagation for Wireless Communication Systems*. Wiley, 2000.

[127] S. R. Saunders and F. R. Bonar. Mobile radio propagation in built-up areas: a numerical model of slow fading. In *[1991 Proceedings] 41st IEEE Vehicular Technology Conference*, pages 295–300, May 1991.

[128] C. Schneider, M. Narandzic, M. Käske, G. Sommerkorn, and R. S. Thomä. Large scale parameter for the WINNER II channel model at 2.53 GHz in urban macro cell. In *2010 IEEE 71st Vehicular Technology Conference*, pages 1–5, 2010.

[129] I. Sen and D. W. Matolak. Vehicle channel models for the 5-GHz band. *IEEE Transactions on Intelligent Transportation Systems*, 9(2):235–245, June 2008.

[130] B. Sklar. Rayleigh fading channels in mobile digital communication systems .i. characterization. *IEEE Communications Magazine*, 35(7):90–100, 1997.

[131] Bernard Sklar. Rayleigh fading channels in mobile digital communication systems part i: Characterization. *Communications Magazine, IEEE*, 35:136–146, 10 1997.

[132] Gerd Sommerkorn, Martin Käske, Christian Schneider, Stephan Häfner, and Reiner Thomä. Full 3D MIMO channel sounding and characterization in an urban macro cell. In *2014 XXXIth URSI General Assembly and Scientific Symposium (URSI GASS)*, pages 1–4, 2014.

[133] Nuan Song. *Ultra Wideband Communications: from Analog to Digital*. Dissertation zur erlangung des akademischen grades doktor-ingenieur, Fakultät für Elektrotechnik und Informationstechnik der Technischen Universität Ilmenau, 2012.

[134] W. Stallings. *Data and Computer Communications*. 8th Ed., Upper Saddle River, New Jersey, 2005.

[135] M. Steinbauer, A.F. Molisch, and E. Bonek. The double-directional radio channel. *IEEE Antennas and Propagation Magazine*, 43(4):51–63, 2001.

[136] R. Stridh, B. Ottersten, and P. Karlsson. MIMO channel capacity of a measured indoor radio channel at 5.8 GHz. In *Conference Record of the Thirty-Fourth Asilomar Conference on Signals, Systems and Computers (Cat. No.00CH37154)*, volume 1, pages 733–737 vol.1, 2000.

[137] G. Stuber. *Principles of Mobile Communications*. 2nd Ed., KLUWER ACADEMIC Publishers, 2002.

[138] H. Suzuki. A statistical model for urban radio propogation. *IEEE Transactions on Communications*, 25(7):673–680, 1977.

[139] S. Tabbane. *Handbook of wireless mobile networks and mobile computing*. Artech House Publishers, Norwood, MA, 2000.

[140] M. Tan and J. Chen. Comparison and analysis of MIMO channel capacity. In *2007 International Conference on Wireless Communications, Networking and Mobile Computing*, pages 299–301, 2007.

[141] Giorgio Taricco. On the convergence of multipath fading channel gains to the rayleigh distribution. *IEEE Wireless Communications Letters*, 4(5):549–552, 2015.

[142] R. S. Thomä, D. Hampicke, A. Richter, G. Sommerkorn, A. Schneider, and U. Trautwein. Identification of time-variant directional mobile radio channels. In *IMTC/99. Proceedings of the 16th IEEE Instrumentation and Measurement Technology Conference (Cat. No.99CH36309)*, volume 1, pages 176–181 vol.1, 1999.

[143] R. S. Thomä, D. Hampicke, A. Richter, G. Sommerkorn, A. Schneider, U. Trautwein, and W. Wirnitzer. Identification of time-variant directional mobile radio channels. *IEEE Transactions on Instrumentation and Measurement*, 49(2):357–364, 2000.

[144] R. S. Thomä, M. Landmann, and A. Richter. RIMAX-A maximum likelihood framework for parameter estimation in multidimensional channel sounding. In *Proceedings of the International Symposium on Antennas and Propagation (ISAP'04)*, page 53–56, 2004.

[145] Reiner S. Thomä, Dirk Hampicke, Andreas Richter, Gerd Sommerkorn, and Uwe Trautwein. MIMO vector channel sounder measurement for smart antenna system evaluation. *Eur. Trans. Telecommun.*, 12(5):427–438, 2001.

[146] W. H. Tranter, K. S. Shanmugan, T. S. Rappaport, and K. L. Kosbar. *Principles of Communication Systems Simulation with Wireless Applications*. Bordentown, NJ, USA: Bernard Goodwin, 2003.

[147] U. Trautwein, K. Blau, D. Bruckner, F. Herrmann, A. Richter, G. Sommerkorn, and R. S. Thomä. Radio channel measurement for realistic simulation of adaptive antenna arrays. In *ITG-Fachbericht 145, The 2nd European Personal Mobile Communications Conference (EPMCC '97) together with 3. ITG-Fachtagung "Mobile Kommunikation,"*, page 491–498, 1997.

[148] H. L. Van Trees, A. B. Baggeroer, and D. L. Snyder. IX. detection and estimation theory. `https://dspace.mit.edu/bitstream/handle/1721.1/55859/RLE_QPR_093_IX.pdf`. Accessed on 2019-08-14.

[149] David Tse. *Fundamentals of Wireless Communication*. Cambridge University Press, 2004.

[150] R. Vaughan. Channels, propagation and antennas for mobile communications. *IET*, 50, 2003.

[151] D. Vlastaras, S. Malkowsky, and F. Tufvesson. Stress test of vehicular communication transceivers using software defined radio. In *2015 IEEE 81st Vehicular Technology Conference (VTC Spring)*, pages 1–4, 2015.

[152] Cheng xiang Wang, Xiang Cheng, and David I. Laurenson. Vehicle-to-vehicle channel modeling and measurements: recent advances and future challenges. *IEEE Communications Magazine*, 47(11):96–103, 2009.

[153] Q. Wang, B. Ai, L. Liu, and Z. Zhong. A tapped delay-based channel model for vehicle-to-vehicle communications. In *5th IET International Conference on Wireless, Mobile and Multimedia Networks (ICWMMN 2013)*, pages 132–135, Nov 2013.

[154] E. Winarno, W. Hadikurniawati, and R. N. Rosso. Location based service for presence system using haversine method. In *2017 International Conference on Innovative and Creative Information Technology (ICITech)*, pages 1–4, Nov 2017.

[155] Qiong Wu. *Non-stationary Vehicle-to-Vehicle Channel Characterization*. PhD dissertation, Ohio university, 2012.

[156] S. Wyne, A. F. Molisch, P. Almers, G. Eriksson, J. Karedal, and F. Tufvesson. Outdoor-to-indoor office MIMO measurements and analysis at 5.2 GHz. *IEEE Transactions on Vehicular Technology*, 57(3):1374–1386, 2008.

[157] Xiongwen Zhao, J. Kivinen, P. Vainikainen, and K. Skog. Characterization of doppler spectra for mobile communications at 5.3 GHz. *IEEE Transactions on Vehicular Technology*, 52(1):14–23, 2003.

[158] Xiongwen Zhao, J. Kivinen, P. Vainikainen, and K. Skog. Characterization of doppler spectra for mobile communications at 5.3 GHz. *IEEE Transactions on Vehicular Technology*, 52(1):14–23, 2003.

[159] Xiongwen Zhao, J. Kivinen, and P. Vainnikainen. Tapped delay line channel models at 5.3 GHz in indoor environments. In *Vehicular Technology Conference Fall 2000. IEEE VTS Fall VTC2000. 52nd Vehicular Technology Conference (Cat. No.00CH37152)*, volume 1, pages 1–5 vol.1, 2000.

[160] Xiongwen Zhao, V. Kolmonen, Suiyan Geng, and P. Vainikainen. Tapped delay line channel models for indoor MIMO radio channels at 5 GHz. In *34th European Microwave Conference, 2004.*, volume 3, pages 1261–1264, 2004.

[161] X. Yang, L. Liu, N. H. Vaidya, and F. Zhao. A vehicle-to-vehicle communication protocol for cooperative collision warning. In *The First Annual International Conference on Mobile and Ubiquitous Systems: Networking and Services, 2004. MOBIQUITOUS 2004.*, pages 114–123, Aug 2004.

[162] Ying-Wen Bai, Wen-Yang Chu, Chien-Yu Chen, Yi-Ting Lee, Yi -Ching Tsai, and Cheng-Hung Tsai. The combination of Kaiser window and moving average for the low-pass filtering of the remote ECG signals. In *Proceedings. 17th IEEE Symposium on Computer-Based Medical Systems*, pages 273–278, June 2004.

[163] T. Zemen. Wireless communications over time-variant channels. *Wien University*, pages 1–192, 2012.

[164] T. Zemen, L. Bernado, N. Czink, and A. F. Molisch. Iterative time-variant channel estimation for 802.11p using generalized discrete prolate spheroidal sequences. *IEEE Transactions on Vehicular Technology*, 61(3):1222–1233, 2012.

[165] T. Zemen and A. F. Molisch. Adaptive reduced-rank estimation of nonstationary time-variant channels using subspace selection. *IEEE Transactions on Vehicular Technology*, 61(9):4042–4056, 2012.

[166] Q.T. Zhang. A generic correlated nakagami fading model for wireless communications. *IEEE Transactions on Communications*, 51(11):1745–1748, 2003.

[167] Yan Zhang, Zunwen He, Wancheng Zhang, Limin Xiao, and Shidong Zhou. Measurement-based delay and doppler characterizations for high-speed railway hilly scenario. *International Journal of Antennas and Propagation*, 2014:1–8, 04 2014.